Integrated lab-on-chip technology for zebrafish embryo sorting and larvae immobilization for drug discovery

A thesis submitted in fulfilment of the requirements for the degree of Doctor of Philosophy

Nurul Hajar Mohd Fuad

MSc. Hons

School of Science

College of Science, Engineering and Health

RMIT University

May 2017

Declaration

I certify that except where due acknowledgement has been made, the work is that of the author alone; the work has not been submitted previously, in whole or in part, to qualify for any other academic award; the content of this thesis is the result of work which has been carried out since the official commencement date of the approved research program; any editorial work, paid or unpaid, carried out by a third party is acknowledged; and, ethics procedures and guidelines have been followed.

Nurul Hajar Mohd Fuad

May 2017

Acknowledgements

The work presented in this thesis would not have been possible without my close association with many people. I take this opportunity to extend my sincere gratitude and appreciation to all those who made this Ph.D. thesis possible.

To my life inspiration, my mother, Mashitah Muhammad and my father, Mohd Fuad Ibrahim because I owe it all to both of you. Thank you for all the supports that I needed throughout this journey.

I am grateful to all my siblings, Nurul Huda, Nurul Haifaa and Nurul Hidayah, who have provided me with the moral and emotional supports in my life. I am also grateful to my in-laws and other family members who have supported me along the way.

I would like to express my sincere gratitude to my supervisor Assoc. Prof. Donald Wlodkowic for the continuous support of my Ph.D. study and related research, for his patience, motivation and immense knowledge. His guidance helped me in all the time of investigation and writing of this thesis. I could not have to have a better supervisor for my Ph.D. study.

I would also like to thank our collaborator, Dr. Jan Kaslin from ARMI, Monash University for the insightful comments, advice, and encouragements regarding this research. It was fantastic to have the opportunity to learn and explore the unique world of zebrafish. Special thanks to Rodney Glanville, from FishCore facilities in providing us the assistance and supplies of zebrafish every week. Without their supports, it would not be possible to conduct this research.

I am also grateful to the following university staff: Dr. Lisa Dias, Leanne Bickford and Shannon Fernandes from Department of Applied Sciences for their unfailing support and assistance for all the essentials needed for postgraduate students.

I thank my fellow labmates: Jin (University of Auckland), Niall (University of Glasgow), Feng, Yushi, Rhys, Milanga, Abhi, Ana, Charlene, and Ben for the great help and support.

And finally, last but not least, my heartfelt thanks to my husband, Mohd Fadly Mohamad Yunus, for his continued unconditional love, support and understanding over the past several years, enabled me to complete the thesis.

To my lovely children, Muhammad Aiman Hazim and Muhammad Aryan Hayyan, who have given me much happiness and keeps me going. You are always my greatest motivation in this challenging journey.

This thesis has been professionally edited by Dr Margaret Johnson of The Book Doctor, in accordance with the guidelines established by the Institute of Professional Editors and the Deans and Directors of Graduate Studies.

Table of Contents

Declaration..i

Acknowledgements..ii

Table of Contents..iv

List of Tables ix

List of Figures x

List of symbols and abbreviations xxvi

Academic Contributions...xxix

Abstract 1

1 Introduction 2

  1.1 Phenotype-based physiological analysis 2

    1.1.1 The role of small model organisms in phenotype-based analysis 3

    1.1.2 Zebrafish as a model organism in biomedicine...4

    1.1.3 Zebrafish as a model organism in ecotoxicology 6

    1.1.4 Phenotyping screening : state-of-the-art using zebrafish embryonic stages 7

    1.1.5 Automation of zebrafish embryonic bioassays: promises and challenges 9

  1.2 Microfluidic lab-on-a-chip (LOC) technologies 10

    1.2.1 Promises of miniaturised analysis for biological sciences..................................13

    1.2.2 Principles of microscale fluid flow 13

    1.2.3 Fabrication methods for LOC devices 17

      1.2.3.1 Material selection for fabricating chip-based devices 17

      1.2.3.2 Conventional methods of fabricating LOC devices 19

    1.2.4 Additive manufacturing: an alternative tool for microfabrication.......................23

1.2.4.1 3D printing technologies 24

1.2.4.2 Applications of 3D printing in microfluidics 32

1.3 Fish-on-chips: chip-based technologies for zebrafish research 38

1.3.1 Culturing embryos on chip-based devices..38

1.3.2 Culturing larvae on chip-based devices..41

1.3.3 High content analysis on chip-based devices 44

1.3.4 Application of LOC devices for zebrafish in drug discovery 45

1.3.4.1 Assessment of cytotoxicity 45

1.3.4.2 Assessment of cardiotoxicity...46

1.3.5 Limitations of current chip-based systems for zebrafish research 47

2 Aims and Objectives 49

3 Materials and Method 50

3.1 Chemicals and materials...50

3.1.1 Chemicals for toxicity tests..50

3.1.2 Low melting point agarose for zebrafish mounting 50

3.2 Zebrafish husbandry and culture...51

3.3 Dechorionation Methods 52

3.4 Acute toxicity test (LC_{10} determination) for cardiovascular toxicity 53

3.5 Fish Embryo Toxicity and Sublethal Embryo Toxicity Index (iFET) 53

3.5.1 End point scoring criteria for FET. 54

3.5.2 End point scoring criteria for the Sublethal Embryo Toxicity Index 54

3.6 Computational fluid dynamics (CFD) analysis and simulation 54

3.7 Multi-layer 3D chip fabrication..55

3.8 Additive manufacturing of off-chip interfaces 55

3.9 Fabrication of polymeric mould for larvae immobilisation devices 56

3.9.1 3D printed master mould 56

3.9.2 PDMS casting 59

3.10 Imaging 60

3.11 Sensing module using differential infrared optical density (DIOD)...........................61

3.12 Image recognition requisition using Roborealm 62

3.13 Actuation of sorting receptacle 62

3.14 Data analysis and controls 62

4 Proof-of-concept Design of Microfluidic Device for Embryo Sorting.........................63

4.1 Introduction 63

4.2 Chip design and fabrication 64

4.3 Zebrafish embryo sorting concept..66

4.4 Discrimination of live from dead embryos using differential infrared optical density (DIOD) 71

4.5 Summary and conclusions 76

5 Millifluidic Device for Immobilisation of Zebrafish Larvae for Cardiotoxicity Analysis 78

5.1 Introduction 78

5.2 Millifluidic chip design and fabrication...79

5.3 Characterisation of 3D-printed moulds for soft lithography.....................................82

5.3.1 Geometric accuracies 82

5.3.2 Surface topography 83

5.4 Device performance for zebrafish larvae trapping..89

5.4.1 The concept of larvae trapping and immobilisation 89

5.4.2 CFD simulations 90

5.5 Improving the design 91

5.6 Biocompatible chip-based physiometer 95
5.6.1 Influence of Tricaine (MS-222) on zebrafish heartbeat 95
5.7 Effect of toxicity on zebrafish heartbeat 97
5.8 Drugs treatment modulates heartbeat using microfluidic device 98
5.8.1 Short-term infusion of drugs 98
5.8.2 Short term infusion–elimination–reinfusion of drugs 100
5.9 Summary and conclusions 102
5.9.1 Design of the chip 102
5.9.2 Effect of all drugs 102
5.9.3 Limitations 103
6 Millifluidics for Dechorionated Zebrafish Embryos 104
6.1 Introduction 104
6.2 Chip design and fabrication 104
6.3 Hydrodynamic trapping of dechorionated embryos 107
6.3.1 Computer fluid simulation 107
6.3.2 Trapping concept 110
6.4 Continuous microperfusion toxicity assays using dechorionated embryos 115
6.4.1 Toxicity analysis using FET protocols 115
6.4.2 Chorion as a barrier to toxicant absorption. 116
6.4.3 Sublethal Fish Embryo Toxicity Index (iFET) 117
6.5 Discussion and conclusions 121
6.5.1 Design of the lab-on-chip device 121
6.5.2 Comparison between FET and iFET scores on embryos 121
6.5.3 Limitations 122
7 Conclusion and Summary 123

7.1 Achievement and impact 123

7.2 Limitations and future work 124

Appendices 126

A1 Software programming 126

A2 Technical specifications of instruments 128

References 134

List of Tables

Table 1.1 Overview of small model organism characteristics for drug screening. Red boxes indicate the poorest in the category (Adapted from reference [8, 11, 21]) 4

Table 1.2. Comparison of microfabrication methods 17

Table 1.3 Comparison of 3D printing technologies 32

Table 3.1 Configuration of 3D printing of polymer larvae chip 57

Table 3.2 Post-processing treatment for different 3D printers 58

List of Figures

Figure 1.1 A transgenic line zebrafish contains enhanced green fluorescent protein (eGFP) under the control of T cell-specific kinase p56^{lck}. In six days post fertilization (dpf) (A) and zebrafish adult (C), the T-cells' fluorescent green thymus is illuminated, as shown by the arrow. (B) No fluorescence is displayed in the thymic area, which indicates an immunodeficiency. (C) The fluorescence has spread from the thymus to the gills, face and body, showing T cell malignancy. (Taken from reference [26]. Reprinted with permission from ©2008 Elsevier Publishing Group). 5

Figure 1.2 Fish embryo test (FET) analysis procedure (left to right): egg collection; the eggs; pre-exposure of fish media in a petri dish; collection of fertilized eggs with an inverted microscope; distribution of the eggs into 24 multi-well plates. (Taken from reference [40]. Reprinted with permission from ©2008 Elsevier Publishing Group)........................ 7

Figure 1.3 Dorsal orientation of zebrafish images at each time point (30, 48 and 72 hpf) for vehicle (0.1% DMSO) and 0.195 µm of butafenacil exposure. O-dianisidine staining was used to assess the presence of haemoglobin in embryos. Haemoglobin-positive cells appeared within the vehicle control embryos after circulation, but were absent following exposure to 0.195 mM of butafenacil. At 48 and 72 hpf, embryos exposed to 0.195 mM butafenacil displayed significantly less haemoglobin than the vehicle controls. Scale bar is 200 µm. (Taken from reference [44]. Reprinted with permission from ©2014 PLOS One). 8

Figure 1.4 Detail configuration of the ZebraFactor system, comprising the WellPlateFeeder (left) and CellSorter (right) using a tubing system as connection. Bar scale is 50 mm. (Taken from reference [55]. Reprinted with permission from ©2011 Society for Laboratory Automation and Screening). 10

Figure 1.5 Three-dimensional microfluidic paper analytical devices (µPAD). (A) Fabrication is by stacking layers of patterned paper with double-sided adhesive tape. (B) Image of designed basket-weave pattern 10 s after coloured dye solutions were added to the sample reservoir. Dotted line indicates the edge of the device. (C and D) Image taken at 2 and 4 min after adding the dyes. The fluids intersect each other on different planes without mixing. The dotted line in (D) represents the cross-sections shown in E, F and G. (E) Cross-section showing a channel connecting top and bottom layers. (F) Three layers of the device, consisting of orthogonal channels at the top and bottom layers of paper. (G) The distribution of coloured fluids in each layer of the device shown in D. Dotted lines depict the edges of the cross section. (Taken from reference [64]. Reprinted with permission from 2008 ©National Academic of Sciences). 12

Figure 1.6 Laminar and turbulent flow streamline characteristics. 14

Figure 1.7 Mass transfer due to a steady diffusion within a microfluidic channel at the boundary of two laminar streams. 16

Figure 1.8 Process flow of the SU-8 microfabrication using photolithography techniques. (a) A 30 µm thick layer of SU-8 material is spin-coated on to a glass substrate. (b) Hot embossing is applied on pre-cured SU-8 at 85°C for 20 minutes in an oven. (c) The other side of the SU-8 layer is exposed to UV light using a UV mask at a dose of 227.6 µW cm^{-2} for 10 minutes. (d) Post baked at 85°C for 2 minutes and the final structure is developed. (e) A layer of 20 µm thick of SU-8 is spin-coated on to a PDMS substrate, followed by post-baking at 85 °C for 30 s (f) The patterned SU-8 layer and the SU-8 cover layer are thermally bonded in an oven at 50°C for 4 minutes. (g) The PDMS substrate is removed from the SU-8 cover layer and sealed micro and nano-channels are formed. (h) The sealed SU-8 channel is exposed to UV light to cross-link the SU-8 cover layer and inlets and outlets are formed. (Taken from reference [148]. Reprinted with permission from ©2014 Royal Society of Chemistry). 20

Figure 1.9 (A) Schematic diagram of the experimental setup for laser ablation methods. (B) An image of the PDMS slab is oriented with the thin edge parallel to the laser beam. (C) Images of micromachined of trenches with different number of passes, *N* and stage velocity, *V.* (D) The micrographs of micromachined channels in borosilicate glass. (Taken from reference [154]. Reprinted with permission from ©2011 Elsevier Publishing Group) 22

Figure 1.10 (A) Schematic diagram of configuration SLA printer with direct write-curing process fabrication. The stage is submerged in liquid resin. The laser moves along the surface of the resin and polymerises the resin row by row until the desired layer is completely cured. The stage is submerged lower into the resin tank until a new layer of liquid resin covers the surface and the polymerisation repeats. (B) Schematic diagram of a configured SLA printer with a projection-based curing method. In this configuration, the stage is submerged at a specific distance in the resin reservoir. In the projection curing method, the digital mirror permits a whole layer to be cured at once. The stage can be elevated by a defined distance and another layer cured. This process repeats until the complete object is printed. (Taken from reference [161]. Reprinted with permission from ©2014 American Chemical Society). 25

Figure 1.11 Schematic diagram of DMD-PP system configuration. (Taken from reference [172]. Reprinted with permission from ©2012 Elsevier Ltd.). 27

Figure 1.12. Schematic diagram of FDM basic principles. Heated nozzle directly extruded polymer and layer by layer polymer is deposited on the platform. (Taken from reference [176]. Reprinted with permission from ©2015 Academy of Dental Materials). 28

Figure 1.13 Different biodegradable polymers scaffolds for tissue engineering were fabricated using FDM method. All the structures were characterized using scanning electron microscope (SEM). (Taken from reference [179]. Reprinted with permission from ©2012 Wiley Periodical Publishing Group). 29

Figure 1.14 Photopolymer-based ink-jet printer using the MJM fabrication concept (Taken from reference [183]. Copyright 2008 CustomPartNet)..30

Figure 1.15 Schematic configuration of the selective laser sintering process (Taken from reference [188]. Reprinted with permission from ©2016 PAGEPress)..........................30

Figure 1.16 Image representation of agarose template fibers bioprinting and the formation of microchannels using the micromolding technique. (A) A bioprinter attached with a piston fitted inside the glass capillary extracts the agarose mixture (inset image). (B) A hydrogel is cast over the bioprinted mould and solidified. (C) The template is removed from the solidified hydrogel. (D) Perfusable microchannels are formed. Inset image shows microchannels perfused with a fluorescent microbead suspension (pink) (scale bar is 3 mm, microchannel diameter is 500 µm) (Taken from reference [193]. Reprinted with permission from ©2014 Royal Society of Chemistry). 31

Figure 1.17 Examples of 3D printed connectors. (A) Rubber-like 3D printed O-rings can be placed on a microfluidic device. The printed O-rings are used to connect different microfluidic chips. (Taken from reference [195]. Reprinted with permission from ©2014 The Royal Society of Chemistry). (B) 3D printed luer adapters on a microfluidic device for easy connection to syringes and tubing. (Taken from reference [196]. Reprinted with permission from John Wiley & Sons, Inc.). 33

Figure 1.18 Microfluidics prototype for cervical sample preparation contains fluid mixer and homogeniser. Two reservoirs are used to store the reagent and the sample separately and can be released using fingertips for mixing (Taken from reference [200]. Reprinted with permission from ©2010 Elsevier Ltd.). 34

Figure 1.19 (A) LAPS chip with microfluidic channel connections. (Taken from reference [203]. Reprinted with permission from ©2015 John Wiley & Sons Inc.).(B) Chip-based prototypes for using Watershed resin. Inset image is the optical transparency assesment during embryo immobilisation. (Taken from reference [166]. Reprinted with permission from ©2015 AIP Publishing LLC). 35

Figure 1.20 Design of microfluidic devices for the generation of microliter droplets-in-oil and the formation of droplet arrays with interdroplet lipid bilayers. (A) The channels (1.10 mm wide x 0.55 mm deep) are cast in PDMS using 3D printed mould. The oil inlets are in yellow and the aqueous inlets in red and green. A delay line for lipid monolayer formation is in orange, and the droplet capture chamber is blue. (B) The droplet capture chamber comprises a rail for droplet positioning. (C) The measured values (bold) are compared with CAD design values (italic). (Taken from reference [213]. Reprinted with permission ©2013 Royal Society of Chemistry). 37

Figure 1.21 Assessment of microenvironmental conditions of zebrafish embryos cultured inside the chip: (A) Three-dimensional streamline flow across the fully loaded device; (B) The shear stress (Pa) contours exerted on each embryo across the entire device. Perfusion was simulated at a flow rate of 0.4mL/min; (C) The performance curve of the microfluidic device as a function of the volumetric flow rate; (D) Time-lapse images of zebrafish embryo development inside the device. (Taken from reference [27]. Reprinted with permission from ©2012 PLOS one Publishing Group). 40

Figure 1.22 Schematic representation of the process involved for the zebrafish larvae immobilisation chip-based device (Taken from reference [232]. Reprinted with permission from ©2014 International Society for Advancement of Cytometry). 42

Figure 1.23 Integrated zebrafish analysis platform (iZAP) for high-throughput electrophysiological monitoring configurations. (A) Schematic diagram of design concept. Inset image represents the position of surface electrodes to the zebrafish brain. (B) An illustration of integrated system of the microfluidic platform. (C) Images of trapped zebrafish larvae in the iZAP microfluidic unit. (D) An image of the iZAP system placed inside an optical-windowed Faraday cage. The red fluid represents the zebrafish medum (Taken from reference [234]. Reprinted with permission ©2016 Macmillan Publishers Limited)..43

Figure 3.1 Images of (A) Live zebrafish embryo at 12 hpf and (B) 24 hpf zebrafish embryo (C) Dead embryos. Bar scale is 400 µm. 51

Figure 3.2. Mechanical dechorionation using sterile needles (Terumo ®) (A) Intact zebrafish embryo 24 h post-fertilisation; (B) Zebrafish embryos held with one needle (C) A small incision in the chorion with the needle (D) Second needle enlarges the slit by in the chorion (E) The chorion is turned upside down to allow the embryo to fall out from the chorion (F) dechorionated embryo. Bar scale is 500 µm..52

Figure 3.3. Illustration of FDM equipment for prototyping (Makerbot Replicator, Brooklyn, NY, USA) 56

Figure 3.4 Additive manufacturing technologies. (A) Stereolithography (SLA) ProJet HD7000 with a maximum build volume of 380 mm x 380 mm x 250 mm; (B) Multi jet machining (MJM) Objet Connex 350 with a net volume of 342 mm x 342 mm x 200 mm; (C) Desktop SLA printer Form1 with a maximum build volume of 125 mm × 125 mm × 165 mm. 57

Figure 3.5 Post processing treatment to remove support materials from 3D printed parts (A) High pressure water jet system manually used at 50-60 Barr to clean the supports (B) UV radiation curing process to increase the clarity and tensile strength of printed parts. 58

Figure 3.6 A set-up for degassing method. The PDMS mixture (sample) was placed inside a desiccator. A high-performance vacuum pump was connected to the desiccator by means of a rubber hose 59

Figure 3.7 Step-by-step process of PDMS fabrication: (A) Curing agent mixed with Sylgard 84 at a 10:1 ratio (B) Printed moulds are fixed to a rectangular mould (85 mm x 35 mm x 10 mm) (C) The mixture is carefully poured into the mould and degassed to remove air bubbles (D) Degassed mixture is cured inside a fan-assisted oven for two hours, before being separated from the printed mould manually. Bar scales are 12 mm. 60

Figure 3.8. Sensing module set-up for DIOD method. A peristaltic pump was used to load embryos at a flow rate of 1500 µL/min. A digital microscope (Dino-Lite) was used for embryo imaging. A single channel of a PMMA microfluidic chip was fabricated to test the viability of the embryos using DIOD. Inset shows a magnified view of the infrared sensors embedded in the channel. Live mbryos were stained with Trypan blue dye solution. 61

Figure 4.1 Overview of 3D chip-based in-flow embryo sorter (A) Detailed CAD drawing showing the details of the main loading, inlet and outlet channels. (B) Multiview projection of sorter wheel embedded with a polymer bearing and eight pairs of Neodymium magnets. (C) Fabricated biocompatible PMMA sorter chip that connects to tubing with an outer diameter of 3 mm. Live and dead embryos are separated via two outlet channels. 65

Figure 4.2 An exploded view of the microfluidic device in the sorter. The function of each independent layer is noted. The layers of PMMA are aligned and thermally bonded to form a permanent seal. The red dotted box contains an exploded view of the sorter wheel, consisting of neodymium magnets and polymer bearings.................................65

Figure 4.3 Built-in microcontroller in the 3D printed housing used to position the shaft to direct embryos from the inlet to the outlet channel. Bar scale is 20 mm......................66

Figure 4.4 A coloured plot 3D simulation of fluid streamlines across the microfluidic chip with velocity (m/s) profile obtained from CFD simulations. The red dotted inset depicts the flow at the embryo trap as the embryo enters the main loading channel. The flow profile is symmetrical because of the laminar flow in a microfluidic system. The blue arrow represents the flow direction inside the chip. 67

Figure 4.5 Visual illustration of the flow switching principle. The simulated fluid streamlines in the sorter trap are at angles 0°, -45° (downwards), and + 45° (upwards) (AC). The device is perfused with 0.04% of Trypan blue dye for imaging, and has a volumetric flow of 1500 µL/min. The experimental condition is comparable to the simulation and depicted in images (D–F). Blue arrow represents the fluid flow inside the microfluidic chip...68

Figure 4.6 Mass transfer across the simulation and experimental stages of the microfluidic device is demonstrated. The device is perfused with 0.04% Trypan blue dye at a volumetric flow of 1500 µL/min. The perfusion time is recorded at 0s, 20s, 40s and 60s. Colour indicates the exchange flow rate concentration inside the device. 69

Figure 4.7. Overview of sorting principle (A) Illustration of embryos flowing towards sorting trap (width 1.6 mm, height 2 mm). Blue arrow represents water flow. B) Single embryo trapped in the sorting pocket. C) Sorter wheel rotated via servomotor to direct embryo into one of the outlet channels. D) Sorted single zebrafish embryo entering outlet channel...70

Figure 4.8 Experimental validation of the sorting concept. A) Live embryo of 16 hpf stained with Trypan blue dye entering inlet channel. B) Embryo trapped and immobilised in a sorting pocket. C) Receptacle is rotated towards the outlet channel. (D) Recovery of embryo moving towards outlet channel. Scale bar size denotes 800 µm. 71

Figure 4.9 Experimental validation of live and dead embryos with embryos flowing in as in a single file at a perfusion rate of 1500 µL/min. Red dotted image depicts the measurement of average voltage, ΔV of the obtained signals over time. Oscilloscope waveform of diverse mixtures of live and dead embryos with values of 29 mV and 1 V. 72

Figure 4.10 Experimental validation of IR sensing (A–B) of live and dead embryos with embryos flowing in in single file at a rate of 1500 µL/min. Detection efficiency and detection purity of dead embryos in diverse mixtures of live and dead specimens were calculated. Detection of dead embryos using robotic vision software 73

Figure 4.11 Robotic image acquisition of Roborealm software for sorting. (A) Real-time video acquisition and detection of dead embryos at a flow of 2500 µL/min. The blue circle indicates detection of the dead embryo when the software recognises it. The designed algorithm specifically used a colour module for tracking the dead embryos (RGB_Filter Gray –> Smooth Hull –> Blob Tracking –> Blob Replace). The blue arrow represents the direction of the fluid flow inside the microchannel. (B) Tracking efficiency of dead embryos rolled inside the microchannel at low to high volumetric flow rates. 74

Figure 4.12 Vision recognition using image intensity for both coagulated (left image) and viable (12 hpf) (right image) embryos. The algorithm was modified to distinguish both types of embryo when the sensing detection process started. (Canny 0-4 -> Smooth Hull -> Circles -> Display Circle -> Write AVI). Average mean intensity values of ≥ 126 (live embryo) and ≤100 (dead embryo) were achieved The red boxes show the mean intensity value that the captured image required. Bar scale is 250 µm.........................74

Figure 4.13 Experimental validation of real time video detection using RoboRealm software (A–B) of live and dead embryos with embryos flowing in in single file at a rate of 1500 µL/min. Detection efficiency and detection purity of dead embryos in diverse mixtures of live and dead specimens were determined. The results suggest that robotic vision detection is more accurate than DIOD sensing. The image processing algorithm was able to differentiate between live and dead embryos flowing through a microfluidic device. In addition, the method reduced tracking inaccuracies and increased the detection sensitivity of the specimens that were distinguished. 75

Figure 5.1 Overview of CAD design of the negative relief mould for larvae immobilisation millifluidic chip. A detailed view of section A is depicted on the (right). 79

Figure 5.2 An illustration of showing zebrafish larvae trapping arrays using different additive manufacturing methods. CO2 laser micromachining used to cut the thermoplastic material of polymethylmethacrylate (PMMA) and designated as the control. The 3D printed moulds were fabricated using stereolithography (SLA; in VisiJet SL Clear and Form Clear resins) and multi-jet modelling (MJM; in Vero Clear resin). 80

Figure 5.3 A PDMS chip-based device to trap 3dpf zebrafish larvae. The main body was fabricated of polydimethylsiloxane (PDMS) with a PMMA mould, bonded to a standard microscope slide (sealing layer). This is referred to later as PMMA-PDMS for the control fabrication. 81

Figure 5.4 A photograph of 3D printed mould and the final fabricated PDMS chip-based device. All PDMS structures were comparable with the control (PMMA-PDMS) in shape and transparency. The soft lithography process does not affect the appearance of the final microfluidic devices. 81

Figure 5.5 Geometrical representation of a single trap. Suction width (A), trap width (B) and entrance width (C) were measured after the 3D printing fabrication. Actual CAD dimensions (in mm) were compared with actual 3D printed mould and PDMS............83

Figure 5.6 Comparison of measured deviations of the trap structures for all fabricated 3D printed moulds. The theoretical width of suction is designed in CAD is to be 300 µm. All printed moulds were comparatively accurate except for Form Clear. Apart from the

PDMS structure made from the PMMA mould, all other additive manufacturing methods were relatively precise. 83

Figure 5.7. Topographic surfaces of 3D printed moulds of the larvae traps are depicted using SEM. The VisiJet Clear was observed to have a smooth surface comparable with the conventional PMMA mould. SEM image for VJC presented more uniformity of the layer resolution of 800 µm (thickness) than the other additive manufacturing methods. 84

Figure 5.8 Comparison of topographic surfaces using SEM, depicting the top surfaces of the larvae trap. All the 3D printed moulds achieved a smooth top surface finish apart from the Form Clear mould, which suffered from incomplete layering of the resin while printing..85

Figure 5.9 Comparison of topographic surfaces using SEM, showing a close view of the suction channel on all 3D printed moulds. Only VisiClear showed good layer deposition. 86

Figure 5.10 Surface topographic analysis of 500 µm x 500 µm area size of top surface of mould structures (left image). The Gaussian distribution on the surface texture is represented by the median height (right image). A smooth surface has a median height of 92 µm and width of 86 µm. 87

Figure 5.11 Quantitative analysis of surface topography of an area of 25 mm^2 the top of VisiJet SL clear printed moulds (left image). The Gaussian distribution was symmetrical on the surface texture (median height) (right image). The surface was smooth and relatively flat compared to the control (PMMA) as is indicated by the small variations in the distribution curve. 88

Figure 5.12 Surface profilometry analysis of the selected scanned area (500 µm x 500 µm) (left image). The skewed Gaussian distribution on the surface roughness (median height) is presented (right image). Large variation in the histogram distribution with relatively rough texture is observed as the peaks are greater than the valleys with R_a value of 28 µm for FC mold...88

Figure 5.13. Overview of larvae trapping principle: (A) Illustration of zebrafish larvae flowing towards entering the trap (0.8 mm (width) x 4.0 mm (height) x 0.8 mm (thick)). Blue arrow represents water flow (rate = 2000 µl/min) (B) Single zebrafish larvae immobilised inside one of the traps (C) Subsequent zebrafish larvae flowing towards next trap (D) Zebrafish larvae immobilised inside the trap and acclimated for fine minutes with a constant flow of 1000 µl/min. 89

Figure 5.14 CFD simulation of the theoretical prediction of fluid flow inside the millifluidic chip with an inlet flow of 1000 µl/min 90

Figure 5.15 Comparison of trapping performance of zebrafish larvae between devices fabricated using different techniques. The volumetric perfusion rate range tested from low to high volumetric flow rate. 91

Figure 5.16 Overview of modified design of the negative relief mould. (A) A detail of the CAD design. A linear array of five traps was designed (green image). Each individual trap has the same dimensions as in the previous design. (B) Realistic image of the printed mould. Inlet and outlet ports (Ø = 2.7 mm) were 3D printed directly (red dotted image). This eliminated the hole punching process for direct tubing...92

Figure 5.17 CFD of the microfluidic device for trapping 3 dpf zebrafish larvae. (A) Predicted velocity streamline of the entire array of the device. The simulation of mass transfer flow (B–D) and experimental fluid flow using 0.01% Trypan blue dye (E–G). Time taken was 0, 30 and 60 seconds. Volumetric perfusion rate used was 1000 µL/min. 93

Figure 5.18 The complete loading of the larvae inside the traps took approximately five minutes depending on the larvae flow gap and flow rate selected. All 3 dpf larvae were anesthetised with 100 mg/L Tricaine before loading. Flow rate for trapping the larvae was 1500 mg/L...94

Figure 5.19 Dose concentration effect of Tricaine on 3 dpf zebrafish larvae at concentrations of 0.02–0.18 mg/ml: (A) at immediate time after being exposed with the Tricaine; (B) heartbeat of zebrafish larvae at time=24 hr. Results are represented as the mean ± standard deviation (SD), n=20. 95

Figure 5.20. Agarose mounting (0.5–1.5%) effect on 3 dpf zebrafish heartbeat. The asterisks denote significant differences from the control group (*p<0.05 and **p<0.01). Results are represented as mean ± standard deviation (SD). (n=20, 3 replicates). 96

Figure 5.21. Effect on 3 dpf zebrafish heartbeat in different environmental conditions. The asterisks denote significant differences from the control group (*p<0.05 and **p<0.01). Results are represented as mean ± standard deviation (SD), n=20. 96

Figure 5.22 Dose-dependent mortality tests: selected toxicants' effects on 3 dpf zebrafish larvae. The curves represent the response for each of the selected cardio-active compunds. The values of LC_{10} were calculated by probit analysis using ToxRat software. Experiments were carried out in triplicate; in each n=20 larvae were pooled for calculation of the concentration. Lead acetate was found to be toxic at low concentrations compared to the others. 97

Figure 5.23 Zebrafish larvae (3 dpf) immobilised on the microfluidic device. Heart rates were recorded for one minute with USB microscope (Dino-Lite) at 60 frames per second. The videoed records of cardiac activity were analysed using DanioScope software. The heart area was selected for analysis. 98

Figure 5.24 Detection of heart rate difference in 3 dpf zebrafish larvae after ten minutes perfused with drugs that decrease and increase heart rate. Cardiac rate increased after the administration of caffeine (A) and lead acetate (D). In contrast, nicotine (B) and verapamil hydrochloride (C) induced a decrease in heartbeat. Each treatment was compared with a vehicle control 0.05% of dimethyl sulphoxide (DMSO). All values represent the mean ±SD (**p<0.01)(n=20). 99

Figure 5.25 Effect of cardioactive compound infusion on heart rate of 3 dpf zebrafish in the microfluidic chip. Fluctuations in bpm are measured as a function of time (minutes) during the infusion. Flow in the microfluidic was 1000 µl/min. Phase I – LC_{10} value for each compound was introduced into the microfluidic chip for ten minutes. Phase II – Infusion of Tricaine solution of 100 mg/L for recovery and to remove the compound solution for ten minutes. Phase III – Re-introduced of the compound solution. Each heartbeat was compared to the baseline. Error bars represent standard deviations and n = 9 for each line. Data is presented by means of ± SD (**P<0.05). 101

Figure 5.26 The illustration of the heart rate response of 3 dpf in zebrafish larvae to cardioactive drugs. Overall, the caffeine exposure showed higher contractions of heartbeats compare to lead acetate. On the other hand, infusion of nicotine showed reduction increase heart rates than verapamil hydrochloride. Blue areas represent exposure of drugs of ten minutes duration (0-10 min) and re-exposure of drugs of ten minutes duration (20-30 min). Green area depicts the withdrawal and elimination of drugs (10-20 min). Note the baseline heart rates are comparable for all drugs tested. 103

Figure 6.1. The design of the negative relief mould for trapping dechorionated embryos. A total of 20 embryo traps and each of the traps interconnected with cross-flow suction channels. Blue arrow represents the direction of fluid flow from inlet to outlet channel. 'T' indicates the number of consecutive traps and 'D' indicates the number of deflector channels. 105

Figure 6.2. Detailed CAD design of the negative relief PDMS–VisiClear mould of the microfluidic device for automatic trapping and immobilisation of 24 hpf dechorionated zebrafish embryos. (A–B): Detailed design showing the dimension of the overall mould, the size of a glass microscope slide. (C–D): Each row consists of four traps and a single deflector channel. (E–F): The drawing shows a single trap connected to a small suction channel. 107

Figure 6.3. The 3D photorealistic rendering of mould and PDMS chip-based microfluidic device. A high-resolution (125 µm) printed mould was fabricated from optical-grade polymer materials. The peeled-off PDMS structure was thermally bonded to a glass slide with inlet and outlet connection ports (Ø = 3.0 mm) for PTFE tubing of internal diameter ID= 1.3 mm. 107

Figure 6.4 A computer fluid dynamic simulation of 3D velocity streamlines (m/s) across the microfluidic device. Overall perfusion was simulated at the perfusion rate of 1000 µL/min. The flow passes from the entrance of each trap through the suction channels and exit through the outlet channel. Inset image denotes vertical cross section at the entrance of the trap. This allows for embryo immobilisation and efficiency of medium and drug exchange. Note that the axis is the coordinate location on the simulation gridlines. 108

Figure 6.5 Analysis of the flow velocity (m/s) when the microfluidic device is perfused at 1000 µL/min. 3D computer simulation of the flow velocity across each of the traps. A higher velocity at the first trap in each row enhanced trapping efficiency. This is a function of the serpentine design of the device. 109

Figure 6.6 Computer fluid simulation and validation of mass transfer in the microfluidic chip. The chip was perfused with 0.04% of Trypan blue solution at volumetric flow rate of 1000 µl/min. The fluid flow images were taken at 0, 10 and 60 seconds of perfusion. The traps achieved 98% of full medium exchange with the Trypan blue solution after 60 seconds. Note the flow pattern match between simulation and experiment. 110

Figure 6.7 Embryo trapping and immobilisation principles. (A) Dechorionated embryos loaded from reservoir and directed into the main channel. The hydrodynamic flow guided the embryo to enter the trap. (B) The next embryo is moved into the next available trap. (C) The process is repeated until all traps are filled. (D) The hydrodynamic force securely retains and immobilises dechorionated embryos inside each trap. 111

Figure 6.8 Trapping experiments with 24 hpf dechorionated embryos. The full loading of the embryos docking inside the microfluidic chip took approximately ten minutes, depending on the flow rate and aspiration flow gap between embryos. 112

Figure 6.9 Embryo trapping efficiency at different perfusion rates. Full loaded embryos with 100% trapping efficiency can be achieved at flow rates of 1500 µL/min. High flow rates reduced the trapping efficiency due to the inability of the suction channels to overcome the velocity and momentum of the embryos moving past. 113

Figure 6.10 Time lapse images of the development of zebrafish embryos during the experiment. Embryos were loaded at 1500 µL/min of flow rate, followed by a constant perfusion rate of 1000 µL/min for on-chip culture for up to 72 hours. The embryos were in dark condition for the duration of experiment. 113

Figure 6.11 Survival rates of zebrafish embryos in a perfused flow rate of 1000 µL/min for 72 hours period. Embryo viability in microperfusion environments was similar to those in static condition using Petri dishes. 114

Figure 6.12 Lethal endpoints (mortality) of zebrafish embryo test at 48 hpf compared with a viable embryo (control). Mortality endpoints of coagulation are depicted. Note the lack of somite formation and non-detachment of tail were not applicable for embryos at 48 hpf. Lack of heartbeat is not illustrated here as it requires video demonstration. 116

Figure 6.13 The effects of copper sulphate on zebrafish embryos with and without chorions after 72 hours of exposure. The biotests were performed in conventional static culture in 24-well plates. All embryos were loaded at 24 hpf. 116

Figure 6.14 Comparison between biotest performed in microfluidic environments and conventional 24 well-plates culture. (A) Mortality (FET) was observed for copper sulphate at concentrations of 0.1 mg/L to 0.5 mg/L. Duration of the test was 72 hours. (B) Cumulative correlation analysis of copper sulphate. Excellent agreement between both microfluidic environment and static conditions, as depicted by Pearson linear correlation analysis (P<0.01). Error bars represent values between SE values performed by three independent experiments. 117

Figure 6.15 The sublethal (iFET) endpoints of the zebrafish embryo toxicity test at 48 hpf, compared with the viable embryo. iFET endpoints of abnormal eye development, pericardial oedema, lack of pigmentation, tail abnormalities, head abnormalities, spine abnormalities and yolk abnormalities are illustrated. Note that other two endpoints, heart abnormalities and blood circulation deficiency, are not demonstrated here because video capturing is required. 118

Figure 6.16 Comparison of biotests performed in a microfluidic environment and conventional static culture of 24 well-plates. iFET (sublethal/teratogenic effects) indicate the several concentrations of (A) caffeine (B) nicotine (C) phenol. Cumulative correlation of analysis of (D) caffeine (E) nicotine (F) phenol. The lab-on-chip experiments were performed at perfusion rate of 1000 µl/min. Duration of all biotests was 72 hours. The error bars represent SE values between three independent experiments. 119

Figure 6.17 Comparison between end-point scores for FET (mortality) and iFET (sublethal/ teratogenic) after exposure of selected compounds on 24 hpf dechorionated embryos. Duration for the test was 72 hours. All tests were conducted with a chip-based device. Note that FET parameters were included in iFET calculations. The introduction of nine sublethal parameters increases the sensitivity beyond that of the standard fish embryo toxicity test........ 121

Figure 7.1 Graphic user interface of real time image processing software (RoboRealm, Machine Vision). (1) Camera connects to the software and the object appear on the image screen. (2) The specific function for image processing is selected in the Modules section. Each inserted module directly processes the image. (3) Selected modules appeared in the processing pipelines screen as algorithms. At completion of all selected modules, the image is displayed. Note the blue circle only appears when all the modules in the pipelines are processed. 126

List of symbols and abbreviations

Symbol	Description
μ	dynamic viscosity
µ_	micro_
µTAS	micro-total analysis system
ν	kinematic viscosity
ρ	density
2D	two-dimensional
2PP	two photon polymerisation
3D	three-dimensional
A	ampere
A	cross sectional area
ABS	acrylonitrite butadiene styrene
ANOVA	analysis of variance
bar	bar
bpm	beats per minute
°C	Celcius degree
c_	centi_
C	concentration of species
CAD	computer aided design
CAS	chemical abstract service
CFD	computer fluid dynamics
CFRP	carbon fiber reinforced plastic
CNC	computer numerical control
COPAS	complex object parametric analyser and sorter
CS/TPP	chitosan tripolyphosphate
dpf	days post fertilization
D	diffusion coefficient
D_H	hydraulic diameter
DMD-PP	digital micromirror device based projection printing
DMSO	dimethyl sulfoxide
eGFP	enhanced green fluorescent protein
EC_{50}	half maximal response
ECG	electrocardiogram
EEG	electroencephalogram
ESEM	environmental scanning electron microscopy
f-FU	5-flurоucil
FC	Form Clear
FDM	fused deposition modelling
FEP	fluorinated ethylene propylene

FET	fish embryo toxicity
FPGA	field programmable gate array
fps	frame rate per second
f	force
g	gram
g_z	gravitational acceleration
h	height
HDPFO	high power density focusing optics
hpf	hours post-fertilization
HTS	high-throughput screening
HVAC	high voltage alternating current
Hz	hertz
iFET	sub-lethal fish embryo toxicity
iZAP	Integrated zebrafish platform
ID	Inner diameter
IR	infrared
k_	kilo_
l	characteristic length scale
L	litre
LC_{50}	medium lethal concentration
LC_{10}	10% lethal concentrations
LED	light emitting diode
LOC	Lab-on-a-Chip
m	metre
m_	milli_
min	minute
M	molar
MJM	multi jet modelling
MPEG	moving picture experts group
n_	nano_
nano-Hap	nanosized hydroxyapatite
N	newton
p_	pico_
P	pressure
Pa	pascal
PC	polycarbonate
PDMS	poly (dimethyl siloxane)
PDLLA	poly (D,L-lactide)
PLA	polylactic acid
PMMA	poly(methyl methacrylate)
PPF	propylene fumarate
PTFE	polyterafluoroethylene, Teflon
OECD	organization for economic co-operation and development

OSTEMER	off-stoichiometry thiol-enes polymer
Re	Reynolds number
RIE	reactive ion etching
rpm	revolutions per minute
s	second
SEM	scanning electron microscopy
SLA	stereolithography
SLS	selective laser sintering
SU-8	epoxy based negative photoresist
t	time
Torr	torr
TG	test guidelines
u	characteristic velocity
USB	universal serial bus
UV	ultraviolet
V	volt
VAST	vertebrate automated screening technology
W	watt
ZEBRA	zebrafish entrapment by restriction array

Academic Contributions

Conferences:

1. MRDB Conference of Australian Regenerative Medicine Institute 2013 (5 November 2013), Monash University, Clayton Campus, Melbourne Australia. (Poster). N.Fuad and D.Wlodkowic *"Proof of Concept of Zebrafish Sorting Microfluidic Devices"*.

2. SPIE Micro Nano Materials Devices and Applications Conferences 2013 (8-10 December 2013) RMIT, Melbourne, Australia. (Poster). Nurul Mohd Fuad and Donald Wlodkowic *"Microfluidic EmbryoSort Technology-Towards in flow analysis, sorting and dispensing of individual vertebrate embryos"*.

3. Higher Degree Research Student Conference 2014 (17 October 2014) College of Science, Engineering and Health, RMIT, Australia. (Poster). Nurul Mohd Fuad and Donald Wlodkowic *"Microfluidic EmbryoSort Technology-Towards in flow analysis, sorting and dispensing of individual vertebrate embryos"*.

4. SPIE Microtechnologies for BioMEMS and Medical Microdevices, Barcelona, Spain (4-6 May 2015). (Poster). Nurul Mohd Fuad, Joanna Skommer, Timo Friedrich, Jan Kaslin and Donald Wlodkowic. *"Miniaturized of in-flow sorter for dispensing fertilized zebrafish embryos for ecotoxicity biotests"*.

5. SETAC Europe 25th Annual Meeting (3-7 May 2015), Barcelona, Spain. (Poster). Nurul Mohd Fuad, Joanna Skommer, Timo Friedrich, Jan Kaslin and Donald Wlodkowic. *"An integrated, micromechanical large particle in-flow sorter (MILPIS)"*.

6. 8th Annual ANZSCDB Melbourne Cell and Developmental Biology Symposium (2 October 2015), Bio21 Institute University of Melbourne, Australia. (Poster).Nurul Mohd Fuad, Feng Zhu, Timo Friedrich, Jan Kaslin and Donald Wlodkowic*."Rapid prototyping of biocompatible polymeric devices for zebrafish larvae immobilization".*

7. SPIE Bio-Photonics Australasia (16-19 October 2016) Adelaide, Australia (Poster). Nurul Mohd Fuad, Feng Zhu, Jan Kaslin and Donald Wlodkowic. *"Applications of stereolithography for rapid prototyping of biologically compatible chip-based physiometers".*

8. 9 th Annual ANZSCDB Melbourne Cell and Developmental Biology Symposium 21st October 2016 Melbourne Brain Centre, Royal Parade, Parkville, 21 October 2016. (Poster). N.Fuad and D.Wlodkowic *"Applications of stereolithography for rapid prototyping of biologically compatible chip-based physiometers".*

Publications:

1. Fuad, N. M., & Wlodkowic, D. (2013, December). Microfluidic EmbryoSort technology: towards in flow analysis, sorting and dispensing of individual vertebrate embryos. In *SPIE Micro+ Nano Materials, Devices, and Applications* (pp. 892347-892347). International Society for Optics and Photonics.

2. Fuad, N. M., Skommer, J., Friedrich, T., Kaslin, J., & Wlodkowic, D. (2015, June). An integrated micromechanical large particle in flow sorter (MILPIS). In *SPIE Microtechnologies* (pp. 951814-951814). International Society for Optics and Photonics.

3. Fuad, N. M., Zhu, F., Kaslin, J., & Wlodkowic, D. (2016, December). Applications of stereolithography for rapid prototyping of biologically compatible chip-based physiometers. In *SPIE BioPhotonics Australasia* (pp. 1001326-1001326). International Society for Optics and Photonics.

Abstract

The major current hurdle to widespread deployment of zebrafish embryos and larvae in large-scale drug discovery is the problem of enabling analytical platforms with high throughput. In order to spearhead drug discovery using zebrafish as a model, platforms need to determine pre-test sorting of organisms to ensure quality control and standardisation, and determine that their in-test positioning is suitable for high-content imaging with modules for flexible drug delivery. Manual procedures for sorting hundreds of embryos are very monotonous and therefore liable to significant analytical errors caused by operators' fatigue. In this thesis, we present an innovative proof-of-concept design for a micromechanical large-particle in-flow sorter.

This thesis investigated infra-red sensor detection and image acquisition and compared them for their ability to distinguish between viable and dead embryos. High-definition additive manufacturing systems for fabrication of 3D printed moulds of the type used in soft lithography were also explored. 3D printing using SLA provides a rapid microfabrication of the moulds with high definition and optical transparency, as is confirmed by both scanning electron microscopy and confocal microscopy. SLA technologies may be applied for the rapid and accurate fabrication of millifluidic devices that can trap millimetre-sized specimens such as living zebrafish larvae. We applied this new manufacturing method in a proof-of-concept prototype device capable of trapping and immobilising living zebrafish larvae for the purpose of recording heart rate variations in cardio-toxicity experiments.

Static conventional culture plates limit the throughput data, and is not suitable for modern compound library screening, while currently available conventional microtiter well plates require manual pipetting, which is labour intensive and time consuming. This research offers promising avenues for the development of a miniaturised, automated system for handling and manipulating zebrafish embryos and larvae, using innovative microfluidic lab-on-chip (LOC) technologies and additive manufacturing technologies.

1 Introduction

1.1 Phenotype-based physiological analysis

Phenotype-based analysis is the study of an organism's biochemical, physiological, morphological and behavioural characteristics. It is a screening process used in drug discovery and biological research to evaluate phenotypic changes or alterations caused by a substance such as a small molecules or peptide on a cell or organism. Phenotypic screening has been fundamental in the finding of new drugs, particularly in traditional and modern pharmacology [1]; for instance, when a genetic mutation occurs through small particle treatment, the change to the phenotype is observed and conclusions about the mechanism underlying the biology are drawn. This improves understanding in the areas of basic and disease biology [2].

Two broad types of screening approach dominated the early stages of drug development: phenotypic and target-based. Both approaches have advantages and limitations, but the contributions of phenotypic screening exceed those of target-based screening [3] because they offer better potential to discover new chemical probes and new biological small-molecule targets. Phenotypic assays also have an advantage over target-based screening because they can identify drug leads and clinical candidates that are likely to possess therapeutic abilities [4]. For example, the compound of drugs were screened in phenotypic assays to identify the active lead compounds that alleviate the disease phenotype, demonstrated by selectively killing the cancer cells [5] .

However, using cell lines in phenotypic screening uses immortalised cell line assays to predict the clinical efficacy of phenotypically discovered drugs. Most target hits from traditional screening are found to be invalid once tested in an animal model such as a mouse model. Factors such as absorption, solubility and toxicological problems in animal studies may present difficulties and lead to analysis failure [6]. Cost limits the use of traditional animal models in large-scale screening, so small model organisms offer a potential alternative as screening tools in drug discovery [7].

1.1.1 The role of small model organisms in phenotype-based analysis

To overcome the drawbacks associated with standard animal models and to avoid unethical procedures, alternatives were recommended under the concept of the 3Rs (replacement–reduction–refinement) of the laboratory use of animals [8]. The concept encourages the replacement of higher vertebrates with microorganisms, plants, eggs, amphibians and invertebrates [9-11] (Table 1.1). This enables less expensive animals to be used to screen large numbers of drugs for toxicity analysis: *reduction* in this context is the minimisation of the number of large animal models used to perform an experiment. With careful experimental design and a sophisticated statistical analysis it is possible to use fewer animals and still obtain valid results. Furthermore, experiment protocols can be refined and simplified to lessen pain or distress in tested animals.

They have been used to study various diseases, memory dysfunction, Parkinson’s disease, cell aging, diabetes and toxicology [12-15]. These invertebrates offer advantages as they are small in size, have a short life cycle, and possess a simple anatomy. A high number can be used in one experiment in a short period of time. However, they have immature organ systems and do not have adaptive immune systems which limits their use in human disease research [7].

Lower vertebrates such as tadpoles (*Xenopus laevis*) [16, 17] and fish are an attractive substitute due to their genetic similarity with higher vertebrates, including mammals. Small fish such as the fathead minnow (*Pimephales promelas*), Japanese medaka (*Oryzias latipes*), and zebrafish (*Danio rerio*) are used as surrogate models for other vertebrates, particularly in the study of developmental biology, genetics and environmental toxicity. Fish offer significant advantages over other mammalian models in biomedical research that focuses on human health [18-20], and can be selected for their size, short life cycle, and high fecundity. With such advantages, these vertebrates are cost effective and valid models for human diseases.

Table 1.1 Overview of small model organism characteristics for drug screening. Red boxes indicate the poorest in the category (Adapted from reference [8, 11, 21])

Model features	Invertebrates		Vertebrates			
	C. Elegans	*Drosophila*	*Zebrafish*	*Xenopus*	*Chicken*	*Mouse*
Average adult size	1 mm	3 mm	4 cm	10 cm	40 cm	10 cm
Generation time	3–5 days	10–14 days	3–4 months	4–6 months	20 weeks	3–4 weeks
Average embryo size	50 µm	100 µm	1 mm	1 mm	4 cm	8 mm
Embryo accessibility	Good	Good	Good	Good	Good	Poor
Cost per embryo	Low	Low	Low	Low	Medium	High
Screening throughput	High	High	Medium	Medium	Low	Low

1.1.2 Zebrafish as a model organism in biomedicine

The freshwater teleost zebrafish (Danio rerio) is an attractive option for biological research over other model species such as the common fruit fly, worms, or tadpoles. It has an approximate size of 1.1–1.3 mm in diameter as an embryo and 2–4 cm as an adult. Zebrafish have been used as experimental models in embryogenesis, organogenesis and general development of vertebrates [22, 23]. This species can be modified genetically, and as a result been used in high-throughput studies in drugs discovery models for human diseases such as neurogenerative disorders [24] and cancer [25].

The unique characteristics of the zebrafish have made it a versatile model, and one with remarkable similarities to mammalian development (Figure 1.1) [26]. Zebrafish are nearly transparent in early development, which allows in vivo visualisation of their development and functions. Advanced microscope technologies allow the imaging of developmental details of the embryos, and assessment of drug effects on internal organs can be captured [27]. Recently, zebrafish have become an outstanding model for studies of heart development and restoration [28]. The zebrafish heart resembles the human heart in many ways: beat rates are reported to be identical where the electrocardiograms (ECG) patterns showed were comparable to ECG patterns in humans [29]. Zebrafish have already been reported as a powerful and versatile vertebrate system that can facilitate accelerated drug discovery. Unlike fruit flies and worms, their transparent embryos are produced in large numbers and are accessible for rapid screening and experimental manipulation. A female zebrafish is capable of producing hundreds of eggs at a time, providing a sample size large enough to be utilised for multiple testing of drugs; this means that, among other advantages, potential drug toxicity problems in early drug discovery pipelines can be rapidly identified in the in vivo pharmacological assessment using zebrafish embryos [30].

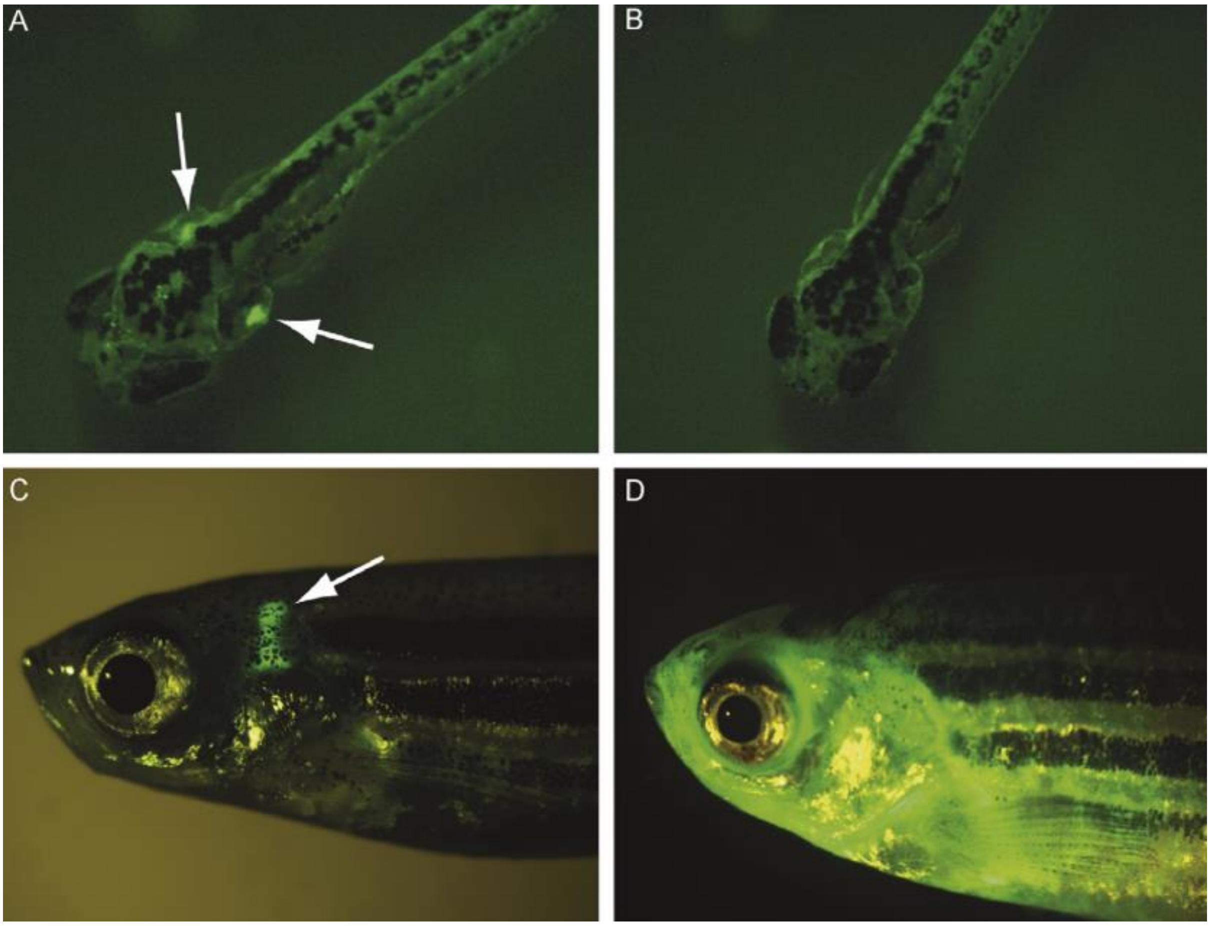

Figure 1.1 A transgenic line zebrafish contains enhanced green fluorescent protein (eGFP) under the control of T cell-specific kinase p56^{lck}. In six days post fertilization (dpf) (A) and zebrafish adult (C), the T-cells' fluorescent green thymus is illuminated, as shown by the arrow. (B) No fluorescence is displayed in the thymic area, which indicates an immunodeficiency. (C) The fluorescence has spread from the thymus to the gills, face and body, showing T cell malignancy. (Taken from reference [26]. Reprinted with permission from ©2008 Elsevier Publishing Group).

The rapid embryonic development of zebrafish compared to other mammalian models also makes it an ideal model for high-throughput screening [31]. For instance, embryos achieved early vertebrate movement defined as twitching at the 19 hour somite developmental stage. Most major organs are developed, including the gut and the vasculature, two days post-fertilisation (dpf), and the embryogenesis stage is completed after five dpf [22]. In addition, during organogenesis the embryos are permeable to small particles and drugs, providing easy access for drug administration [32].

1.1.3 Zebrafish as a model organism in ecotoxicology

There is increasing awareness and concern about the environmental effects of industrial waste. In this regard, zebrafish offer many advantages which make them highly attractive in toxicology studies. They represent an attractive model for the environmental risk assessment of chemical pollutants since they are able to perform on a small scale with high-throughput analysis. They are reported to be a powerful in vivo model system for measuring biological interactions and mechanisms to deal with a toxic substance [33]. Given the other advantages of zebrafish, the effect of both short- and long-term exposure to chemical pollutants including carcinogenic agents can carried be studied conveniently. Toxicity tests may then be designed to measure specific concentrations of chemicals that induce an effect on the organisms.

The study of acute toxicity on zebrafish started in the 1980s to examine the effect of wastewater and effluents from industrial wastage [34] but it is now incompatible with current animal welfare legislation because the end point is mortality and the fish suffer distress and pain [35, 36]. The fish embryo test (FET) is a promising substitute for the acute toxicity test, and can evaluate the toxicity effect at an early stage of the life cycle. The early life stages of zebrafish provide a useful alternative experimental model because at this stage the fish are more sensitive than the adults [37, 38].

One of the first applications for zebrafish embryos in ecotoxicology was promoted by Nagel et al. to develop an alternative to the 96-h acute fish toxicity test [39]. It demonstrated that the replacement tests were comparable with the conventional acute toxicity test [40]. Originally, FET analysis was designed as alternative to the acute toxicity test such as OECD

TG 203 (Figure 1.2) [40]. Since then, the test using zebrafish embryos has been optimised, standardised and validated by an OECD validation study, and adopted as OECD TG236 to assess toxicity in embryonic forms of fish [40]. Additional lethality endpoints makes the FET a versatile tool for multitude toxic effects detection, including teratogenicity, neurotoxicity, genotoxicity and mutagenicity [36, 40].

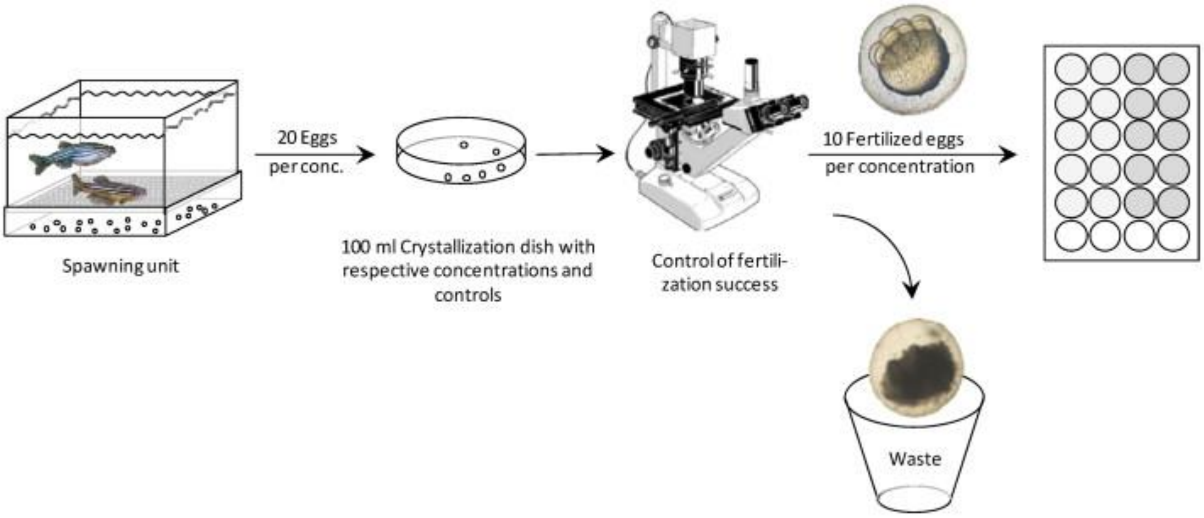

Figure 1.2 Fish embryo test (FET) analysis procedure (left to right): egg collection; the eggs; pre-exposure of fish media in a petri dish; collection of fertilized eggs with an inverted microscope; distribution of the eggs into 24 multi-well plates. (Taken from reference [40]. Reprinted with permission from ©2008 Elsevier Publishing Group).

1.1.4 Phenotyping screening : state-of-the-art using zebrafish embryonic stages

Zebrafish are known as the most suitable model organism for phenotype screening to high-content screening (HCS). It is a well known emerging system for *in vivo* studies related to human disease and drug discovery. Zebrafish have also been used to study pathogenic mechanisms in different conditions including cancer and drug discovery.

HCS assays are used for identifying potentially hazardous compounds, using transgenic zebrafish (TG) (fli1:egfp) that steadily express enhanced green fluorescent protein (eGFP) within the vascular endothelial cells [41-43]. The development of a 384-well HCS assay by Leet et al. has enabled screening of the chemicals affecting cardiovascular development and functions within individual live embryos of 5 to 72 hpf exposed to doses at non-teratogenic concentrations [44] (Figure 1.3). It incorporates both morphological and functional endpoints in a larger sample size and in a wide range of concentrations. With this, a HCS assay provides a robust whole-organism-based platform for preclinical toxicology that focuses on the rapid identification of chemicals.

In addition, engineered pigment-free phenotype transgenic zebrafish models (TG) can be used to identify targeted gene expression through the expression of fluorophores [43, 45]. Recently, Green et al. developed a new TG with a fluorescent estrogen response element (ERE) reporter and silenced skin pigmentation (Casper phenotype). High sensitivity assays are applicable for chemical screening with image analysis for quantifying whole-body responses to estrogenic chemicals. This enables the visualisation of estrogen induced tissue-specific transcriptions in an intact zebrafish in real time. It improves the ability to predict potentionally adverse outcomes in human and wildlife populations.

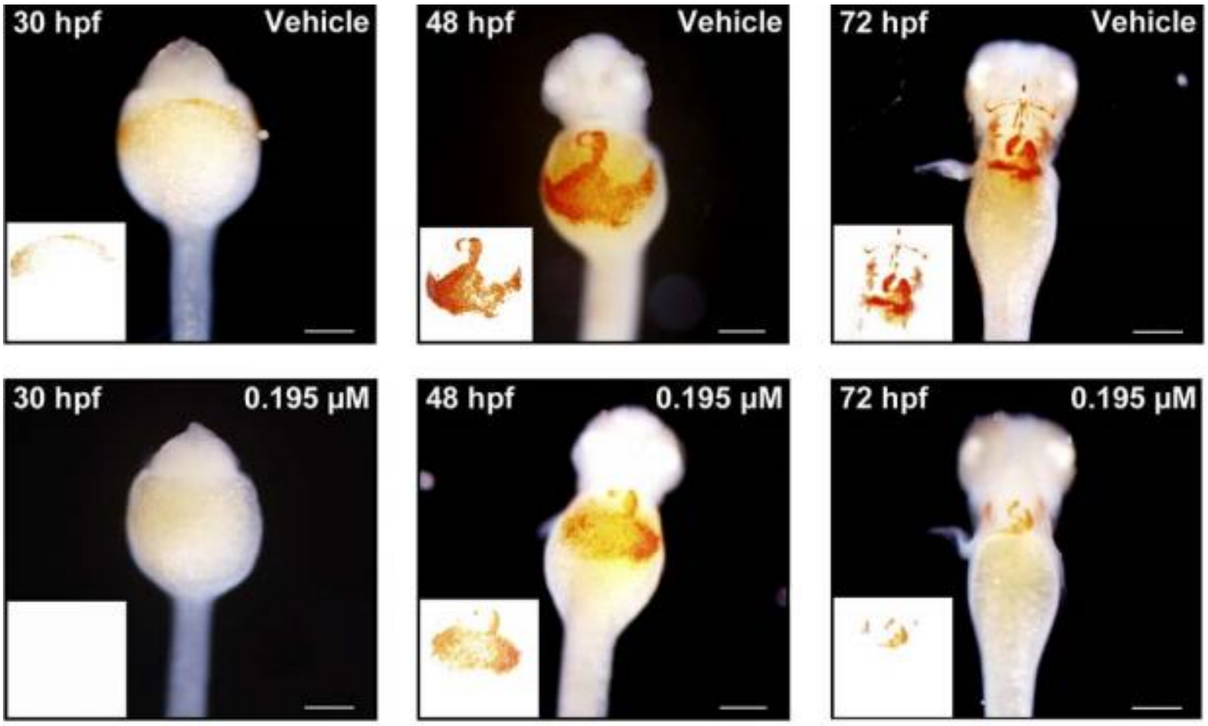

Figure 1.3 Dorsal orientation of zebrafish images at each time point (30, 48 and 72 hpf) for vehicle (0.1% DMSO) and 0.195 μm of butafenacil exposure. O-dianisidine staining was used to assess the presence of haemoglobin in embryos. Haemoglobin-positive cells appeared within the vehicle control embryos after circulation, but were absent following exposure to 0.195 mM of butafenacil. At 48 and 72 hpf, embryos exposed to 0.195 mM butafenacil displayed significantly less haemoglobin than the vehicle controls. Scale bar is 200 μm. (Taken from reference [44]. Reprinted with permission from ©2014 PLOS One).

Despite the advantages of embryonic zebrafish model system for phenotypic screening, procedures such as dispensing, treating and analysing zebrafish embryos are still labour-intensive, manual procedures. Conventional microtiter plates are still used for drug screening bioassays [46-48]. This manual dispensing technique is time consuming and does not offer the high-throughput processing capacity required by the pharmaceuticals industry. Alternative tools or approaches such as automation for drug screening are being developed to allow more rapid and more successful identification in drug candidate selection with high-throughput outcomes.

1.1.5 Automation of zebrafish embryonic bioassays: promises and challenges

In the last two decades, drug research has developed tremendously and high-throughput screening has become the foundation technology of pharmaceutical research. Its development has been influenced by advances in the automation system for handling and manipulation of zebrafish embryos, which is still being developed [49]. For example, the conventional 96-well plates have been replaced with 384-well microplates [50], and a fluorescence-based detection system [51] and screening robot approach have been fully adapted to high-throughput screening [52, 53]. However, these advancements concentrate on automation screening of the chemical libraries, and it is necessary that the general handling and manipulation of small model organisms such as zebrafish embryos must be performed in an automatic manner to generate comparable, homogeneous and reliable data.

The Complex Object Parametric Analyzer and Sorter (COPAS) Biosort (Union Biometrica, MA, USA) allows the automatic dispensing of large numbers of small organisms into multiwell plates to avoid manual manipulation of the embryos [54]; it improves both quality and screening output. It can rapidly sort objects based on various criteria, including optical density and length. ZebraFactor has been developed for embryo sorting and dispensing systems which incorporate robotic manipulations (Figure 1.4) [55]. Although its speed no greater than that of manual dispensing, it offers a great advantages as an unsupervised and continuous operation that may improve high-throughput screening. Recently, advanced technology integrating robotic and micro-capillary fluidics was developed for full automation [56, 57]. This greatly simplifies in vivo specimen manipulation and cellular organ imaging, which can now process multiple organisms simultaneously.

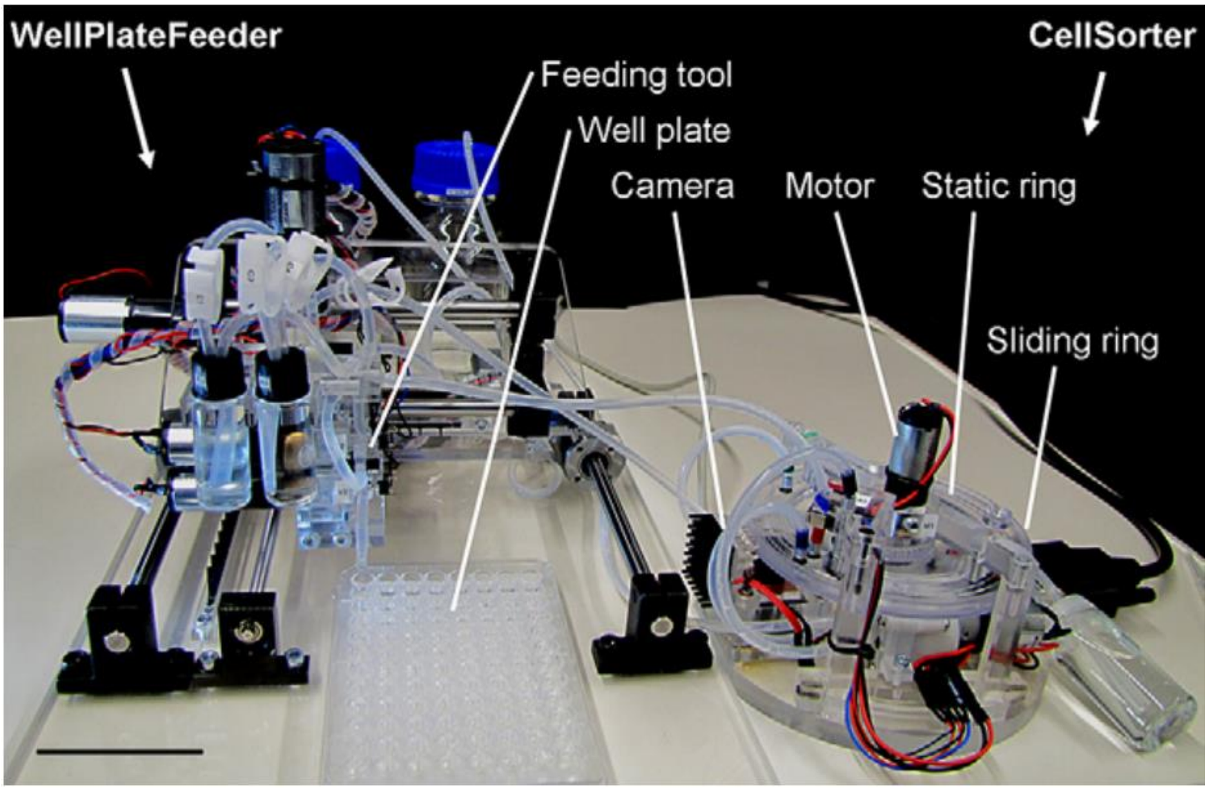

Figure 1.4 Detail configuration of the ZebraFactor system, comprising the WellPlateFeeder (left) and CellSorter (right) using a tubing system as connection. Bar scale is 50 mm. (Taken from reference [55]. Reprinted with permission from ©2011 Society for Laboratory Automation and Screening).

Although labour intensive manipulations have been improved by such highly advanced high-throughput screening, the technologies still lack reliable, user friendly, affordable laboratory automations. Moreover, some advanced systems require expensive visual and automation equipment which increases the cost of operations. With the introduction of microfluidic technologies, innovative devices for automatic manipulation and bioanalysis of zebrafish offer new opportunities for high-throughput screening.

1.2 Microfluidic lab-on-a-chip (LOC) technologies

Microfluidics is an advance technique that enables the manipulation of small amounts of fluids at a range of 10^{-6} to 10^{-12} litres, using fabricated microchannels with dimensions in the sub-millimetre scale. Microfluidics was realised first in 1950s as a small droplet of liquids dispensed in nano- and sub-nanolitre scales [58], followed by a miniaturised ink jet printer nozzle that involved a gas chromatograph (GC) built on a silicon wafer; this was designed in

Stanford University in collaboration with IBM [59, 60]. Microfluidics enables the precise control of small volumes of fluids, and miniaturised fluid handling system is possible.

The impact of microfluidic technologies in research has increased enormously in the last few years. Recent design development and utilisation of microfluidic devices for millilitre scales of fluid transport have been used in a variety of applications such as in life science industries for biomedicine and pharmaceuticals. This includes the development of drugs design, delivery and detection [61-63] and analytical devices such as point-of-care diagnostic devices (Figure 1.5) [64-66]. At industrial level, microfluidic technologies are used for rapid chemical analysis and high-throughput screening [67-69]. In biomedicine, demands for an implanted or ingested microdevice for non-invasive diagnostic and surgery have increased [70-72]. Other areas of application are in the transport of liquids and gases in aerospace [73, 74]. Automotive engineering industries [75, 76] and microreaction engineering [77, 78] are interested in optical-based sensors [79-81].

Major advantages of microfluidics are the need to consume only a small quantity of fluids and reagents, with less hazard to the environment [82]. Microfluidics allows detection and separation at micron/nano spatial resolution; it is cost effective and only requires shorter trasport time for rapid analysis [83]. With the emergence of fabrication methods, microfluidics are able to differentiate the physical properties of fluids moving in large and small channels.

In conjunction with the rise of microfluidics, there has been rapid development and fabrication of microdevices such as micromixers [84, 85], microvalves [86, 87], microsensors [88-90], microreactors [91, 92] and micropumps [93-95]. Each microdevice has specific functions and is a fundamental component in the realisation of a fully integrated microfluidic system, such as LOC or the micro total analysis system. An integrated functional microfluidic LOC system contains a number of different microdevices that achieve full automation in a single chip [96-98]. Particle transport processes such as reactions, mixing, separations and manipulation of particle at miniaturised scale are integrated and fully functional, producing high-throughput outcomes [99]. Microfluidics is the platform for LOC applications, offering a set of fluidic unit operations that allows the implementation of different applications in a well defined, low cost, fabrication technology [100, 101].

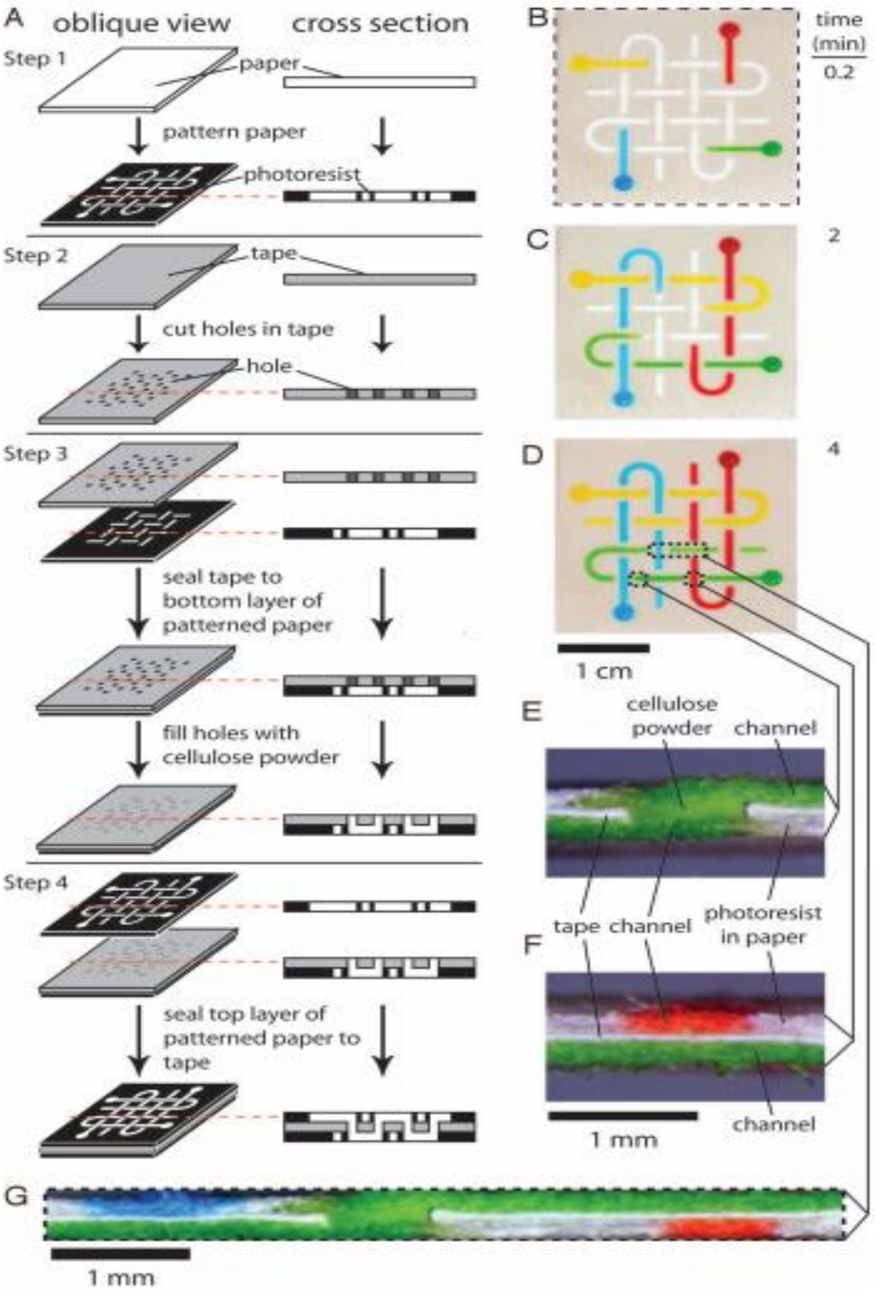

Figure 1.5 Three-dimensional microfluidic paper analytical devices (µPAD). (A) Fabrication is by stacking layers of patterned paper with double-sided adhesive tape. (B) Image of designed basket-weave pattern 10 s after coloured dye solutions were added to the sample reservoir. Dotted line indicates the edge of the device. (C and D) Image taken at 2 and 4 min after adding the dyes. The fluids intersect each other on different planes without mixing. The dotted line in (D) represents the cross-sections shown in E, F and G. (E) Cross-section showing a channel connecting top and bottom layers. (F) Three layers of the device, consisting of orthogonal channels at the top and bottom layers of paper. (G) The distribution of coloured fluids in each layer of the device shown in D. Dotted lines depict the edges of the cross section. (Taken from reference [64]. Reprinted with permission from 2008 ©National Academic of Sciences).

1.2.1 Promises of miniaturised analysis for biological sciences

Recent developments in the design and application of microfluidic devices for fluid transport offer applications in pharmaceuticals and biomedicine, including life sciences. Microfluidic devices are becoming increasingly popular for applications across the biological sciences. They are useful because of their faster response time, their requirement of small fluid volumes, and their controllable flows at microscale [102]. Miniaturised LOC technologies are capable of (i) substantially reducing fluid volumes and operational costs [100], (ii) simplifying complex assay protocols [103-105]; (iii) precisely manipulating cell microenvironments to obtain high through-put outcomes [106-108]; (iv) providing scalability factors [109]; and (v) screening multiple batches simultaneously [110, 111]. Diverse microfluidic systems are making their way into biomedical research, from relatively simple functions to multiple analytical systems, and are used in wide range of applications including cell analysis, metabolomics, immunoassays and point of care diagnostics [105, 112, 113].

Miniaturisation of LOC has led to a new approach to biological screening and experimentation. With the reduction of the number of uncontrolled parameters in a single experiment, a high number of different combination parameters can be examined. Its greatest potential lies in the physical components of the microscale transport system, which can utilise microfluidics to perform experiments that are not possible at macroscale, allowing new functionality and experimental standards to develop.

1.2.2 Principles of microscale fluid flow

The physics of fluid flow in a microfluidic system changes due to scaling factors. In fluid dynamics, the assumption inherent to the understanding of fluid mechanical behaviour is that the system will obey all the concepts of conservation laws including the conservation of mass, momentum and energy. Fluids are treated as continuous, under the continuum assumption, although in reality they comprise molecules. Measurable properties such as density, temperature and pressure vary from one volume to another depending on the molecular properties [114].

Fluids at microscale level do not flow at extreme velocities. The velocity at the boundary layer is assumed to be zero, with a non-slip condition. The motion of an incompressible Newtonian fluid flow through a control volume can be described by the simplified Navier Stokes equation:

$$\left[\frac{\partial u}{\partial t} + (u.\nabla)u\right]\rho = -\nabla P + \mu\nabla^2 u + f \qquad (1)$$

where u is vector velocity, ρ is density of fluid, t is time, P is pressure, μ is dynamic viscosity and f represents the body forces (e.g. gravity ρg_z, where g_z is defined as gravitational acceleration).

The left side of the equation represents the inertial acceleration per unit of volume. On the right of the equation defined as overall force per unit volume, due to the effects of viscosity and the pressure gradient. Viscosity in this context refers to the effectiveness of the momentum of the diffusion process, while inertia indicates the change in overall momentum of the fluid flow [114].

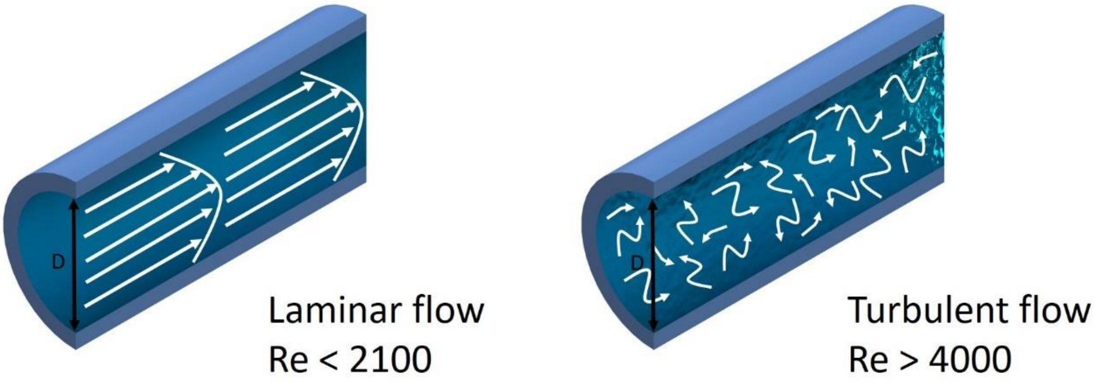

Figure 1.6 Laminar and turbulent flow streamline characteristics.

There are two different fluid flow regimes governing fluid mechanics: turbulent and laminar flow (Figure 1.6) . Turbulent flow describes an irregular flow that forms eddies and vortices. This phenomenon can be explained using the inertial terms in the Navier–Stokes equation, the time-dependent acceleration $\left(\frac{\partial u}{\partial t}\right)$ and convective acceleration $(u.\nabla u)$. Laminar or viscous flow, on the other hand, occurs when the streamline of fluid flow is smooth and parallel layers of fluid slide side by side without the creation of eddies and vortices. In laminar flow there is no velocity component perpendicular to the main flow direction. It has a constant velocity at a given pressure difference from one end to the other, provided that the dimensions are constant throughout the system.

Fluid behaviour is characterised by the magnitude of the inertial and viscosity terms. In laminar flow, the rate of momentum transfer (determined from the fluid viscosity) is high in comparison with the total amount of momentum (from inertial force). This is due to the suppression of the viscosity towards the flow acceleration. In contrast, when the total momentum rate goes beyond the diffusion momentum rate, a combination of the time dependent acceleration and convective acceleration leads to a turbulent regime.

The flow regime can be characterised by the Reynolds number, R_E, which gives the ratio of inertial to vicious forces. R_E is a dimensionless quantity used to predict the flow patterns in different flow regimes:

$$R_E = \frac{\rho v L}{\mu} \ldots\ldots\ldots (\mathbf{2})$$

where ρ is fluid density, v is the characteristic velocity of fluid, L is the characteristic length and μ is fluid viscosity.

The R_E equation depends on the geometrical shape of the channel in which the fluid flows. For flow in a cylindrical channel, the R_E numbers are generally defined as:

$$R_E = \frac{\rho u D}{\mu} = \frac{uD}{v} = \frac{QD}{Av} \ldots\ldots (\mathbf{3})$$

where D is the hydraulic diameter of the channel (circular), ρ is the density of fluid, u is the velocity of fluid, v is the kinematic viscosity$\left(v = \frac{\mu}{\rho}\right)$, Q is the volumetric flow rate $Q = Au$ and A is the channel cross-section area.

For a rectangular channel, the heights and widths of the channels are comparable and the hydraulic diameter is defined as:

$$D = \frac{4A}{P} \ldots\ldots\ldots\ldots (\mathbf{3a})$$

where A is the cross sectional area and P is the rectangular perimeter. Laminar flow occurs when $R_E < 2100$ and turbulent flow occurs when $R_E > 4000$ [115]. In the case of microscale channels in microfluidic system, the fluid flow is mostly in the laminar regime ($R_E < 100$) [116].

Molecular diffusion or mass transfer occurs when two or more fluids are mixed within a microfluidic channel. The transport phenomenon is characterised by a random thermal movement of the particles; the net movement is classified as movement from more concentrated to less concentrated areas (Figure 1.7). The diffusing particles are homogenised throughout a finite volume. Diffusion coefficients and distance of the mass transfer determine the time taken for a complete diffusion. Mass transfer in diffusion exhibits a potential delay that is not significant at the microscale level in a microfluidic channel width of less than 500 µm. The time interval of exchange fluid in mass transfer in microchannels takes several seconds to minutes.

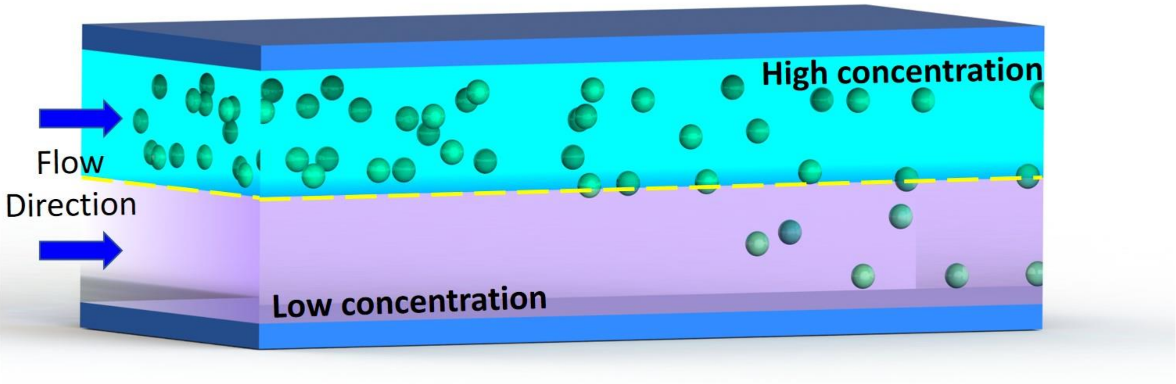

Figure 1.7 Mass transfer due to a steady diffusion within a microfluidic channel at the boundary of two laminar streams.

1.2.3 Fabrication methods for LOC devices

A wide variety of methods was developed for the fabrication of microfluidic devices, including reactive ion etching [117], wet etching [118, 119], plasma etching [120], conventional tool-based machining [121, 122], hot embossing [123], laser ablation [124, 125], photolithography and soft lithography. In the following sections, a brief description of some of the more common methods is presented. Table 1.2 presents the list of methods, with assessment of their cost, speed, and achievable feature size.

Table 1.2. Comparison of microfabrication methods

Method	Material	Cost	Speed	Feature size
Conventional machining	Metals, ceramics, polymers, composites	High	Fast	< 200 µm
Laser Micromachining	Metals, polymers, ceramics	Low	Fast	Variety
Photolithography	Polymers	High	Slow	< 10 µm
Soft lithography	Polymers	Low	Fast	< 10 µm
Hot embossing	Metals, polymers	High	Slow	< 10 µm
3D printing	Metals, polymers	Low	Fast	< 200 µm

1.2.3.1 Material selection for fabricating chip-based devices

Appropriate material selection is essential in the fabrication of microfluidic chip-based devices. Materials are generally chosen based on their suitability for a particular application. Critical issues such as thermal stability, mechanical behaviour, chemical properties, electrical characteristics, optical properties and biocompatibility are factors that need to be carefully considered in order to obtain maximum performance from a microdevice.

In the early stages of the development of microfluidics, devices were fabricated on a silicon wafer or glass substrate [102, 126, 127], mainly because microelectronics and fabrication techniques were well established in the semiconductor industry. Glass materials have the advantages of outstanding corrosion resistance, optical transparency, dielectric characteristic, and good insulator; however, using it as a substrate material has significant drawbacks: in particular, the complicated procedures required to manufacture it result in an expensive end product [126, 128]. Polymers such as polymethylmethacrylate (PMMA) [129-131], and polydimethylsiloxane (PDMS) [132-134] are more promising materials for fabricating microfluidic devices because they have optical properties comparable with glass, and are in addition disposable, inexpensive, and with higher flexibility.

PMMA, or acrylic, is an optically transparent material. It has excellent rigidity and mechanical characteristics, which make it is one of the dominant materials used for microfluidic device fabrication. Each PMMA sheet is non-porous and the surface exhibits a hydrophobic layer which reduces the contamination effect on the microfluidic operation [135, 136]. Although inert in neutral aqueous solution, it has low stability against alcohol and organic solvent which limits is use for some LOC applications [137].

PDMS is currently the most widely used polymer material for LOC device fabrication. The polymer has excellent properties such as being optically transparent to light between 240 to 1100 nm, and having thermal stability and and low surface tension [138, 139]. In microfluidic devices, where quantification of chemical substances are involved, the most important properties are permeability, elasticity and surface quality [140]. The porous nature of PDMS makes the material highly permeable compared with other elastomers; this enables small molecules to diffuse in the polymer, which makes it suitable for biological applications [132, 141]. The apparent permeability and biocompatibility make it the most suitable material for microfluidic devices designed to carry out the in situ biological experiment presented in this thesis.

PDMS exist in highly coiled conformers, which makes them elastic. When the material is stretched the polymer unwind; when the tension is released, the polymer recoils. Elasticity depends directly on the amount of crosslinking, and during PDMS fabrication adding more or less curing agent to the elastomer base can alter this. The recommended ratio is 10:1 (elastomer base:curing agent) by weight [126, 142]. Due to its flexibility, PDMS are used in microfluidic applications where materials need to be bent or twisted [143].

1.2.3.2 Conventional methods of fabricating LOC devices

Standard available fabrication methods for microfluidic devices are not always suitable for fabricating LOC devices, and need to be carefully selected based the overall size of the final structures, material availability and cost of operation. In particular, the method chosen must be inexpensive and simple, as most LOC devices are fabricated in sophisticated laboratories with limited engineering facilities. This section briefly discusses the rapid microfabrication method of developing LOC devices.

- **Photolithography**

The most basic type of microfluidic fabrication is photolithography. Conventionally, processes involve silicon-based fabrication derived from semiconductor fabrication [144]. Photolithography employs patterns created by photosensitive material. A thin layer of photoresistant material is fabricated using a spin coater machine, then exposed to UV radiation through a photomask. After exposure, the areas that are more soluble in a designated solvent are removed and the remaining, more resistant structures remain on the substrate in the form of a negative [145]. However, this traditional method of lithography exhibits a low quality of transfer pattern due to insufficient flow of the polymer. This is due to the non-uniform size and placement of the desired structures on the mold. The method has a high replication precision of 99.5 % of the SU-8 layer, as illustrated in Figure 1.8.

Mask-based lithography essentially imitates the features present on the mask, which is the primary structure. Complex structures required more time to fabricate and the cost of mask creation is considerable, so maskless photolithography is preferable for short-time microfluidic fabrication. This method uses a digital micromirror device that acts as a programmable mask and selectively reflects the incident light [146]. A small feature size in the sub-millimetre range, from 40 – 700 µm, is reliable for maskless lithography. Leigh and associates have developed a maskless micropatterning system that employs a fluorescence microscope with programmable X-Y stage and dry film photoresist. A scaffold template is fabricated for protein/cell patterning, or optically guided cell encapsulation for biological applications [147].

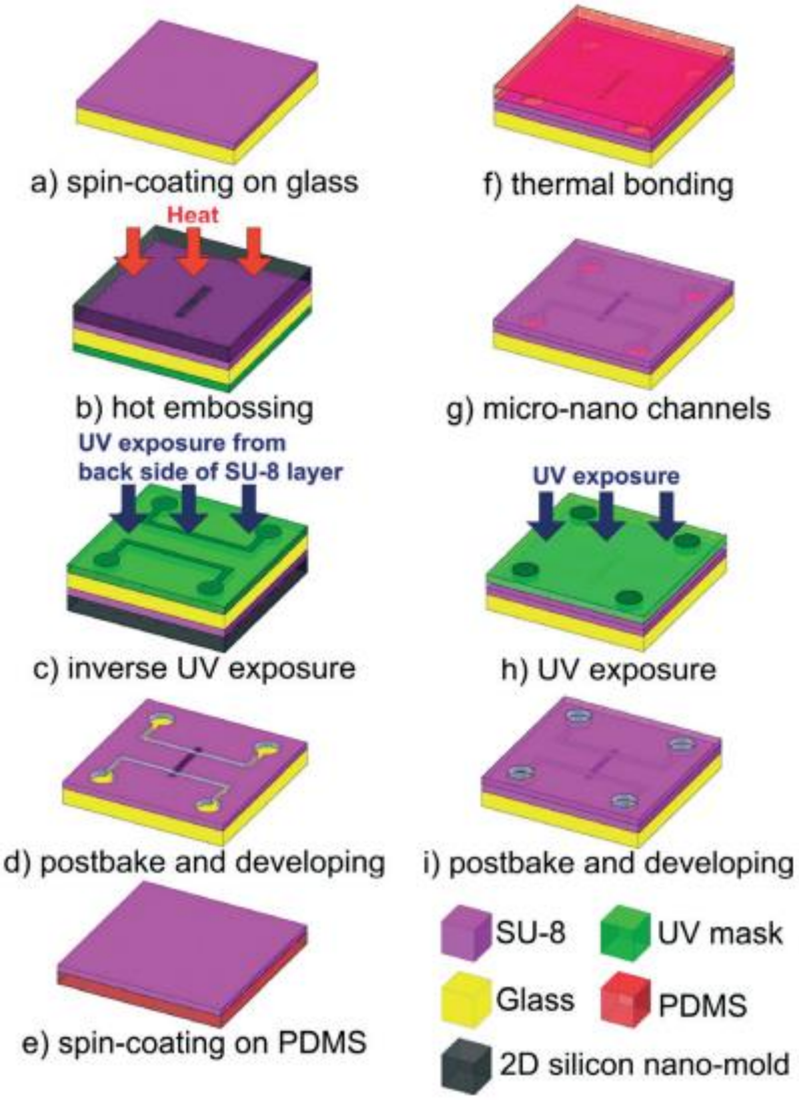

Figure 1.8 Process flow of the SU-8 microfabrication using photolithography techniques. (a) A 30 µm thick layer of SU-8 material is spin-coated on to a glass substrate. (b) Hot embossing is applied on pre-cured SU-8 at 85°C for 20 minutes in an oven. (c) The other side of the SU-8 layer is exposed to UV light using a UV mask at a dose of 227.6 µW cm^{-2} for 10 minutes. (d) Post baked at 85°C for 2 minutes and the final structure is developed. (e) A layer of 20 µm thick of SU-8 is spin-coated on to a PDMS substrate, followed by post-baking at 85 °C for 30 s (f) The patterned SU-8 layer and the SU-8 cover layer are thermally bonded in an oven at 50°C for 4 minutes. (g) The PDMS substrate is removed from the SU-8 cover layer and sealed micro and nano-channels are formed. (h) The sealed SU-8 channel is exposed to UV light to cross-link the SU-8 cover layer and inlets and outlets are formed. (Taken from reference [148]. Reprinted with permission from ©2014 Royal Society of Chemistry).

- **Soft lithography**

Soft lithography in poly (dimethyl methyl siloxane: PDMS) is the state-of-the-art microfluidic fabrication method. This method is time effective compared with silicon technology, requiring less than two days' fabrication time. This technique is based on printing and moulding, using patterned elastomeric stamps. Soft lithography enables control of the molecular structures of the surfaces, and fabrication of complex patterns is possible. This fabrication process is more convenient, inexpensive than conventional photolithography [149], and is most suitable for biological microfluidic devices. In addition, the process is maskless and it can save more time compare to the conventional lithography process. Its structure exhibits an inert surface that avoids adhesion with the protein and cells in the chip [142]. Khademhosseini et al. present a novel method for patterning cellular co-cultures using soft lithography to immobilise cells and protein onto a glass substrate without adherence to the surface, a method particularly suitable for fabricating controlled cellular co-cultures for cell–cell interaction studies and tissue engineering applications [150].

Replication method from using a mould for patterning can be replicated many times in soft lithography fabrication. It uses rigid master moulds made from elastomeric material that facilitates the separation of master and replica or substrate. PDMS is widely used for this because of its rigidity, non-toxicity and commercial availability. It also has transparent properties, and its hydrophobic surface is permeable to nonpolar gases such as nitrogen, oxygen and carbon dioxide, which makes it suitable for biological samples [151]. A high aspect ratio of its structures such as nanopillars, 300 nm to 1 µm in diameter, are possible using replica moulding [152].

Recently, Sticker et al. investigated an alternative material of elastomer, photosensitive thermoset (OSTEMER), used for multilayer fabrication of microfluidic devices. Three different membranes OSTEMER, flexible (FEP) and PDMS, enable the integration of microfluidic parts such as microvalves and micropumps [153].

- **Laser micromachining**

Laser micromachining is a type of non-contact material removal process, mainly used industrially to create structures by direct machining. Laser beams spot scan the surface. Laser machining is an ablation process directed towards material substrate by absorption of the laser photons by the material, thus increasing its temperature and evaporation. The material’s removal occurs because of thermal mechanisms and laser interactions between materials. Laser micromachining has several advantages in the fabrication of complex cross-sectional shapes that are difficult to machine using conventional lithography processes. Multi-photon absorption is mainly from a transparent material if the intensity peak is high. This has been demonstrated by Darvishi et al. in the fabrication of tapered microchannels in borosilicate glasses and PDMS of transparent solids [154]. A Schematic diagram of the laser set-up is shown in Figure 1.9.

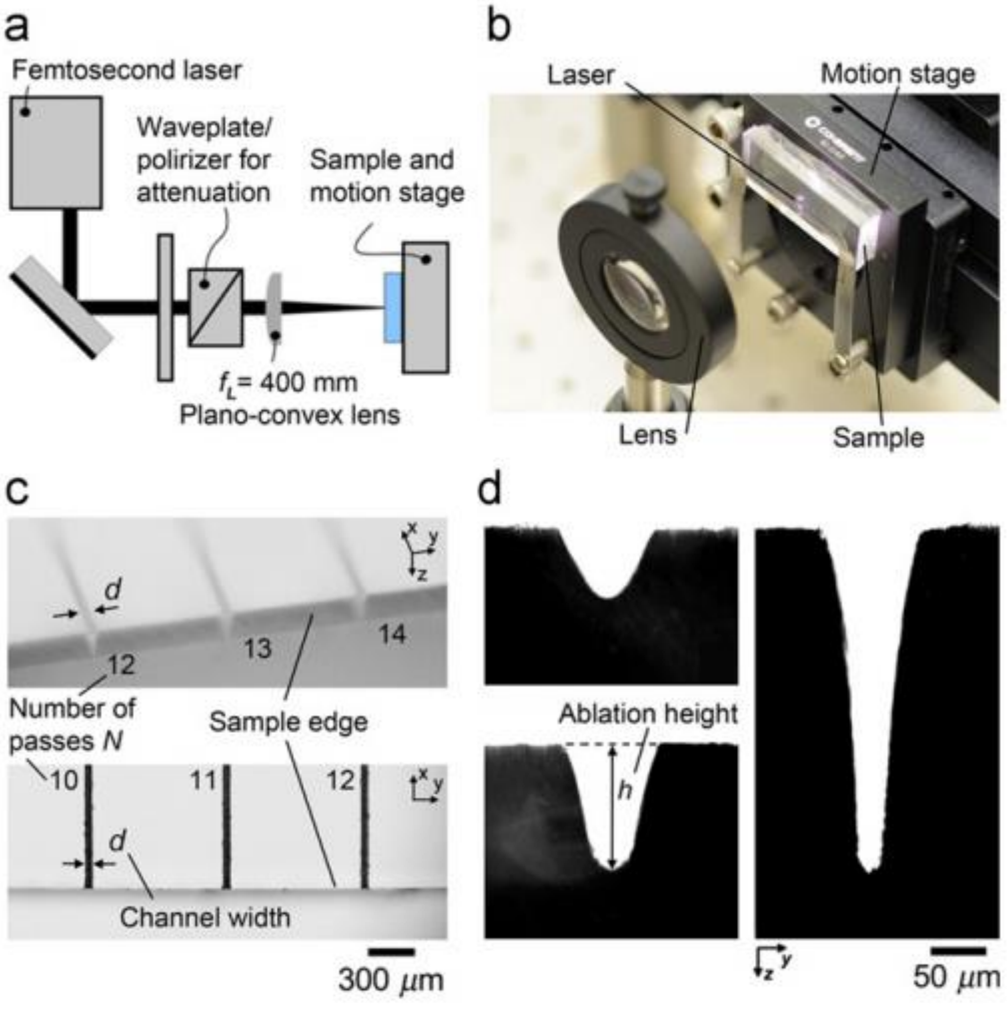

Figure 1.9 (A) Schematic diagram of the experimental setup for laser ablation methods. (B) An image of the PDMS slab is oriented with the thin edge parallel to the laser beam. (C) Images of micromachined of trenches with different number of passes, *N* and stage velocity, *V.* (D) The micrographs of micromachined channels in borosilicate glass. (Taken from reference [154]. Reprinted with permission from ©2011 Elsevier Publishing Group)

Ultrafast laser (pulse duration < 1 ps) interaction with material is different from conventional lasers. A non-linear mechanism is applied which is directly exert the energy coupling into the material, which is then ionised, and the bonds are broken directly by electron-photon reaction [155]. Recently, ultrafast laser machining has been used to fabricate structures on thermal and shock-resistance materials, taking advantage of its high speed cutting using picosecond lasers. Both homogenous and non-homogeneous glass was machined using ultrafast laser beams on a single-pass and single-shot configuration [156]. Post-processing of the machined surface is required, using a wet etching process to remove debris.

The CO_2-type laser depends on a discharge from a gas chamber filled with carbon dioxide, hydrogen, nitrogen and helium. The laser wavelength is around 10 µm. This laser is often used to fabricate microchannels in poly(methyl methacrylate)(PMMA) material [157]. Hong et al. have demonstrated direct laser machining of PMMA with a CO_2 laser to fabricate microchannels with a width below 100 µm and depths from a few tens to a hundred micrometres. A high surface quality was observed: no post-processing is needed with this method [136]. The surface roughness is influenced by the grooves' spacing and the orientation of the scanning direction between successive layers. Laser micromachining is a one-step process, but thermal damage around the cutting areas gives it inaccurate dimensions which limit its applications.

Some of the techniques discussed above are labour intensive, require enough space to hold multiple pieces of equipment, need long processing times and use materials with limited biocompatibility. For example, photolithography technique consists of multiple steps, from selection of the material to fully functional chip, and this consumes considerable time. A more rapid fabrication method is preferred, particularly as some operators may not have the time to learn a complex fabrication process.

1.2.4 Additive manufacturing: an alternative tool for microfabrication

In recent research, the advancement of additive manufacturing or 3D printing technologies has simplified the fabrication of LOC devices by reducing the work to a single step. There are some remarkable advantages associated with 3D printing, including a low cost set-up, rapid prototyping, and a three dimensional (3D) digital design. 3D printing technology is currently the best solution to problems of more conventional methods of fabricating LOC device.

1.2.4.1 3D printing technologies

3D printing is a rapid one-step manufacturing process, employing an additive layer-by-layer manufacturing process based on a sequence of cross-sectional slices from 3D model data. Its basic principle is much like that of a traditional laser printer or ink jet printer, but the multi-coloured ink is replaced by polymer or resin. 3D printing consists of two main processes, design and fabrication. The first step in designing is to use 3D CAD or other engineering drawing software for full modelling of the structures. The printer able to configure the file format and sliced into 2D sequential cross sections slices depending on the resolution (layer thickness) of the printer. At the end of the process, the printer deposits layer by layer of polymer or resin and form a complete 3D structures.

Several different methods employ the 3D printing concept: stereolithography (SLA), Multi Jet Modelling (MJM) and fused deposition modelling (FDM), and all are well established in prototyping microfluidic devices [158]. The factors that determine the quality of printing are layer by layer thickness (accuracy), printing speed, type of materials and build size. 3D printing technologies currently used to fabricate microfluidic devices mainly use photopolymer resin as the build material, to make the channel directly for the sub-sequence process of replica moulding.

- **Stereolithography (SLA)**

The SLA fabrication process, also known as micro-stereolithography (µSLA), is one of the available 3D printing technique, that can create fine structures [159]. It was first established by Hall in 1986, creating a layer-by-layer 3D object from photosensitive liquid solidified on exposure to ultraviolet (UV) light [160]. SLA allows rapid and easy fabrication of functional prototypes, and does not require any production tooling prior to printing. The basic principle is the use of structured light such as a laser beam to scan the surface of resin that polymerises and solidifies upon exposure to UV. Conceptually, a thin layer of curable resin is stacked parallel and on top of another when printing takes place. The platform moves down in the z direction after one layer is printed, and this process is repeated until the whole structure is formed. A liquid bath of curable resin is used on top of the movable stage. During the process, the table is lowered each time by a distance that determines the resol layer thickness of the printer. An optical scanner scans the laser beam across the curable resin in the x and y planes. Both bath configuration and optical set-up are convenient, implementable set-ups [161] (Figure 1.10).

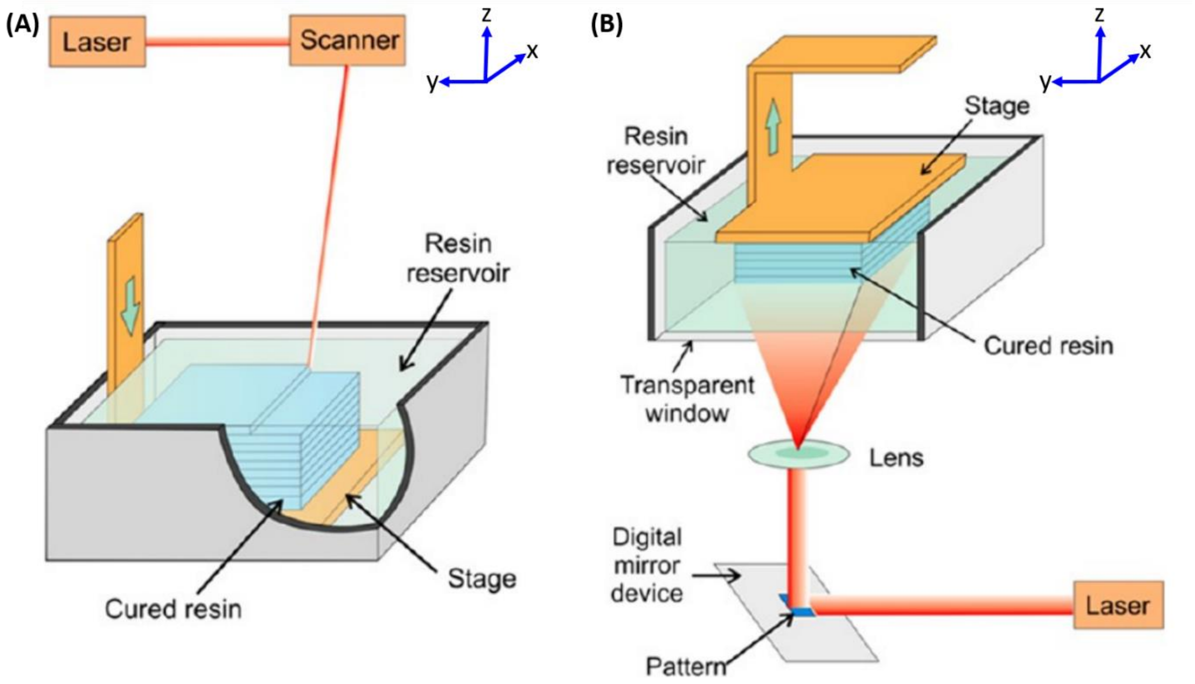

Figure 1.10 (A) Schematic diagram of configuration SLA printer with direct write-curing process fabrication. The stage is submerged in liquid resin. The laser moves along the surface of the resin and polymerises the resin row by row until the desired layer is completely cured. The stage is submerged lower into the resin tank until a new layer of liquid resin covers the surface and the polymerisation repeats. (B) Schematic diagram of a configured SLA printer with a projection-based curing method. In this configuration, the stage is submerged at a specific distance in the resin reservoir. In the projection curing method, the digital mirror permits a whole layer to be cured at once. The stage can be elevated by a defined distance and another layer cured. This process repeats until the complete object is printed. (Taken from reference [161]. Reprinted with permission from ©2014 American Chemical Society).

In SLA, the cure depth determines the z axis resolution (layer thickness), which is controlled by the photoinitiator and irradiant exposure conditions such as wavelength, power and exposure time. UV absorbers are available for the fabrication of transparent or optical grade parts. The layer thickness is usually within the range of 50–200 µm; with microstereolithography, however, resolutions up to 5 µm can be achieved [162].

One of the advantages of using SLA fabrication is the fine precision of the feature resolution up to 50 µm. SLA systems have become the most widely used and commercialised form of

3D printing [163], but in other applications, are able to fabricate structures at low cost due to the low usage of the liquid medium. SLA adapts to a variety of monomers and resins as material parts of the liquid medium. The monomers used in photopolymerisation-based part-printing have a low viscosity that is capable of rapid polymerisation and produces cross-linked polymers. With fast curing monomers and short radiation exposure time, the photoinitiator that remains able to be post-cured in an UV oven to complete the curing process [164].

The 3D printer has become smaller and more affordable since its first commercialisation; it is likely to reach a stage where it can print structures even at home [165]. For example, the Form1+type high resolution (25-100 µm) developed by FormLabs company is a type of personal desktop SLA model able to print structures that achieve industrial standards at an affordable price. It can print structures up to 25 µm thick with a minimum feature size of 300 µm [166].

SLA is heavily used in areas as diverse as engineering, manufacturing and art [167]. Its high precision printing has attracted researchers to apply the technology in biological and medical sciences. The use of additive manufacturing technologies in bone tissue engineering has gained much interest in recent years, and 3D printing was found a suitable method of printing porous scaffolds with good surface quality [168]. A study conducted in 2009 by Lan et al. fabricated a 3D porous scaffold from poly (propylene fumarate: PPF) polymer using µSTL with a porosity of 65%. Results found that using a biomimetic coating on the scaffold can be useful in bone tissue engineering [169]. In addition, a well defined 3D model of porous structures has been successfully prepared with SLA, using poly(d, l-lactide)/nanosized hydroxyapatite (PDLLA/nano-Hap) composite resins [170].

- **Digital micro-mirror device based projection printing (DMD–PP)**

DMP–PP technology uses the same working principle as SLA, but has a controllable digital mirror that can reflect the laser light into the entire plane to cure the full layer at once. This is unlike the standard SLA system, where the laser is used to scan the shape of the printing object. Unwanted printing areas are digitally masked by the DMD–PP system [171]. Unlike SLA, DMP-PP does not require the movement of the printing stage because the focal configurations can be automatically adjusted by the tilting convex lens in the system [172] (Figure 1.11). This technology has improved the printing time, and is considered to be the next advancement of SLA [173].

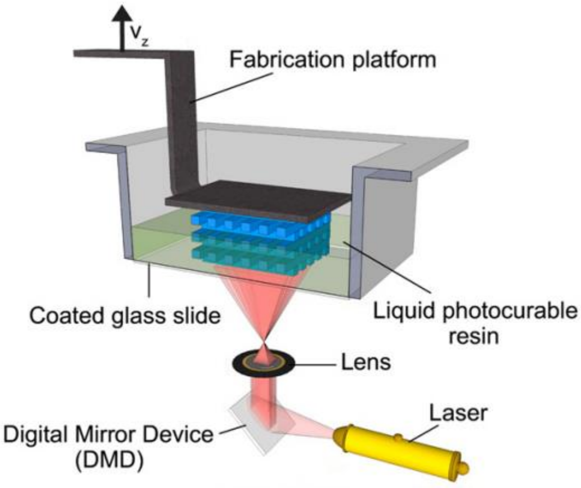

Figure 1.11 Schematic diagram of DMD-PP system configuration. (Taken from reference [172]. Reprinted with permission from ©2012 Elsevier Ltd.).

- **Two-photon polymerisation (2PP)**

Two-photon polymerisation is a direct writing technology which uses femtosecond laser pulses to write the design into the photosensitive resin. The process is similar to SLA in that the pulse laser activates the polymerisation process of the resin [174]. In this process, two photons are absorbed simultaneously by the photo initiator and act as one photon for the polymerisation reaction to begin. This allows the process to write directly any 3D patterns into a volume of photosensitive resin. Most of the materials used are transparent, near-infrared and highly absorptive in the UV spectral range. 2PP technology allows the laser beam to be focused by adjusting the laser pulse energy and the number of applied pulses. This improves the printing resolution thickness up to 150 nm by providing a smaller laser beam diameter of 10-200 µm; however, the writing or tracing method is slower than SLA [112].

- **Fused Deposition Modelling (FDM)**

FDM is a method for rapid prototyping, which depends on surface chemistry, thermal energy and layer-by-layer technology [175]. Thermoplastic materials such as polycarbonate

(PC) are melted in a heating element to a semi-solid condition. This melted polymer is extruded through a nozzle onto a platform table, layer by layer. The table moves upwards as the extrusion process continues, and as it moves the melted material solidifies to form a complete model, as illustrated in Figure 1.12 [176]. Recent developments have shown that FDM has great potential in clinical applications[177], tissue engineering [178, 179] (Figure 1.13) and diagnostic platform [180] A wide range of materials can be used in FDM, such as carbon fibre reinforced plastic (CFRP), to improve physical properties such as tensile strength and the flexural properties of the prototypes [181]. FDM is cheap and reliable for prototyping substrates and mass production; however, the lines of the layers can be seen on the surface of the prototype, and may affect the final structures of the product [182].

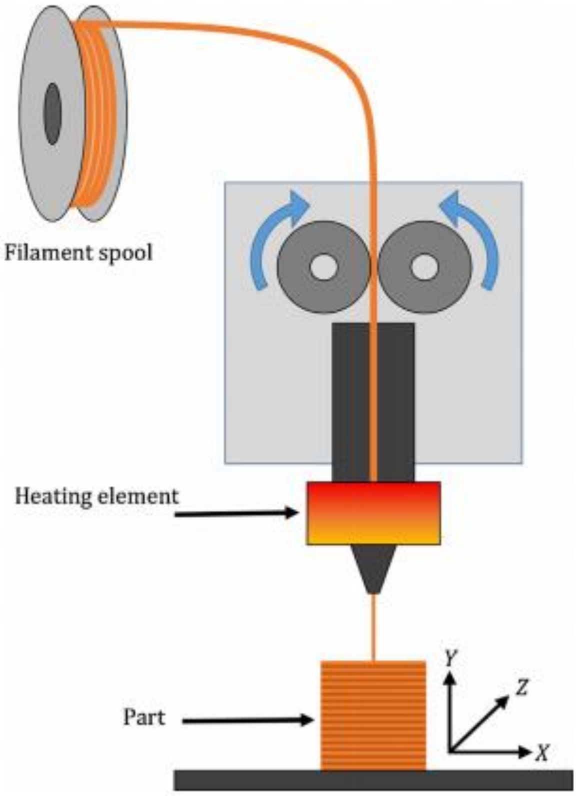

Figure 1.12. Schematic diagram of FDM basic principles. Heated nozzle directly extruded polymer and layer by layer polymer is deposited on the platform. (Taken from reference [176]. Reprinted with permission from ©2015 Academy of Dental Materials).

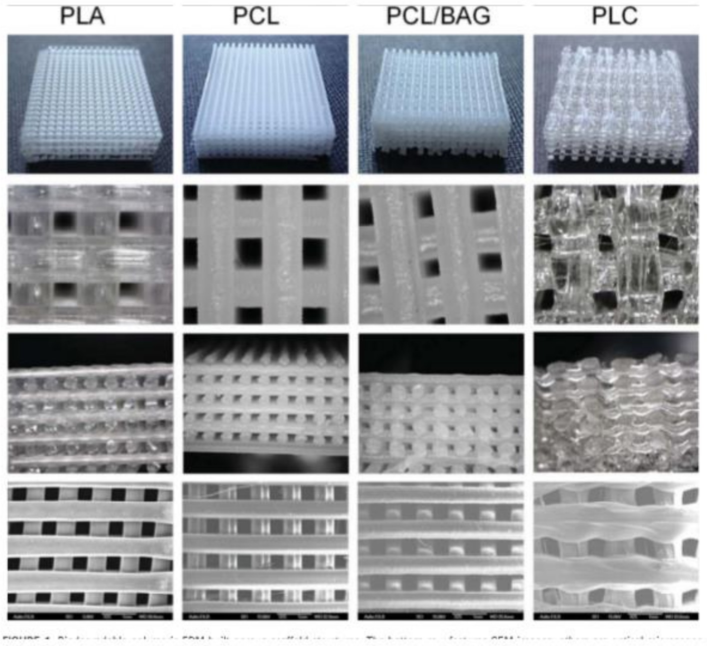

Figure 1.13 Different biodegradable polymers scaffolds for tissue engineering were fabricated using FDM method. All the structures were characterized using scanning electron microscope (SEM). (Taken from reference [179]. Reprinted with permission from ©2012 Wiley Periodical Publishing Group).

- **Multi Jet Modelling (MJM)**

MJM is a type of contactless printing technique capable of reproducing digital image data on the substrate materials using picolitre droplets. This process is similar in concept to commercial ink jet printers; the main difference is that the material used instead of ink prints photoresin or wax material. The heads release material onto the tray and where it is cured by UV light and solidified. After this the build tray is lowered and building the next layer begins. This fabrication process is fast, produces a high quality final product, and is able to print with multiple materials simultaneously [183] (Figure 1.14).

MJM can be used to deposit conductive tracks based on organic silver particles and copper precursors. Due to their high surface-to-volume ratio, the use of nanoparticles reduces the sintering temperature in order to render the conductive tracks [184]. Park et al. have demonstrated a direct-wired MJM using copper nanoparticles of 40–50 nm to fabricate metal-like patterns that are highly conductive after undergoing heat treatment [185].

MJM has shown great potential in various applications, including electronics and biomedicine. For example low-cost lithium microbatteries are fabricated using ionogel, which gives the batteries a liquid-like electrolyte performance [186]. Traditionally, this is done using a physical vapour deposition technique, which is more expensive and time-consuming. Interestingly, Caro et al. explored the possibility of MJM by printing a film consisting of chitosan-tripolyphosphate nanoparticles (CS/TPP); this film is used as packaging to extend the life of fresh fruit [187].

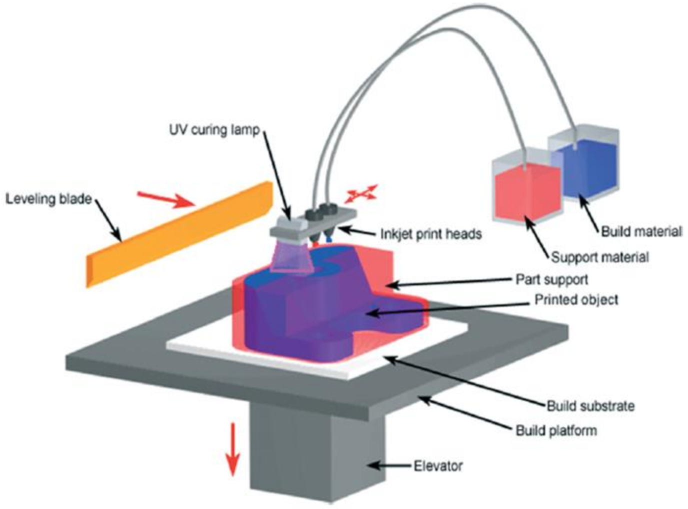

Figure 1.14 Photopolymer-based ink-jet printer using the MJM fabrication concept (Taken from reference [183]. Copyright 2008 CustomPartNet).

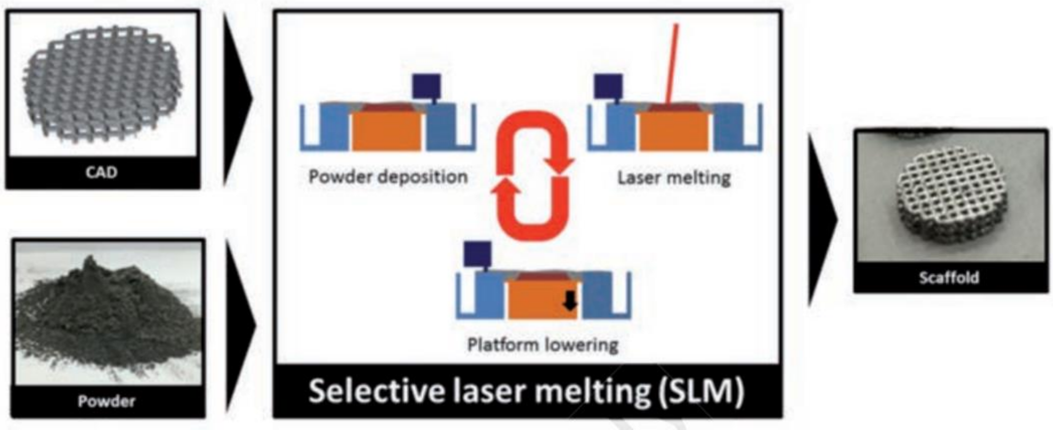

Figure 1.15 Schematic configuration of the selective laser sintering process (Taken from reference [188]. Reprinted with permission from ©2016 PAGEPress).

- **Selective laser sintering (SLS).**

Direct selective laser sintering is a powder-based layer-additive rapid-prototyping process. The laser beam is used as the heating element for scanning, and as the powder melts, it forms predetermined shapes [188, 189] (Figure 1.15). As the first layer is scanned, a second layer of loose powder is deposited on the surface; and the heating process is repeated from bottom to top layer until the structure is complete. This technology has a great advantage of direct printing using metals, while other printers are limited to polymers or plastics. Unlike resins, metals and ceramic powders are incompressible structures, so no additional support material is needed to print overhanging structures; however, post-processing is needed to remove residue from small and narrow structures [190].

- **Bioprinting**

Recent advances in additive manufacturing technologies have enabled 3D printing of biological materials such as cells to be placed in the printer and dispense it layer by layer to form a complex functional living tissues. Customised 3D printer scaffolds for tissue generation or organ engineering can be fabricated using bioprinters [112]. However, challenges remain in the integration of a vascular network, because engineered tissue does not get a sufficient supply of nutrients and gas exchange during perfusion [191]. Bioprinters vary significantly between manufacturers, and each printer is designed for specific biological materials such as cells, agarose, hydrogels or other viscous biocompatible materials [192, 193] (Figure 1.16).

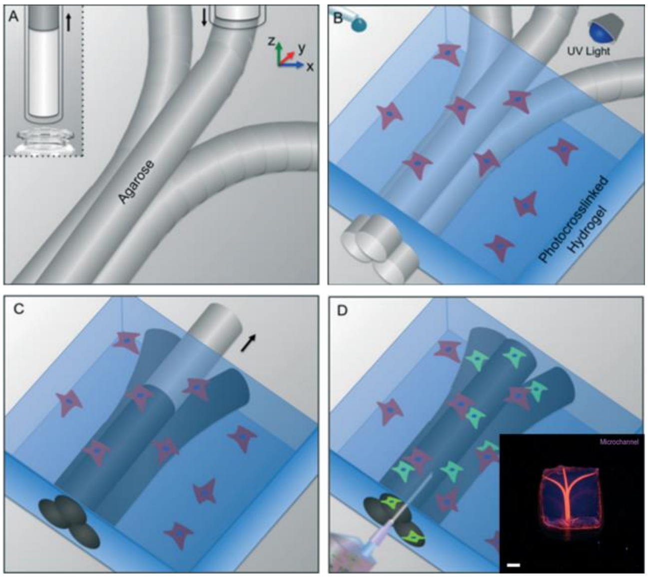

Figure 1.16 Image representation of agarose template fibers bioprinting and the formation of microchannels using the micromolding technique. (A) A bioprinter attached with a piston fitted inside the glass capillary extracts the agarose mixture (inset image). (B) A hydrogel is cast over the bioprinted mould and solidified. (C) The template is removed from the solidified hydrogel. (D) Perfusable microchannels are formed. Inset image shows microchannels perfused with a fluorescent

microbead suspension (pink) (scale bar is 3 mm, microchannel diameter is 500 µm) (Taken from reference [193]. Reprinted with permission from ©2014 Royal Society of Chemistry).

3D printing fabrication has advantages and limitations. Every printer has different applications and uses different materials. Table 1.3 presents the characteristics of the 3D printing technologies described in this chapter.

Table 1.3 Comparison of 3D printing technologies

3D printing	Material (s)	Resolution (µm)	Speed	Cost	Special feature (s)	Surface finish
SLA[159, 160, 162, 164, 165, 167, 173]	Photopolymer resins	<100	Medium	Medium	High resolution	Smooth
DMD–PP [161, 172, 173]	Photopolymer resin	<100	Fast	Medium	Rapid fabrication	Smooth
2 PP [112, 174]	Photopolymer resins	<100	Slow	High	Ultra precise resolution	Smooth
FDM [175-182]	Thermoplastics, Polycarbonate,	>200	Fast	Low	Inexpensive, desktop size, and wide range of materials	Rough
MJM [183-187]	Photopolymer	<100	Medium	Medium	Multiple materials used	Smooth
SLS [188-190]	Metal, Polymers	<100	Medium	Medium	Metals used (option for investment casting)	Rough
Bioprinting [112, 191-193]	Cells, DNA	<100	Slow	High	Biological materials	Smooth

1.2.4.2 Applications of 3D printing in microfluidics

In comparison with conventional microfabrication methods, 3D printing features capability in fabricating high-resolution (up to 16 µm) complex structures with a single step in an inexpensive fabrication process. Recent advances and development have spurred growing interest in biological and biomedical fields, and this has led to investigations into applications of this technology in fabricating microfluidic and LOC devices.

- **Interconnection ports**

Common techniques used to interconnect microfluidic devices with other instrumentation are inserting tubing into punched holes or using adhesive to seal the tubing onto PDMS slabs. However, lack of reliability in the connection ports can cause a device failure due to leakage and back pressure. The use of 3D printed features can solve this problem by integrating a connection mechanism that can not be achieved in the traditional soft lithography technique. For example, Lee et al. have successfully integrated threaded ports that fit commercial finger-tight adapters with 3D printed microfluidics for more reliable and convenient connection with external tubing [194]. In addition, with multimaterial 3D printing, O-rings can be printed directly onto microfluidic devices to create tight seals and connections [195] (Figure 1.17 A). Customized 3D printed luer adapters and threaded fittings have also been reported [196] (Figure 1.17 B).

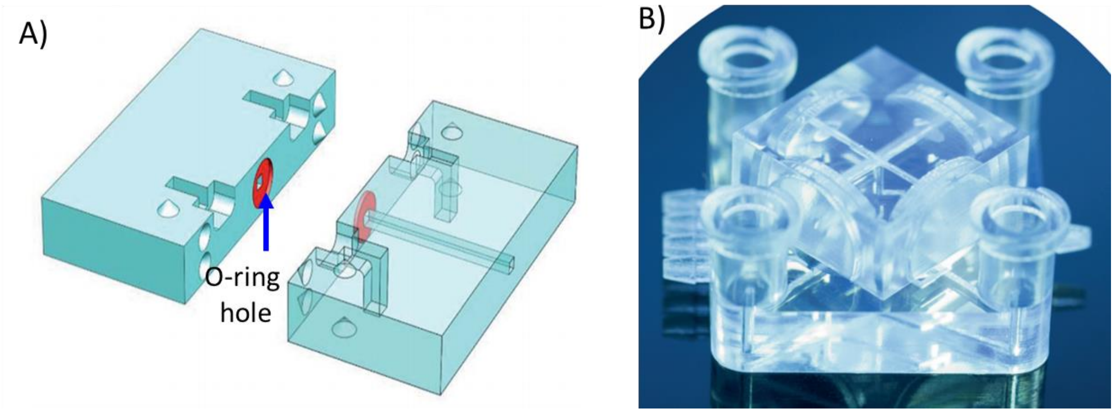

Figure 1.17 Examples of 3D printed connectors. (A) Rubber-like 3D printed O-rings can be placed on a microfluidic device. The printed O-rings are used to connect different microfluidic chips. (Taken from reference [195]. Reprinted with permission from ©2014 The Royal Society of Chemistry). (B) 3D printed luer adapters on a microfluidic device for easy connection to syringes and tubing. (Taken from reference [196]. Reprinted with permission from John Wiley & Sons, Inc.).

- **Complex flow microfluidic components**

Efficient and precise flow control of fluid is an important factor when designing microfluidic devices. At microscale, fluids exhibiting laminar flow may cause insufficient mixing between reagents [197]. Chip mixing mechanisms have previously been integrated into microfluidic devices through a complex fabrication [198, 199]. With the capabilities of 3D printing, a microfluidic device with complex structures can be fabricated in a few steps. For example, Lee et al. adapted SLA technologies to develop 3D printed channels with a turn- and-twist pattern, including a separate unit to mix the flows for alpha-fetoprotein biomarker detection. It has proved that microfluidic devices may be printed in a straightforward, rapid, and user-friendly way [194]. Bonyar et al. designed a microfluidic device, printed using MJM technologies. The prototype is used to transport cervical samples from the clinic to the laboratory. The printed device comprises a mixer and homogeniser for gynaecological cervical sample preparation [200] (Figure 1.18). 3D printed pumps and valves for fluid handling and manipulation have also been reported [201, 202].

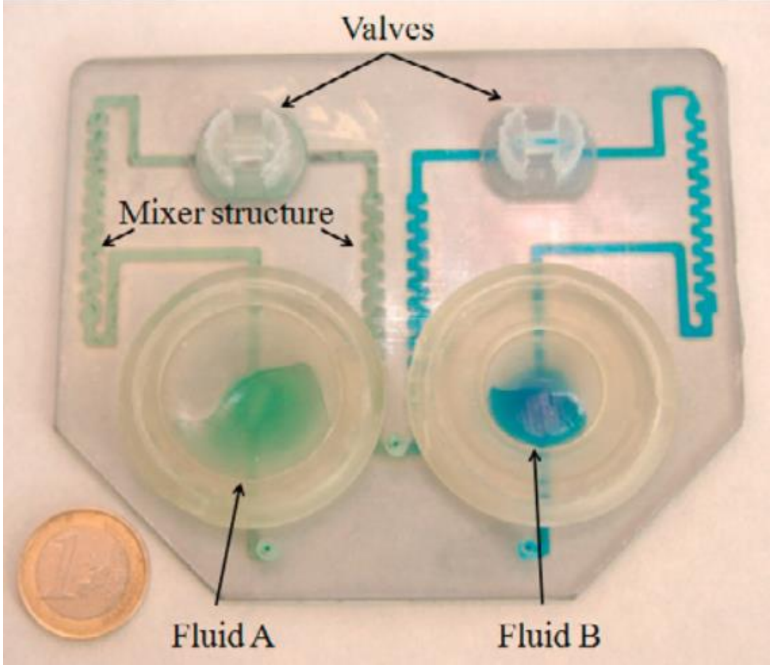

Figure 1.18 Microfluidics prototype for cervical sample preparation contains fluid mixer and homogeniser. Two reservoirs are used to store the reagent and the sample separately and can be released using fingertips for mixing (Taken from reference [200]. Reprinted with permission from ©2010 Elsevier Ltd.).

- **On chip device for cells and organism integration**

Application of microfluidic technologies for *in situ* analysis of cells and small model organisms are attracting a growing interest. Although a number of cells and organisms-on-chip have been reported [203-205], 3D printing technologies are able to enhance the complexity, versatility and reusability of models. Takenaga et al. used an SLA 3D printer (Asiga, Picoplus 27) to directly fabricate a microfluidic unit, and assembled it on a light-addressable potentiometric sensor (LAPS) chip for cell culture [203]. An optimised cell culturing was achieved within the printed microfluidics-based LAPS chips by adjusting the foetal calf serum concentrations of the cell culture medium. The cell growth curve showed a comparable result between the culturing cells in a printed chip and in a cell culture flask. For a small batch series of chips for cell culture, 3D printing is promising, offering a rapid and cost-effective design of a new sensor. However, studies on the biocompatibility of printing resins are still in development. 3D printing resins are being developed that are expected to be non-toxic to cells [168] (Figure 1.19 A).

Zhu et al. have demonstrated the feasibility of a range of 3D printers from SLA and MJM systems to print directly the millifluidic chip device for culturing zebrafish embryos. SLA technologies show superior resolution and feature quality compared with MJM technologies. Selected SLA polymers have optical properties enabling high resolution imaging with 50 MHz pixel digitization [166]. However, most printed chip devices have been found to be semi- transparent, and require labour-intensive polishing to make the outside device transparent and smooth. The inner wall of the fully sealed channel cannot be polished, and it is almost impossible to observe the inside channel without additional treatment (Figure 1.19 B).

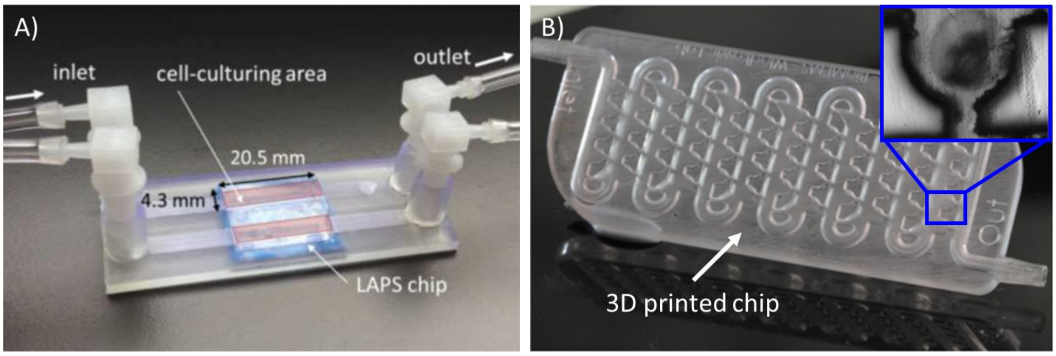

Figure 1.19 (A) LAPS chip with microfluidic channel connections. (Taken from reference [203]. Reprinted with permission from ©2015 John Wiley & Sons Inc.).(B) Chip-based prototypes for using Watershed resin. Inset image is the optical transparency assesment during embryo immobilisation. (Taken from reference [166]. Reprinted with permission from ©2015 AIP Publishing LLC).

- **Master mould fabrication for soft lithography**

Conventionally, soft lithography involves using high resolution up 150 nm of photomasks and exposing the photoresist materials to UV radiation to create a positive master mould; this involves challenging tasks such as aligning the layers of photoresist [206]. In addressing problems, several researchers have reported using conventional machining such as high speed micromilling to create durable metal master moulds [121, 207, 208]. However, this method is not always convenient as tool wear and breakage are critical issues in tool-based micromachining. 3D printing technology is an innovative alternative that allows greater control of complex 3D geometry than conventional microfabrication with a minimum feature size of 100 µm.

The capabilities of 3D printing are not yet fully developed, even in experimental works where flexibility and speed are essential. 3D-printed structural elements have only been applied in several experiments, such as for oral surgery [209, 210]. Although 3D printing is capable of directly printing microfluidic devices, Zhu et al. have highlighted significant biocompatibility issues with the resins currently available for 3D printing [211], a large majority of which are toxic to biological specimens. This precludes the fabrication of monolithic millifluidic devices and their applications with living cells, tissues and small model organisms [166].

With the development of higher-resolution (up to 25 µm) printers, 3D printing is now used to fabricate millifluidic and microfluidic structures such as master moulds for soft lithography processes, which can now be created using one step printing. Additionally, 3D printing of a mould does not require a mask to be fabricated as in conventional soft lithography process, where 3D printing directly fabricates the mould. The overall cost of the fabrication process therefore is reduced and the several steps required to pattern the master mould in soft lithography are simplified.

Different 3D printers such as SLA and MJM have been used to fabricate master moulds. Each printer is investigated and its characteristics noted prior to PDMS fabrication in soft lithography (Figure 1.20)[212, 213]; the examination considers the printer's ability to replicate dimensional accuracy, shape conformity and surface feature [212]. The moulds are then applied to several applications such as pneumatic balloon actuators for robotic applications [214], mixers and peristaltic valves [215], and capillary channels [216]. The 3D printed moulds enable rapid prototyping of structures, unattainable in existing soft lithography techniques.

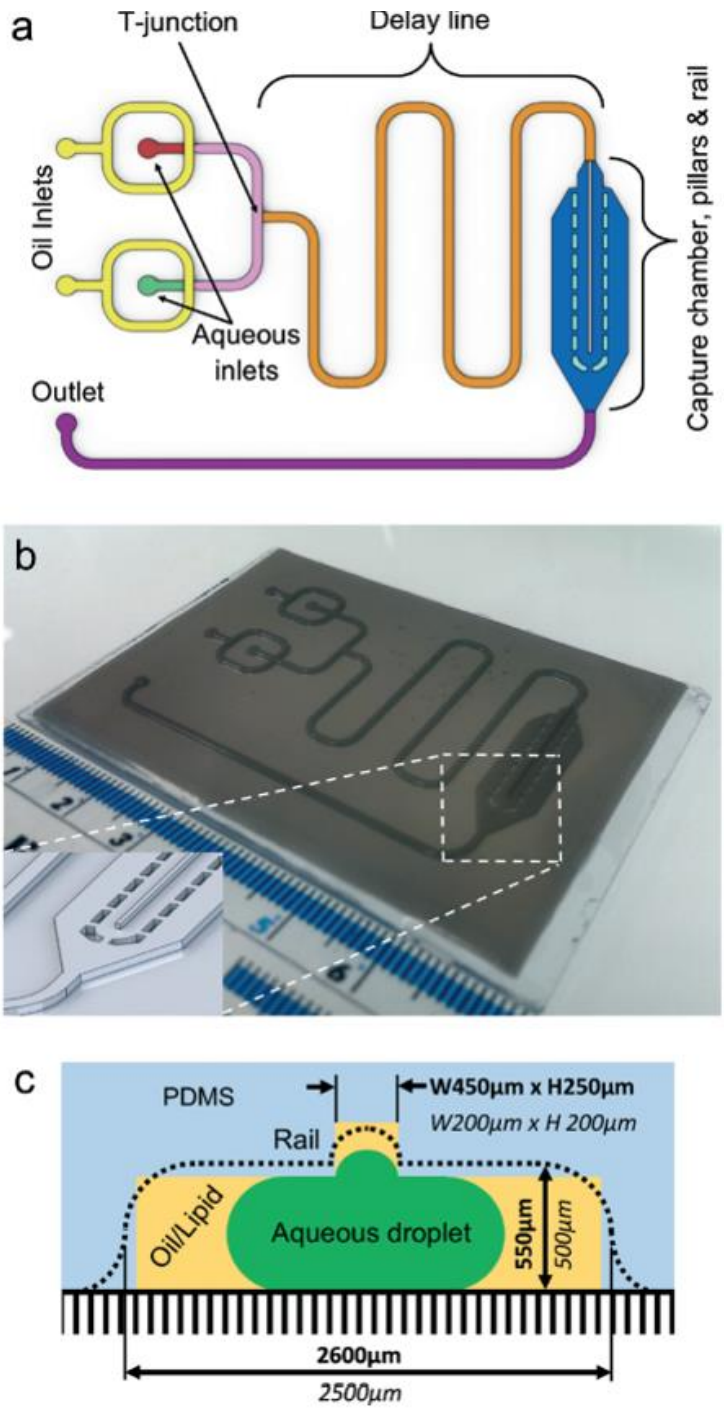

Figure 1.20 Design of microfluidic devices for the generation of microliter droplets-in-oil and the formation of droplet arrays with interdroplet lipid bilayers. (A) The channels (1.10 mm wide x 0.55 mm deep) are cast in PDMS using 3D printed mould. The oil inlets are in yellow and the aqueous inlets in red and green. A delay line for lipid monolayer formation is in orange, and the droplet capture chamber is blue. (B) The droplet capture chamber comprises a rail for droplet positioning. (C) The measured values (bold) are compared with CAD design values (italic). (Taken from reference [213]. Reprinted with permission ©2013 Royal Society of Chemistry).

1.3 Fish-on-chips: chip-based technologies for zebrafish research

Small model organisms assays that utilise zebrafish are still performed in multi-well microtiter plates and are laborious and time consuming [217]. The conventional static microenvironment of the embryos may limit the compounds available to the organisms because of surface adsorption, degradation and other factors [218]. Lammer et al. have improved the model by introducing a flow-through system in which the conventional 24-well plate is modified with drilled holes [218]. Although the overall cost of fabrication is low, the procedure is complex and time consuming. Even when applied, the liquid surface tension limits the imaging acquisition as upright imaging is difficult to achieve, so even with this improvementthe system does not offer proper miniaturisation and automation.

Apart from improvement to the conventional microtiter plates, innovative designs using microfluidic technologies which are able to improve automation with simplified methodology have been demonstrated. A variety of microfabrication and microfluidic LOC devices have been developed for the phenotyping and screening of zebrafish embryos and larvae.

1.3.1 Culturing embryos on chip-based devices

The microfluidic-based culture of zebrafish at the embryonic stage has been developed from semi-manual devices to recent automated and integrated platforms. Microfluidic segment technique was first introduced in 2007 by Funfak et al. using perfluoromethyldecalin (PP9) as the carrier liquid and Teflon (PTFE) as the tube material in the shape of a coil [219]. Embryos were transferred from a microtiter plate by means of a syringe pump. The team used an ingenious method of air bubbles to provide fluid segment stability. Fluid flow and image acquisition were controlled by dedicated software. The effects of copper on zebrafish embryo survival and physiological development were observed inside a specially created segment [219]. Although the segmented flow system with integration of the image platform was capable of achieving high levels of automation, there were significant limitations on the imaging platform. The coil-shaped Teflon tube inhibited the quality of the imaging.

Two years later, a PDMS-based microfluidic bioreactor for zebrafish was developed by Shen etal. [220]. A funnel-shaped aperture immobilised the embryos and the chip was submerged in a Petri dish containing fish medium that incorporated a gravity-driven pump to deliver the test substance through the microchannels. However, the embryos were still manipulated manually within the aperture using a pipette, limiting throughput.

Later, several chip-based flow-through systems were developed that were integrated with a concentration gradient generator [221, 222]. Photolithography was used to fabricate several layers of glass plates consisting of embryo culture chambers. The medium solution and drug delivery via a concentration gradient generator were perfused by a controlled syringe pump. However, complex and uneconomical fabrication techniques using photolithography were used to fabricate the devices, and the laborious manual handling of the embryos limited the throughput of the systems.

- **Hydrodynamic influenced embryo trapping arrays**

With the development of microfluidic devices, manual procedures were still needed to load embryos into the miniaturised chip devices, making them vulnerable to damage as the embryos, in an early stage of development, were extremely fragile. To overcome this limitation a miniaturised chip device was developed capable of loading embryos without human intervention.

Akagi et al. was the first to design and developed a microfluidic devices that implemented a hydrodynamic embryo array concept for automated trapping, immobilisation and on-chip perfusion of zebrafish embryos as illustrated in Figure 1.21 [27]. The serpentine design of the microchannels allowed the hydrodynamic forces to guide the embryos inside one of the embryo traps. With the flow generated in the channels, sufficient drag was generated to immobilise the embryos once they were trapped, and could sustain long-term immobilisation for up to 72 hours. The recovery of the embryos from the device was by pumping the medium from the outlet [27]. The conceptual design of the traps and the twisted flow channel created an orderly trapping of embryos without affecting the trapping efficiencies. A similar chip design was also fabricated using additive manufacturing technologies, using multiple 3D printers with different polymer materials [166].

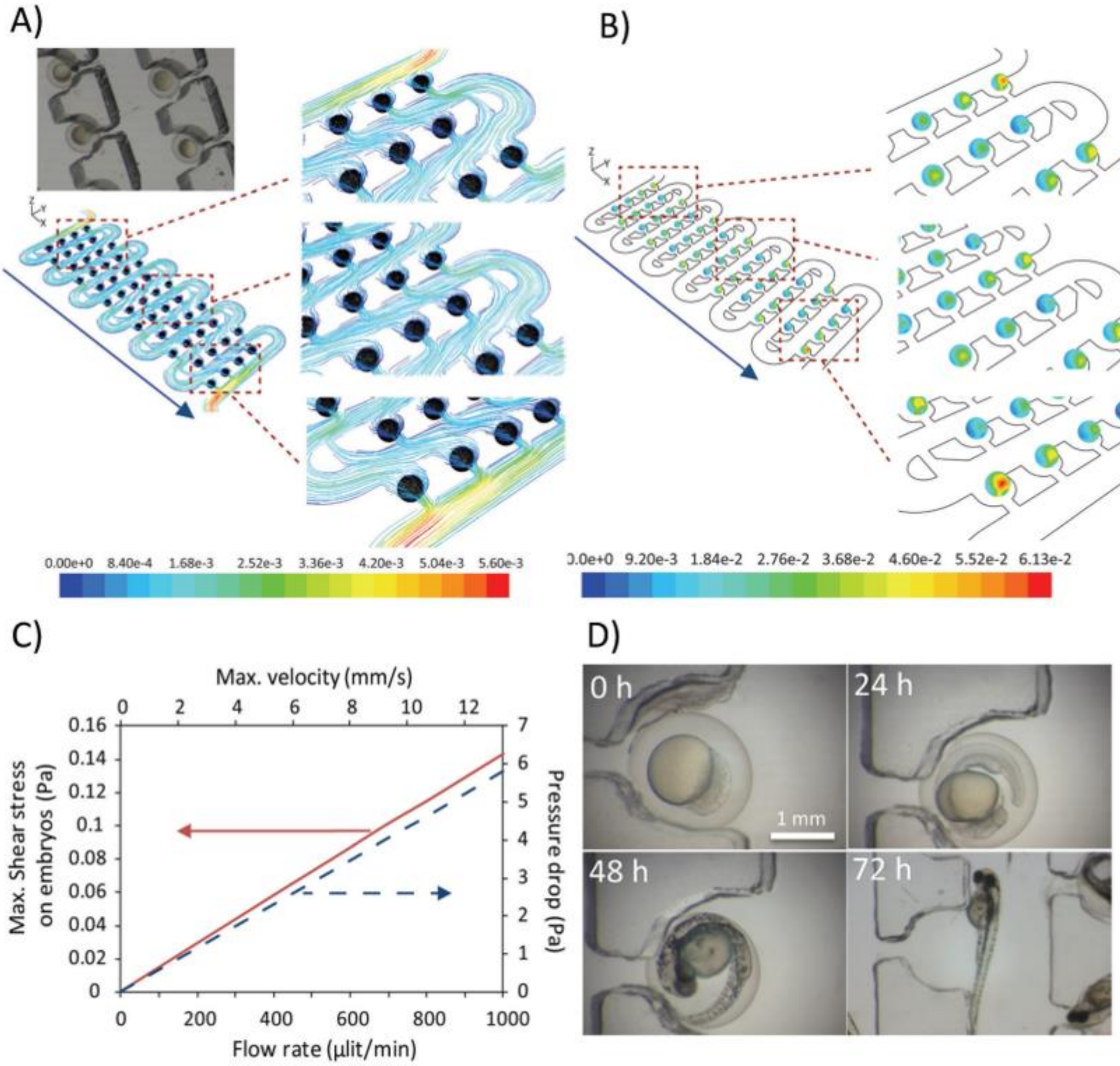

Figure 1.21 Assessment of microenvironmental conditions of zebrafish embryos cultured inside the chip: (A) Three-dimensional streamline flow across the fully loaded device; (B) The shear stress (Pa) contours exerted on each embryo across the entire device. Perfusion was simulated at a flow rate of 0.4mL/min; (C) The performance curve of the microfluidic device as a function of the volumetric flow rate; (D) Time-lapse images of zebrafish embryo development inside the device. (Taken from reference [27]. Reprinted with permission from ©2012 PLOS one Publishing Group).

In the continuing work of this group, Akagi et al. developed a microfluidic device for real-time analysis of the transgenic zebrafish embryos [223, 224]. A U-shaped heating manifold surrounded the trapping area, designed to maintain the temperature throughout the embryos' development. Each embryo was gravitationally docked in the designed traps, which connected to a suction channel controlled by a piezoelectric ultrasonic pump. This design offered a rapid fabrication with an automated embryo manipulation and perfusion system.

Recently, a PDMS chip-based design of a microfluidic platform with integrated fluidic actuation was developed. A microvalve system was embedded to pneumatically control the fluid flow using actuators [225]. With this system, renewable fluid manipulation can be achieved within ten seconds. Although the device is still under development, the microvalve design is a promising concept for well-controlled fluid delivery applications.

1.3.2 Culturing larvae on chip-based devices

In contrast to embryos that exhibit uniform spherical geometry, eletheuro-embryos or larvae have a non-uniform shape; their swimming bladders offer a challenge to real-time on-chip imaging, creating problems associated with larvae immobilisation and high metabolic rates.

Conventionally, anesthetised zebrafish larvae were mounted onto agarose gel in a Petri dish [226-229]. Recently, with the advancement of 3D printing technologies, a homeostatic chip-based platform for zebrafish larvae immobilisation was developed with a customised agarose mounting configuration [230]. Moisture and heat can be controlled via circulating buffers and heated water at the bottom of the agarose strip set-up, to control the homeostatic condition of the larvae. With this newly developed configuration, imaging of hundreds of larvae simultaneously can be achieved. Although its methods are affordable, manual orientation of the larvae on the agarose is, as always, laborious and time-consuming, and controlling the orientation of the larvae is also difficult and tedious.

To solve the orientation problem, an agarose-free larvae immobilisation system was developed to allow imaging in either lateral or dorsal orientation [231]. The Zebrafish Entrapment by Restriction Array (ZEBRA) microfluidic device was developed and fabricated using both PDMS and polystyrene. The device consists of two layers: the top layer, a mechanically machined fluidic channel for larvae holding chambers; and a bottom layer as the sealing base. The chamber is designed to enable both orientations of larvae. The loading procedure is assisted by a passive pump drive (surface tension-driven) towards the docking position. Although the low-cost chip in its design facilitates high resolution of 800 lines/mm imaging of zebrafish larvae, manual handling is still needed.

Later, Akagi et al. developed a proof-of-concept LOC device to immobilise zebrafish larvae for environmental scanning electron microscopy (ESEM) imaging, using infrared laser micromachining of the PMMA substrate [232]. Multiple semispherical microwells were designed for the specimen reservoir to hold the yolks of the larvae. Gentle suction by blotting the medium is used to trap and immobilise the larvae, which can be linearly aligned and immobilised in a simple configuration (Figure 1.22). Although this approach avoids extensive preparation procedures, manual blotting to hold the larvae is still not convenient in high-throughput imaging procedures.

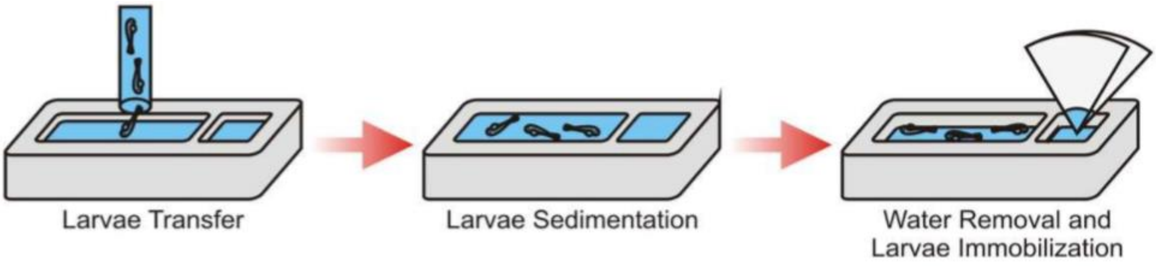

Figure 1.22 Schematic representation of the process involved for the zebrafish larvae immobilisation chip-based device (Taken from reference [232]. Reprinted with permission from ©2014 International Society for Advancement of Cytometry).

The next step to hydrodynamically trapping the larvae was to develop a PDMS microfluidic chip-based device for a fish trap array that immobilised intact larvae at dorsal and lateral positions simultaneously developed by Lin et al. [233]. Several trapping channels are linearly arrayed to trap and immobilise the larvae, each designed to fit the tail of the larvae. The microfluidic devices are designed to facilitate tail-forward trapping. A direction-switching loop in the system adjusts the alignment of the larvae before loading them to the chip device. The larvae are transferred by a capillary-based syringe pump coupled to a triggered electronic valve. High-speed photodetection confirms the loading of the larvae and determines the tail direction [233]. This configuration reduces the level of human intervention, but although the system suits high-throughput applications, the set-up is complex and the overall cost is high.

In 2016, Hong et al. presented an integrated zebrafish analysis platform (iZAP) for long-term high-throughput electrophysiological monitoring [234]. The system comprises a PDMS microfluidic unit, multielectrode array and integrated electronic unit amplifiers. The microfluidic unit is designed as an open chamber with a large inlet pool where zebrafish larvae (5–7 dpf) swim freely. The trap channels are shaped as half cylinders, with one end open and gradually tapering to a half cone. When zebrafish are loaded they spontaneously swim along the channels and are restrained inside. The custom-built multichannel head stage amplifiers are integrated with surface microelectrodes directly in contact with the zebrafish heads to obtain continuous electroencephalogram (EEG) signals during drug treatment. This integrated microfluidic system greatly facilitates electrophysiological monitoring of zebrafish models. IZAP demonstrates a non-invasive and long-term approach to electrophysiological imaging using vertebrate epilepsy models, but the fabrication process is complex, particularly where it involves photolithography procedures for the PDMS microfluidic unit. Schematic configurations of the system is illustrated in Figure 1.23.

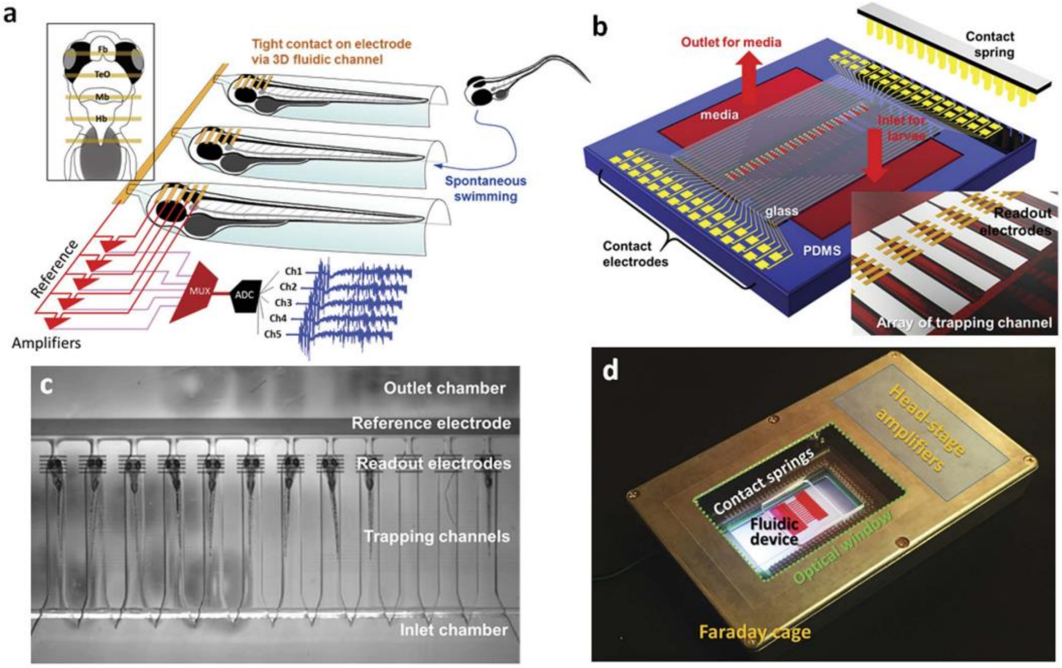

Figure 1.23 Integrated zebrafish analysis platform (iZAP) for high-throughput electrophysiological monitoring configurations. (A) Schematic diagram of design concept. Inset image represents the position of surface electrodes to the zebrafish brain. (B) An illustration of integrated system of the microfluidic platform. (C) Images of trapped zebrafish larvae in the iZAP microfluidic unit. (D) An image of the iZAP system placed inside an optical-windowed Faraday cage. The red fluid represents the zebrafish medum (Taken from reference [234]. Reprinted with permission ©2016 Macmillan Publishers Limited).

1.3.3 High content analysis on chip-based devices

Due to the unique characteristics of zebrafish, they are mainly used in sophisticated screening or analysis to assess the physiological effects of a chemical substance in living vertebrates. Their transparency, which makes it easy to collect numerous data points in a single organism using high quality imaging with 640 x 480 pixel resolution, makes them suitable for high-throughput screening and high content analysis. High content analysis encompasses a fully automated manipulation, imaging and data processing system to collect detailed information from the organisms. The integration of an automation platform system provides a higher level of content analysis from in situ screening.

To improve the microfluidic chip-based zebrafish embryo culture system, an innovative integrated laboratory automation system was developed and demonstrated by Wang et al. [235]. A microfluidic actuator, temperature regulator and image acquisition system were integrated in a single automated system, designed to perform automatic immobilisation, culture and chemical treatment of the developing embryos. The integrated units were controlled by Field Programmable Gate Array (FPGA), a microcontroller that enables real-time control of the embryos.

Akagi et al. reported an advancement to the high-content-analysis chip-based platform by adding a separate drug delivery manifold with miniaturised piezoelectric pumps to enable embryo loading and drug delivery [236]. A servomotor-actuated pinch valve is used to control drug delivery; and an optically transparent indium tin oxide (ITO) heating element replaces the previous flow-through heating system [236]. For imaging acquisition, a miniaturised fluorescent USB microscope equipped with LED illumination is used. This fully automatic system allows suitable visual imaging of developing vasculature patterns in response to treatment, without the need for specimen re-orientation.

The same group later developed an innovative high-throughput flow-through chip-based device for zebrafish embryo trapping arrays [237]. The device is able to trap and immobilise up to 252 embryos in a flow-through embryo-culturing device for real-time imaging. The hinge-like cradle manifold provides an interface between the tubing and the connection ports to avoid leaking and air bubbles, and therefore does not require for manual insertion of the connection tubes.

1.3.4 Application of LOC devices for zebrafish in drug discovery

Modern drug discovery depends on automatic screening to evaluate the efficacy of the test candidates, cytotoxicity, and possible side effects of the drugs. Because of their low consumption of samples and reagents, microfluidics have been applied in cell-based bioassays and the phenotyping of multicellular organisms [238]. They have also been used to evaluate drug dosage dependence on-chip, to test compound toxicity and evaluate cells' dynamical behaviour [239].

Zebrafish have been used to study the pharmacological effect of drugs. Microfluidic LOC technologies offer advantages over conventional microtiter plates for culturing zebrafish embryos and larvae. It provides non-invasive culture conditions and high quality imaging (640 x 480 pixel resolution), as well as the ability to access the embryos at any developmental stage [240]. It is an ideal platform for on-chip cultivation and manipulation in preclinical drug discovery applications. It is widely adopted because it is reproducible, economical, amenable to modification, and can be integrated with other technologies [241].

1.3.4.1 Assessment of cytotoxicity

Microdevices offer great opportunities to develop new drugs and to assess the effects of toxicity on the tissues and cells of zebrafish embryos or larvae. Phenotype-based evaluations can be performed to determine the toxicity measurements of drug candidates, similar to morphologically-based cytotoxicity assessments. Yang et al. proposed a microfluidic system to investigate the toxicity and teratogenicity of doxorubicin, cisplatin, vitamin C and 5-flurouracil (f-FU) on the phenotype characteristics of the zebrafish embryos [221]. The toxicities of the drugs were evaluated based on observations of such things as pigmentation, heart rate, body motion and shape, development of notochord, and tail and fin morphology. A dose response curve for doxorubicin was plotted at different stages of development. The drugs had irreversible and fatal side effects [221].

A microfluidic embryo array was also used to perform preliminary toxicity tests for analysis of heavy metals dissolved into the zebrafish medium. Akagi et al. performed a flow-through perfusion toxicity test using copper solution [236]. The fatality or mortality rate of the chip perfusion set-up was significantly higher than that in static FET experiments. The continuous perfusion capabilities shown in microfluidics technologies, permitted a rapid exchange of the copper solution [236], indicating that microfluidic devices can be readily applied to perform FET assays on zebrafish embryos.

Later the same group automated the zebrafish embryo µFET test using microfluidic LOC technologies [242]. A continuous flow-through perfusion system was implemented to test drugs such as phenol, nicotine, caffeine and copper sulphate on immobilised zebrafish embryos. Results of the dose response curve achieved from the chip-based system were comparable with the static protocols performed in microtiter plates [242]. The work proved that FET analysis performed in a microperfusion system can be an inexpensive protocol in aquatic ecotoxicology.

1.3.4.2 Assessment of cardiotoxicity

Drug-induced cardiac dysfunction leads to high mortality. Zebrafish have been used to study the toxicity of chemicals on cardiac development and function. Zebrafish embryos develop rapidly, and heartbeat starts 22 hours post-fertilisation (hpf) and is fully functional at 48 hpf, exhibiting a complex repertoire of ion channels and metabolic processes [243]. Medium throughput assays for cardiotoxicity analysis based on morphological endpoint toxicity have been developed where cardiovascular changes are visually assessable without dissection [244]; these cardiotoxicity studies have been useful in understanding the impact of specific toxicants on heart function [244-248].

Using microfluidic LOC technologies in the assessment of cardiovascular drug effects gives researchers the ability to control the fluid flow conditions such as shear stress and flow rate. The small volume of fluid used in microfluidics system is suited to monitoring the effects of drug administration on organisms such as zebrafish embryos, making microfluidics advantageous for studies of cardiovascular physiology because of their amenability to pharmacological modifications [249]. Although microfluidic technologies are still evolving, there are some works already reporting on the use of microfluidics as a platform for cardiotoxicity studies using zebrafish.

In 2014, Li et al. a microfluidic system for a phenotype-based evaluation of the toxicity and teratogenicity of drugs, using zebrafish [250]. Developmental stages were evaluated by changes in physiological indicators such as heart rate, hatch rate, survival rate and morphological measurements. The heartbeat was quantitatively measured for 20 seconds at 24, 48, 72 and 96 hpf. The study showed that higher concentrations of aminophylline (Apl) resulted in faster heartbeat and the fish suffered from pericardial oedema. Cardio-vascular assessment of drug-treated embryos is an important stage in embryonic cardiac developmental toxicity studies.

1.3.5 Limitations of current chip-based systems for zebrafish research

Laboratory microfluidic automation of in situ analysis using zebrafish embryos and larvae is still in its infancy. Besides, manual procedures associated with sorting hundreds of embryos are very monotonous and as such prone to significant analytical errors due to operator fatigue. The major obstacle to the widespread deployment of zebrafish in large-scale drug development studies is the lack of efficient high-throughput analytical platforms. In general, zebrafish embryos are collected and separated manually to sort the fertilised (live) from the unfertilised (dead) ones, or to sort transgenic from non-transgenic clones before loading to the microfluidics. Laborious manual evaluation is required to confirm fertilisation status, viability, or the presence of a transgene linked to a fluorescent protein. Subsequent dispensing of single developing embryos to multiwell plates to perform toxicity analysis is also predominantly manual, prone to errors and inter-operator variability [251]. In addition, manual techniques introduce the risk of cross-contamination and carry-over that can significantly affect the outcome of drug discovery screenings.

Although zebrafish embryo sorters such as CellBot and ZebraFactor are available, these systems are large, complex, and expensive [252]. There is also a lack of chip-based LOC microfluidics available for sorting zebrafish embryos. A miniaturised, reliable and user-friendly embryo chip-based device for embryos sorting is still unavailable.

Recently MacDonald et al. investigated the biocompatibility of various resins of 3D printers with zebrafish embryos [253]. The results showed that all photopolymer resins were toxic to the embryos, causing fatality. The fabrication of chip-based devices using a printed mould is advantageous for zebrafish culture compared to direct printing of a chip-based device.

Currently few studies use microfluidic platforms using zebrafish embryos for cardiotoxicity studies. The microfluidic system developed for dynamic cardiotoxicity studies overcomes the limitations of using microtiter plate [250], but still relies on a manual count of the heartbeat readings, which is not suitable in high-throughput analysis. Moreover, several hatched embryos are placed in one chamber, which makes the data prone to error.

Most recent studies have focused on zebrafish embryos with the chorion still intact. There is a possibility of generating false negative results in developmental toxicity studies because of the limited permeability of the chorions to certain compounds. It is suspected that the intact chorion influences chemical uptake and in some cases is a barrier to metal nanomaterials [254, 255]. Dechorionation of the embryos can overcome this [256]. Despite microfluidics evolving, there is a lack of development in the design and fabrication of a reliable microdevice for dechorionated embryos.

2 Aims and Objectives

The research herein is aimed as a step towards the development of a microfluidics LOC system able to handle zebrafish embryos and larvae for drug discovery and environmental research. No currently available method provides a reliable platform for automated immobilisation, long term perfusion culture, quality imaging and analysis in a single low-cost and robust microfluidic system. For this reason, the goal of this thesis is to develop microfluidic and millifluidic devices to address the problem described in Chapter 1. The thesis objectives are as follows:

i. To develop a proof-of-concept design for micromechanical large particles in a flow sorter that is capable of detecting, sorting and dispensing living zebrafish embryos for drug discovery applications
ii. To design and develop a PDMS chip-based millifluidic device capable of trapping and immobilising living zebrafish larvae for recording heart rate variations in cardiotoxicity analysis, using methods available with new, improved soft lithography.
iii. To develop a microfluidic LOC device for trapping and immobilisation of dechorionated embryos for long-term microperfusion for ecotoxicology experiments.

In this thesis, Chapter 3 describes the general materials and fabrication methods of zebrafish LOC devices and experiments. This is followed by a description of the development of microdevices for detection methods to distinguish between live and dead embryos, in Chapter 4. Chapter 5 describes new approaches made possible by soft lithography to fabricate the design of millifluidic devices for trapping and immobilising zebrafish larvae. Finally, a microfluidic device for the immobilisation of dechorionated zebrafish embryos is described and presented in Chapter 6. The thesis concludes with a summary of the potential impact of this work for biomedical communities, and offers a consideration of future development in Chapter 7.

3 Materials and Method

This chapter describes the materials used in the experiments, including test chemicals for the biological tests and materials for device fabrication. The methodology associated with the research is also presented. This chapter describes procedures for animal culture, prototyping, data acquisition and analysis. All procedures and steps taken in the experiments are discussed in detail.

3.1 Chemicals and materials

3.1.1 Chemicals for toxicity tests

Caffeine (C0750; CAS No. 58-08-2; 194 mol weight), lead acetate (CAS No: 546-67-8; 443.38 mol weight), phenol (CAS No: 108-95-2; 94.11 mol weight), verapamil hydrochloride (V4629; CAS No. 152-11-4; 491.06 mol weight) and propranolol hydrochloride (CAS No: 318-98-9; 295.8 mol weight) were purchased from Sigma-Aldrich, Australia. Copper sulphate pentahydrate $CuSO4.5H2O$ (CAS No: 7758-99-8; 249.68 mol weight) was purchased from Thermo Fisher Scientific, Australia. All were in powder form. Chemical solutions were prepared by dissolving solids in E3 media in volumetric flasks with serial dilutions.

Nicotine (N3876; CAS No. 54-11-5; 162 mol weight) and dimethyl sulfoxide (DMSO) (W387520; CAS No. 67-68-5; 78 mol weight were obtained from Sigma-Aldrich (St. Louis, MO, USA) in liquid form. All other chemicals were of the highest quality and provided by local suppliers. All vehicle controls were prepared by adding DMSO in E3 media.

3.1.2 Low melting point agarose for zebrafish mounting

Mounting plates were prepared by adding a small volume of 1.5% agarose (Carl Roth) in E3 to half-fill the 90 mm Petri dishes, and stored at 4°C. The mounting agar was prepared by melting 0.5-1.5% of low melting point (LMP) Agarose (Sigma Aldrich) in E3 media. 1.5 ml of each aliquot of fresh mounting agar was kept at 37°C in a liquid heat bath.

3.2 Zebrafish husbandry and culture

All animal research was carried out with approval from the RMIT University Animal Ethics Committee and Monash University Animal Ethics Committee.

Adult wild type zebrafish embryos (*Danio rerio* (AB line; Zebrafish International Resource Center, Eugene, OR, USA) were kept in a temperature- and light-controlled aquaculture facility in a standard 14 hour light, ten hour dark cycle. The zebrafish were fed with artemia twice daily. Embryos were obtained by mating four to five pairs of adult zebrafish for natural spawning; on average, this generated 200–300 embryos These were collected and washed of all debris, transferred to a petri dish and maintained in an incubator (Thermo Scientific, Heratherm TM Advanced Microbiological Incubator) at 28.5±0.5 °C in embryonic E3 medium (5 mM NaCl, 0.17 mM KCl, 0.33 mM $CaCl_2$, 0.33 mM $MgSO_4$, 0.1% methylene blue), and observed the stages of embryonic developmentof the zebrafish.

A few zebrafish embryos of 12 and 24 hpf (hours post-fertilisation) stages were loaded in an embryo sorter and dechorionated chip devices. Larvae of 3 dpf (days post-fertilisation) were used for a larva immobilisation experiment. This research was conducted with approval from the Royal Melbourne Institute of Technology Animal Ethics Committee (approval AEC 1404). Healthy fertilised embryos were seen to be clear and transparent after collection, while dead embryos were black and opaque in colour as shown in Figure 3.1**.**

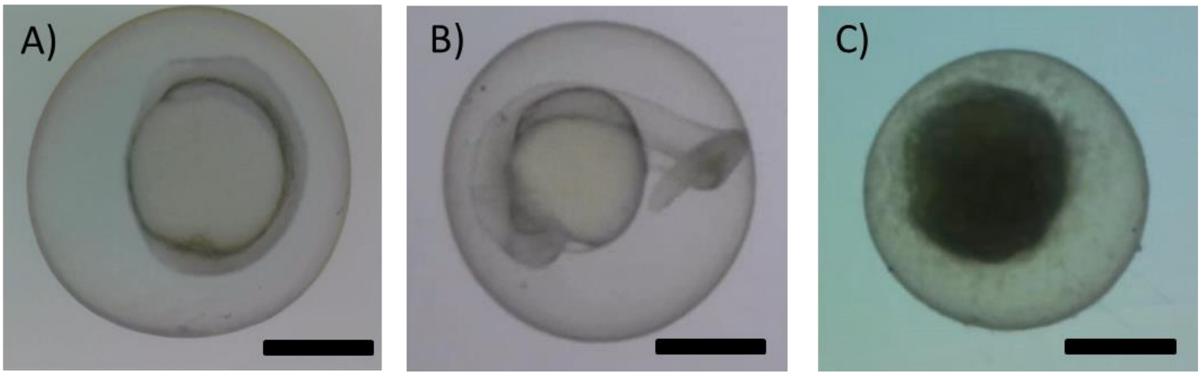

Figure 3.1 Images of (A) Live zebrafish embryo at 12 hpf and (B) 24 hpf zebrafish embryo (C) Dead embryos. Bar scale is 400 µm.

3.3 Dechorionation Methods

Mechanical Dechorionation

Dechorionation was carried out on 24 hpf embryos in 90 mm glass Petri dishes filled with E3 medium. The chorions were removed with sharp sterile needles (Terumo Medical Corporation, Terumo®, Japan) by gently incising a lit along the chorion. The needle enlarged the slit and turned the chorion upside down until the embryo fell out (Figure 3.2 A–F). It is important to make a big enough incision for the embryos to leave the chorion without damaging the edges of the chorion. Excess pressure should also be avoided to avoid any injury to the embryo. After dechorionation, all embryos were carefully placed in agarose-coated 90 mm glass Petri dishes with polyethylene transfer pipettes (Livingstone, Australia) with an end opening diameter of 1.8 mm.

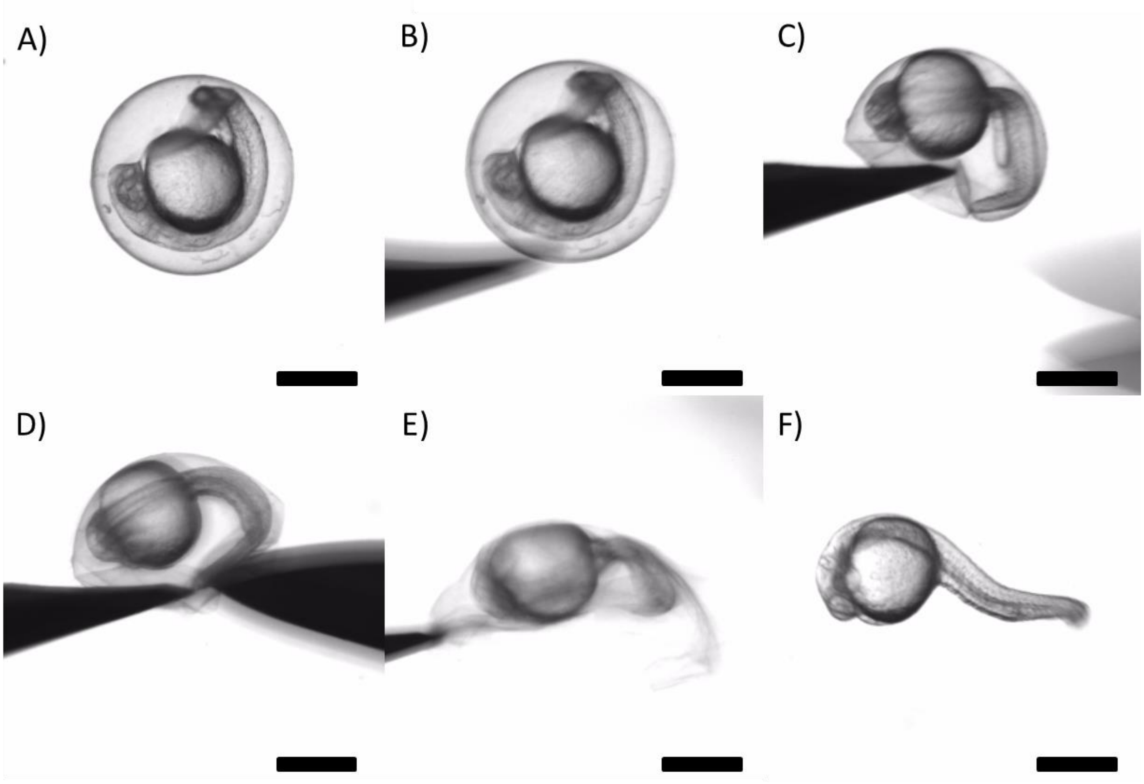

Figure 3.2. Mechanical dechorionation using sterile needles (Terumo ®) (A) Intact zebrafish embryo 24 h post-fertilisation; (B) Zebrafish embryos held with one needle (C) A small incision in the chorion with the needle (D) Second needle enlarges the slit by in the chorion (E) The chorion is turned upside down to allow the embryo to fall out from the chorion (F) dechorionated embryo. Bar scale is 500 µm.

3.4 Acute toxicity test (LC_{10} determination) for cardiovascular toxicity

All stock solutions were prepared in E3 mediums and serial dilutions were carried out before the experiments. The toxicity analysis was performed using the standard protocol (OECD 236) guidelines. Twenty zebrafish larvae at 3 dpf were transferred into each petri dish containing 40 ml of E3 medium. The petri dishes were covered with parafilm and incubated at a constant temperature of 27 ± 0.5°C. These procedures were carried out in darkness to protect the compounds from light-induced decomposition. Dissolved oxygen was kept above 80% during the experiment. After the 24-hour treatment in the petri dishes, the mortality curve was plotted and a 10% lethal concentration (LC_{10}) was calculated by probit analysis ToxRat software (ToxRat Solutions, Alsdorf, Germany). This concentration was then used to assess cardiovascular toxicity.

3.5 Fish Embryo Toxicity and Sublethal Embryo Toxicity Index (iFET)

A static Fish Embryo Toxicity (FET) analysis was performed on 24 hpf dechorionated embryos according to the the standard protocol (OECD 236) [257]. Twenty four dechorionated embryos were transferred into 24-well plates with one embryo per well. Each well contained 2 ml of positive control (3,4-dichloroaniline), negative control (E3 medium) and test concentrations. The plates were covered with adhesive foil and incubated at 27 ± 0.5°C. The lethal and sublethal end points were determined according to standard protocol and recorded every 24 hours.

A non-static chip-based perfusion FET was carried out using a millifluidic chip-based device and a modified static standard protocol. Twenty dechorionated embryos at 24 hpf were loaded onto the microfluidic array. The chip-based devices were perfused in a closed loop system with a volumetric flow rate of 1000 µL/min, attached to an external stock of test concentrations in 50 mL falcon tubes, via polytetrafluoroethylene (PTFE) tubing 1.3 mm in diameter. The embryos were immobilised and incubated up to 72 hours at 2.7 ± 0.5°C in a dark environment.

3.5.1 End point scoring criteria for FET.

Precise observations of toxicity were performed based on four lethal end-points: (i) coagulation of fertilised embryos, (ii) lack of somite formation, (iii) non-detachment of the tail from the yolk sac, and (iv) lack of heartbeat. The toxicity was recorded with a positive score for any of the end-points listed. All the scored data were used to calculate the median lethal concentration (LC_{50}) [257].

3.5.2 End point scoring criteria for the Sublethal Embryo Toxicity Index

A set of calculations newly developed by Wigh and colleagues increases the sensitivity of conventional FET scoring criteria by including sublethal and teratogenic conditions [258]. There are nine additional sublethal endpoints as toxicity indicators: (i) abnormal and disturbance of eye development, (ii) formation of oedema, (iii) blood circulation deficiency, (iv) lack in pigmentation (v) abnormalities in tail formation, (vi) abnormalities in head formation, (vii) abnormalities in spine formation, (viii) abnormalities in yolk formation, and (ix) heart abnormalities. All sublethal toxicity experiments were recorded every 24 hours for 72 hours in the experiment.

The sublethal toxicity index was quantified using the formula:

$$iFET = \frac{(9 \times N_D) + N_{SL}}{9 \times N} \times 100\%$$

where N = total number of embryos, N_D = number of dead embryos (FET-mortality end points), and N_{SL} = number of sublethal indicators recorded according to the nine listed scoring criteria at the end of the experiments. The iFET results were calculated as a percentage of dechorionated embryos showing both lethal and sublethal abnormalities.

3.6 Computational fluid dynamics (CFD) analysis and simulation

Optimisation of fluid flow of the chip design was guided by CFD simulations using COMSOL Multiphysics® Software (COMSOL Inc., MA, USA) to create the geometrical and mesh generation. A flow rate between 1000–2000 µL/min at the inlet pressure to be 0 Pa at the outlet were implemented. Boundary conditions were set to non-slip conditions at all surfaces, top, bottom and sidewalls, of the channels.

3.7 Multi-layer 3D chip fabrication

The 3D chip was designed and fabricated using Computer Assisted Design (CAD) packages including CorelDraw X4 (Corel Corporation, Canada) and Solidworks 2013 (Dassault Systems SolidWorks Corp, Concord, MA, USA). Subsequent prototyping and fabrication was accomplished using a contactless 30 W CO_2 laser cutting system equipped with high-power density focusing optics (HDPFO)^{TM} (Universal Laser Systems, Scottsdale, AZ, USA) at 50 µm. A biocompatible material of poly-methyl methacrylate sheeting (PMMA/Acrylic), which is a transparent thermoplastic, was precisely laser cut in a range of 0.5–3.0 mm thickness to build integrated channels and trapping regions.

Each layer of sorter was stacked vertically and thermally bonded at 110°C for up to two hours in a fan-assisted oven (Thermo ScientificTM, HERAthermTM, General Protocol Oven, USA). The PMMA layers were aligned with a precision measuring tool, L-square. A uniform mechanical force was applied with two mini clamps to provide a constant force over the full surface during bonding. The PMMA sheets were then positioned between two aluminium plates (5 mm thick) that allowed the transfer of heat to the contact surface. Bonding pressure was adjusted by controlling the loads applied to the top of the plate. Direct laser machining of apertures achieved tubing inter-connections of 2.9 mm (outer diameter), capable of incorporating the 1/16-inch PTFE tubing (Cole Palmer Instrument Company, Vernon Hills, IL, USA) and permit free passage to zebrafish embryos and larvae.

3.8 Additive manufacturing of off-chip interfaces

All the prototype casings were designed and fabricated using fused deposition modelling (FDM) (Makerbot Replicator, Brooklyn, NY, USA) (Figure 3.3). High quality PLA thermoplastic with high tensile strength was made with a resolution up to 200 µm of layer thickness. The CAD designs were saved in the STL (standard stereolithography) format for printing. Printed support structures of the end product were removed manually with specialised removal equipment. The extruder nozzle was heated to 110°C before printing. The table platform was calibrated before any printing took place.

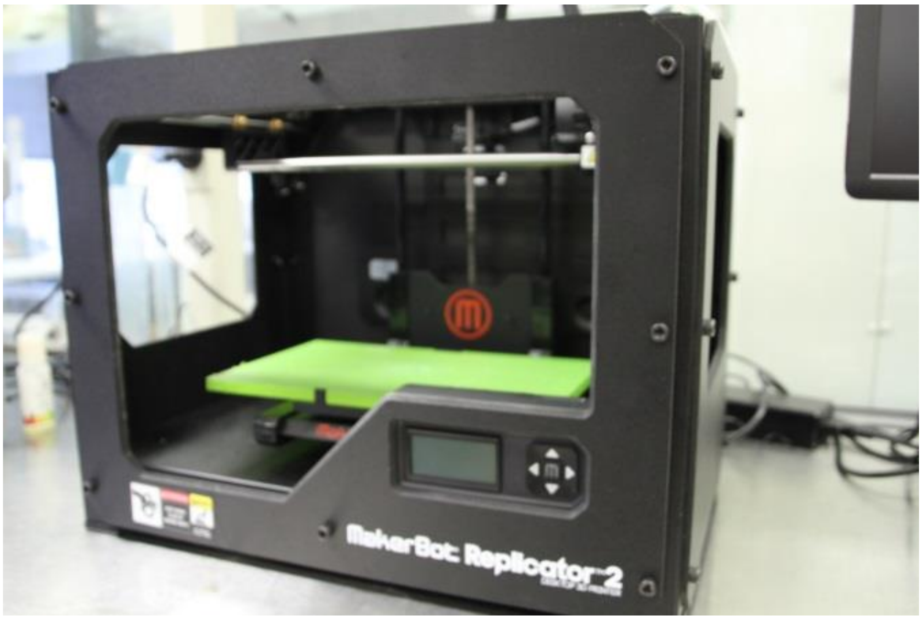

Figure 3.3. Illustration of FDM equipment for prototyping (Makerbot Replicator, Brooklyn, NY, USA)

The system was connected to an external high-precision multichannel Miniplus Evolution peristaltic pump equipped with a MF1 pump head (Gilson Inc, Middleton, WI, USA) using PTFE 1/16-inch tubing. Calibrated PVC tubing (1.3 mm diameter; Gilson Inc.) was fitted in a cartridge to accommodate the required range (1000–2000 µm) of flow rate. All devices were primed with 100% ethanol (v/v) in advance for wetting purposes and to eliminate the formation of air bubbles. Chips were filled up with the standard E3 fish medium.

3.9 Fabrication of polymeric mould for larvae immobilisation devices

3.9.1 3D printed master mould

In this research, ProJet HD 7000 (3D Systems Inc., USA), Objet Connex 350 (Stratasys Ltd.) and Form1 (FormLabs, USA) were used for fabrication of the master mould (Figure 3.4). With these 3D system printers, VisiJet SL CLear polymer was used for both substrate and support because it can generate a fine lattice beneath the substrate to create the support structures. VeroClear was used as the base material. For Objet Connex 350, FullCure705 was selected for the substrate material and Support 705 for the support materials. Both contain an acrylic oligomer and a photoinitiator that cures under UV light as it prints. FormClear polymer resin was used both as base and support material in Form1 printer, and no other support material needed. Each printer uses different processes to form 3D prototypes, as detailed in Table 3.1. All printing used the same parameters, such as 100 µm of layer resolution.

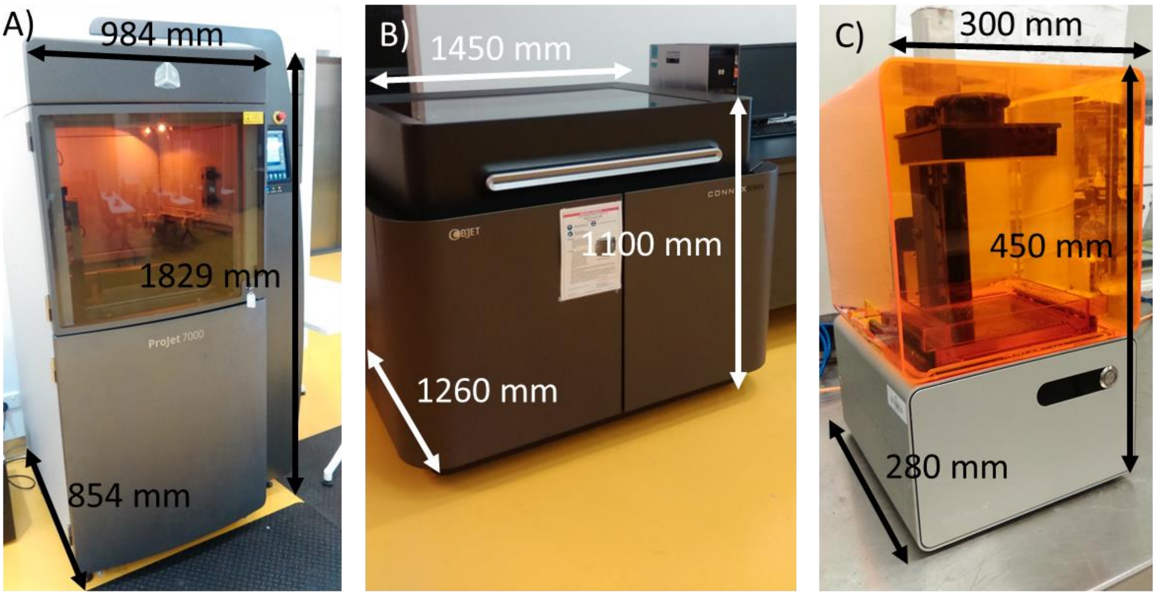

Figure 3.4 Additive manufacturing technologies. (A) Stereolithography (SLA) ProJet HD7000 with a maximum build volume of 380 mm x 380 mm x 250 mm; (B) Multi jet machining (MJM) Objet Connex 350 with a net volume of 342 mm x 342 mm x 200 mm; (C) Desktop SLA printer Form1 with a maximum build volume of 125 mm × 125 mm × 165 mm.

Table 3.1 Configuration of 3D printing of polymer larvae chip

Company	Model	Technology	Materials	Accuracy (x–y resolution)	Layer thickness (z–resolution)
3D Systems	ProJet HD7000	SLA	VisiJet SL Clear	25 µm	25 µm
Stratasys	Objet Connex 350	MJM	Vero Clear	25 µm	16 µm
FormLabs	Form1	SLA	Form Clear	20–85 µm	16 µm

Post processing was needed to remove all the supports printed to hold the overall shape of the design (Table 3.2). All the printed moulds were treated with solvents such as isopropyl alcohol to clean the surface, and water jet cleaning washer (PowerBlast, Kranzle, Germany) was used carefully to remove support materials (Figure 3.5 A). Next, radiation treatment using electromagnetic UV (ProCure 350, 3D Systems Corporation, USA) was introduced for a minimum of 30 minutes to ensure all resins solidified completely and to improve the clarity of the printed surfaces (Figure 3.5 B). This process also enhanced the tensile strength of each mould so a good quality of structure could be fabricated using replica moulding with PDMS.

Table 3.2 Post-processing treatment for different 3D printers

Model	Post Processing Treatments			
	Solvent	**Water Jet Cleaning**	**Compressed air**	**UV Curing**
Projet HD7000	Isopropyl alcohol	No	Yes	30 minutes
Objet Connex 350	Isopropyl alcohol	Yes	Yes	30 minutes.
FormLabs	Submerged in isopropyl tank for 10 minutes	No	Yes	6 hours

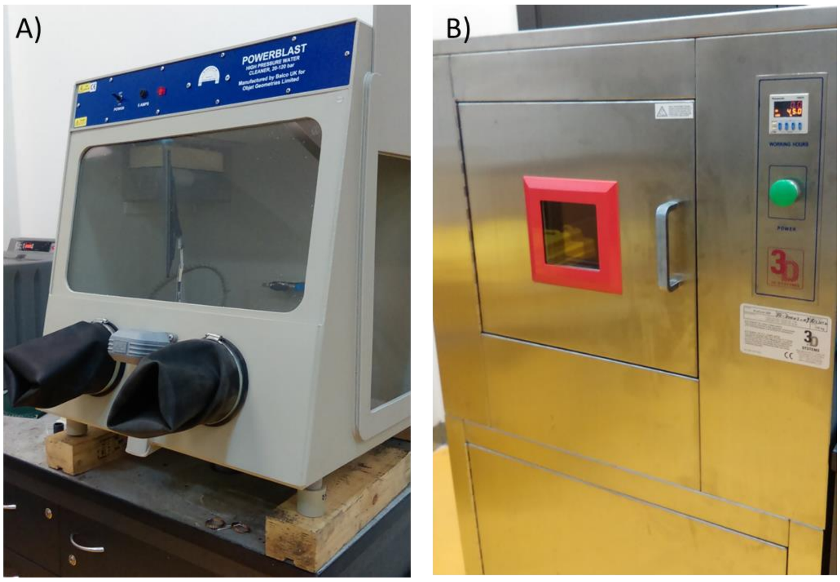

Figure 3.5 Post processing treatment to remove support materials from 3D printed parts (A) High pressure water jet system manually used at 50-60 Barr to clean the supports (B) UV radiation curing process to increase the clarity and tensile strength of printed parts.

3.9.2 PDMS casting

The bonded PMMA master mould was used for replica moulding in poly(dimethylsiloxane)(PDMS; Sylgard 184, DowCorning Corp, Midland, MI, USA) [126]. The PDMS was prepared at a ratio of 10:1 (w/w) of elastomer base to curing agent and then degassed at 40 Torr for 30 minutes in a vacuum chamber using a dessicator with 6.4 mm of internal diameter tubing port. A high voltage alternating current (HVAC) high performance rotary pump (VacuMaster 3CFM Vacuum Pump, Robinair, MI, USA) was connected with a desiccator to remove any residual air bubbles in the PDMS mixtures as shown in Figure 3.6.

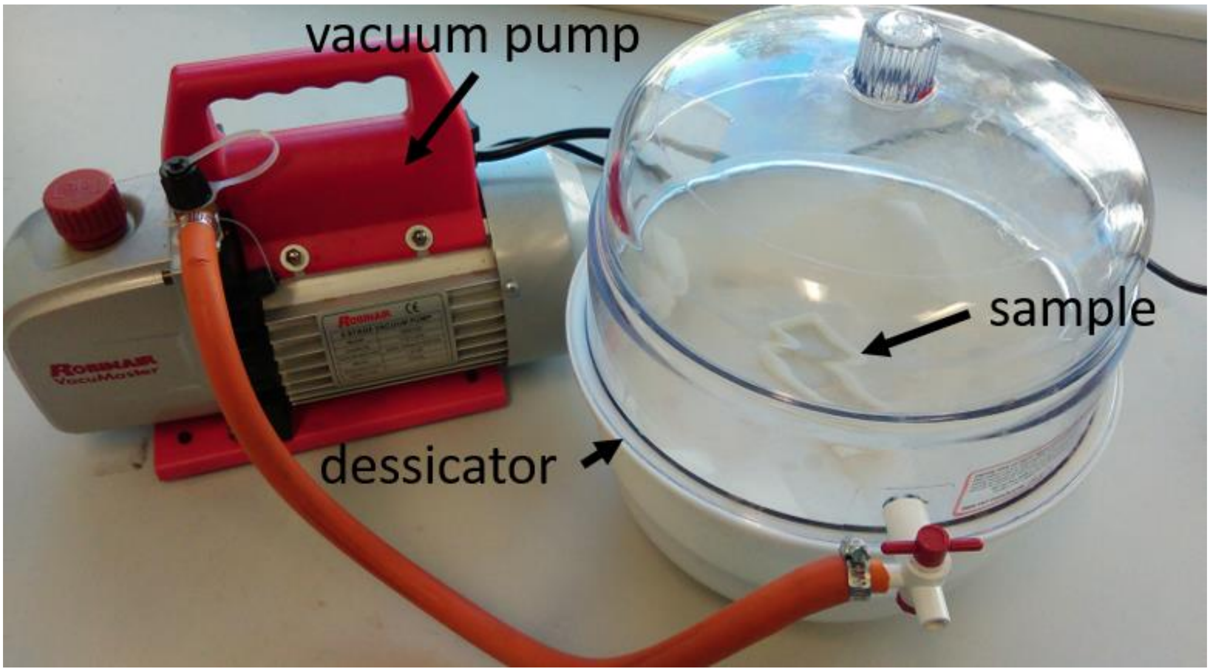

Figure 3.6 A set-up for degassing method. The PDMS mixture (sample) was placed inside a desiccator. A high-performance vacuum pump was connected to the desiccator by means of a rubber hose

The PDMS mixture was poured in a master mould as illustrated in Figure 3.7 to achieve a substrate thickness of approximately 5 mm, and degassed in a sealable vacuum desiccator for 20 minutes to clear air bubbles, then cured thermally at 70°C for two hours. Cured PDMS was peeled off the mould, mechanically diced, and bonded to 76.2 mm x 25.4 mm x 1.1 mm standard glass microscope slides using oxygen plasma surface activation (Harrick Plasma, NY, USA). Microfluidic connections were manually bored using an appropriate stainless steel biopsy punch of 3.0 mm diameter (Paramount Surgimed Ltd, New Delhi, India). Both PDMS and glass-topped surfaces were exposed with plasma for approximately four minutes inside the chamber.

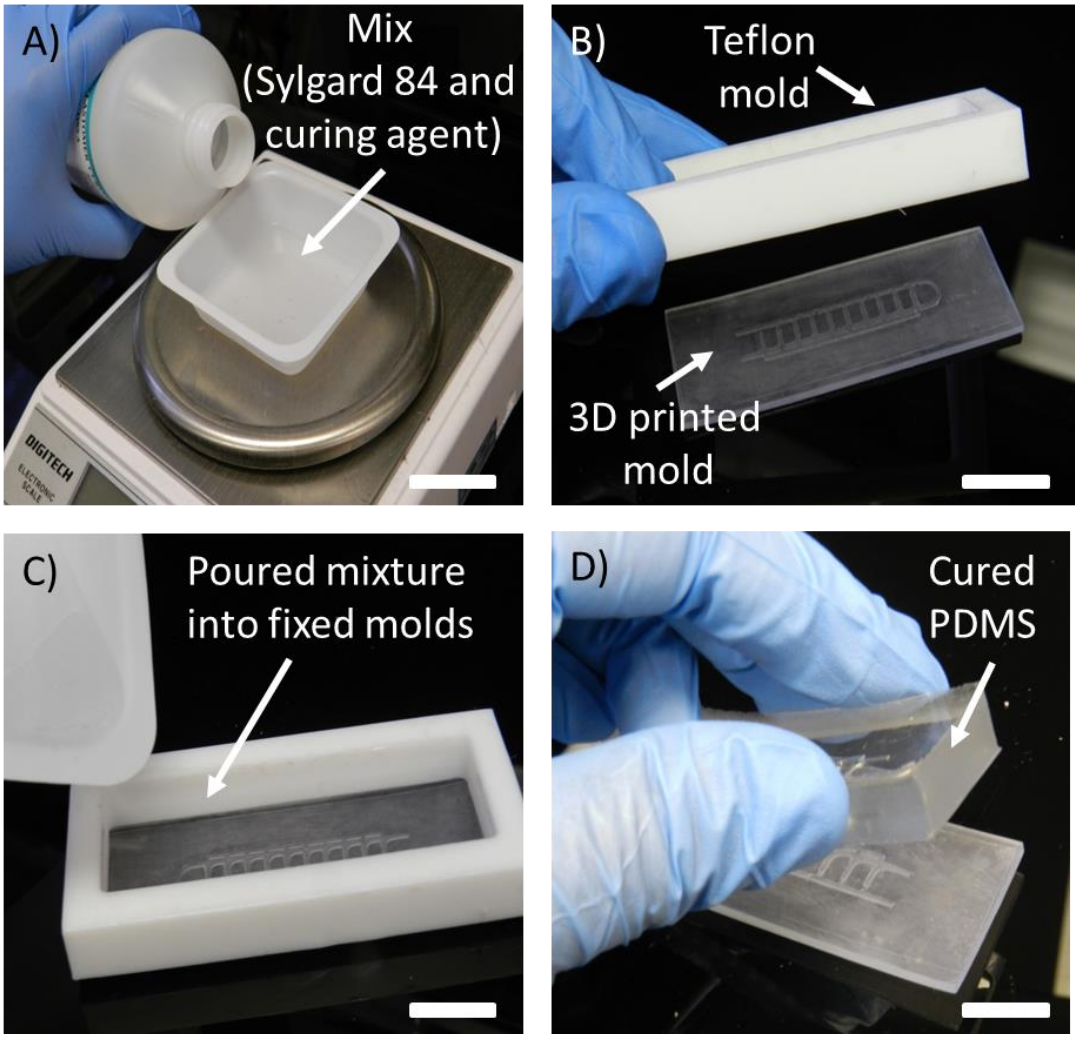

Figure 3.7 Step-by-step process of PDMS fabrication: (A) Curing agent mixed with Sylgard 84 at a 10:1 ratio (B) Printed moulds are fixed to a rectangular mould (85 mm x 35 mm x 10 mm) (C) The mixture is carefully poured into the mould and degassed to remove air bubbles (D) Degassed mixture is cured inside a fan-assisted oven for two hours, before being separated from the printed mould manually. Bar scales are 12 mm.

3.10 Imaging

Time lapse imaging of the embryos and larvae on the chip-based device were performed using Nikon SMX18 (Nikon Corp., Tokyo, Japan) equipped with a Retiga TM 4000DC cooled CCD camera. The stereomicroscopic system was controlled by a built-in software package (NIS-Elements Ar) for image analysis. All visual and image acquisitions of the acute toxicity test were observed under the dissecting stereomicroscope. A miniaturised Universal Serial

Bus (BUS) microscopy (AMT7013MT Dino-Lite Premier, Dino-Lite, AnMo Electronics Corp, New Taipei City, Taiwan) with a rate of 60 frames per second, was used for imaging and video recording.

All scanning electron microscopy images were taken using a FEI Quanta 200 ESEM (2002) operating at 30 kV and spot size of 5.0 in high vacuum conditions. Before being loaded into the scanning electron microscopy, samples were coated with Au/Pd using an in-house sputter coater operating at 15 mA for one minute. All optical profilometry images were analysed with a non-contact surface profiler, BRUKER ContourGT-I Optical Microscope with stitching mode enabled. A USB microscope (Dino-Lite) with a backlight was also used in embryo and larvae observations.

Video recorded files of zebrafish cardiac activity were analysed using DanioScope (Noldus Information Technology, Netherlands). Each file was converted into an MPEG 4 (MP4) audio file before analysis.

3.11 Sensing module using differential infrared optical density (DIOD)

The primary detection module enabled oscilloscopic identification of differential infrared optical density (DIOD) by employing infrared (IR) emitters and receivers embossed in the microfluidic chip, as shown in Figure 3.8.

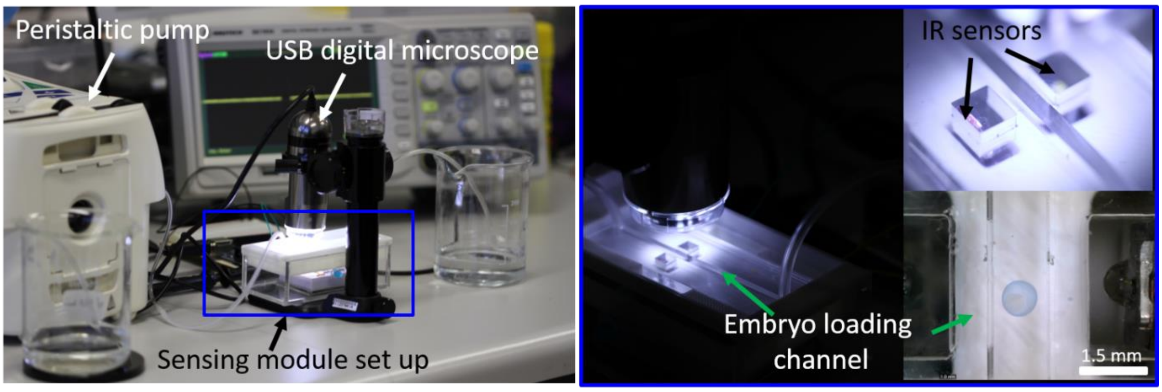

Figure 3.8. Sensing module set-up for DIOD method. A peristaltic pump was used to load embryos at a flow rate of 1500 µL/min. A digital microscope (Dino-Lite) was used for embryo imaging. A single channel of a PMMA microfluidic chip was fabricated to test the viability of the embryos using DIOD. Inset shows a magnified view of the infrared sensors embedded in the channel. Live mbryos were stained with Trypan blue dye solution.

3.12 Image recognition requisition using Roborealm

Real-time video tracking of embryos was performed using RoboRealm (Machine Vision) software. Dead embryos were detected and tracked in real time based on a colour and blob algorithm to filter their image intensity as a population of embryos moved in single file inside the microfluidic channel. A miniaturised USB bright field and polarisation microscope (AM7013MT Dino-Lite Premier; AnMo Electronics Corporation, New Taipei City, Taiwan) was used in proof-of-concept experiments to acquire a video stream at 30 frames per second. Specimen illumination was provided by eight integrated ultra-bright white LEDs controlled by dedicated software (DinoCapture2.0; AnMo Electronics Corporation). The miniaturised USB microscope was powered and controlled through a USB2.0 interface with an external PC computer running the Windows 7 operating system (Microsoft, Redmont, WA, USA). The video stream from AM7013MT Dino-Lite Premier was fed via a USB2.0 interface to a PC running RoboRealm software.

3.13 Actuation of sorting receptacle

Precise control over the rotational movement of the sorting receptacle was realised with a Dynamixel AX-12A robotic actuator (Robotis Ltd). The AX-12A actuator had a torque of 16.5 kgcm and no-load speed of 0.196 sec/60° at 12 V, with a maximum current of 900 mA. The AX-12A robotic actuator was controlled by a CM-530 microcontroller (Robotis Ltd) based on 32-bit ARM Cortex M3 architecture. The programming was performed in a native RoboPlus environment (Robotis Ltd).

3.14 Data analysis and controls

Toxicity data was analysed using ToxRat (ToxRat Solutions GmbH, Alsdorf, Germany). All data illustrations and presentations were performed using GraphPad Prism 7 (GraphPad Software, Inc, USA) software packages. A standard one-way analysis of variance (ANOVA) model was applied to perform independent comparisons for each toxicant concentration, with significance at $p<0.05$. All experiments were performed at least twice, with three independent replicates per concentration tested unless otherwise indicated.

4 Proof-of-concept Design of Microfluidic Device for Embryo Sorting

4.1 Introduction

At present, the major hurdle to widespread deployment of zebrafish embryos and larvae in large-scale drug development projects is the lack of analytical platforms enabling high throughput. To spearhead drug discovery with the use of zebrafish as a model, platforms need to integrate automated pre-test sorting of organisms (to ensure quality control and standardisation) and their in-test positioning (suitable for high-content imaging) with modules for flexible drug delivery. The major obstacles to the sorting of millimetre-sized particles such as zebrafish embryos on chip-based devices are their substantial diameter (above one millimetre) and mass (above one milligram), both of which lead to rapid gravitational-induced sedimentation and high inertial forces.

Zebrafish embryos are encapsulated by chorion described as an acellular envelope surrounding the mature eggs with a diameter ranging from 1.0–1.2 mm. Furthermore, each of the embryo approximately has a mass of 850 µg to 1050 µg. Thus, it permits gravitational-induced sedimentation force, high linear and angular momentum of the moving embryos in the fluid flow in the sub-millimetre sized channels. Therefore, this was initially a challenge in handling process of the embryos in a microfluidic system. However, in this research, these characteristics were utilised as for proof-of-concept method in embryo sorting principle.

In this chapter, I present an innovative proof-of-concept design of a micromechanical large particle in-flow sorter that capable of analysing, sorting and dispensing living zebrafish embryos for drug discovery applications. The system consisted of a microfluidic network, revolving micromechanical receptacle actuated by robotic servomotor and opto-electronic sensing module.

4.2 Chip design and fabrication

The microfluidic circuitry comprises a main inlet and outlet channels with a rectangular cross-section of 1.6 mm (width) x 3.0 mm (height) for embryo loading and sorting, as illustrated in Figure 4.1 A. The main part of the chip is housed with the sorter wheel, which is an embedded revolving micromechanical receptacle 19 mm in diameter with an embryo trap engraved by a laser in raster mode to a depth of 1.8 mm (blue dotted circle, Figure 4.1 B–C). The embryo trap has semicircular geometry with a diameter of 1.5 mm and an opening of 1.25 mm.

A mounting hole of 3.0 mm (diameter) x 2.0 mm (depth) is laser machined in the middle of the receptacle and a polymer bearing is press fitted to facilitate the smooth rotation of the receptacle. Eight neodymium magnets of 3 mm (diameter) x 2 mm (thickness) and a strength of 1.32 Tesla are embossed in the receptacle to enable non-contact actuation by an external servomotor (Figure 4.3 C).

The miniaturised sorter comprises four layers of PMMA (Figure 4.2), cut using high definition laser micromachining. The top layer (thickness = 2.0 mm) consists of the circular holes (Ø = 2.9 mm) for inlet and outlet channels. The second layer, 3.0 mm thick, contains the main loading channel for embryos and the outlet channels. The third layer contains a circular cut (Ø = 20 mm), 35.16 mm from the inlet channel. Both second and third layers are 3.0 mm thick. The fourth layer (60 mm x 25 mm x 1.5 mm) is used as the bottom sealant layer for an enclosed microfluidic system.

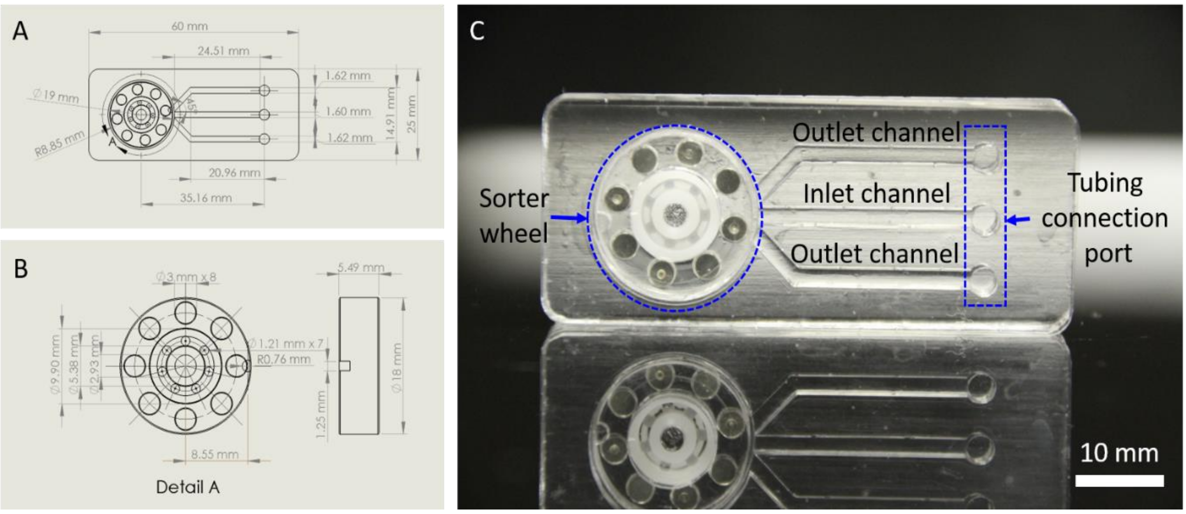

Figure 4.1 Overview of 3D chip-based in-flow embryo sorter (A) Detailed CAD drawing showing the details of the main loading, inlet and outlet channels. (B) Multiview projection of sorter wheel embedded with a polymer bearing and eight pairs of Neodymium magnets. (C) Fabricated biocompatible PMMA sorter chip that connects to tubing with an outer diameter of 3 mm. Live and dead embryos are separated via two outlet channels.

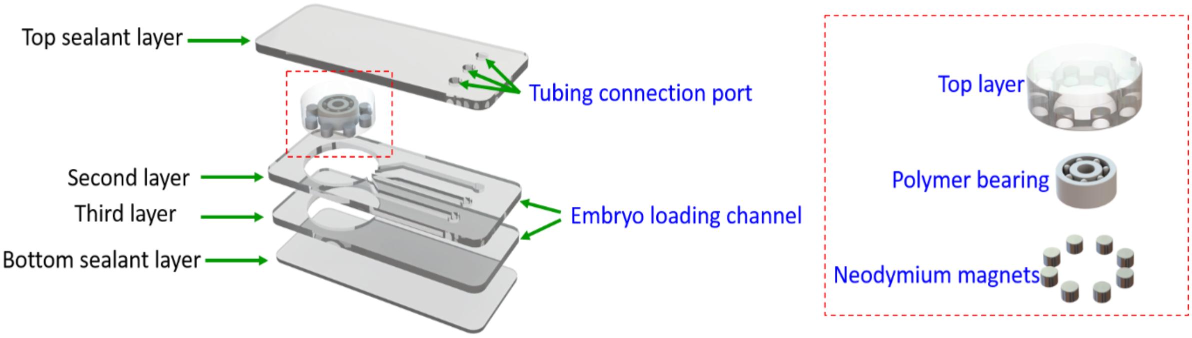

Figure 4.2 An exploded view of the microfluidic device in the sorter. The function of each independent layer is noted. The layers of PMMA are aligned and thermally bonded to form a permanent seal. The red dotted box contains an exploded view of the sorter wheel, consisting of neodymium magnets and polymer bearings.

The prototype of the miniaturised sorter was fabricated using both infrared laser micromachining and fused deposition modelling (FDM). The design consists of four main modules: i) the microfluidic 3D chip formed by four independent layers of PMMA (Figure 4.2), ii) embedded revolving micromechanical receptacle, iii) 3D printed external interface, and iv) electronic control panel, (Figure 4.3). The 3D printed housing was designed to hold the chip and servomotor in alignment.

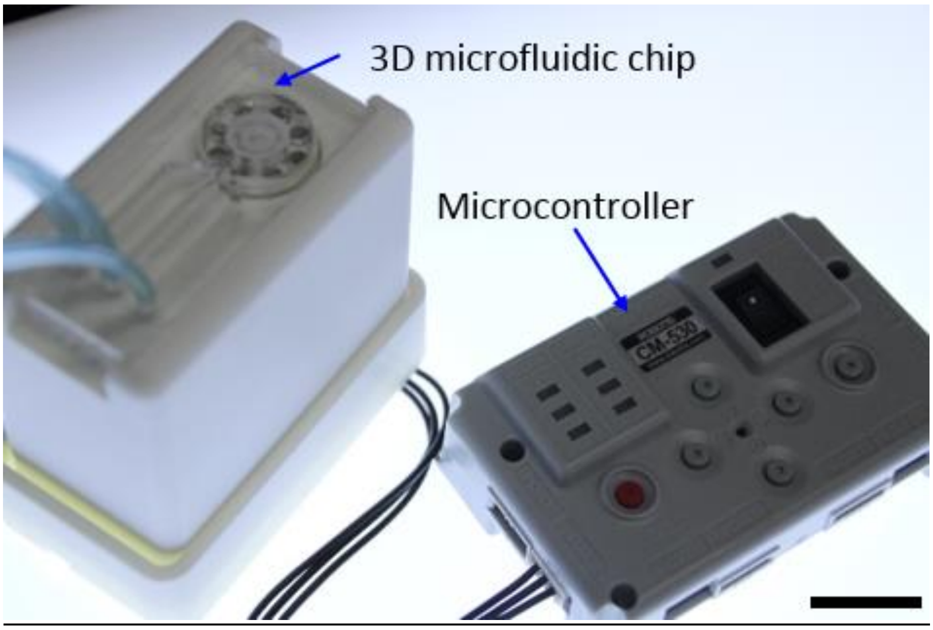

Figure 4.3 Built-in microcontroller in the 3D printed housing used to position the shaft to direct embryos from the inlet to the outlet channel. Bar scale is 20 mm.

4.3 Zebrafish embryo sorting concept

The design of the device harnesses hydrodynamic forces to move the embryos in a passive flow from one channel to another. Computational fluidic dynamics (CFD) simulations, initially performed (COMSOL Multiphysics v4.4) to predict flow velocity, pressure drop and uniformity of mass transfer inside the device, indicated that at a perfusion rate of 1500 µL/min, flow velocities inside the chip varied from 0.0028 m/s to 0.0016 m/s, at input and output respectively. Higher velocity (red streamline) was observed in the main loading channel as simulated (Figure 4.4). This enhanced the momentum of the embryos moving towards the trap. The trap had a constant flow of 0.0037 m/s. A circular flow around the receptacle had an average velocity of 44 x 10^{-6} m/s that provided sufficient suction to immobilise the embryos inside the trap as depicted in Figure 4.4.

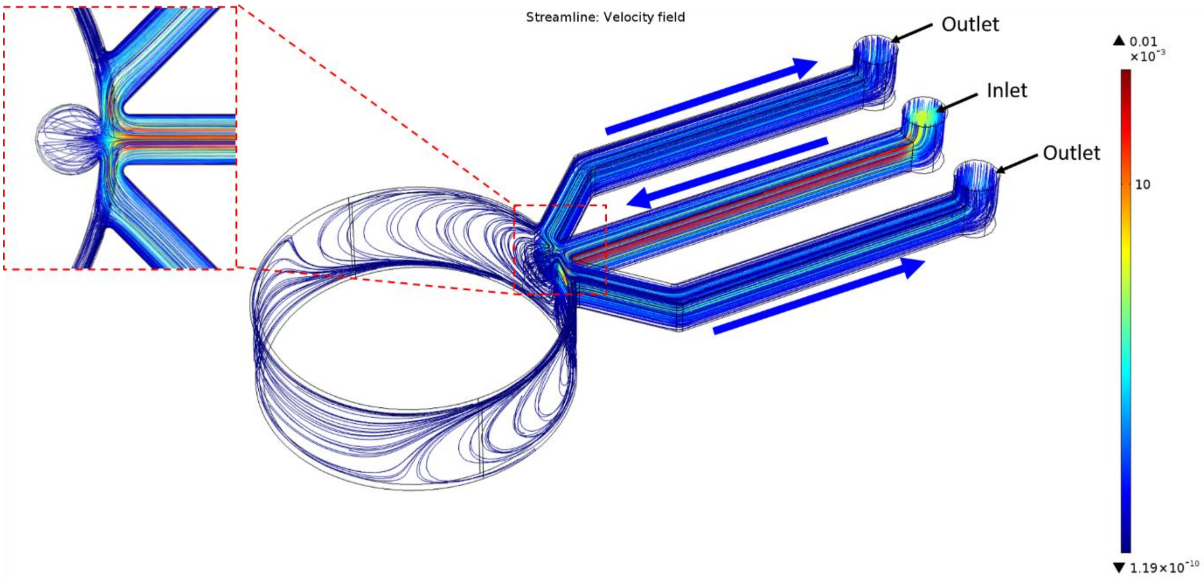

Figure 4.4 A coloured plot 3D simulation of fluid streamlines across the microfluidic chip with velocity (m/s) profile obtained from CFD simulations. The red dotted inset depicts the flow at the embryo trap as the embryo enters the main loading channel. The flow profile is symmetrical because of the laminar flow in a microfluidic system. The blue arrow represents the flow direction inside the chip.

In the sorting process, the mechanical receptacle is designed to capture the embryo and place it into the appropriate channel. The fluid streams inside the microfluidic chip were validated experimentally when the sorter receptacle was positioned at different angles relative to the outlet channel from the main loading channel. The rotation of the receptacle towards the outlet channels changed the flow conditions, enabling embryos to be recovered from the trap (Figure 4.5). The dimension allowance between the sorter wheel and the main loading channel enabled the fluid to flow from the inlet to the outlet channel at a velocity of 0.0075 m/s. The position upwards has a velocity of (0.00050 m/s) and downwards has a velocity of (0.00055 m/s). These give sufficient force to hold the embryos while the receptacle moves to the outlet channel.

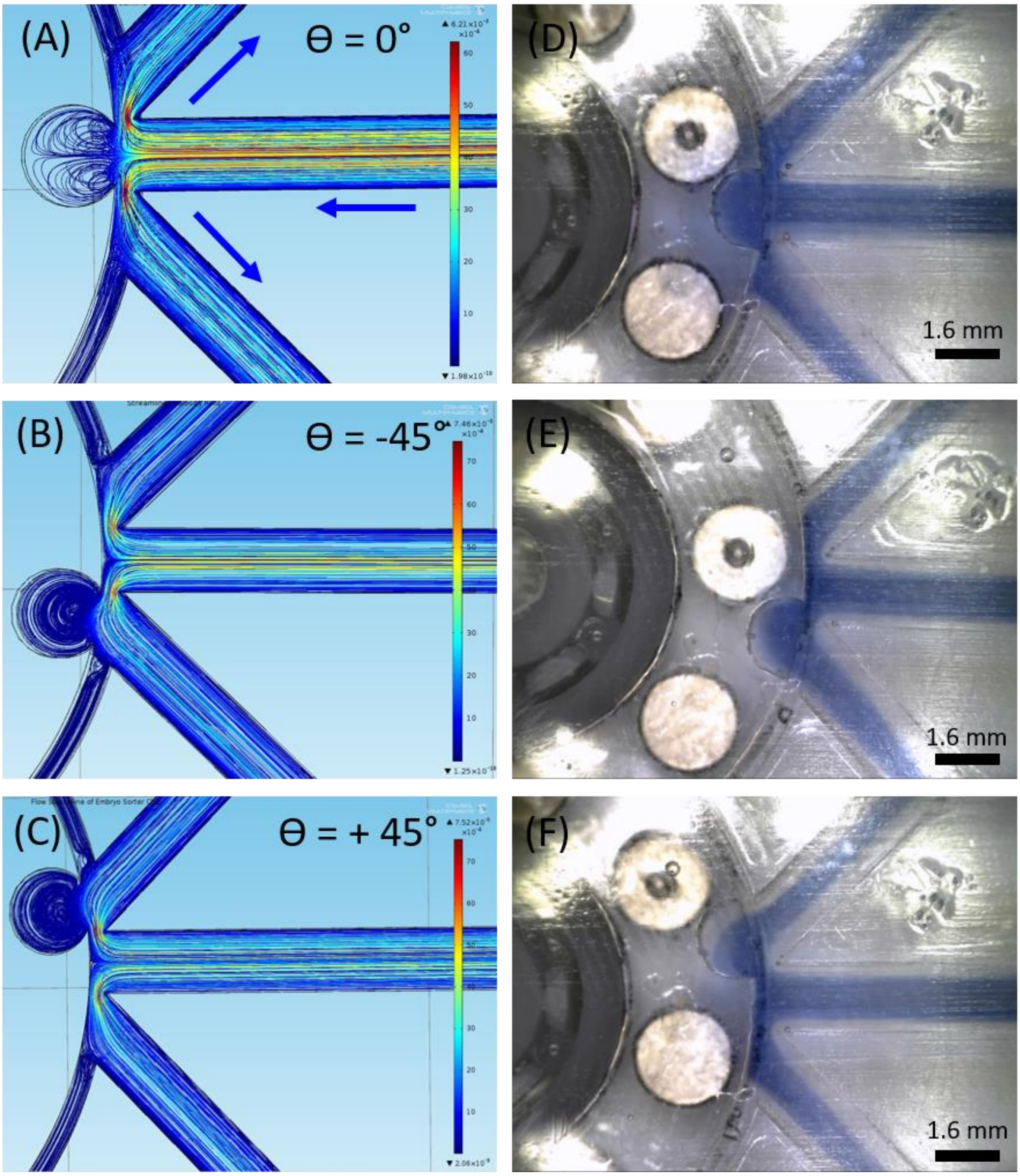

Figure 4.5 Visual illustration of the flow switching principle. The simulated fluid streamlines in the sorter trap are at angles 0°, -45° (downwards), and + 45° (upwards) (AC). The device is perfused with 0.04% of Trypan blue dye for imaging, and has a volumetric flow of 1500 µL/min. The experimental condition is comparable to the simulation and depicted in images (D–F). Blue arrow represents the fluid flow inside the microfluidic chip.

Next, the mass transfer uniformity inside the microfluidic device was predicted and validated experimentally using a dyed solution as the model probe. The chip was primed with ethanol solution during the experimental validation stage to eliminate air bubbles, followed by flushing with the fish embryo medium. The simulation showed that the medium exchange rate reached 100% within 60 seconds with a perfusion flow of 1500 µL/min. The simulation also predicted that higher exchange rate at the main loading channel than either outlet channel. Thus, the microperfusion pattern was in excellent agreement with the CFD simulation (Figure 4.6).

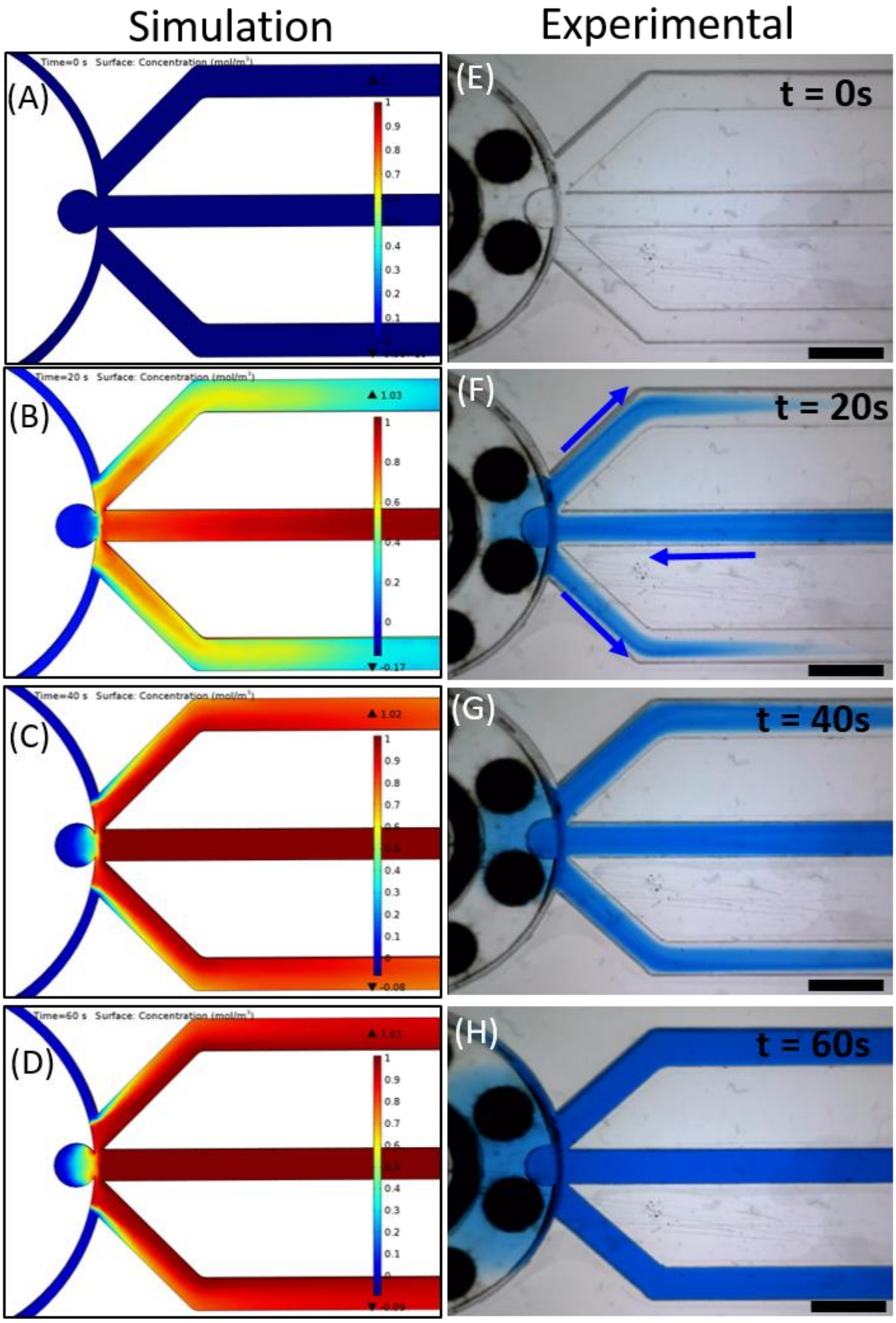

Figure 4.6 Mass transfer across the simulation and experimental stages of the microfluidic device is demonstrated. The device is perfused with 0.04% Trypan blue dye at a volumetric flow of 1500 µL/min. The perfusion time is recorded at 0s, 20s, 40s and 60s. Colour indicates the exchange flow rate concentration inside the device.

The microfluidic system was designed to the one-embryo-capture-sort concept (Figure 4.7), taking advantage of the gravitational-induced sedimentation of the embryos and low pressure force from a peristaltic pump working constantly at both outlet channels. Upon entering the device, the embryos rolled along the bottom surface of the channel under the influence of a drag force. The design enabled the sorter wheel to receive and immobilise an individual embryo using hydrodynamic forces. Only a single embryo was docked in the receptacle's trap, and following docking the receptacle rotated 45° clockwise or anticlockwise towards an output channel, thus enabling positive and negative sorting, as shown in Figure 4.8.

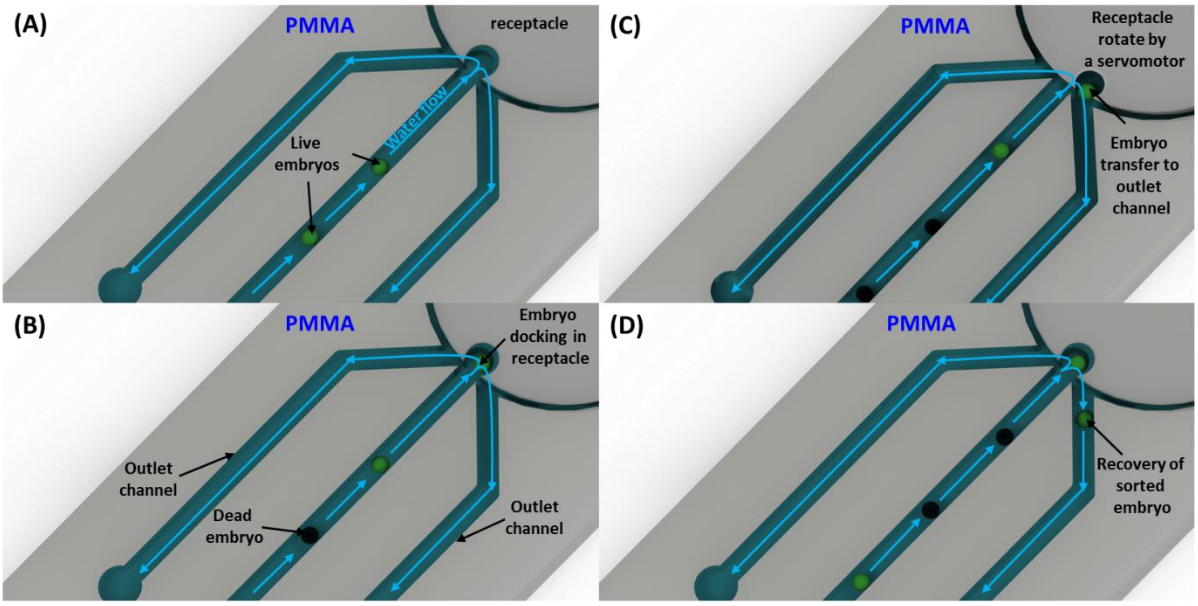

Figure 4.7. Overview of sorting principle (A) Illustration of embryos flowing towards sorting trap (width 1.6 mm, height 2 mm). Blue arrow represents water flow. B) Single embryo trapped in the sorting pocket. C) Sorter wheel rotated via servomotor to direct embryo into one of the outlet channels. D) Sorted single zebrafish embryo entering outlet channel.

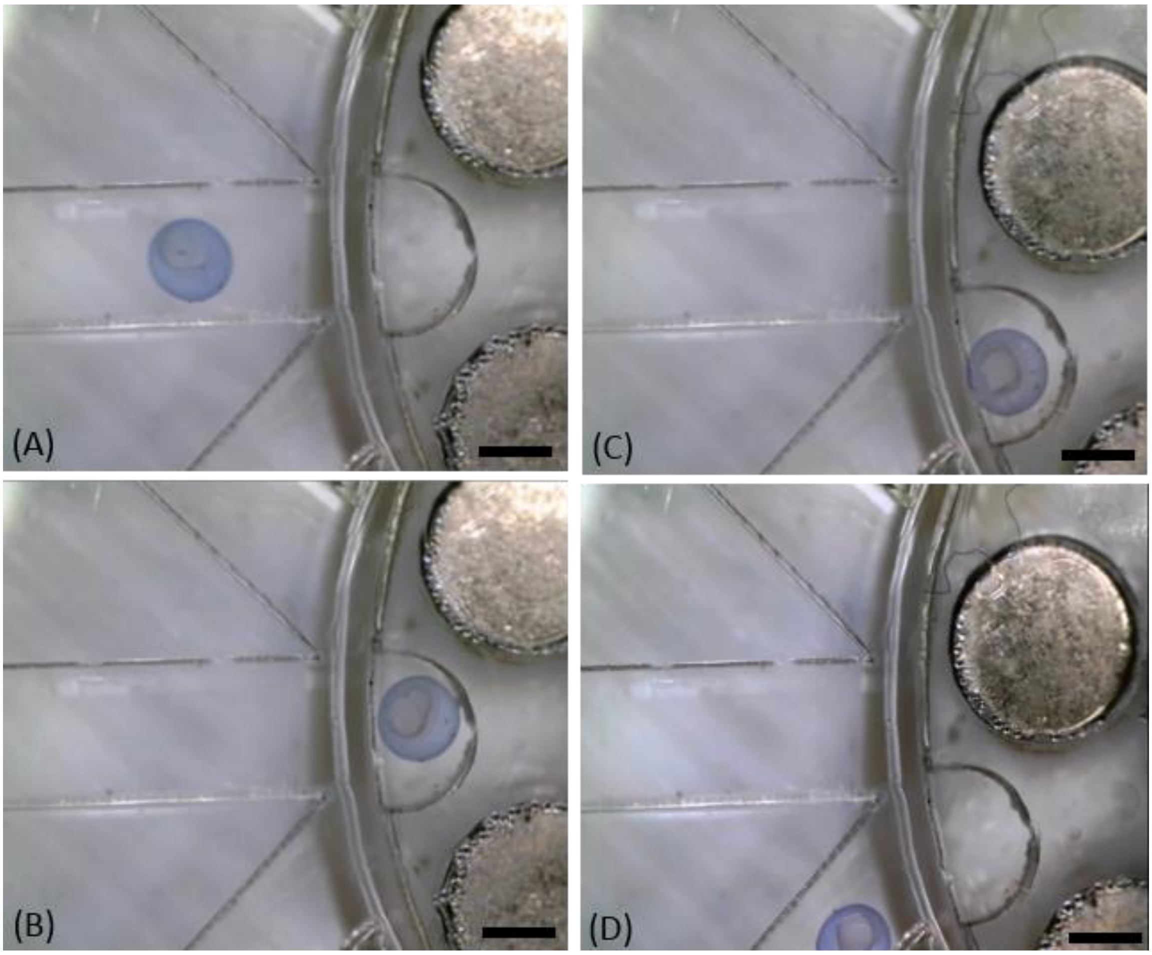

Figure 4.8 Experimental validation of the sorting concept. A) Live embryo of 16 hpf stained with Trypan blue dye entering inlet channel. B) Embryo trapped and immobilised in a sorting pocket. C) Receptacle is rotated towards the outlet channel. (D) Recovery of embryo moving towards outlet channel. Scale bar size denotes 800 µm.

4.4 Discrimination of live from dead embryos using differential infrared optical density (DIOD)

Transparent objects such as Live embryos absorb light at a certain wavelength [259]. This absorption is measurable in the intensity response. We used a standard infrared (IR) emitter and receivers. With this, one of the embryo detection concepts was to use the electronic sensor detection module enabling oscilloscopic identification of DIOD by employing IR emitters and receivers, embossed within the chip. This straightforward detection method exploited optical characteristics of embryos: the IR sensors used a light sensor like LED to detect a specific light wavelength in the IR spectrum. When a dark or solid object passed through the sensor, less light was received by the sensors. This difference in the light received was measured by a voltage threshold as shown in Figure 4.9.

The live specimens were optically transparent, while dead embryos were opaque due to the release of proteolytic enzymes during tissue necrosis, which led to a pronounced coagulation of embryo tissues. To enable detection of live vs dead specimens based on DIOD, an IR emitter and detector were embossed in opposite walls of the microfluidic channel. The embryos was introduced by passive pumping automatically, moving past in a single line, were exposed to the IR beam and a digital storage oscilloscope detected and recorded the characteristics of the light by measuring voltage output from the IR detector (Figure 4.9). The average output signals from the oscilloscope were calculated as, $\Delta V = V_2 - V_1$, where V_1 is the voltage source and V_2 is the voltage threshold. The latter could then be programmed to trigger the actuation of the revolving receptacle that mechanically redirected live and dead embryos into separate streams.

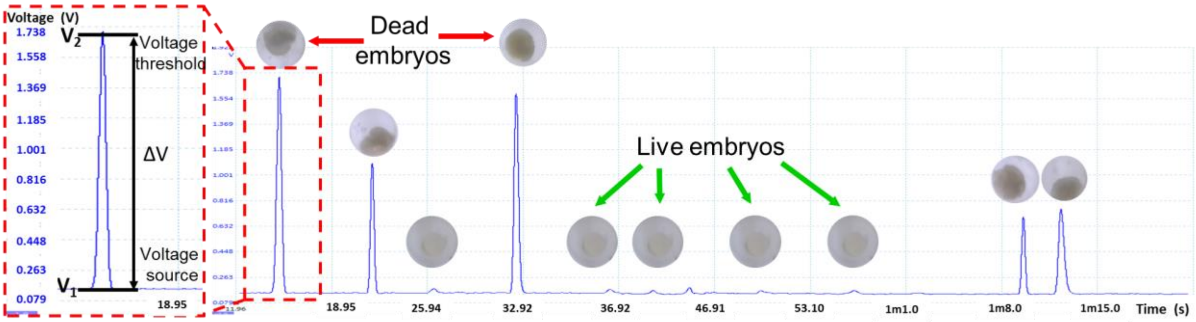

Figure 4.9 Experimental validation of live and dead embryos with embryos flowing in as in a single file at a perfusion rate of 1500 µL/min. Red dotted image depicts the measurement of average voltage, ΔV of the obtained signals over time. Oscilloscope waveform of diverse mixtures of live and dead embryos with values of 29 mV and 1 V.

To establish baseline voltage values, live and dead embryos (n=100) were initially flown through the microfluidic IR detection module at a constant flow rate of 1500 µL/min. We were successfully able to discriminate live and dead embryos by their DIOD values alone, with average voltage values of ≤ 100 mV and ≥ 500 mV established for live and dead embryos, respectively. To perform a preliminary performance validation of the DIOD detection concept, live and dead embryos were mixed in different ratios: i) 100% live embryos, ii) 90% live embryos, iii) 50% live embryos, iv) 1% live embryos, and v) 100% dead embryos. These were flowed through the microfluidic IR detection module at a constant rate of 1500 µL/min. During those experiments the AM7013MT Dino-Lite Premier microscope was positioned above the IR sensing module to validate accuracy of oscilloscopic identification of differential infrared optical density.

The results indicated that DIOD sensing was able to achieve 90–100% detection efficiency for live embryos and 60–87% for dead embryos, as illustrated in Figure 4.10 A. Fewer than 26% of embryos were aborted and more than 50% purity of the detected dead embryos was achieved during the detection process, as shown in Figure 4.10 B . Although the results of the DIOD sensing method are promising, they were affected by significant voltage variability, mostly due to lack of signal amplification and signal-to-noise issues.

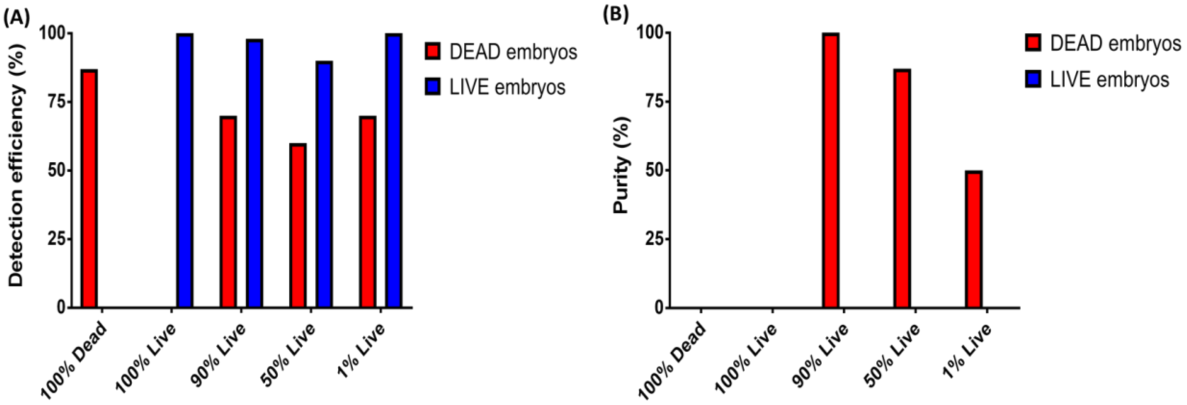

Figure 4.10 Experimental validation of IR sensing (A–B) of live and dead embryos with embryos flowing in in single file at a rate of 1500 µL/min. Detection efficiency and detection purity of dead embryos in diverse mixtures of live and dead specimens were calculated. Detection of dead embryos using robotic vision software

To eliminate problems associated with DIOD sensing method, we explored the potential of robotic vision software algorithms that could detect and track in real time a population of embryos moving in a single file inside a microfluidic channel. A customised algorithm was created in RoboRealm software to enable detection and tracking of dead embryos, based on their black colour intensity. During those experiments, the AM7013MT Dino-Lite Premier microscope was positioned above the microfluidic channel and set to an optical magnification of 45X. This corresponded to a field of view of 60 mm^2 that was deemed sufficient to identify embryos rolling on the surface of the chip-based device. The video stream, at 30 frames per second, was fed via a USB2.0 interface to a PC running RoboRealm software; see Figure 4.11 A.

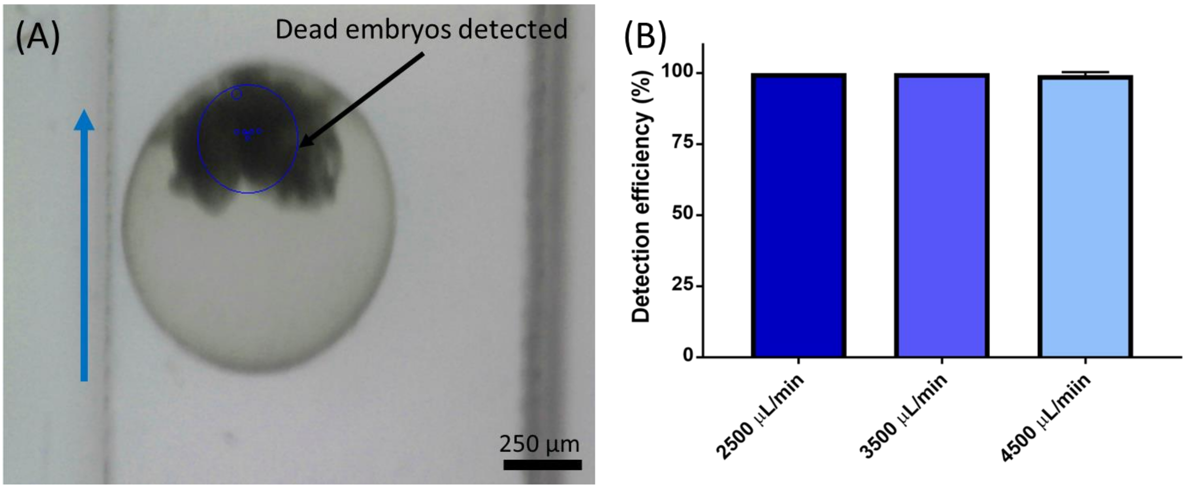

Figure 4.11 Robotic image acquisition of Roborealm software for sorting. (A) Real-time video acquisition and detection of dead embryos at a flow of 2500 µL/min. The blue circle indicates detection of the dead embryo when the software recognises it. The designed algorithm specifically used a colour module for tracking the dead embryos (RGB_Filter Gray –> Smooth Hull –> Blob Tracking –> Blob Replace). The blue arrow represents the direction of the fluid flow inside the microchannel. (B) Tracking efficiency of dead embryos rolled inside the microchannel at low to high volumetric flow rates.

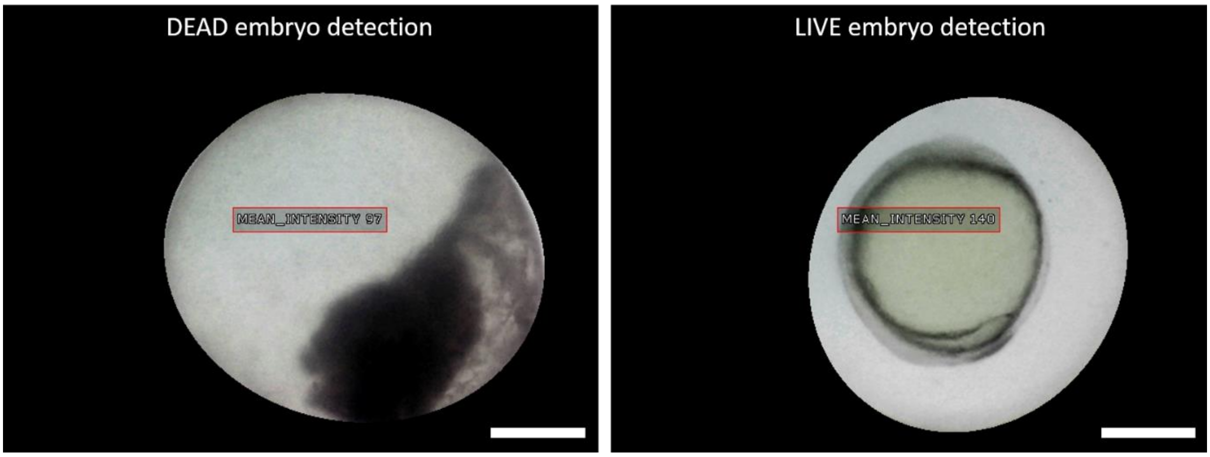

Figure 4.12 Vision recognition using image intensity for both coagulated (left image) and viable (12 hpf) (right image) embryos. The algorithm was modified to distinguish both types of embryo when the sensing detection process started. (Canny 0-4 -> Smooth Hull -> Circles -> Display Circle -> Write AVI). Average mean intensity values of ≥ 126 (live embryo) and ≤100 (dead embryo) were achieved The red boxes show the mean intensity value that the captured image required. Bar scale is 250 µm.

A pilot study was carried out to determine the accuracy and repeatability of the image tracking system. The results shown in Figure 4.11 B indicate that the robotic vision sensing method can achieve 100% detection efficiency when a pure population of dead embryos is loaded on a chip-based device. The embryos were successfully tracked and detected while flowing at a high rate in the microfluidic channel. This showed that the robotic vision software was capable of achieving a high accuracy of detection. However, the programmed algorithm was capable of detecting only the coagulated embryos, due to the transparency characteristics of the live embryos.

The image of the embryos later were captured in a static condition for image processing. The algorithm was modified to meet the requirements of detecting translucent specimens such as live embryos. It masked the background of the image concentrating on the area of the embryos. With this modification, mean intensities of the image were captured and measured (Figure 4.12), and live and dead embryos were distinguishable with the calculated intensities.

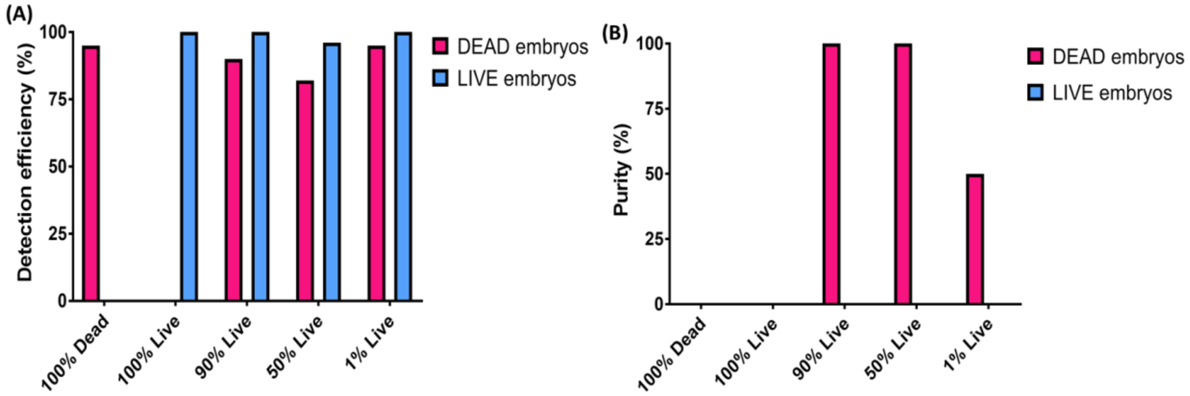

Figure 4.13 Experimental validation of real time video detection using RoboRealm software (A–B) of live and dead embryos with embryos flowing in in single file at a rate of 1500 µL/min. Detection efficiency and detection purity of dead embryos in diverse mixtures of live and dead specimens were determined. The results suggest that robotic vision detection is more accurate than DIOD sensing. The image processing algorithm was able to differentiate between live and dead embryos flowing through a microfluidic device. In addition, the method reduced tracking inaccuracies and increased the detection sensitivity of the specimens that were distinguished.

Further exploration was undertaken to detect both living and dead embryos when they appeared in different proportions. The preliminary performance was validated by mixing embryos at different ratios i) 1% live and 99% dead; ii) 50% live and 50% dead; iii) 90% live and 10% dead. These were run at a flow of 1500 µL/min. In almost all instances the real-time video tracking algorithm achieves more than 96% and 82% detection efficiency of live and dead embryos respectively (

Figure 4.13 A). Fewer than 18% of embryos were aborted and 100% detection purity of dead embryos was achieved during the real-time video detection if the proportion of live embryos was more than 50% (

Figure 4.13 B).

4.5 Summary and conclusions

The application of LOC technologies for in situ manipulation and handling of small model organisms such as zebrafish embryos has attracted a great amount of interest in various fields and particularly in biomedicine. The use of microfluidic chip-based devices for this application is limited because of the constraints imposed in fabricating a device on a millilitre scale, and because of biocompatibility issues, and manual procedures are time consuming and prone to errors, limiting research efficiency. There have been some achievements in developing cytometrics for large particle analysis and robotic automation sorting systems, but these are complex and users must be trained in their use [54]. Simpler detection methods and procedures are needed to improve the operation of sorting embryos.

A proof-of-concept design for a micromechanical large particle in-flow sorter, capable of analysing, sorting and dispensing live vs. dead zebrafish embryos, has been demonstrated. The core design features an embedded revolving micromechanical receptacle actuated in a non-contact mode using a robotic servomotor. The microfluidic sorter was developed to distinguish between live and dead embryos. A sensing method linked with image processing was found more efficient than wavelength sensing methods such as IR sensors. The programmable machine vision system is capable of detecting embryos whether they are moving or in stasis.

This work demonstrates a new concept for sorting and handling zebrafish embryos in miniaturised chip-based devices. A simple and compact microfluidic device was fabricated to overcome current problems of size associated with available sorting systems. This newly developed design offers a new paradigm for miniaturised and automated sorting devices capable of handling large particles such as embryos and small model organisms.

However, this study focused only on the development of the conceptual design, its fabrication, and the testing of various detection methods to distinguish between two types of embryo. This was due to limitations in integrating the software with the motion system (servomotor). A continuous feedback system in the form of accurately positioned set points is required in an accurate sorting mechanism. The RoboRealm software often crashed when the servo control was turned on, resulting in the system being unable to decode the embryo images. Upcoming work will concentrate on the development of a fully integrated sorting system combined with automated loading, real-time sorting decision-making algorithms and automatic dispensing of embryos for further pharmacological testing.

5 Millifluidic Device for Immobilisation of Zebrafish Larvae for Cardiotoxicity Analysis

5.1 Introduction

Most commonly used methods to fabricate millifluidic devices for large model organisms utilise either direct infrared laser ablation in PMMA or laser micro-machining of PMMA moulds combined with replica moulding in poly(dimethylsiloxane) (PDMS, Sylgard 184) elastomer [27]. Most recently, additive manufacturing methods such as stereolithography (SLA) have been shown as one viable alternative for the fabrication of optically transparent microfluidic as well as millifluidic devices. [166].

This chapter describes the capability of high-definition 3D printing in additive manufacturing systems to fabricate optical-grade transparent moulds suitable for replica moulding for millifluidic chip-based devices. As mentioned in Chapter 1, using standard photolithography processes to creates prototypes of millimetre scale, high-aspect ratio devices required for large metazoan organisms is difficult and time consuming. The main objective of this project was to investigate the feasibility of using 3D printing for the direct, one-step creation of non-planar PDMS chip-based microfluidic devices with higher dimension accuracy and surface quality than is currently achieved. A design for a direct PMMA mould was selected as the control for comparison with other fabrication techniques; this was then fabricated using three different 3D printers and three different printing materials. The reproduction quality of such features as geometric accuracy of the printed moulds was assessed. Prototypes were evaluated using SEM and quantitative 3D topographic surface mapping using optical profilometry. The x-y and z resolution of the printed moulds were also evaluated and compared.

Here we demonstrate the design and development of PDMS millifluidic devices for trapping and immobilising living zebrafish larvae. The developed devices were used for the physiological cardiac rate assessment of the larvae under the continuous influence of drugs or chemicals.

5.2 Millifluidic chip design and fabrication

The millifluidic chip was fabricated using a combination of 3D-printed negative relief moulds and soft lithography. The initial CAD design for the mould, shown in

Figure 5.1, enabled automated docking and immobilisation of living zebrafish larvae in a linear array of ten traps (0.8 mm x 0.8 mm x 3.5 mm) with curvilinear corners (r = 1.5 mm) (

Figure 5.1). This feature ensured smooth movement of the larvae during docking and avoided specimen damage. The design utilised a hydrodynamic trap principle with a passive hydrodynamic flow for larvae docking and immobilisation, as described in Chapter 4 (4.3) [27]. Control devices were fabricated using conventional techniques as described in Chapter 3 (3.7) [166].

The suction channel was positioned at the top of each trap channel that is connected to an outlet channel. A thrust channel (0.7 mm x 0.8 mm x 0.8 mm) was located vertically at the opposite of the entrance to each trap, to increase the hydrodynamic flow of that trap.The inlet and outlet connection ports, with diameters of 3.0 mm, were used for direct tubing (Ø internal diameter= 1.3 mm).

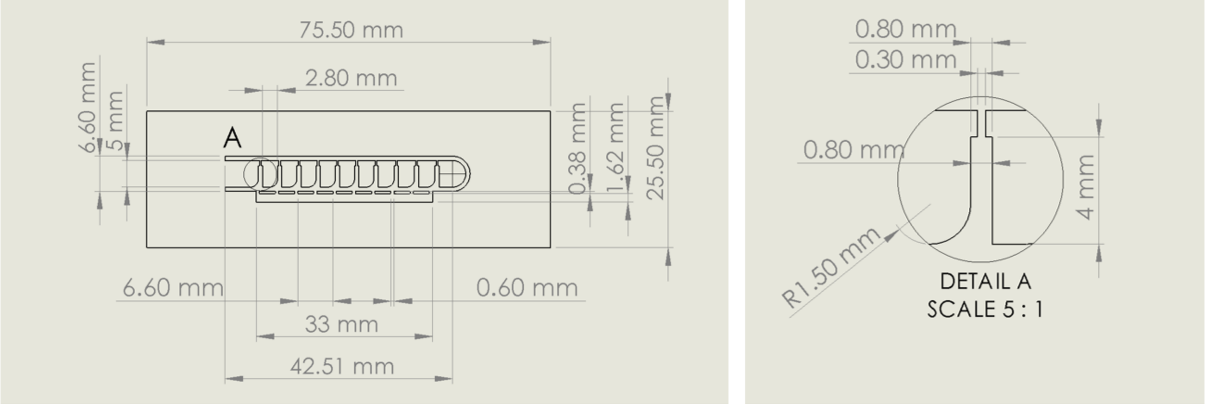

Figure 5.1 Overview of CAD design of the negative relief mould for larvae immobilisation millifluidic chip. A detailed view of section A is depicted on the (right).

The overall internal volume of the device was approximately 230.2 µl, while the volume for a single trap was 2.29 µl. A control comprising devices fabricated by conventional techniques, such as soft lithography in PDMS and infrared laser computer numerical control (CNC) micromachining in PMMA, was described in Chapter 3 (3.7) [166].

The relief mould was then printed on VisiJet SL Clear (VJC), Vero Clear (VC) and Form Clear (FC) materials. None of the printed moulds required additional bonding procedures, but the relief mould fabricated from PMMA materials needed thermal bonding; it was selected as the control for this study. The final surface finish of all printed moulds and final microfluidic device were comparable with the control, except that the mould was tinted and not fully transparent (Figure 5.2). All moulds were further used to fabricate elastomeric PDMS structures using soft lithography as illustrated in Figure 5.3 and Figure 5.4. The inlet and outlet connection ports (Ø = 3.0 mm) were manually punched holes; both PDMS structures were cleaned and bonded using oxygen plasma cleaner equipment.

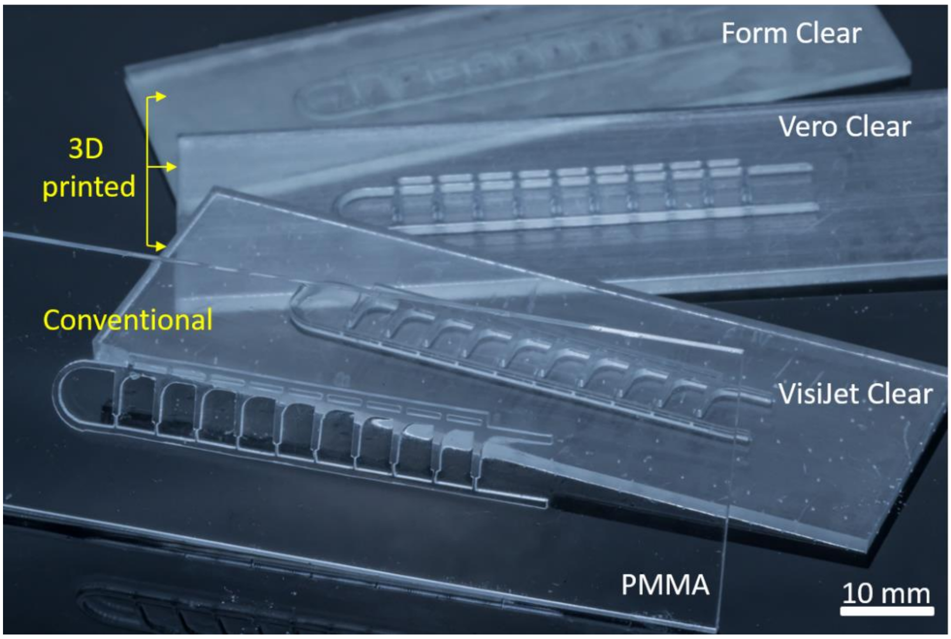

Figure 5.2 An illustration of showing zebrafish larvae trapping arrays using different additive manufacturing methods. CO2 laser micromachining used to cut the thermoplastic material of polymethylmethacrylate (PMMA) and designated as the control. The 3D printed moulds were fabricated using stereolithography (SLA; in VisiJet SL Clear and Form Clear resins) and multi-jet modelling (MJM; in Vero Clear resin).

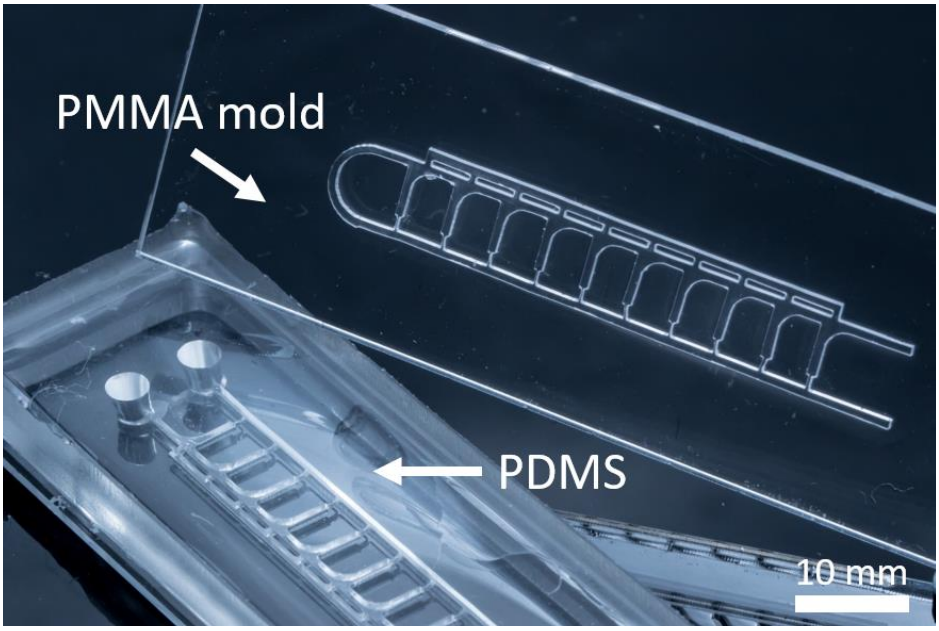

Figure 5.3 A PDMS chip-based device to trap 3dpf zebrafish larvae. The main body was fabricated of polydimethylsiloxane (PDMS) with a PMMA mould, bonded to a standard microscope slide (sealing layer). This is referred to later as PMMA-PDMS for the control fabrication.

Figure 5.4 A photograph of 3D printed mould and the final fabricated PDMS chip-based device. All PDMS structures were comparable with the control (PMMA-PDMS) in shape and transparency. The soft lithography process does not affect the appearance of the final microfluidic devices.

5.3 Characterisation of 3D-printed moulds for soft lithography

The reproductive quality of additive manufacturing for both SLA and MJM systems was investigated using the smallest features of the prototype, such as the suction channels and other trapping regions, as shown in Figure 5.5. Prototypes were evaluated on their critical key features: aspects of 3D printed LOC devices such as geometric representation accuracies, material structure and optical transparency using scanning electron microscopy examination, and quantitative 3D topographic surface mapping using optical profilometry. The x-y and z resolution of additive fabrication compared favourably with other forms of rapid manufacturing such as direct infrared laser ablation in PMMA and laser micro-machining of PMMA moulds combined with replica moulding in poly(dimethylsiloxane) (PDMS, Sylgard 184) elastomer. [27] The latter process will here be referred to as PMMA-PDMS and is the control fabrication. All 3D printed moulds and PDMS structures were characterised in detail to determine their geometric accuracies and surface morphology.

5.3.1 Geometric accuracies

Surface characteristics of geometric patterns differing from the theoretical (designed) dimensions depended on the process of additive manufacturing used in 3D printers. Nominal dimensions were designed in CAD; three different widths, illustrated in Figure 5.5, were selected for geometrical measurement. The accuracy of the printing was evaluated by comparing the selected dimension with the actual dimension of the smallest features of the prototypes, 300 µm (Figure 5.6). Both moulds and PDMS were measured accordingly and some variations in the dimensions were found. SLA fabrication methods produced 20% fewer deviations than the others. In practice, the dimension of the PDMS structure is larger than in theory, a result of the moulding and demoulding process.

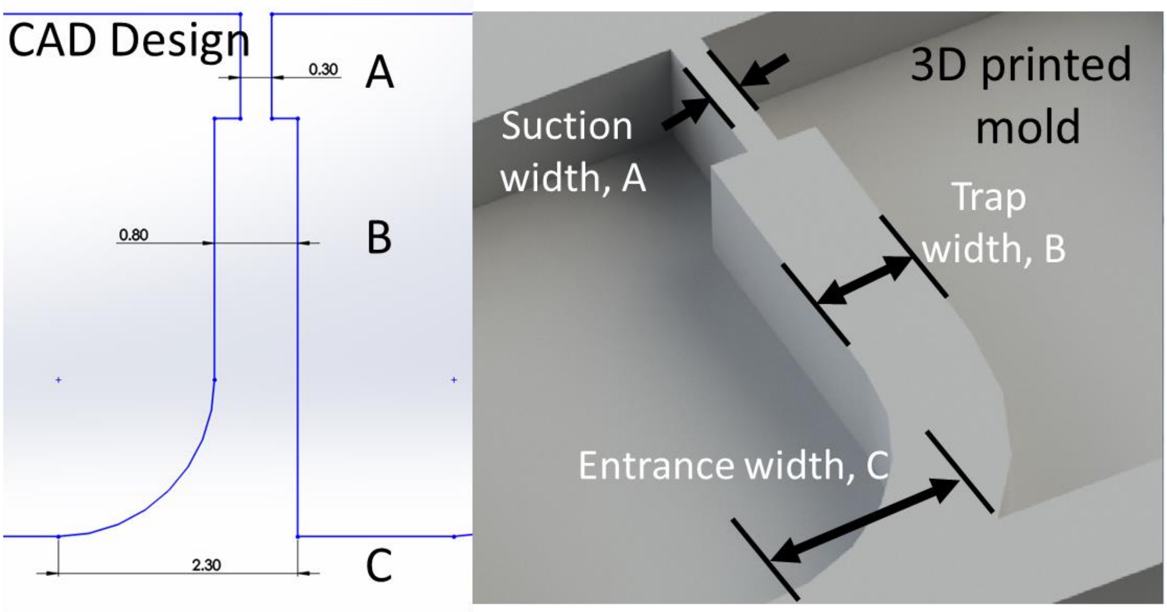

Figure 5.5 Geometrical representation of a single trap. Suction width (A), trap width (B) and entrance width (C) were measured after the 3D printing fabrication. Actual CAD dimensions (in mm) were compared with actual 3D printed mould and PDMS.

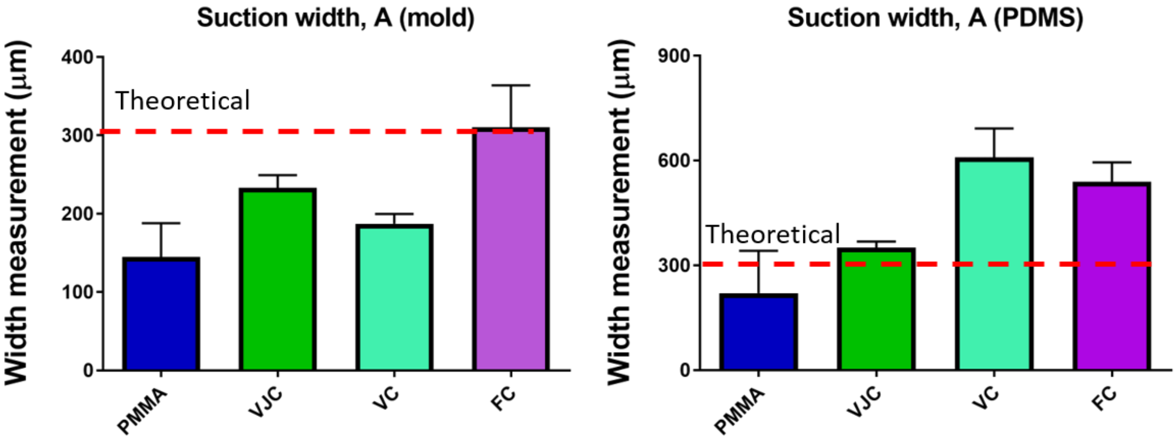

Figure 5.6 Comparison of measured deviations of the trap structures for all fabricated 3D printed moulds. The theoretical width of suction is designed in CAD is to be 300 µm. All printed moulds were comparatively accurate except for Form Clear. Apart from the PDMS structure made from the PMMA mould, all other additive manufacturing methods were relatively precise.

5.3.2 Surface topography

Surface topography, such as the surface roughness of the fabricated structures of the 3D printed moulds, is important as poor surface quality will affect the performance of the device. Higher surface roughness on the 3D printed mould surface affects the outcome of the fabricated relief negative PDMS. Moreover, a rough surface will encourage a turbulent rather than a laminar flow in the system. A detailed assessment of the surface topography was made of all 3D printed materials. To obtain a good conductivity and sensitivity of the scanned surface, all printed moulds were coated with gold in prior of imaging.

- **Scanning Electron Microscopy**

The surface topography of the 3D printed moulds and PDMS were first analysed using a scanning electron microscope for visual comparison with the control PMMA mould surfaces. The VJC mould showed smooth top and bottom surfaces, while the VC showed an uneven ‘wavy’ texture: a direct thermal effect of instant UV curing after the resin layers were injected on the surface. By comparison, the Form Clear showed roughness on all printed surfaces, as illustrated in Figure 5.7. On the bottom surface of the FC moulds, porous structures were noticeable, which caused damage to the PDMS structure during soft lithography.

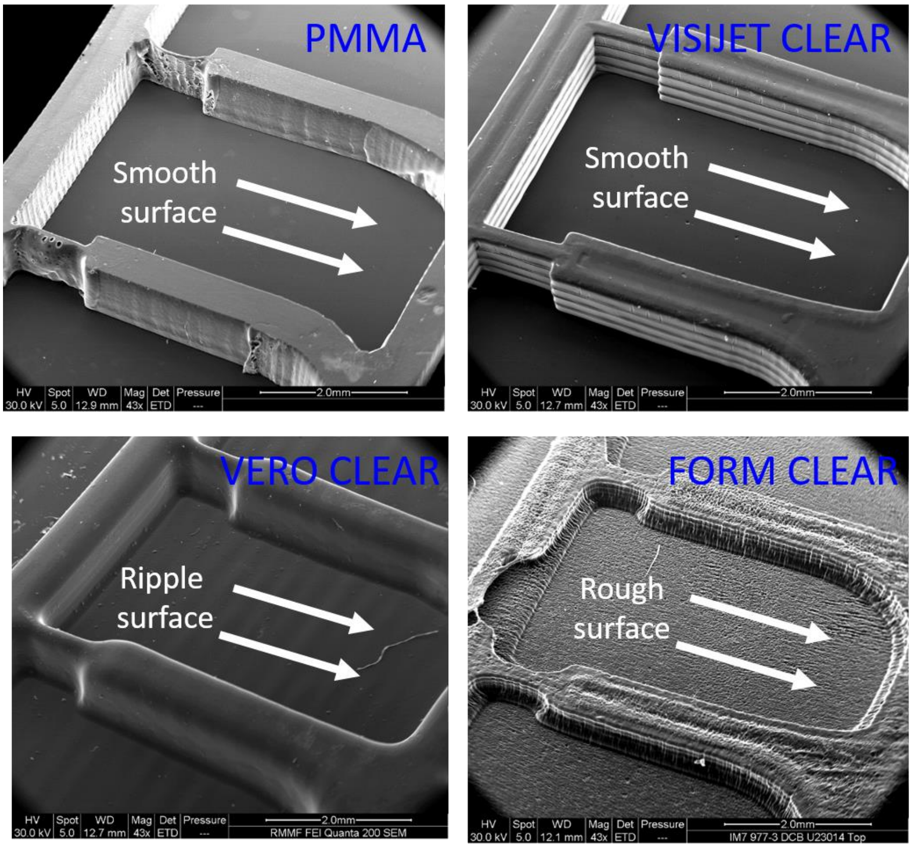

Figure 5.7. Topographic surfaces of 3D printed moulds of the larvae traps are depicted using SEM. The VisiJet Clear was observed to have a smooth surface comparable with the conventional PMMA mould. SEM image for VJC presented more uniformity of the layer resolution of 800 µm (thickness) than the other additive manufacturing methods.

Next, the view was magnified and focused on the top surface of the printed 3D structures (Figure 5.8). Debris caused by removing material by laser ablation had accumulated on the top PMMA surface, as it could not escape from the cutting zone while being machined. There was also evidence of incomplete deposition of the resin on the FC mould. Some resin materials were not polymerised and thus collapsed at the centre of the structure, producing a large, deep indentation.

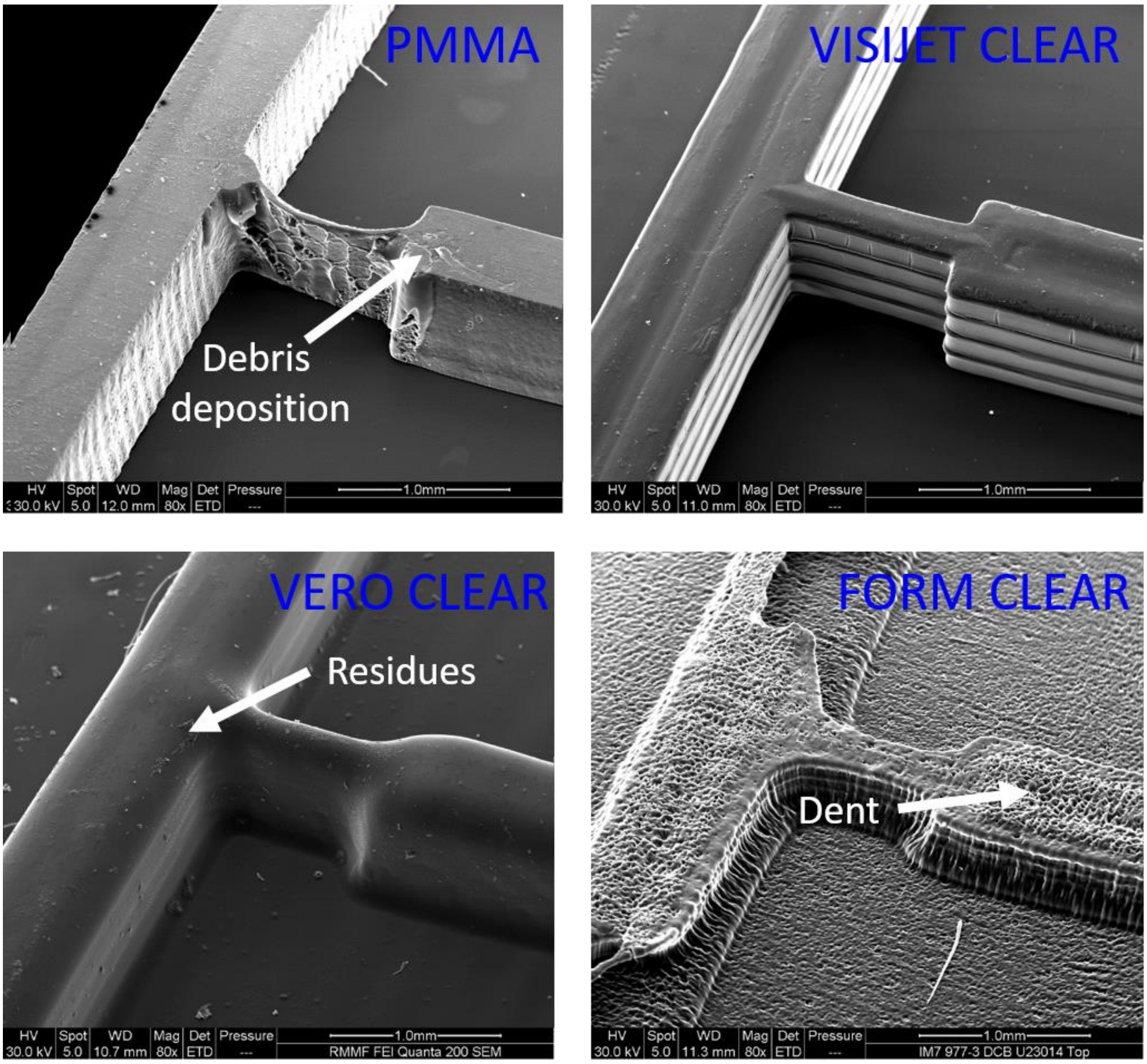

Figure 5.8 Comparison of topographic surfaces using SEM, depicting the top surfaces of the larvae trap. All the 3D printed moulds achieved a smooth top surface finish apart from the Form Clear mould, which suffered from incomplete layering of the resin while printing.

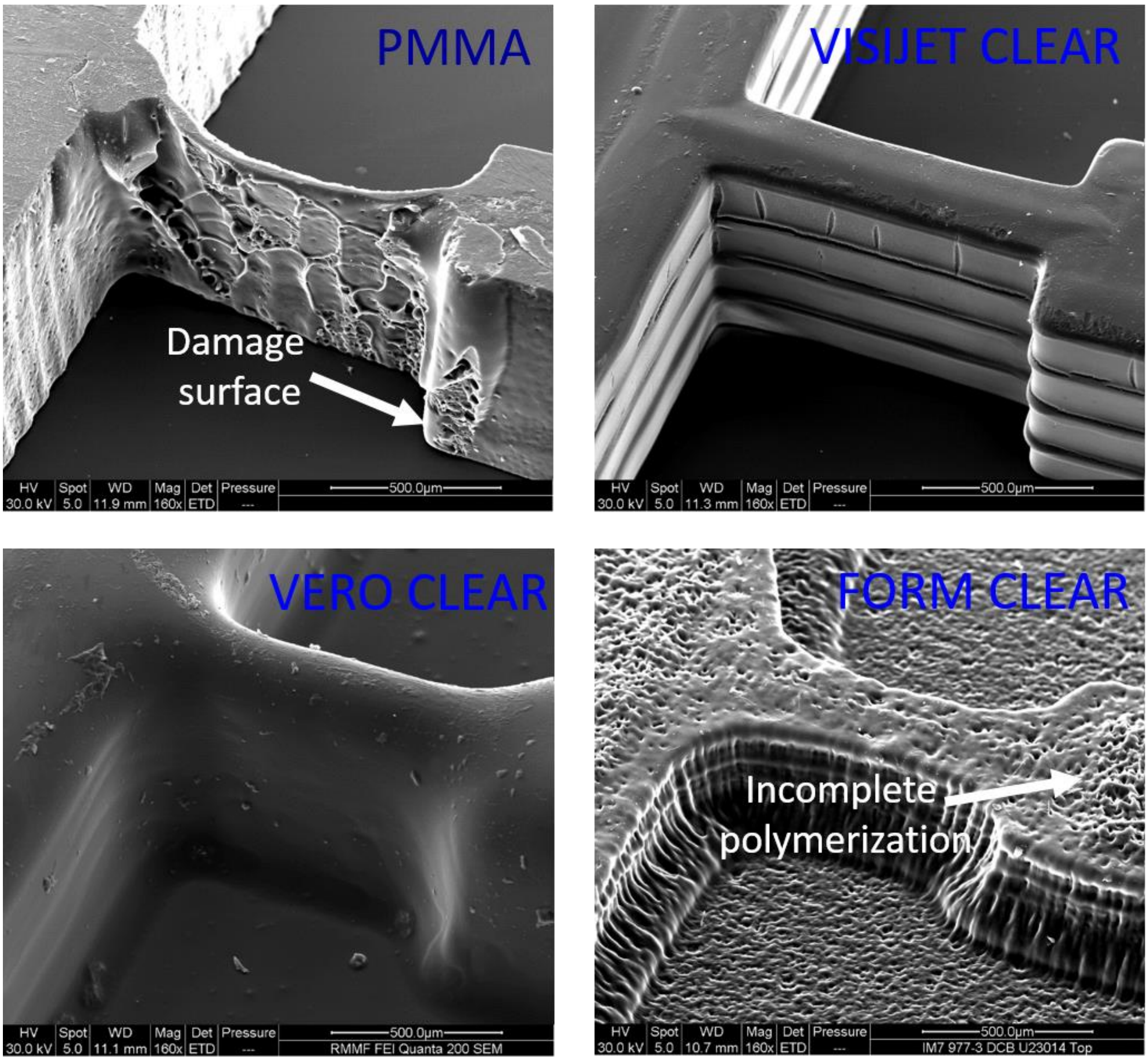

Figure 5.9 Comparison of topographic surfaces using SEM, showing a close view of the suction channel on all 3D printed moulds. Only VisiClear showed good layer deposition.

Each suction channel was magnified to observe the vertical walls; the deposition layer of the resins in all 3D printed moulds were also depicted. VJC and VC had uniform sidewalls and FC showed deformed structures. Although the desired thickness is achievable in PMMA, laser technology failed to cut the materials with a dimension of less than 300 µm. The damage to the surface was an effect of the laser, which produced a small heat-affected zone at the end of the process (Figure 5.9).

- **Optical profilometry**

To evaluate the surface analysis, 3D surface mapping of optical profilometry was used. An area of 500 µm x 500 µm was scanned by the laser beam at both top and bottom surfaces. A surface mapping contour was presented as the outcome. The red area represented the peak while the blue areas indicated valleys. The green zone was set as the reference panel. The the heights on the surface were presented as a Gaussian distribution, and so a surface roughness was obtained for each scanned surface.

The surface profiles of both PDMS and printed mould surfaces were analysed. Importantly, when prototypes were examined using optical microscopy, significant differences in surface roughness were readily observed in the different resins used in manufacturing. A significance difference in average roughness, R_a for the top (mould) of PMMA, VJC and FC, were readily observed in the different resins utilised for manufacturing. Overall, traps and channel microstructures embedded within the chip were consistently fabricated with the highest accuracy, in VJC with R_a =18 µm (Figure 5.11) compared with PMMA (Figure 5.10). They reflected the outcome of different post-treatment processes to remove support materials.

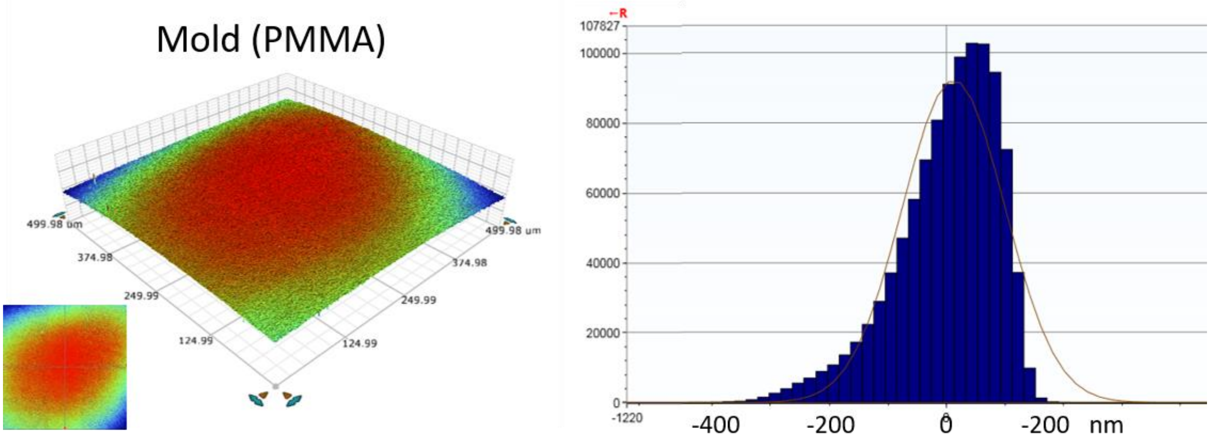

Figure 5.10 Surface topographic analysis of 500 µm x 500 µm area size of top surface of mould structures (left image). The Gaussian distribution on the surface texture is represented by the median height (right image). A smooth surface has a median height of 92 µm and width of 86 µm.

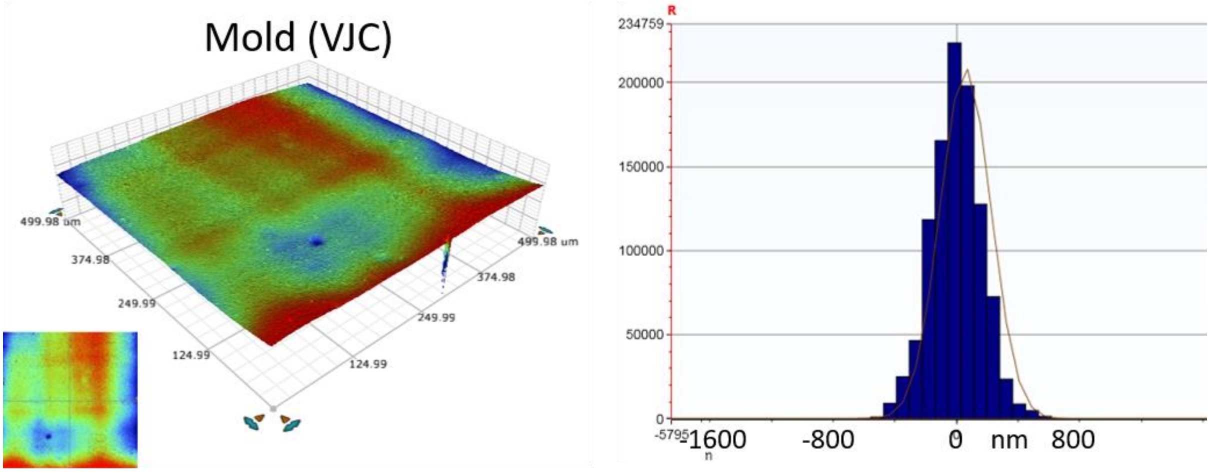

Figure 5.11 Quantitative analysis of surface topography of an area of 25 mm^2 the top of VisiJet SL clear printed moulds (left image). The Gaussian distribution was symmetrical on the surface texture (median height) (right image). The surface was smooth and relatively flat compared to the control (PMMA) as is indicated by the small variations in the distribution curve.

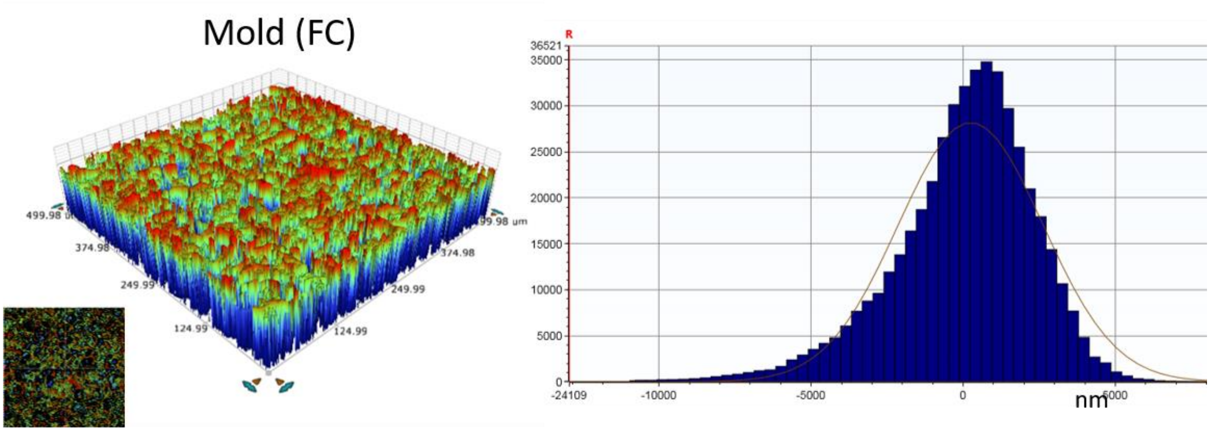

Figure 5.12 Surface profilometry analysis of the selected scanned area (500 µm x 500 µm) (left image). The skewed Gaussian distribution on the surface roughness (median height) is presented (right image). Large variation in the histogram distribution with relatively rough texture is observed as the peaks are greater than the valleys with R_a value of 28 µm for FC mold.

In contrast to PMMA and VJC moulds, the FC surface showed a random view of the peaks and valleys. Although the variation was equally distributed, void spaces clearly observed in areas of the map resulted in rough surface texture (Figure 5.12). This is due to incomplete polymerisation during printing and post-processing of the support resin. The irregularities in the texture promoted adhesion during the soft lithography process, which damaged the PDMS. This indicated that FC was not suitable for printing structures less than 300 µm in dimension.

5.4 Device performance for zebrafish larvae trapping

5.4.1 The concept of larvae trapping and immobilisation

The millifluidic system was designed for automatically trapping and positioning larvae, based on the gravity-induced sedimentation of the larvae and the low-pressure suction at the top of the traps. Low pressure from a peristaltic pump was applied at the outlet of the chip, and larvae were then with head facing forward, one at a time at a set interval, from a reservoir into the inlet channel. Upon entering the device, the anesthetised 3dpf zebrafish larvae with heads facing forward flowed along the microchannel under influence of a drag force. This design allowed some individual zebrafish larvae to be trapped and immobilised by the hydrodynamic forces. The trapped zebrafish increased the flow resistance. redirecting the main stream flow to the other channels. The following larvae bypassed the occupied trapping channel and were directed into the next trap. After the larvae were trapped, they remained immobilised and a flow rate of 1000 µl/min was continuously perfused to maintain positive pressure throughout the system, as shown in Figure 5.13.

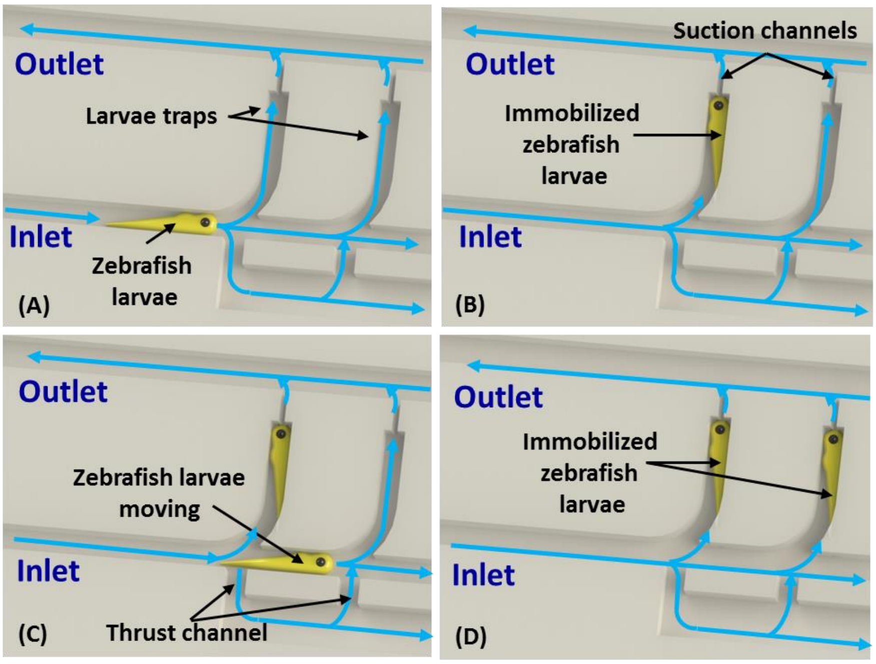

Figure 5.13. Overview of larvae trapping principle: (A) Illustration of zebrafish larvae flowing towards entering the trap (0.8 mm (width) x 4.0 mm (height) x 0.8 mm (thick)). Blue arrow represents water flow (rate = 2000 µl/min) (B) Single zebrafish larvae immobilised inside one of the traps (C) Subsequent zebrafish larvae flowing towards next trap (D) Zebrafish larvae immobilised inside the trap and acclimated for fine minutes with a constant flow of 1000 µl/min.

5.4.2 CFD simulations

CFD simulations were initially performed (COMSOL Multiphysics v4.4) to predict flow velocity, pressure drop and uniformity of mass transfer inside the device (Figure 5.14). The simulation indicated that at a flow rate of 1000 µl/min, velocities inside the chip varied from 0.0026 m/s to 0.013 m/s, at input and output respectively. The trap had a constant velocity of 0.02 m/s with a constant flow pressure of 28 Pa, and the thrust channel (velocity = 0.036 m/s) and suction channel (velocity = 0.06 m/s) were able to immobilise the zebrafish larvae.

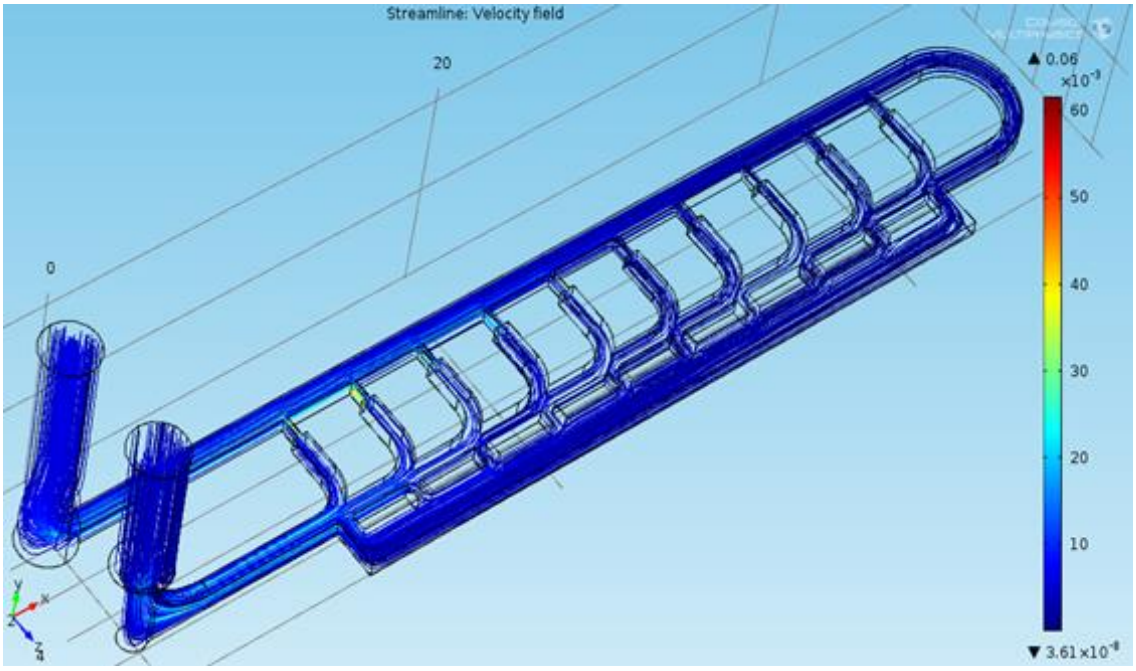

Figure 5.14 CFD simulation of the theoretical prediction of fluid flow inside the millifluidic chip with an inlet flow of 1000 µl/min

The functional characteristics of additively manufactured prototypes were investigated next. The design of the chip allowed automatic trapping of individual larvae using hydrodynamic forces. Upon entering the device, the anesthetised zebrafish encountered a drag force that guided them to a trapping region. Every trapped zebrafish larva increased the flow resistance and redirected the streamline to subsequent traps. After the larvae were trapped, they could remain immobilised for up to 24 hours. Trapping efficiency was calculated as the number of captured larvae divided by the number of larvae injected into the device (Figure 5.15). The results indicate that efficiency was greatly affected by feature reproduction and surface topology caused by different techniques of additive manufacturing. Fewer than six larvae could be trapped in an array consisting of 10 traps, in all fabricated PDMS chip-based devices.

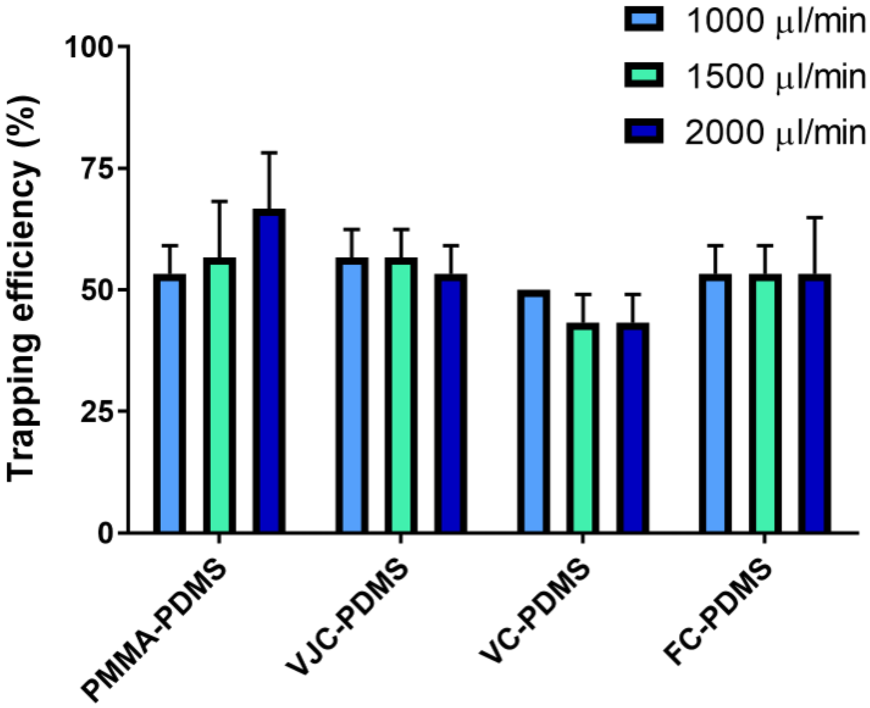

Figure 5.15 Comparison of trapping performance of zebrafish larvae between devices fabricated using different techniques. The volumetric perfusion rate range tested from low to high volumetric flow rate.

5.5 Improving the design

Amendments were made to the design of the PDMS chip-based design. Given the low trapping efficiency of the earlier design, the number of traps was reduced to achieve higher efficiency. Five traps in a linear array were placed in an area similar to that of a standard microscope slide. Additional mirrored arrays were placed to act as replicates of the opposite array (Figure 5.16 A).

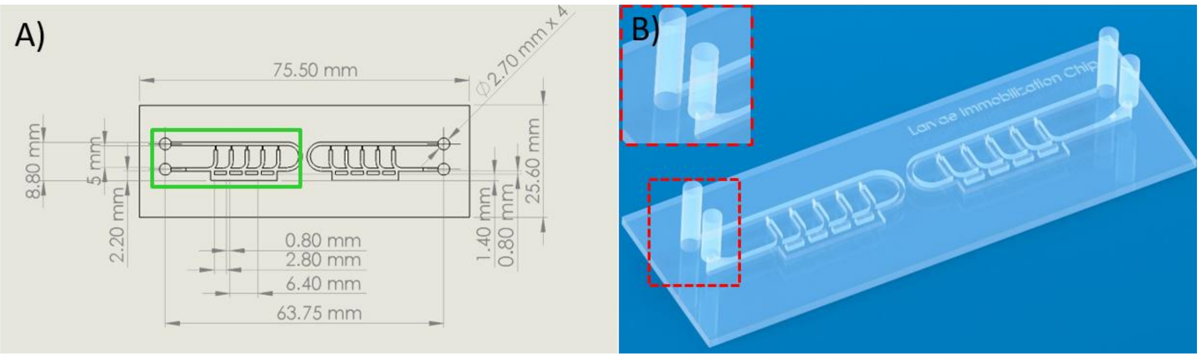

Figure 5.16 Overview of modified design of the negative relief mould. (A) A detail of the CAD design. A linear array of five traps was designed (green image). Each individual trap has the same dimensions as in the previous design. (B) Realistic image of the printed mould. Inlet and outlet ports (Ø = 2.7 mm) were 3D printed directly (red dotted image). This eliminated the hole punching process for direct tubing.

A new CFD simulation was run to envisage fluid flow inside the microchannels (Figure 5.17 A). The inlet and outlet velocities were 0.014 m/s and 0.0055 m/s respectively. A wider thrust channel (0.80 mm) was located opposite the entrance to the trap, providing a hydrodynamic force that increased the velocity (0.0078 m/s), focusing on the single trap. The overall internal volume of the device was approximately 189 µl while the volume for a single trap was 2.29 µl.

Mass transfer experiments with 0.04% Trypan blue dye (Life Technologies Corp, CA, USA) visually demonstrated the flow of fluid inside the microfluidic chip (Figure 5.17 B-G). The mass transfer experiment was conducted to predict the perfusion time of the toxicant or chemicals, from entering the inlet and moving to all traps and finally to the outlet channel. A 100% drug delivery across the whole device took less than a minute at a flow rate of 1000 µL/min. Next, negative relief moulds were printed, using VC materials for all millifluidic devices because of the good surface integrity and performance it demonstrated earlier in Chapter 5 (5.2).

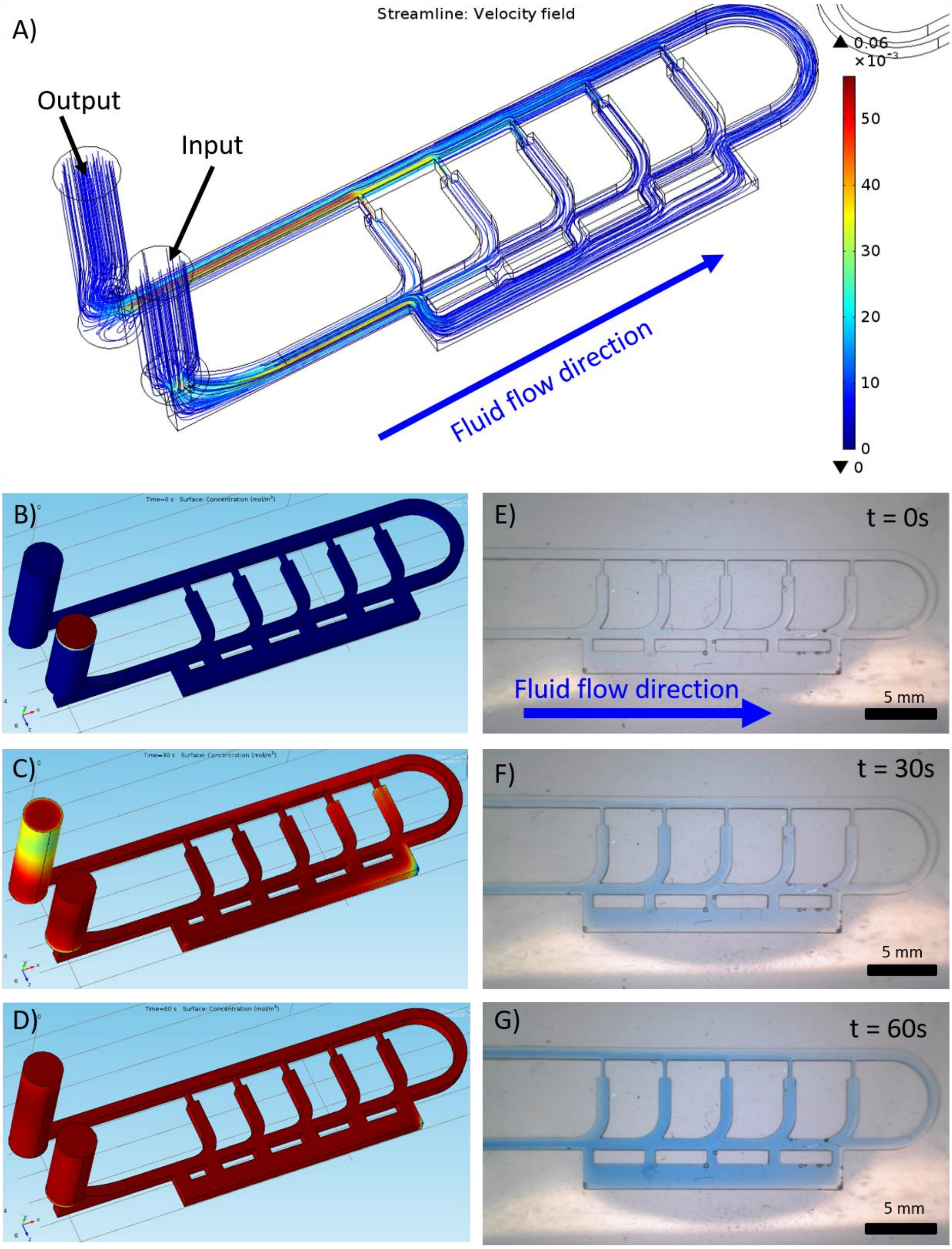

Figure 5.17 CFD of the microfluidic device for trapping 3 dpf zebrafish larvae. (A) Predicted velocity streamline of the entire array of the device. The simulation of mass transfer flow (B–D) and experimental fluid flow using 0.01% Trypan blue dye (E–G). Time taken was 0, 30 and 60 seconds. Volumetric perfusion rate used was 1000 µL/min.

The hydrodynamic force of the fluid led the moving larvae inside the loading channel. The thrust channel increased flow towards the trap and guided the larvae inside. The microfluidic array used the concept of a single-larvae-trap allowed only one larva per trap at any time. The larvae did not trap in sequential order because they were partially anesthetised; twitching larvae moved to the next trap. Eventually, 100% trapping efficiency was achieved with this modified design (Figure 5.18).

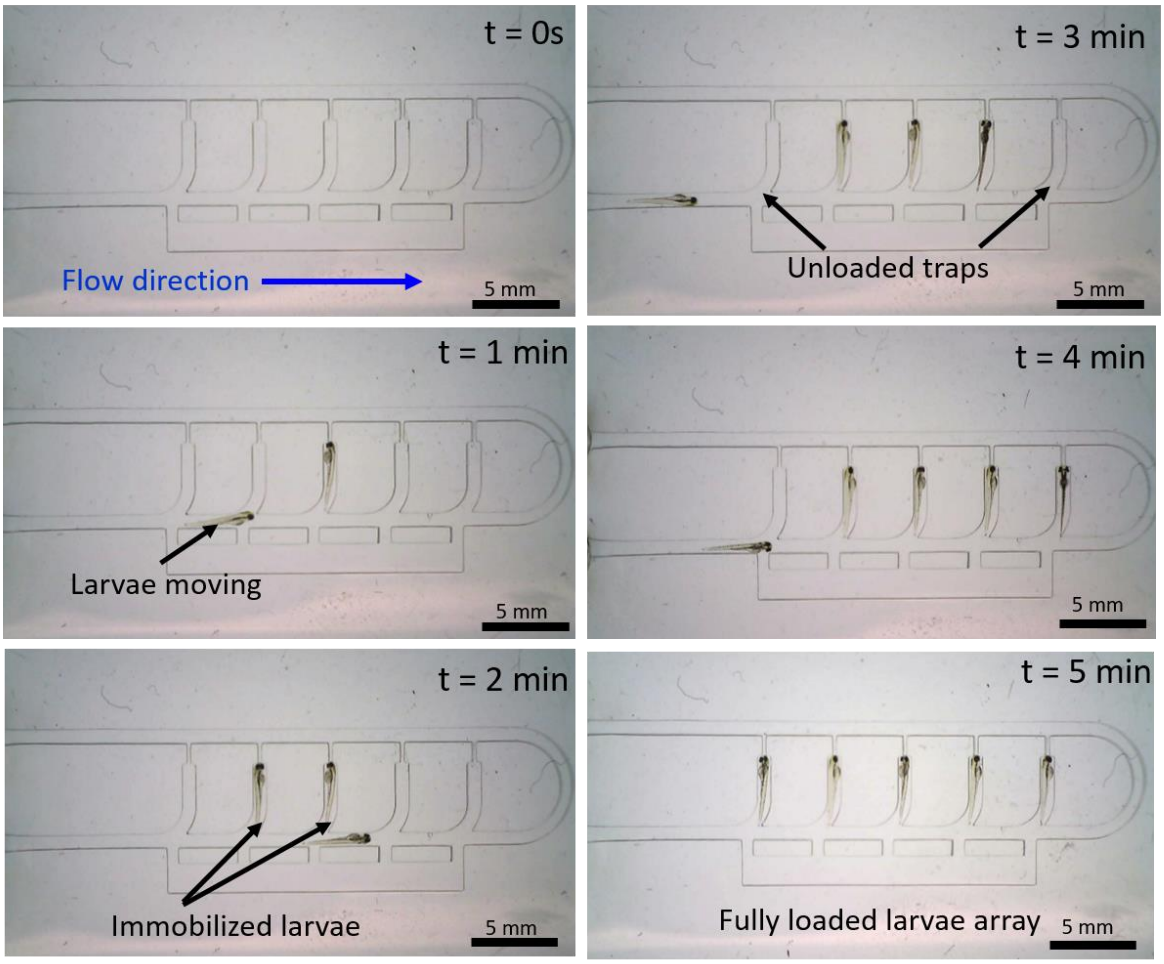

Figure 5.18 The complete loading of the larvae inside the traps took approximately five minutes depending on the larvae flow gap and flow rate selected. All 3 dpf larvae were anesthetised with 100 mg/L Tricaine before loading. Flow rate for trapping the larvae was 1500 mg/L.

5.6 Biocompatible chip-based physiometer

5.6.1 Influence of Tricaine (MS-222) on zebrafish heartbeat

Zebrafish larvae can be immobilised by applying anaesthetic drugs such as Tricaine that inhibit muscle contraction by suppressed the nerve membrane. This has an effect similar to other anaesthetic drugs [260]. A range of Tricaine concentrations from the low dose of 0.01 mg/ml to 0.8 mg/ml have been used as sedatives for zebrafish larvae [261, 262]. Tricaine suppresses contractions in smooth and cardiac muscles, and reduces the heart rate significantly at doses greater than 0.17 mg/ml [263]. The Tricaine concentrations selected were as low as possible: up to 0.20 mg/ml for cardiac analysis. In this work, the heart rate of the 3 dpf larvae were examined at selected doses of 0.02 mg/ml – 0.18 mg/ml Figure 5.19 A–B. A reduction in heart rate was found to be higher (15%–45%) than in the control group when the Tricaine concentration increased at time = 0 hr; but a substantial reduction was observed after 24 hours of exposure at a value of 44%–66% from the control.

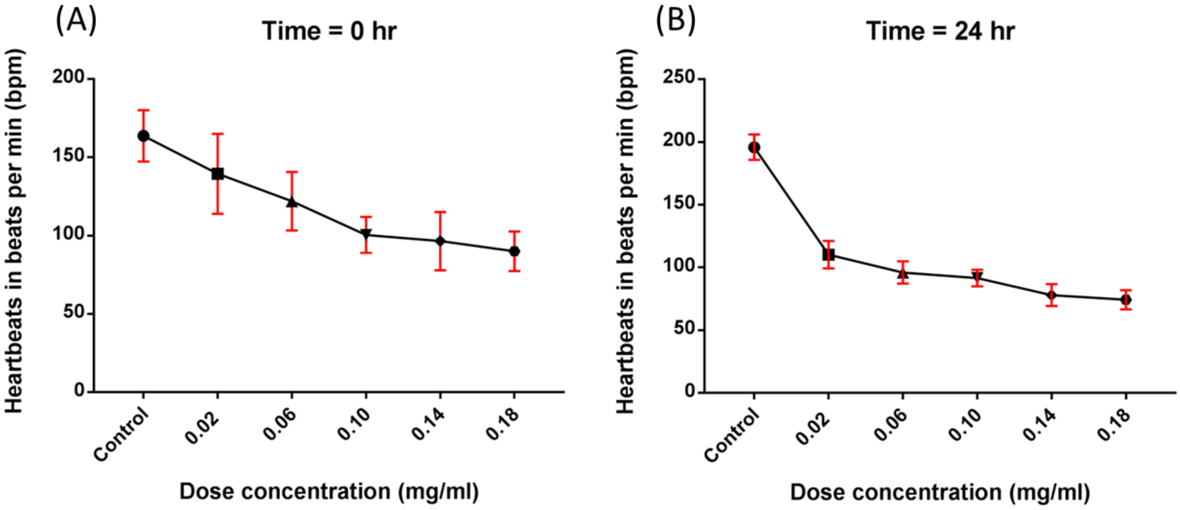

Figure 5.19 Dose concentration effect of Tricaine on 3 dpf zebrafish larvae at concentrations of 0.02–0.18 mg/ml: (A) at immediate time after being exposed with the Tricaine; (B) heartbeat of zebrafish larvae at time=24 hr. Results are represented as the mean ± standard deviation (SD), n=20.

Conventionally, mounting media such as agarose have been used for various microscopic imaging purposes as their refractive indexes are comparable with water [264]. The effect of the mounting medium on the zebrafish heartbeat was studied in 0.5–1.5% agarose. Heart rates of 3 dpf larvae were found to be significantly increased at 1.5% of agarosecompared with the larvae inside the petri dishes. This is due to a hypoxic response in the larvae, compared to those freely swimming [265]. Zebrafish suffer environmental stress when placed in higher concentrations of mounting media, as seen in Figure 5.20. The same effect was observed when the larvae were trapped inside the microfluidic chip in Figure 5.21, due to the release of stress hormones such as adrenaline in preparation for an escape response. [266]. This behavioural response in zebrafish does not lead to mortality and stress, so such microfluidic devices can be used as toxicity assays.

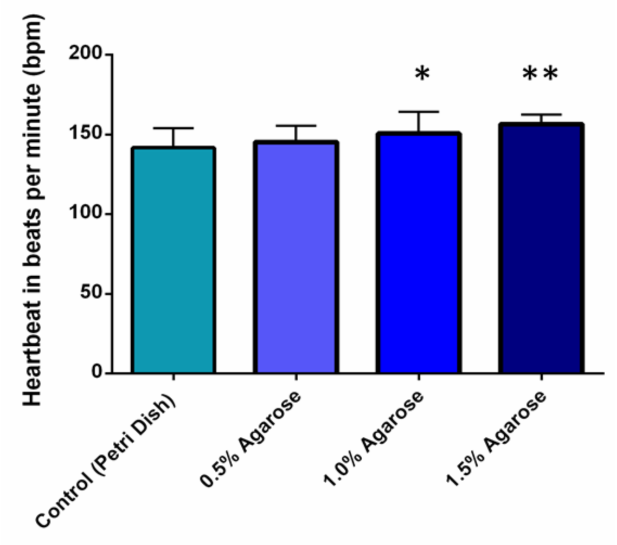

Figure 5.20. Agarose mounting (0.5–1.5%) effect on 3 dpf zebrafish heartbeat. The asterisks denote significant differences from the control group (*p<0.05 and **p<0.01). Results are represented as mean ± standard deviation (SD). (n=20, 3 replicates).

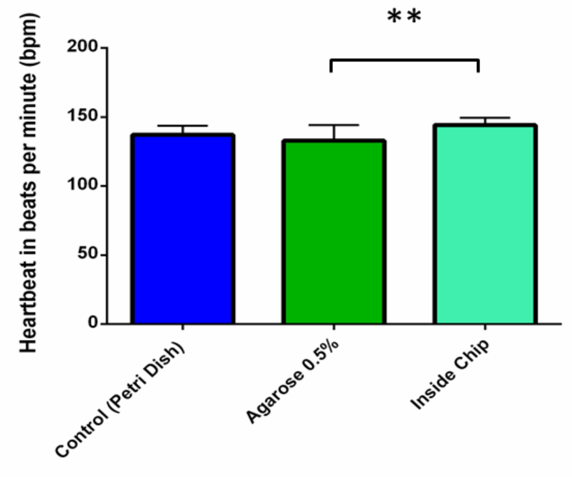

Figure 5.21. Effect on 3 dpf zebrafish heartbeat in different environmental conditions. The asterisks denote significant differences from the control group (*p<0.05 and **p<0.01). Results are represented as mean ± standard deviation (SD), n=20.

5.7 Effect of toxicity on zebrafish heartbeat

Acute toxicity biotests were performed using selected cardio-active compounds: caffeine, nicotine, verapamil hydrochloride and lead acetate. The compound toxicity profiles were evaluated using a standard bioassays protocol according to OECD guidelines for the testing of chemicals. In the toxicity tests, 3 dpf zebrafish larvae were used. A 10% lethal concentration (LC_{10}) was used; each lethality curve was determined and plotted using the probit analysis ToxRat software. According to the corresponding concentration–response curve illustrated in Figure 5.22, LC_{10} was 195 mg/L for caffeine, 162 mg/L for nicotine, 102.58 mg/L for verapamil hydrochloride and 32.88 mg/L for lead acetate. The same concentrations of LC_{10} were used as solvents for cardiovascular assessment (heartbeat measurement) of the larvae in the microfluidic arrays.

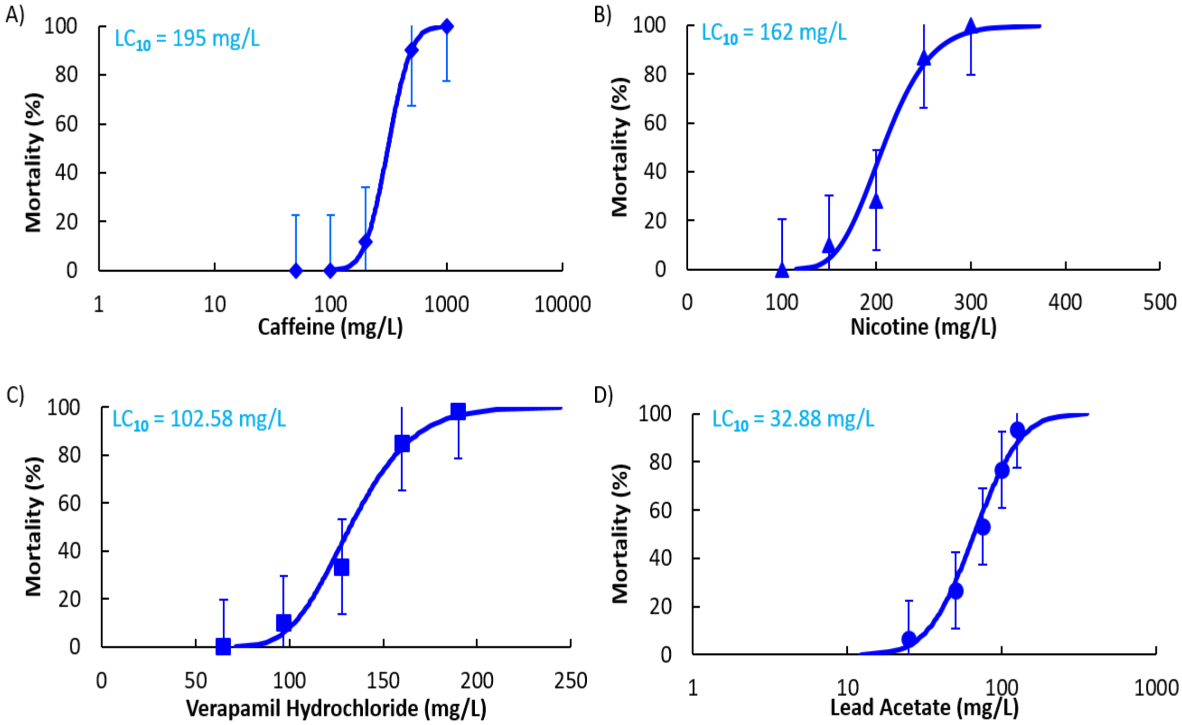

Figure 5.22 Dose-dependent mortality tests: selected toxicants' effects on 3 dpf zebrafish larvae. The curves represent the response for each of the selected cardio-active compunds. The values of LC_{10} were calculated by probit analysis using ToxRat software. Experiments were carried out in triplicate; in each n=20 larvae were pooled for calculation of the concentration. Lead acetate was found to be toxic at low concentrations compared to the others.

5.8 Drugs treatment modulates heartbeat using microfluidic device

5.8.1 Short-term infusion of drugs

This study validated the applicability of the newly designed PDMS chip-based devices for real-time monitoring of heart rate variations in zebrafish larvae. It also investigated the effects of sublethal concentrations of various compounds (LC_{10}) on the heart rate of zebrafish. For this purpose, the anesthetised 3 dpf larvae were loaded into the devices and perfused with LC_{10} of caffeine, nicotine, verapamil hydrochloride and lead acetate (Figure 5.23). The selected compound did not affect the zebrafish heart development. Monitoring of the heart rate variations was performed via non-invasive video microscopy.

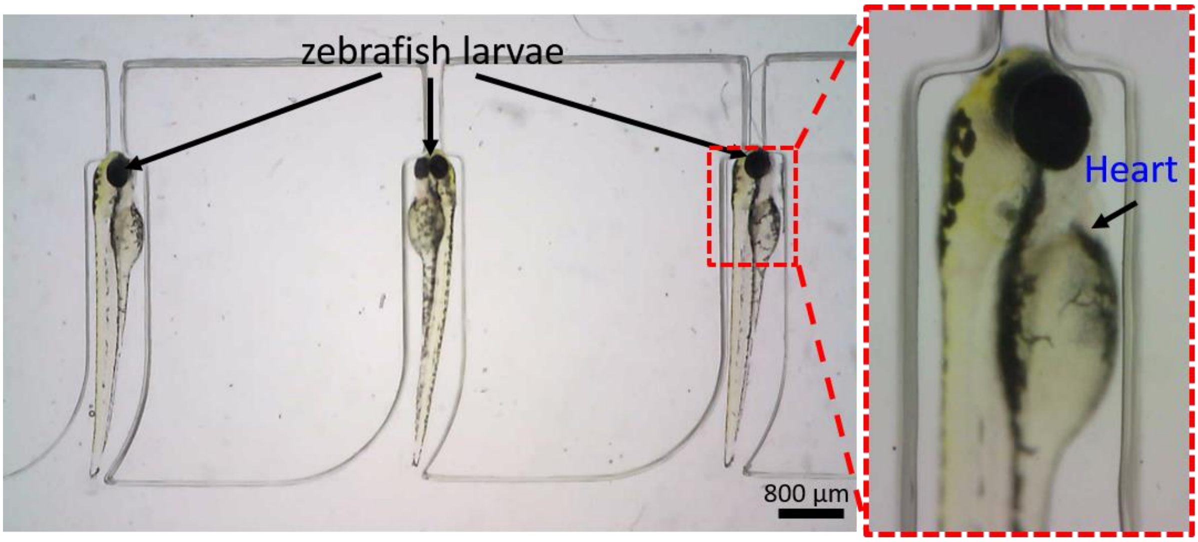

Figure 5.23 Zebrafish larvae (3 dpf) immobilised on the microfluidic device. Heart rates were recorded for one minute with USB microscope (Dino-Lite) at 60 frames per second. The videoed records of cardiac activity were analysed using DanioScope software. The heart area was selected for analysis.

Caffeine is a widely consumed stimulant of the central nervous system (CNS). A high intake of caffeinated drinks increases the risk of cardiovascular disease [267]. It was observed that the heart rate increased significantly to over 150 beats per min (bpm) when larvae were exposed to 195 mg/L of caffeine (Figure 5.24 A). This was due to its antagonistic effect on adenosine receptors, that increased the muscle contraction of the heart. The same trend has been observed in previous reports showing that caffeine has strong effects on the cardiovascular system and blood vessels [268, 269].

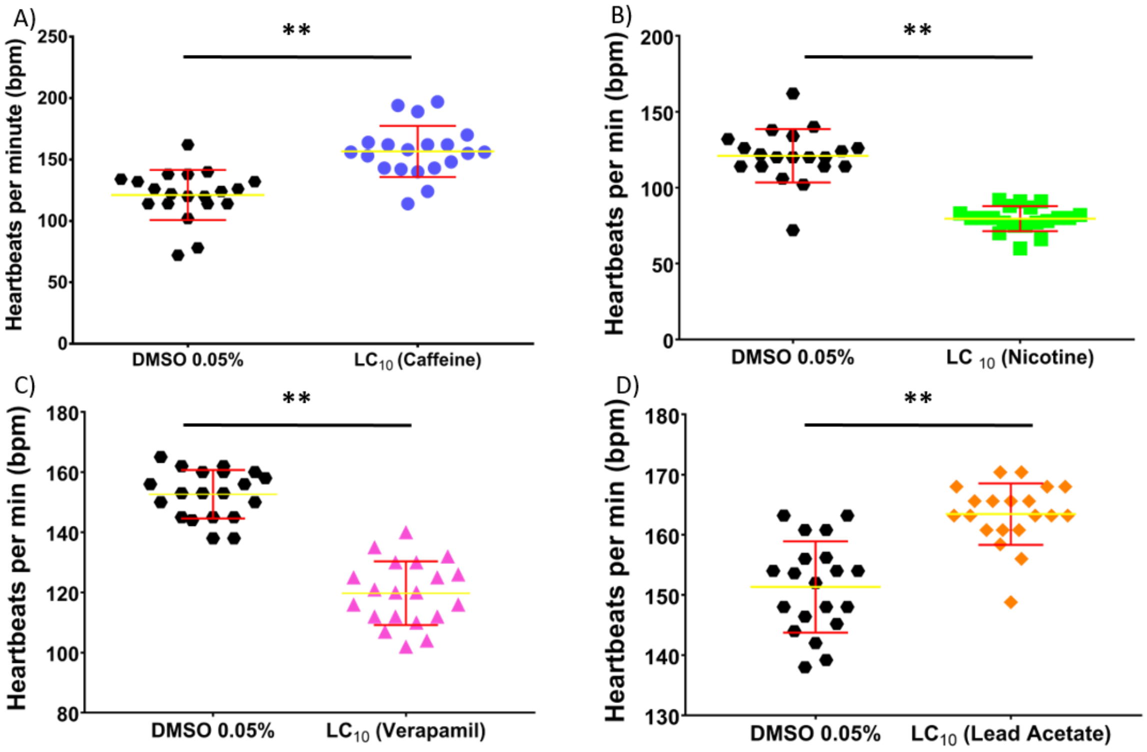

Figure 5.24 Detection of heart rate difference in 3 dpf zebrafish larvae after ten minutes perfused with drugs that decrease and increase heart rate. Cardiac rate increased after the administration of caffeine (A) and lead acetate (D). In contrast, nicotine (B) and verapamil hydrochloride (C) induced a decrease in heartbeat. Each treatment was compared with a vehicle control 0.05% of dimethyl sulphoxide (DMSO). All values represent the mean ±SD (**p<0.01)(n=20).

Nicotine, one of the alkaloids found in tobacco, is highly addictive. Tobacco is mainly used in cigarettes; it induces many diseases that affect the heart and liver as well as causing cancers [270]. Previous reports have shown that all components inside cigarette smoke, including nicotine, can infuse into the human placenta and influence foetal development [271]. In this study, sublethal concentrations of LC_{10} were infused into the microfluidic system. They were followed by a significant reduction of 34% in the embryos' heartbeat compared with the control group, as shown in Figure 5.24 B. This reduced heart rate indicates that nicotine is a possible cause of cardiac failure [272, 273].

Verapamil is a antihypertensive drug that acts as a calcium channel blocker and is used in the treatment of hypertension, supraventricular arrhythmias and angina pectoris [274]. Short-term exposure to verapamil in these tests showed a decrease in cardiac contractions of 20% compared to the control (Figure 5.24C). This result is consistent with earlier reports that have shown that verapamil causes bradycardia and atrial ventricle block in zebrafish [244]. The calcium blocker agent reduced myocardial contractility, heart rate and impulse conduction of the heart; it helped to calm the blood vessels and thereby reduced the workload on the heart [275].

Lead (Pb) has the potential to affect human health. It induces a broad range of dysfunctionalities, biochemical, physiological, and neurological, in humans [276]. In this test, the zebrafish experienced the same effect after being exposed to lead acetate concentration of 32.88 mg/L as shown in Figure 5.24 D. The heart contractions were found to be statistically significantly higher, by 7%, than the control treatment. This indicates an adaptive response by the zebrafish larvae to exposure to heavy metal concentrations [277].

5.8.2 Short term infusion–elimination–reinfusion of drugs

Next, the capability of the microfluidic chip for determining heart contractions per period was tested. An advantage of working with immobilised zebrafish larvae in the device is that the effect on the heartbeat of administering and withdrawing drugs can be analysed. Another advantage is that the observation of the positioned larvae can be done as a single process without the need of additional preparation to change the test concentration. This approach is more convenient and permits a high throughput.

The results indicate that the heart rate increased significantly after seven minutes of caffeine treatment at a concentration of 195 mg/L, steadily reaching ten minutes of infusion at 170 bpm (Figure 5.25 A). During the elimination period, it was observed that the heartbeat slowly recovered to almost 149 bpm, close to the initial rate, before infusion took place. The same trend occurred on re-infusion of the caffeine after ten minutes.

The overall effect of continuous nicotine administration decreases the heartbeat. The beats significantly decreased after six minutes from 152 bpm to 97 bpm, until the end of ten minutes of infusion. The heart beat then rose sharply during the elimination period, to between 11 and 13 minutes, and gradually reduced to 147 bpm. It was observed during re-infusion that the heartbeat reading was more stable than at the initial administration of nicotine. This shows that the response of nicotine is more effective than during 10 minutes initial infusion.

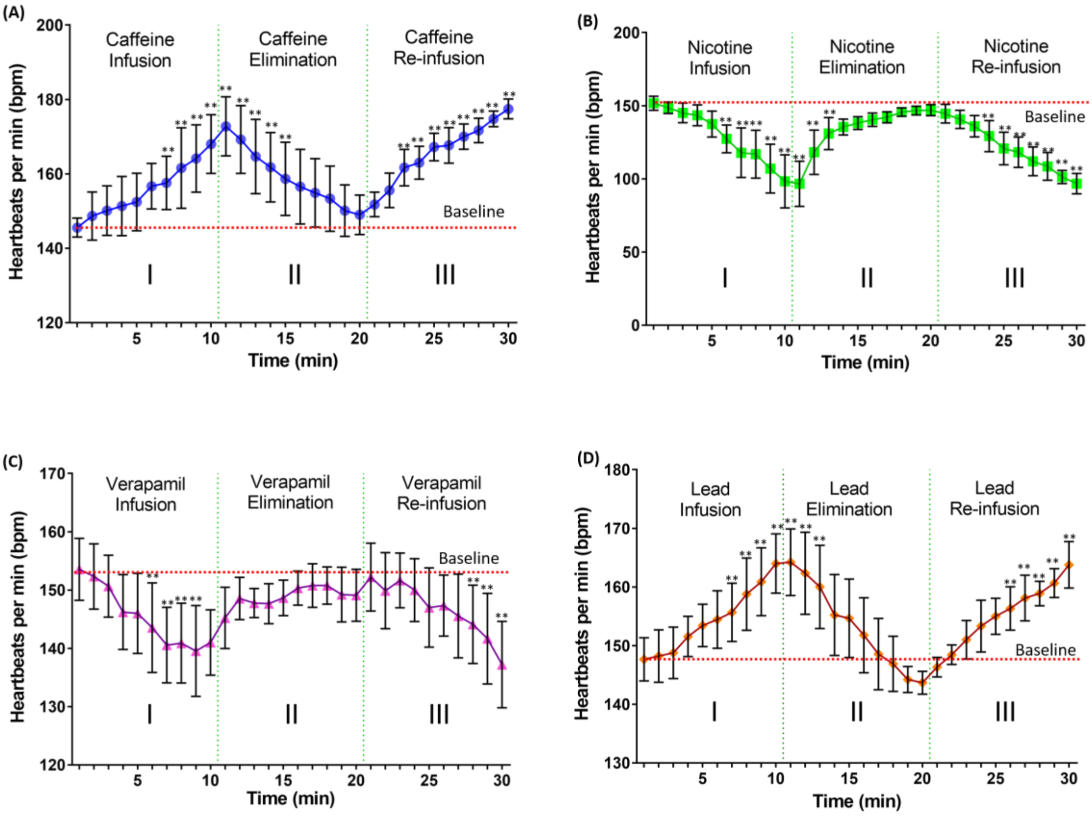

Figure 5.25 Effect of cardioactive compound infusion on heart rate of 3 dpf zebrafish in the microfluidic chip. Fluctuations in bpm are measured as a function of time (minutes) during the infusion. Flow in the microfluidic was 1000 µl/min. Phase I – LC_{10} value for each compound was introduced into the microfluidic chip for ten minutes. Phase II – Infusion of Tricaine solution of 100 mg/L for recovery and to remove the compound solution for ten minutes. Phase III – Re-introduced of the compound solution. Each heartbeat was compared to the baseline. Error bars represent standard deviations and n = 9 for each line. Data is presented by means of ± SD (**P<0.05).

The effect of verapamil on the heart rate of zebrafish larvae can be seen in the infusion period, where a significantly reduced heart beat of 154 to 140 bpm and steady contractions were observed during the ten minutes of drug withdrawal. After this the heart rate gradually reached the initial baseline at recovery period. It was observed that in the reinfusion timeline, the effect of the drugs was slow compared with that of the initial administration. This is due to the effect of drug tolerance following re-infusion.

In contrast, exposure to heavy metal, in this case lead acetate, produced a steadily higher heart rate within ten minutes of perfusion. In the elimination period, the heart experienced a rapid recovery to below the baseline contractions at 144 bpm. The repeated intake of lead acetate was found to produce a more steady heartbeat compared than in the first administration.

5.9 Summary and conclusions

5.9.1 Design of the chip

The use of additive manufacturing technologies for fabricating moulds with high aspect ratios of width to height (1:1-3) was explored. We successfully applied millifluidic technologies fabricated using SLA technology in a proof-of-concept manipulation of cardiac function in zebrafish larvae. A biocompatible chip-based physiometer for cardiac analysis, capable of trapping and immobilising zebrafish larvae, was also demonstrated. With this, heart rate variation in zebrafish larvae could be determined for cardiotoxicity studies. This is a novel method of monitoring the heartbeat of immobilised zebrafish larvae that can be applied to cardiotoxicity analysis in drug discovery.

The newly developed microfluidic device is a new platform for cardiotoxicity assessment. The system is low cost, simple, non-invasive and operator independent. It allows more convenient heartbeat monitoring without the need of trained operators. Moreover, it only requires a single operation, with no need for additional procedures as in conventional methods of agarose mounting, in which zebrafish are transferred for new analysis.

5.9.2 Effect of all drugs

Compounds of selected drugs induced cardiovascular toxicity in zebrafish larvae. Caffeine and lead acetate showed heart rate-stimulating effects which increased the heart beat from the baseline by 16% and 9% respectively. In contrast, nicotine and verapamil stimulated an antagonist reaction to the heartbeat (Figure 5.26). All the drugs were observed have an effect on the heartbeat, although the concentration of Tricaine used did not affect heartbeat during infusion or elimination of the drug. By using the flow-through system for drug infusion, the consequences of taking drugs continuously can be seen.

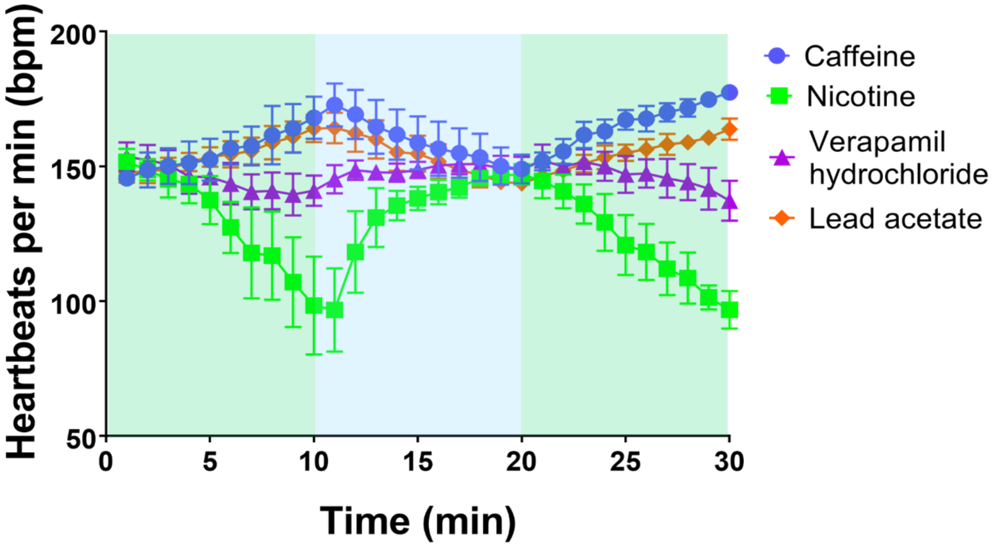

Figure 5.26 The illustration of the heart rate response of 3 dpf in zebrafish larvae to cardioactive drugs. Overall, the caffeine exposure showed higher contractions of heartbeats compare to lead acetate. On the other hand, infusion of nicotine showed reduction increase heart rates than verapamil hydrochloride. Blue areas represent exposure of drugs of ten minutes duration (0-10 min) and re-exposure of drugs of ten minutes duration (20-30 min). Green area depicts the withdrawal and elimination of drugs (10-20 min). Note the baseline heart rates are comparable for all drugs tested.

5.9.3 Limitations

A possible limit of this method is the linear placement of larvae inside the device. The design placing the larvae have the effect of the larvae does not have the same amount of drug intakes. The variation in heartbeat could be reduced when every minute reading takes place. A linear array for trapping zebrafish larvae is not the most effective way to determine precise heartbeat readings.

6 Millifluidics for Dechorionated Zebrafish Embryos

6.1 Introduction

Zebrafish embryos are surrounded by chorion, a thin membrane of around 1.5–2.5 µm thickness, to protect the unhatched embryo at early development from 2 hpf (cleavage period: approximately 64 cell stage) to 24 hpf (pharyngula period: Prim-5 stage). The chorion potentially presents a barrier and protects its embryo from penetration by chemical substances. As reduced vulnerability to the compound chemicals affects the results in acute toxicity studies, dechorionation (chorion removal) is used to investigate the sensitivity of chemical toxicities.

In this chapter, we present a novel technology of lab-on-chip for automated embryo toxicity testing used in ecotoxicology and drug discovery applications. The biocompatible miniaturised LOC consists of arrays for loading, trapping and immobilising a single dechorionated embryo in a flow-through perfusion environment. The microfluidic chip-based device was fabricated using soft lithography, as described in Chapter 3. The PDMS-VisiClear chip-based device has optical-grade transparency, suitable for imaging the development of the dechorionated embryos. This system enables a continuous perfusion system of medium or toxicant exchange during embryo development.

To validate the designed microfluidic system, dynamic computer simulations of the fluid flow were analysed and verified with experimental analysis. This proof-of-concept chip is a new platform for studies of morphology and of microfluidic toxicity testing (µFET) of dechorionated embryos. With this, we developed a novel and inexpensive technology in handling dechorionated embryos which offers great advantages in toxicity studies.

6.2 Chip design and fabrication

The proof-of-concept PDMS microfluidic chip consists of three main features: (i) the main channel for embryo loading and transport (inlet and outlet microchannels); (ii) the trap for embryo docking and immobilisation; and (iii) suction channels that facilitate the hydrodynamic trapping of the embryos (Figure 6.1). All traps (T1–T20) were interconnected with the main embryo loading channel. Deflector channels (D1–D5) are positioned in each row of the linear array traps.

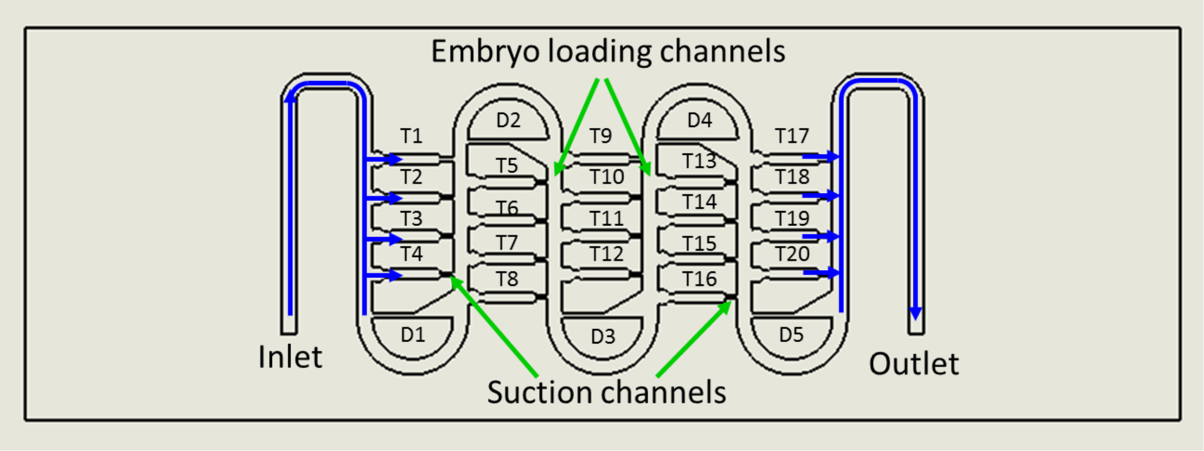

Figure 6.1. The design of the negative relief mould for trapping dechorionated embryos. A total of 20 embryo traps and each of the traps interconnected with cross-flow suction channels. Blue arrow represents the direction of fluid flow from inlet to outlet channel. ‘T’ indicates the number of consecutive traps and ‘D’ indicates the number of deflector channels.

The CAD design for the mould as shown in Figure 6.2 enabled automated docking and immobilisation of 20 living 24 hpf dechorionated zebrafish embryos. The microfluidic device featured three integrated modules: (i) the curvilinear serpentine-shaped main channel with microchannels (width = 1.0 mm, height 0.7 mm) for embryo loading and medium perfusion as shown in Figure 6.2 A–B; (ii) a total of 20 embryo traps consisting of four individual traps at a distance of 1.52 mm (y-direction) in five rows with a hydrodynamic deflector to facilitate embryos towards other traps (Figure 6.2 C–D); and (iii) an array of suction channels (width = 0.2 mm, length = 0.87 mm , height = 0.7 mm) that connected the embryo traps with the main loading channel (Figure 6.2 E–F). The integrated modules of microchannels and traps allowed only single embryo docking through the well-shaped entrance, and smooth sliding towards the trap. The microfluidic design of the traps employed a passive hydrodynamic flow to dock and immobilise zebrafish embryos as described in Chapter 5 (5.4) [27]. This feature avoided specimen damage and allowed development of the embryo inside the chip.

The overall internal volume of the device was approximately 288.7 µl and the volume of a single trap was 2.31 µl. The PDMS chip-based devices (illustrated in Figure 6.3) were fabricated using a combination of 3D-printed VisiClear negative relief mould and soft lithography, as described in Chapters 3 (3.9) and 5 (5.2). The negative relief mould was fabricated with a top surface roughness of R_a= 11 µm. A biocompatible and optically transparent PDMS, similar in size to a standard microscope slide, was fabricated. Holes were punched vertically at the inlet and outlet ports to connect PTFE tubing to the microchannels for fluidic sample interfacing: for instance, a closed perfusion loop used a peristaltic pump linked to the tubing to provide a constant flow rate of 1000 µL/min for drug delivery.

This proof-of-concept design has the advantage of being a one-step automatic hydrodynamic loading system for dechorionated zebrafish embryos. The design allows embryo docking and long-term immobilisation inside the traps. Significantly, the geometrical design of the traps assures only one embryo occupies a trap at a time, without obstructing other embryos' passage towards the channels. The deflectors (D1–D4), on the other hand, were designed to enhance trapping efficiency by changing the trajectory of the embryos and pushing them towards the traps.

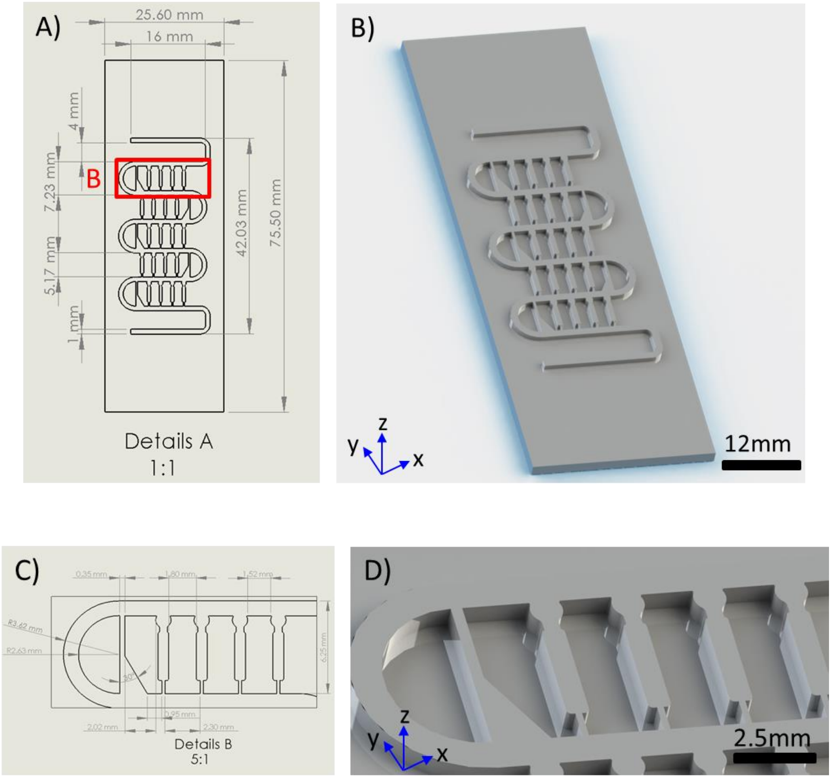

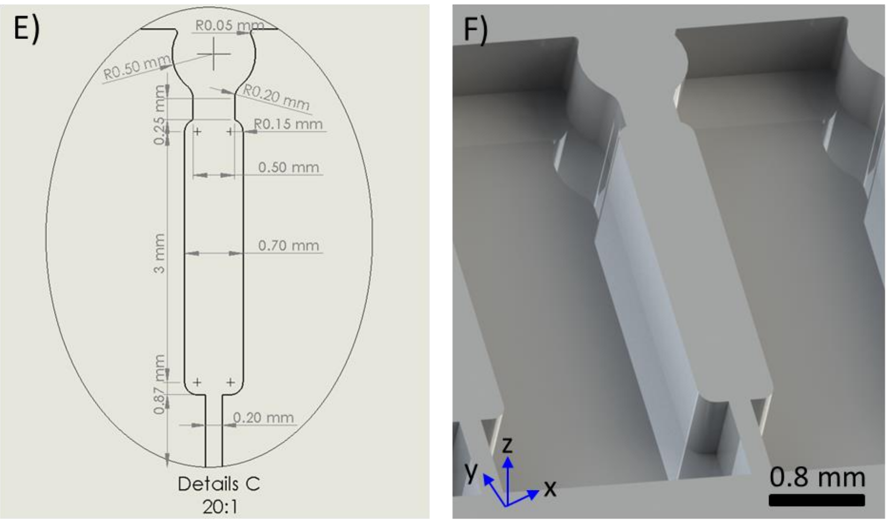

Figure 6.2. Detailed CAD design of the negative relief PDMS–VisiClear mould of the microfluidic device for automatic trapping and immobilisation of 24 hpf dechorionated zebrafish embryos. (A–B): Detailed design showing the dimension of the overall mould, the size of a glass microscope slide. (C–D): Each row consists of four traps and a single deflector channel. (E–F): The drawing shows a single trap connected to a small suction channel.

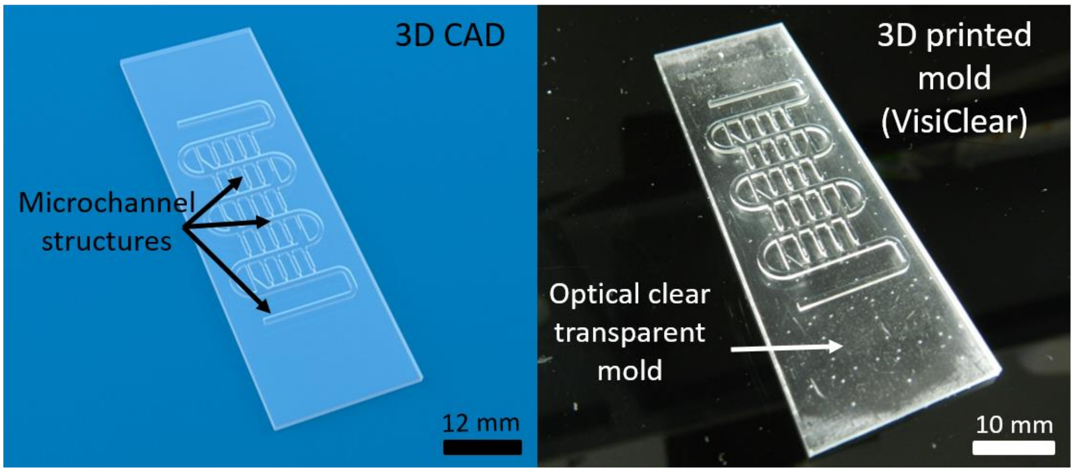

Figure 6.3. The 3D photorealistic rendering of mould and PDMS chip-based microfluidic device. A high-resolution (125 µm) printed mould was fabricated from optical-grade polymer materials. The peeled-off PDMS structure was thermally bonded to a glass slide with inlet and outlet connection ports (Ø = 3.0 mm) for PTFE tubing of internal diameter ID= 1.3 mm.

6.3 Hydrodynamic trapping of dechorionated embryos

6.3.1 Computer fluid simulation

The proof-of-concept design of the microfluidic device enabled the passive hydrodynamic trapping of a single dechorionated embryo. Computational Fluidics Dynamics (CFD) simulations were initially performed (COMSOL Multiphysics v4.4) to predict flow velocity, pressure drop and uniformity of mass transfer inside the microfluidic device. The simulation of velocity profile presented in Figure 6.4 indicates that at a perfusion rate of 1000 µl/min, velocities inside the chip varied from 0.005 m/s to 0.013 m/s, at input and output respectively. There was a constant velocity of 0.011m/s in all the traps. A fluid velocity of 0.033 m/s in the suction channels immobilised the dechorionated zebrafish embryos for up to 72 hours.

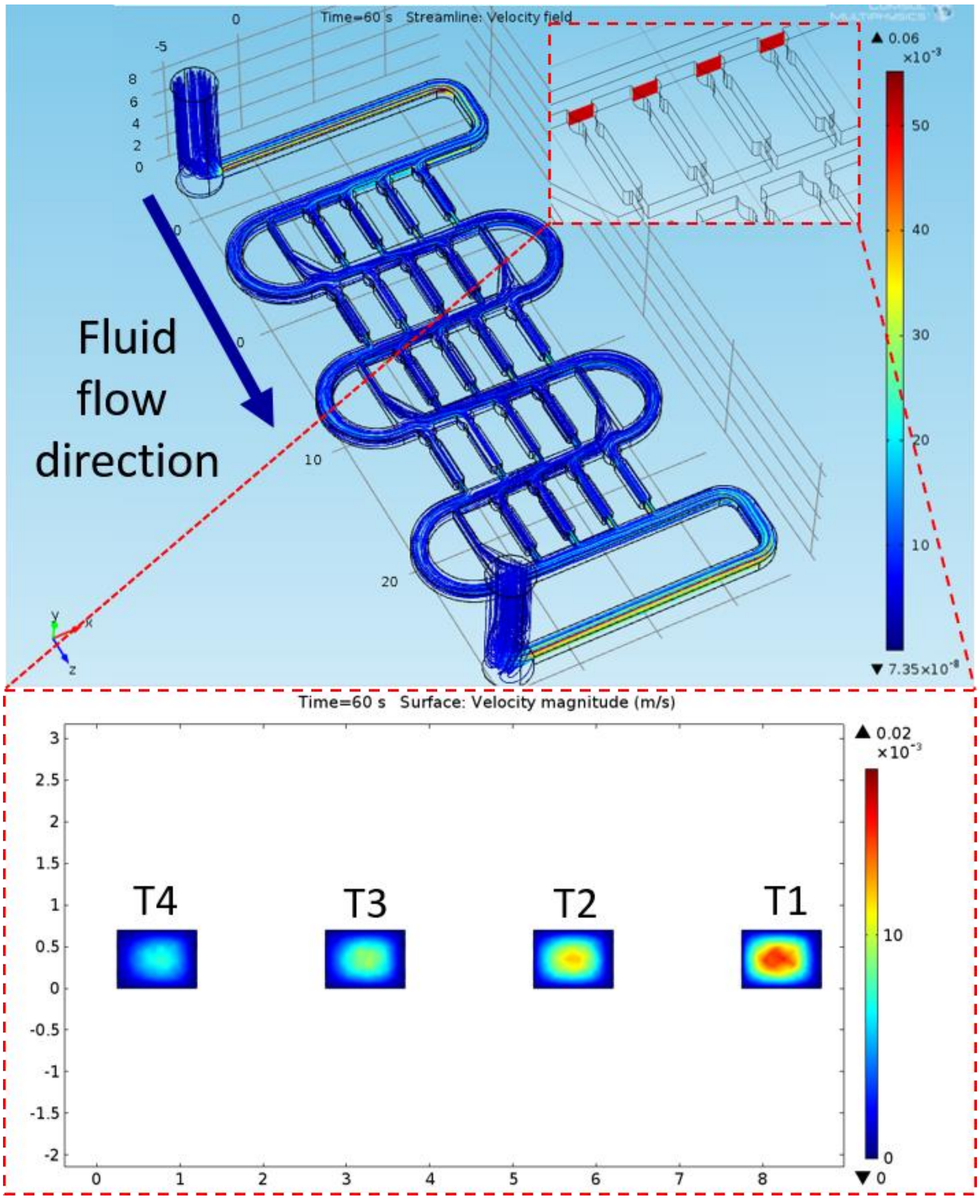

Figure 6.4 A computer fluid dynamic simulation of 3D velocity streamlines (m/s) across the microfluidic device. Overall perfusion was simulated at the perfusion rate of 1000 µL/min. The flow passes from the entrance of each trap through the suction channels and exit through the outlet channel. Inset image denotes vertical cross section at the entrance of the trap. This allows for embryo immobilisation and efficiency of medium and drug exchange. Note that the axis is the coordinate location on the simulation gridlines.

The flow velocity was highest across first trap of each row. This was due to the increased flow from the designed deflectors (D1–D4) at each of the rows, designed to increase the trapping efficiency and push the embryos into the traps; the velocity of moving embryos was (>> 1.5–2.0) higher than the turning channels of the main loading channel (Figure 6.5).

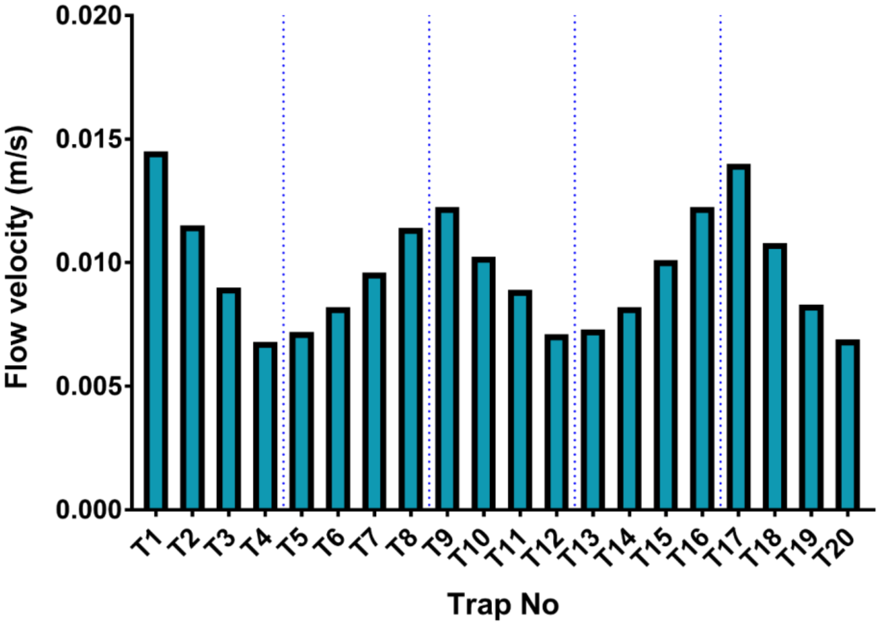

Figure 6.5 Analysis of the flow velocity (m/s) when the microfluidic device is perfused at 1000 µL/min. 3D computer simulation of the flow velocity across each of the traps. A higher velocity at the first trap in each row enhanced trapping efficiency. This is a function of the serpentine design of the device.

A uniform and efficient delivery of drugs into immobilised embryos is important for long-term microperfusion studies in ecotoxicology and for drug discovery. The design of each trap permitted the toxicants/drugs to flow around the embryos. Computation of mass flow resulted in the distribution of the drugs inside the microfluidic device at a given perfusion rate. These mass transfer simulations were validated experimentally using a 0.04% Trypan blue dye (Life Technologies Corp, CA, USA) to visually demonstrate the flow of fluid inside the entire microfluidic chip (Figure 6.6).

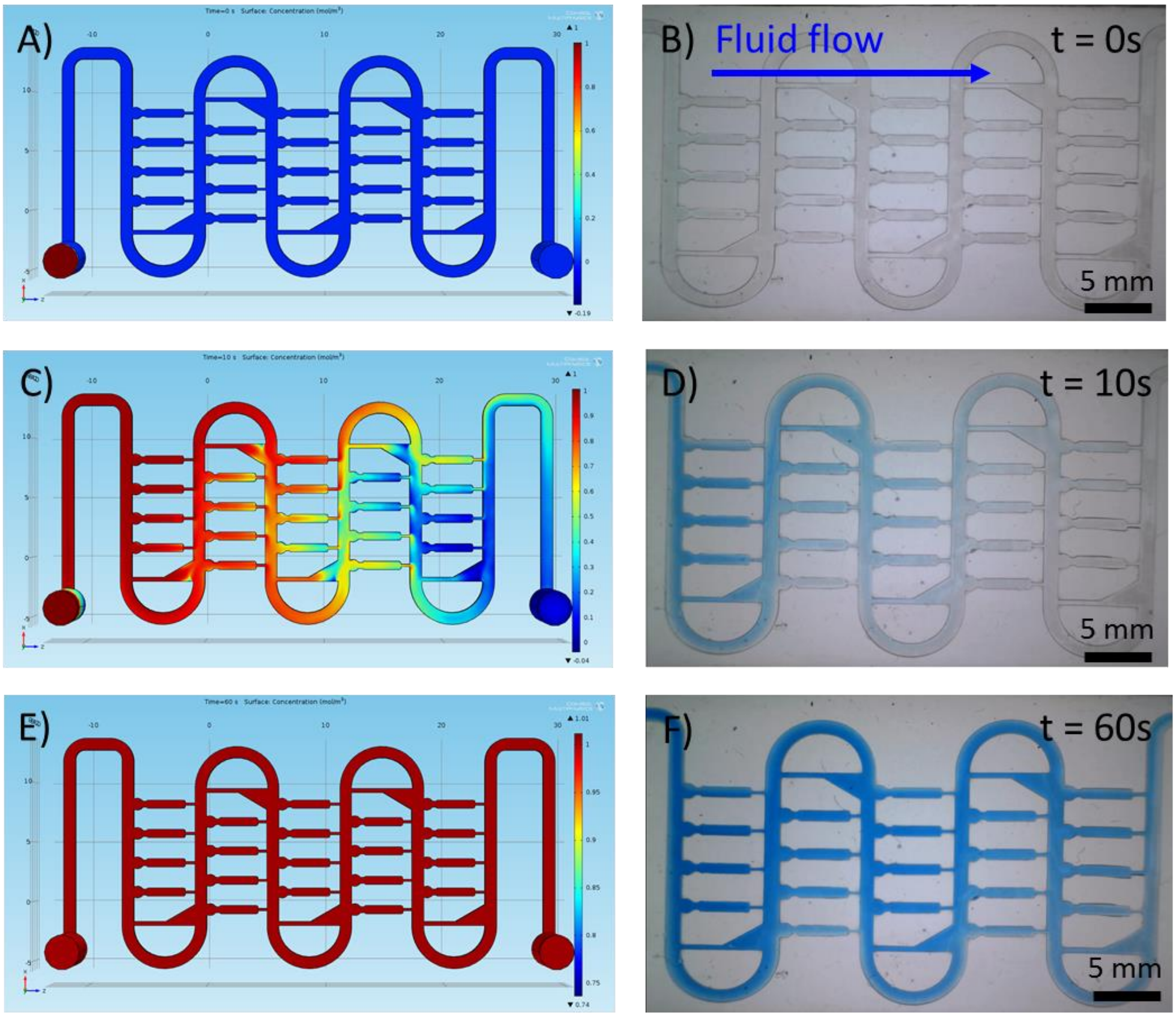

Figure 6.6 Computer fluid simulation and validation of mass transfer in the microfluidic chip. The chip was perfused with 0.04% of Trypan blue solution at volumetric flow rate of 1000 µl/min. The fluid flow images were taken at 0, 10 and 60 seconds of perfusion. The traps achieved 98% of full medium exchange with the Trypan blue solution after 60 seconds. Note the flow pattern match between simulation and experiment.

6.3.2 Trapping concept

The zebrafish embryos were mechanically dechorionated, giving higher survival rates of ≥90% than the enzyme-supported treatment using Pronase [256]. Conceptually, the 24 hpf dechorionated zebrafish embryos were introduced into the device by drag force from the fluid pressure inside the microchannel (Figure 6.7 A–B). The design enabled the trapping and immobilisation of an individual embryo using hydrodynamic forces. The embryos trapped in the microchannels reduced the flow towards the trap, increased the mainstream flow to empty channels. The next embryo in line passed by the occupied trapping channel and went in the next empty trap (Figure 6.7 C–D). After all the embryos were trapped, they remained immobilised under a perfusion rate of 1000 µl/min throughout the system. The trapping of living dechorionated embryos is demonstrated experimentally in Figure 6.8. It is observed that embryo trapping did not occur in sequence because of the nature of the moving embryos, twitching while entering the trap. However, the low flow pressure inside occupied traps enabled other embryos to enter empty traps until all were fully loaded.

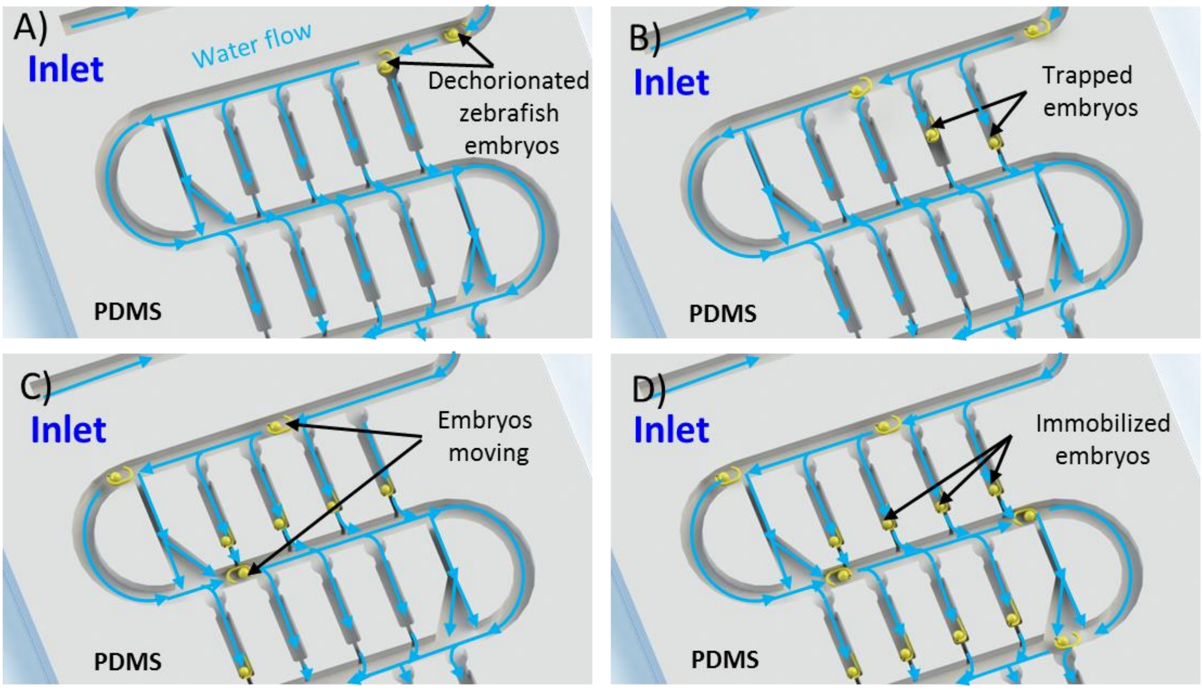

Figure 6.7 Embryo trapping and immobilisation principles. (A) Dechorionated embryos loaded from reservoir and directed into the main channel. The hydrodynamic flow guided the embryo to enter the trap. (B) The next embryo is moved into the next available trap. (C) The process is repeated until all traps are filled. (D) The hydrodynamic force securely retains and immobilises dechorionated embryos inside each trap.

To validate the trapping performance of the microfluidic device, a computer-controlled stepper motor-driven peristaltic pump is connected to it. Introduced dechorionated embryos rolled freely along the main loading channel towards the available traps. This process was repeated until all traps were occupied by an embryo (Figure 6.8). Trapping efficiency was also investigated to determine the optimum fluid flow to achieve the maximum possible number of trapped embryos. Flow rates from 1500 to 2500 µl/min were tested, and it was found that a flow lower than 1000 µl/min, provided insufficient hydrodynamic force to move the embryos through the channels due to their mass (sedimentation (gravitational force) >> hydrodynamic force). If the fluid flow was too high, the embryos missed the traps and were flushed towards the exit channel, so that the numbers of trapped embryos decreased as the flow inside the microfluidic channels rose (Figure 6.9). At a flow rate of 1500 uL/min, more than 98% of introduced embryos were trapped in the microchannels. Finally, an optimal flow rate of 1500 µl/min achieved 100% efficiency, calculated by using this formula:

$$\%\,Trapping\ efficiency = \frac{Numbers\ of\ trapped\ embryos}{Total\ number\ of\ embryos\ introduced} \times 100\%$$

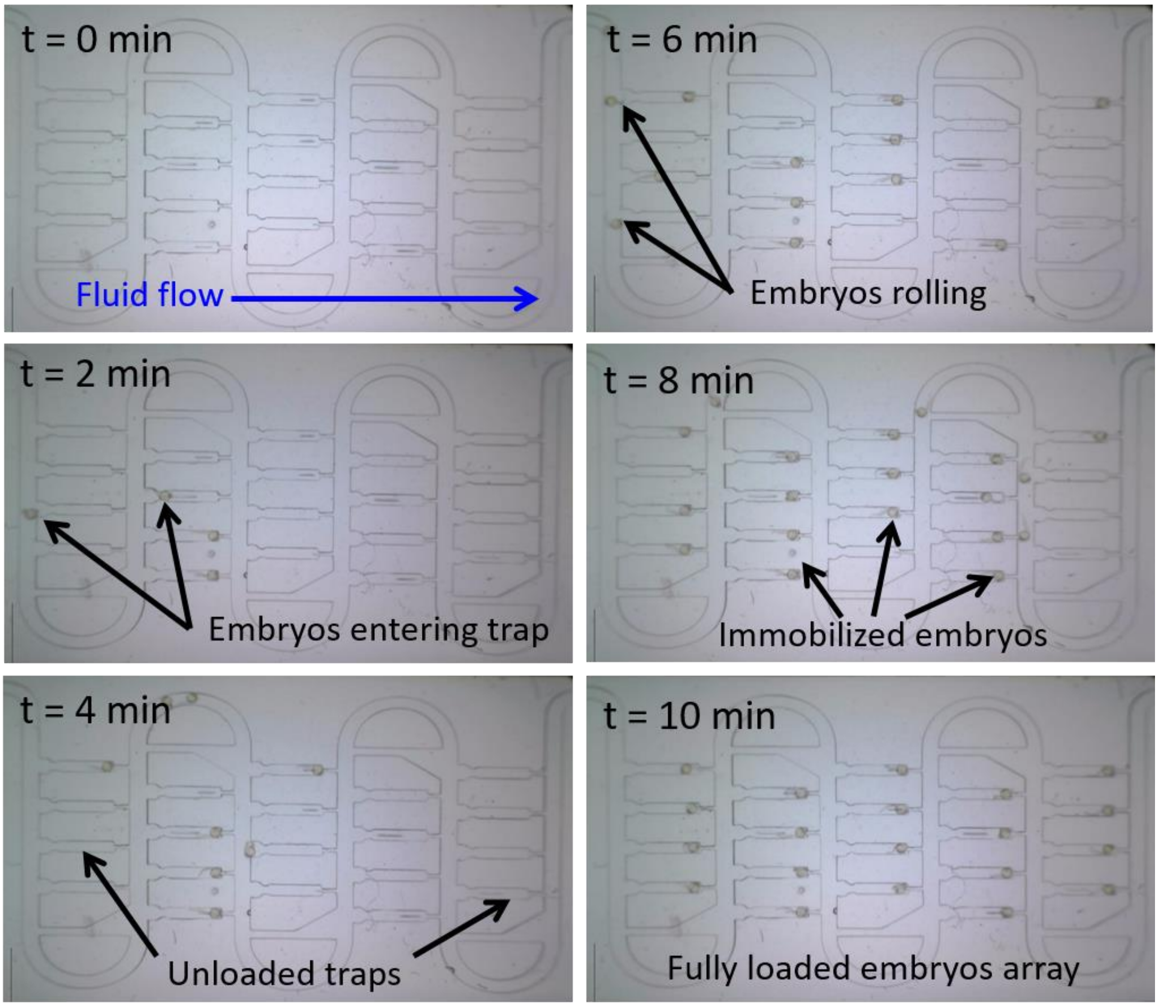

Figure 6.8 Trapping experiments with 24 hpf dechorionated embryos. The full loading of the embryos docking inside the microfluidic chip took approximately ten minutes, depending on the flow rate and aspiration flow gap between embryos.

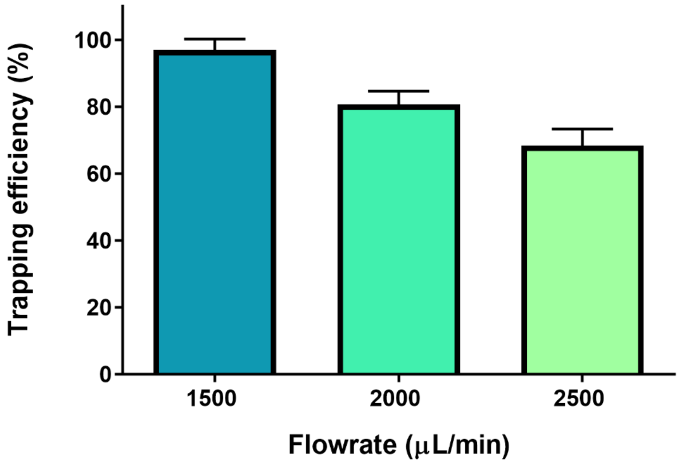

Figure 6.9 Embryo trapping efficiency at different perfusion rates. Full loaded embryos with 100% trapping efficiency can be achieved at flow rates of 1500 µL/min. High flow rates reduced the trapping efficiency due to the inability of the suction channels to overcome the velocity and momentum of the embryos moving past.

Water pressure and shear stress exerted on the embryos are difficult to measure in an on-chip microenvironment, so experiments were conducted to perform a long-term culture of the embryos in microperfusion condition from 24 until 96 hpf. All the trapped embryos went through the usual developmental stages during perfusion, including tail detachment (24 hpf), pigmentation (48 hpf), protruding mouth (72 hpf) and development of the swim bladder (96 hpf) (Figure 6.10).

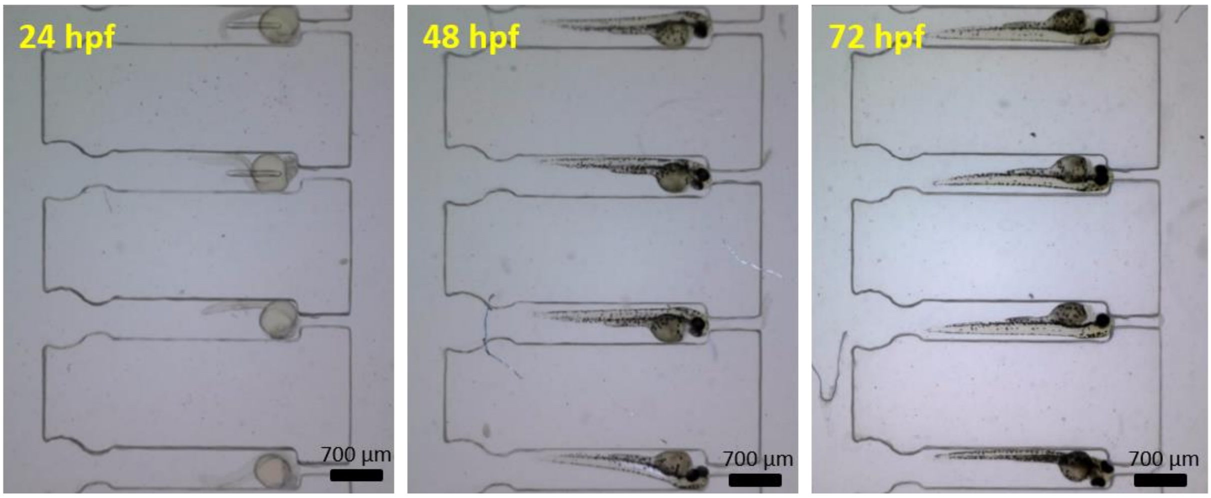

Figure 6.10 Time lapse images of the development of zebrafish embryos during the experiment. Embryos were loaded at 1500 µL/min of flow rate, followed by a constant perfusion rate of 1000 µL/min for on-chip culture for up to 72 hours. The embryos were in dark condition for the duration of experiment.

Uniform development was observed across all the immobilised embryos. In addition, a survival test conducted at 24, 48 and 72 hours returned results comparable with those from a the static environment (Figure 6.11). Most of the trapped embryos survived in the continuous perfusion flow rate of 1000 µl/min applied inside the microfluidic chip.

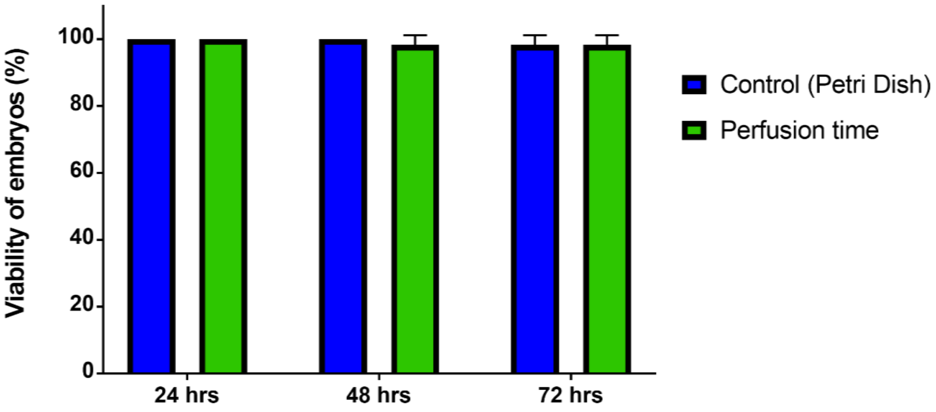

Figure 6.11 Survival rates of zebrafish embryos in a perfused flow rate of 1000 µL/min for 72 hours period. Embryo viability in microperfusion environments was similar to those in static condition using Petri dishes.

The design of the microfluidic chip with one embryo for one trap is intended to address problems associated with the standard protocols using Petri dishes. Its advantages are that it significantly simplifies drug/toxicant treatment without displacing the embryos. The microfluidic environment, such as the fluid flow, is controllable under continuous perfusion. The embryos are isolated and avoid embryo-to-embryo interaction. In addition, image acquisition is improved. enhancing data analysis. None of these features can be replicated in the standard protocol.

The capability of performing environmental toxicology without having to displace each embryo is important as it increases output performance. Although static protocol using conventional Petri dishes is the cheapest way to assess toxicity, it is insufficient for testing more toxicant compounds. This is due to the high compound adsorption, lack of supplied oxygen, uncontrollable changes in medium and degradation of the test compound. These conditions limit the efficiency of the static exposure of the standard fish embryo toxicity test (FET) [218]. Lammer et al. have suggested that the dynamic acute in a flow-through system should be the preferred option for environmental toxicity analysis. With continuous perfusion of the toxicants, chemical analysis of the medium can be carried out because of the known volume used for the test compared with standard FET analysis. This improves the quality assurance and the reliability of the data for a comprehensive interpretation of toxicity analysis.

6.4 Continuous microperfusion toxicity assays using dechorionated embryos

The application of this microfluidic embryo array is for drug toxicity screening. The proof-of-concept system was investigated by conducting FET based on the standard protocol (OECD TG 236). The objective of this experiment was to determine if the FET and Sublethal Embryo Toxicity Index (iFET) carried out on the microfluidic chip-based device was equal to or better than results from the standard toxicity test using static multiwall plates. Overall outcomes from microfluidic device performance were expected to overcome the limitations of the standard tests.

To validate and compare the performance of each method, a median lethal dose concentration (LC_{50}) for FET and half maximal response (EC_{50}) for iFET were calculated using the scoring criteria stated in the protocols. Several commonly used reference toxicants were selected to determine the effectiveness of the microfluidic device with a range of chemical compounds.

6.4.1 Toxicity analysis using FET protocols

The standard FET test (OECD TG236) protocol was first used to test the toxicity of the selected compounds. This protocol lists four lethal endpoints, such as coagulation of the embryo, lack of somite formation, non-detachment of tail, and lack of heartbeat (Figure 6.12). The endpoints were scored every 24 hours up to 72 hours. One of the heavy metal compounds, copper sulphate pentahydrate ($CuSO_4H_2O$), was selected as the reference toxicant for the tests because it is one of the toxic chemicals found in the environment. Copper is mostly found in the aquatic environment and has been identified as one of the most significant pollutants in water [278]. This substance is found to be toxic at low to high concentrations, leading to mortality of the zebrafish embryos.

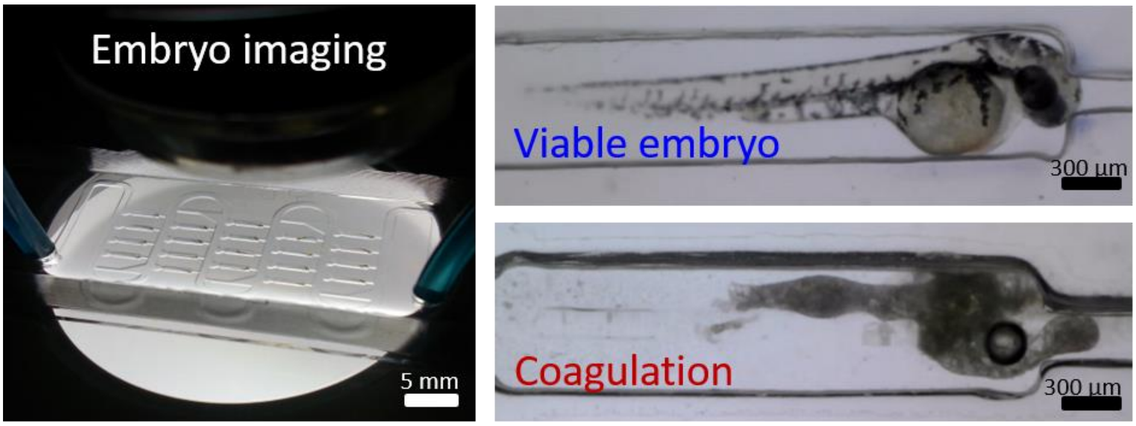

Figure 6.12 Lethal endpoints (mortality) of zebrafish embryo test at 48 hpf compared with a viable embryo (control). Mortality endpoints of coagulation are depicted. Note the lack of somite formation and non-detachment of tail were not applicable for embryos at 48 hpf. Lack of heartbeat is not illustrated here as it requires video demonstration.

6.4.2 Chorion as a barrier to toxicant absorption.

The envelope surrounding the embryos, the chorion, was found to be a barrier to the toxicant, and FET protocols were tested both with and without the chorion present. The results show that a LC50 value of 0.237 mg/L can be obtained at lower concentrations for dechorionated embryos (Figure 6.13). The corresponding values of LC50 for zebrafish embryos with the chorion were found to be 0.258 mg/L. This shows that the existence of a chorion surrounding an embryo may lead to less sensitivity to the toxicants in drug toxicity tests.

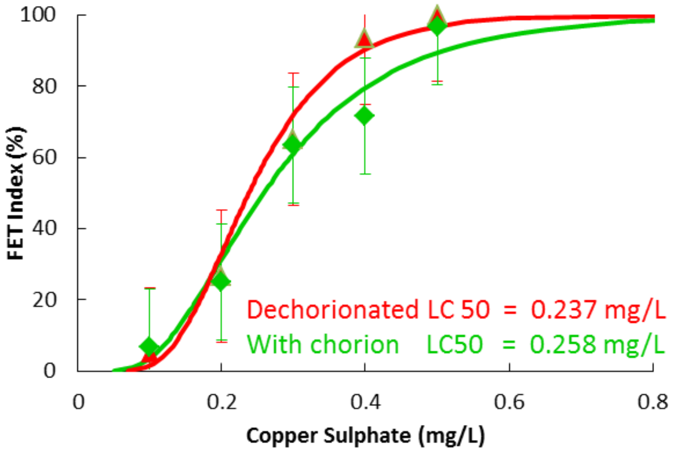

Figure 6.13 The effects of copper sulphate on zebrafish embryos with and without chorions after 72 hours of exposure. The biotests were performed in conventional static culture in 24-well plates. All embryos were loaded at 24 hpf.

The mortality results show that copper sulphate is toxic at lower concentrations without chorions. The value of LC_{50} using FET protocols was found at a lower concentration of 0.217 mg/L using microperfusion in a microfluidic environment, compared with the conventional static culture (Figure 6.14 A). A strong correlation was found for the relationship between both conditions, with a regression value of $R^2 = 0.9912$ showing that the microfluidic condition is reliable and can be used with the same protocols (Figure 6.14 B).

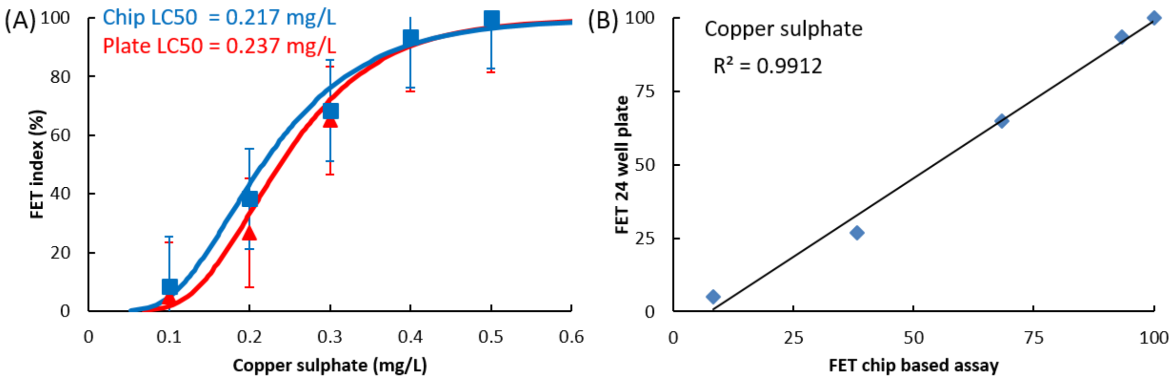

Figure 6.14 Comparison between biotest performed in microfluidic environments and conventional 24 well-plates culture. (A) Mortality (FET) was observed for copper sulphate at concentrations of 0.1 mg/L to 0.5 mg/L. Duration of the test was 72 hours. (B) Cumulative correlation analysis of copper sulphate. Excellent agreement between both microfluidic environment and static conditions, as depicted by Pearson linear correlation analysis ($P<0.01$). Error bars represent values between SE values performed by three independent experiments.

6.4.3 Sublethal Fish Embryo Toxicity Index (iFET)

A new calculation by Wigh et al. was used to calculate the iFET index [258]. This system was applied to further the conventional mortality-based FET toxicity test by including sublethal and teratogenicity factors. In order to validate and compare the performance of the methods, median lethal dose concentrations (LC_{50}) for iFET were calculated using the scoring criteria stated in the protocols in Chapter 3 (3.5.2). The scores were based on observable sublethal endpoints during imaging acquisition analysis (Figure 6.15). Commonly used reference toxicants, caffeine, phenol and nicotine, were selected to determine the applicability of the microfluidic device on the range of chemical compounds.

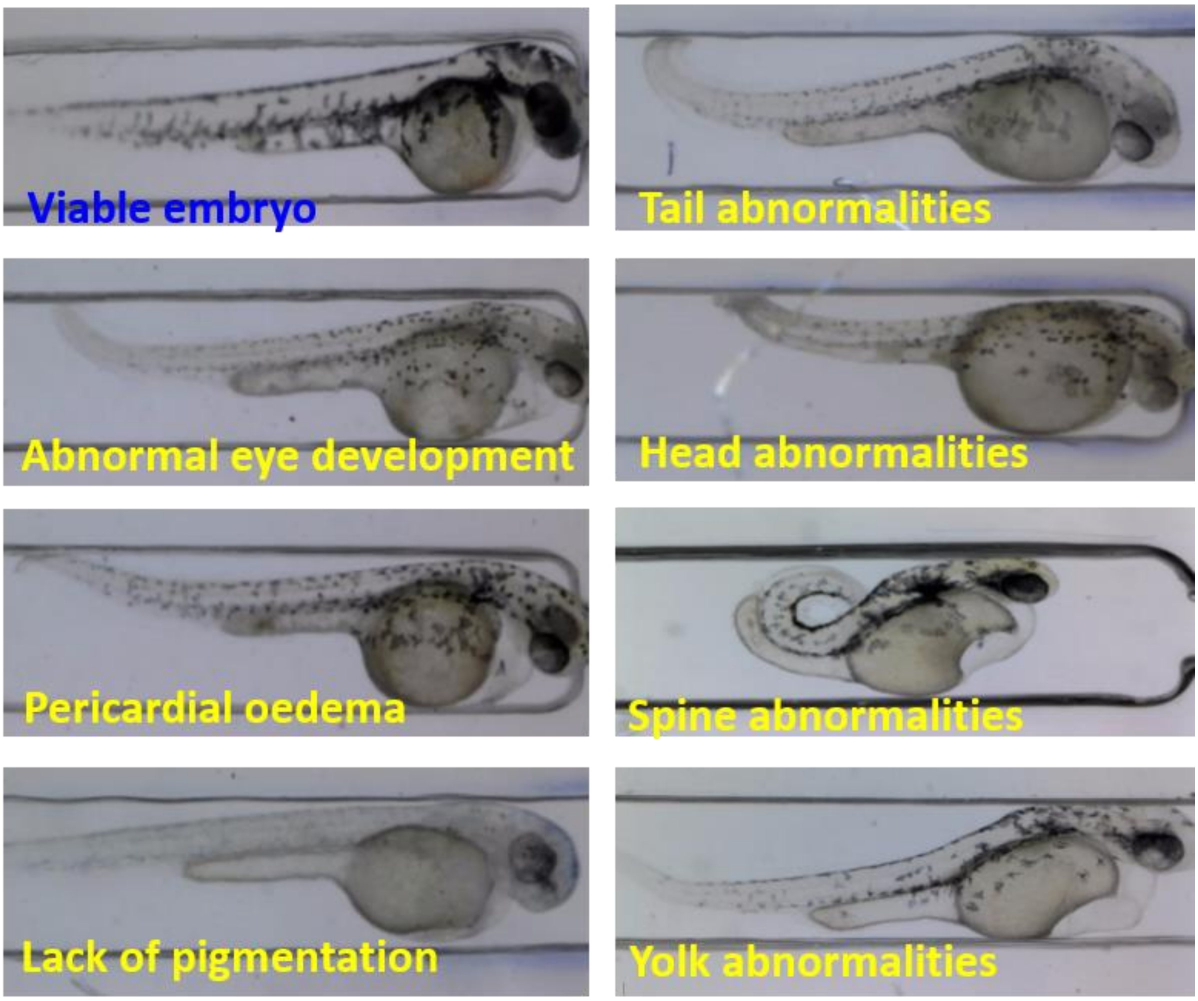

Figure 6.15 The sublethal (iFET) endpoints of the zebrafish embryo toxicity test at 48 hpf, compared with the viable embryo. iFET endpoints of abnormal eye development, pericardial oedema, lack of pigmentation, tail abnormalities, head abnormalities, spine abnormalities and yolk abnormalities are illustrated. Note that other two endpoints, heart abnormalities and blood circulation deficiency, are not demonstrated here because video capturing is required.

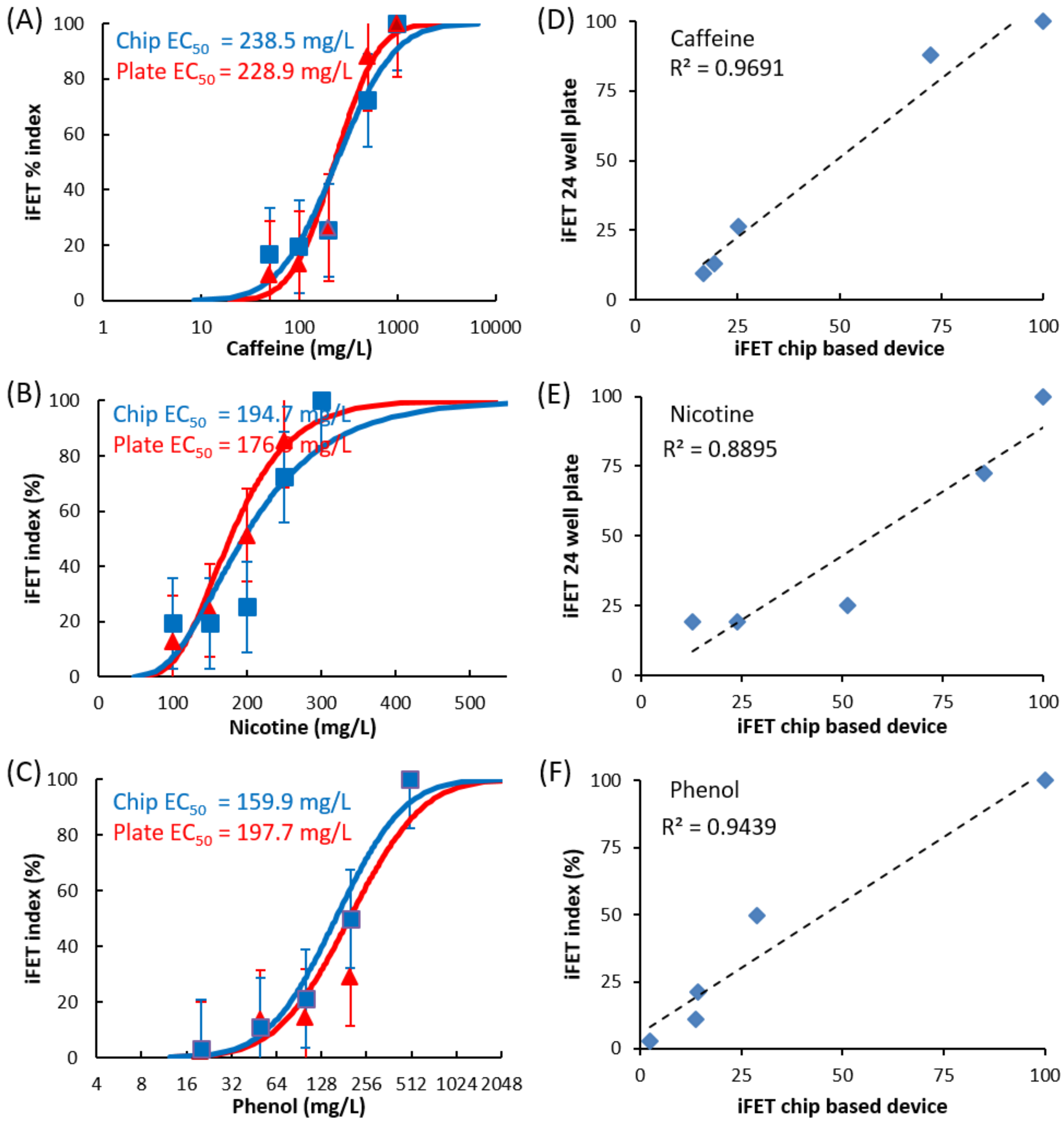

Figure 6.16 Comparison of biotests performed in a microfluidic environment and conventional static culture of 24 well-plates. iFET (sublethal/teratogenic effects) indicate the several concentrations of (A) caffeine (B) nicotine (C) phenol. Cumulative correlation of analysis of (D) caffeine (E) nicotine (F) phenol. The lab-on-chip experiments were performed at perfusion rate of 1000 µl/min. Duration of all biotests was 72 hours. The error bars represent SE values between three independent experiments.

The sublethal or teratogenic effects (iFET) were observed when 24 hpf dechorionated zebrafish embryos were exposed to caffeine, nicotine and phenol. These toxins lead to developmental abnormalities which do not cause death. For caffeine, iFET scores of 238.5 mg/L and 228.9 mg/L were determined using microperfusion and static conditions respectively (Figure 6.16 A). Linear correlation analysis for both conditions was found to have R^2 value of 0.97 (Pearson and Lee linear correlation test, P<0.01) (Figure 6.16 D). For nicotine exposure with concentrations of 100 to 300 mg/L, iFET scores were 194.7 mg/L and 176.9 mg/L under conditions of microfluidic chip-based device vs static reference, which produced R^2 value of 0.89 (Pearson and Lee correlation test, P<0.01) (Figure 6.16 B–E). Lastly, exposure to phenol returned iFET scores of 159.9 mg/L and 197.7 mg/L for the microfluidic system vs well-plate conditions. For both experimental set-ups, the R^2 value was 0.94 (Pearson and Lee correlation test, P<0.01) (Figure 6.16 C–F). Of all the compounds in the biotests, the iFET EC_{50} value of nicotine was higher than in the 24 well-plate static conditions. This shows that nicotine is less toxic to dechorionated zebrafish embryos, and corresponds to the correlation value of <90%. This was due to the characteristics of the compound itself, which is light sensitive and prone to oxidation [242]. .

Agreement between both microperfusion and static conditions was found in all used compounds including the FET and iFET protocols. The results demonstrate that a flow-through microperfusion system can increase the sensitivity commonly found in conventional 24 well- plates in OECD protocols. This system also provides more advantages compared to the static system, such as less absorption from polystyrene materials and constant renewal of the chemical compounds throughout the experiment. It also proves that a continuous perfusion system will have constant oxygen concentrations, which are important for living organisms such as zebrafish embryos.

The automated trapping and immobilisation of dechorionated embryos simplified the manual handling required by conventional toxicity tests using well plates. Using a newly designed testing platform such as microfluidic device can overcome the limitations of current ecotoxicology technologies.

6.5 Discussion and conclusions

In this project, a chip-based microfluidic device for 24 hpf dechorionated zebrafish embryo toxicity assays is developed and presented. It overcomes the laborious work in manual handling of specimens by employing hydrodynamic, automatic trapping and immobilisation of embryos. The chip also allows dechorionated embryos to be cultured in individual traps, which improves the imaging of each one. The biotest can be carried out under a continuous flow for up to 72 hours without any disturbance to the development of the embryos.

6.5.1 Design of the lab-on-chip device

A microfluidic lab-on-chip device was developed that successfully loaded, trapped and immobilised 24 hpf dechorionated embryos. It has the potential to replace conventional methods of handling small model organisms. Microfluidic systems are small and compact, offering great advantages in terms of space. In designing a microfluidic system for small model organisms such as zebrafish embryos, survival rates throughout the perfusion time are the main concern, especially for dechorionated embryos: long-term perfusion for up to 72 hours was performed to verify this was possible.

6.5.2 Comparison between FET and iFET scores on embryos

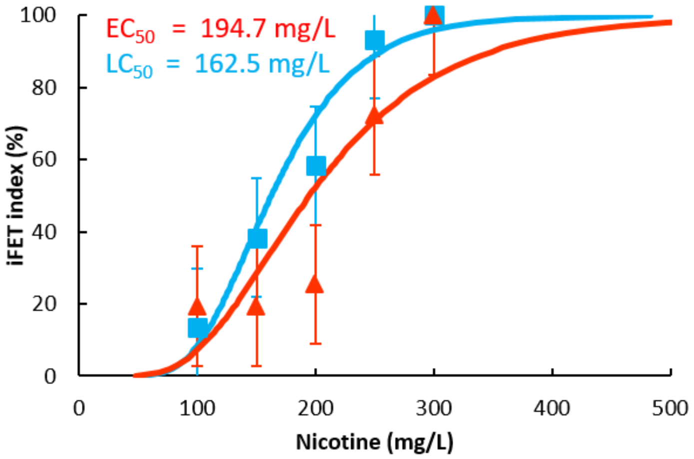

Figure 6.17 Comparison between end-point scores for FET (mortality) and iFET (sublethal/ teratogenic) after exposure of selected compounds on 24 hpf dechorionated embryos. Duration for the test was 72 hours. All tests were conducted with a chip-based device. Note that FET parameters were included in iFET calculations. The introduction of nine sublethal parameters increases the sensitivity beyond that of the standard fish embryo toxicity test.

In a standard fish embryo toxicity test, only FET endpoints are scored to determine the mortality rate of the embryos. Some compounds such as caffeine, phenol and nicotine do not cause mortality at very early stages of exposure, and is observed to have only a teratogenic effect on or to cause severe abnormalities in the embryos. Introducing sublethal endpoints to the standard protocol of the embryo test improves the sensitivity of the toxicants.

In the toxicity experiments, the results were scored using both FET endpoints (LC_{50}) and iFET endpoints (EC_{50}). EC50 values were 16 to 20% higher than LC50 values for caffeine and phenol (Figure 6.17). On the other hand, for unstable compound such as nicotine, the LC50 values were higher than EC50 values by 32%.

6.5.3 Limitations

The design of this microfluidic chip-based device was primarily to trap 24 hpf to 96 hpf by following the standard protocol for embryo toxicity testing. Toxicity data above this point could not be achieved in this case, and specially designed chambers will need to be developed to accommodate embryos up to 120 hpf. Standard FET protocols such as OECD 236 may not be suitable for embryo studies after 24 hpf, which make them less sensitive at later developmental stages than 8 hpf embryo for some compounds. A modified FET test needs to be developed to improve the accuracy of results.

7 Conclusion and Summary

The practice of using zebrafish embryos as model organisms for bioassays has increased tremendously in biomedical and environmental studies. However, few lab-on-chip technologies that are available for handling embryos allow automated trapping and high-throughput screening in a flow-through environment. The primary objective of this thesis is to fill the gap caused by this lack. First it develops a method to distinguish between viable (live) and dead embryos. Next, it explores the use of additive manufacturing technologies capable of fabricating high aspect ratios to replace the conventional lithography process of mould-making. This is followed by designing and developing a millifluidic chip-based device for trapping and immobilising zebrafish larvae for use in cardiac analysis. Finally, a lab-on-chip device for loading, trapping and immobilisation of dechorionated embryos is fabricated.

7.1 Achievement and impact

In Chapter 4, a method to develop a system able to separate live and dead embryos is demonstrated. In comparison with conventional and current embryo sorting technologies, this system is simple and compact. A proof-of-concept design for a micromechanical large particle in-flow sorter for zebrafish embryos, capable of analysing, sorting and dispensing live vs dead zebrafish, is demonstrated. This design provides a new paradigm for miniaturised and automated sorting devices capable of handling large particles such as embryos and small model organisms. This preliminary work offers a platform for improving available sorting mechanisms and equipment.

Chapter 5 presents a biocompatible chip-based physiometric microfluidic device for monitoring the cardiac function of zebrafish larvae. By employing the capabilities of 3D printing technologies, the time-consuming process of fabricating a mould are eliminated. Stereolithography technologies capable of producing high-aspect ratios with high-grade optical transparency of moulds improve the conventional method of fabricating PDMS chip-based devices using laser cutting. This new device is capable of monitoring heartbeat without human intervention, overcoming the limitations of manual work in mounting the larvae on agarose. Moreover, as a non-invasive technique this device can be used to see variations in heart rate, which is able to overcome the problmes of manual counting of heartbeat.

Chapter 6 describes the use of lab-on-chip technologies in fabricating microfluidic PDMS chip-based devices for dechorionated zebrafish embryo biotests carried out under continuous perfusion. This device is capable to perform biotests that are more effectively than conventional manual bioassays.

7.2 Limitations and future work

A detection method was developed to sort zebrafish embryos., and a sorting concept design was fabricated that could directly move sorted embryos into required channels. As a fully automation system to integrate detection and sorting still needs to be developed, future work will concentrate on developing a fully integrated sorting system combined with automated loading, real-time sort decision-making algorithms and automated dispensing of embryos for pharmacological testing.

A proof-of-concept of microfluidic design for cardiotoxicity studies on zebrafish larvae was developed here. Heart rates were measured using non-invasive methods; however, it is not clear how exactly absorption and elimination rates need to be addressed in order to achieve a precise calculation of the amount of drugs associated with the process. The larvae should be placed in array where perfusion can be carried out simultaneously with the drugs absorption of the drugs. Future works will concentrate on improving the design for pharmacological applications, particularly by integrating a monitoring system directly with programmable algorithm software to enable automatic counting of the heart beat.

A microfluidic chip device was fabricated for loading, trapping and immobilising live dechorionated embryos. Its design, however, is suitable for trapping embryos only up to 72 hours. This is because the embryos begin to swim after 96 hpf, and toxicity of the larvae beyond this period can not yet be achieved. In future, developmental work should focus on microperfusion arrays capable of docking embryos up to 120 hpf or more in specially designed chambers.

In brief, future research work will improve on the design to increase the throughput or the automation for loading and unloading of the zebrafish embryos. In addition, an integration approach of the these developed devices will also develop so that it can perform the sorting, drug testing and analysis in one Fish-on-Chip system.

Appendices

A1 Software programming

Roborealm software

Specifications

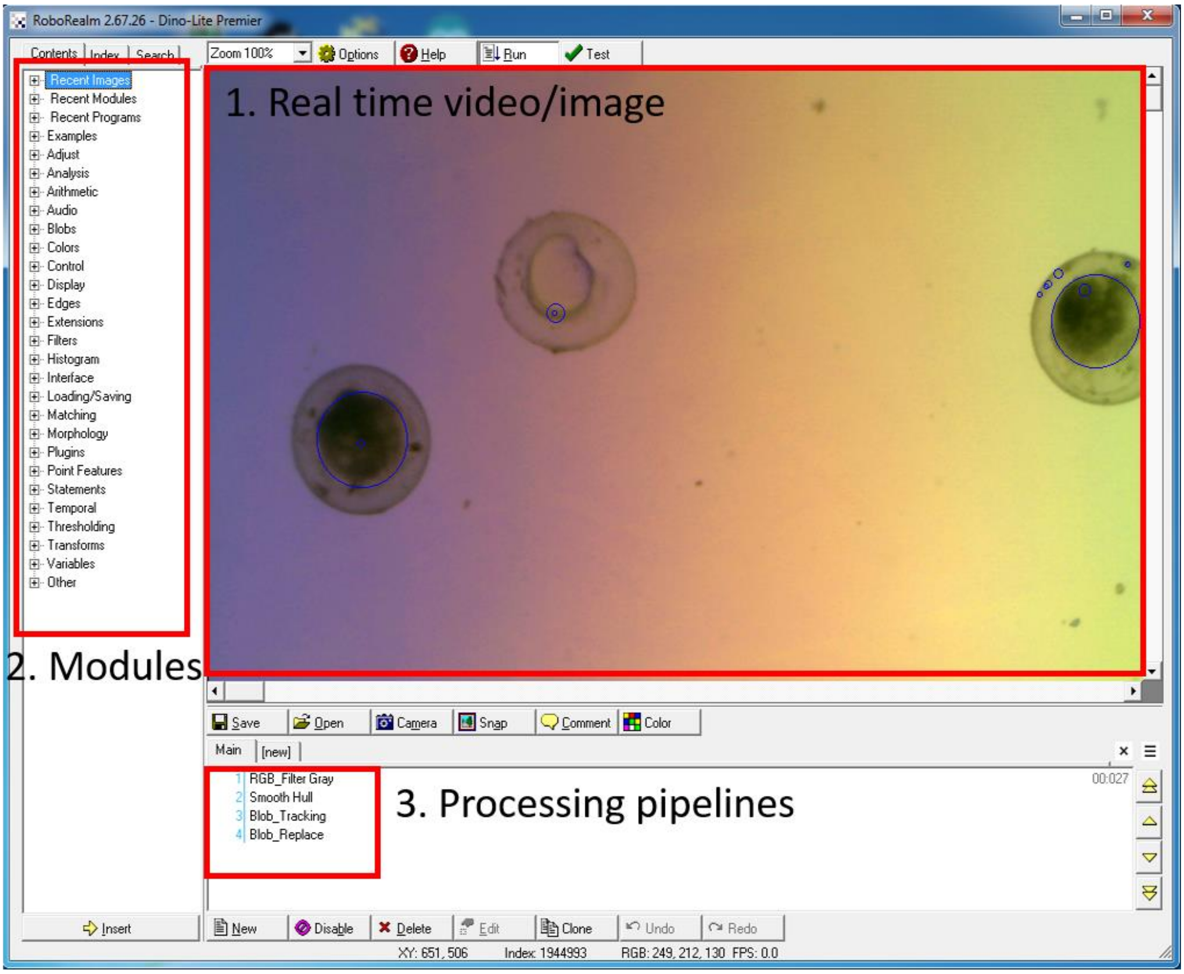

Figure 7.1 Graphic user interface of real time image processing software (RoboRealm, Machine Vision). (1) Camera connects to the software and the object appear on the image screen. (2) The specific function for image processing is selected in the Modules section. Each inserted module directly processes the image. (3) Selected modules appeared in the processing pipelines screen as algorithms. At completion of all selected modules, the image is displayed. Note the blue circle only appears when all the modules in the pipelines are processed.

Definition of algorithm terms used in image processing in Chapter 4.0:

1. RGB filter

   This module identifies and focuses on the colour pixels within an image at a given threshold and with specified colours to track. The grey filter was selected based on the colour of the current image.
2. Smooth Hull

   This is used to smooth a blob shape’s border without loss of sharp edges.
3. Blob tracking

   This module tracks an object identified from others by its pixels. It labels it with a specific identifier to differentiate it from other objects.
4. Blob replace

   The white blob in the current image will be replaced with another specific colour or shape that can be selected in the interface.
5. Canny

   This module is developed as for edge detection, and selects only the edges around the current image.
6. Circles

   This module recognises contours within a circular image. It is normally run after a contour-based module such as Canny. The module determines the contours inside a circular shape and selects that specific shape for subsequent image processing.
7. Display circle

   The shape of a circle can be drawn based on a single point and the radius. The circle will be displayed on the image screen.
8. Write AVI

   The processed video can be saved to an AVI video file and can then be played back on any AVI player. This module allows playback of the video without running the Roborealm software.

A2 Technical specifications of instruments

Microfabrication equipment

No	Instruments	Specifications/
1.	CO2 Laser Cutting System (Universal Laser Systems, VLS 3.50)	Size/Dimensions: 864 mm x 365 mm x 635 mm Work Area: 610 mm x 305 mm Optical lenses: Standard and High Power Density Focus Optics (HDPFO) Beam spot size: 100 µm (Standard 40 µm (HDPFO) Laser power: 30 W
2	Stereolithography 3D printer (ProJet HD 7000, 3D Systems)	Size/Dimensions: 1860 mm x 982 mm x 2070 mm Build Volume: 380 mm x 380 mm x 250 mm Layer resolution: 125 µm Accuracy: 0.025–0.05 mm Materials: VisiJet SL Clear, VisiJet SL Black, VisiJet SL Flex Support Material:
3	MultiJet Machining (Objet Connex 350, Stratasys)	Size/Dimensions: 1400 mm x 1260 mm x 1100 mm Build Volume: 342 mm x 342 mm x 200 mm Layer resolution: 16 µm

		Accuracy: 200 µm Materials: VeroClear, VeroPureWhite, VeroGray Support materials: SUP705 (remove by water jet)
4	High Resolution Desktop 3D Printer (Form1, FormLabs)	Size/Dimensions: 300 mm x 280 mm x 450 mm Build Volume: 125 mm x 125 mm x 165 mm Layer resolution: 25–200 µm Accuracy: 300 µm Materials: FormClear resin Support materials: Same as work material
5	Fused Deposition Modelling Desktop 3D Printer (MakerBot Replicator, Stratsys)	Size/Dimensions: 528 mm x 441 mm x 410 mm Build Volume: 295 mm x 195 mm x 165 mm Layer resolution: 100 µm Accuracy: 100–400 µm Materials: PLA filament Support materials: PLA filament

6	Peristaltic Pump (Miniplus Evolution, Gilson, Inc.)	Pump head: MF (medium flow) Flow rate: PVC tubing – up to 47 mL/min Isoversinic – up to 70 mL/min Silicone – up to 31 mL/min
7	Water bath (TW2, Julabo Labortechnik GmbH) Equipped with microprocessor technology with PID temperature controller.	Size/Dimensions: 170 mm x 160 mm x 260 mm Bath size: 150 mm x 130 mm x 110 mm Water volume: 1–2 Litre Working temperature range: 20–99.9 °C Temperature stability: ±0.2 °C
	Oxygen Plasma (Harrick Plasma,)	Size/Dimensions: 216 mm x 254 mm x 203 mm Features: Desktop unit Adjustable RF power settings (Low, medium, high) Maximum power: 18 W Working pressure: 200 mTorr
	Microscope (Leica)	
	USB Microscope (Dino-Lite, AnMo Electronics	

	Corporation, Taiwan) AM-3713 TB	Size/Dimensions: 1050 mm (length) x 320 mm (diameter) Weight: 105 g Resolution: VGA (640x480 pixels) Optimal magnification: 10–70x, 200x Sensor type: CMOS Max frame rate: 60 fps
	AD7013MZT(R4)	Size/Dimensions: 1050 mm (length) x 320 mm (diameter) Weight: 140 g Resolution: 2592 X 1944 pixels Optimal magnification: 10–50x, 240x Sensor type: CMOS Max frame rate: 30 fps
	LED Base Illumination Stage (BL-ZW1 Dino-Lite backlight pad)	Size/Dimensions: 100 mm x 90 mm x 20 mm Features: Adjustable polarisation Operating voltage: 5V Light intensity: Over 5000 cd/m2
	3D Optical Microscope (BRUKER, Contour GT-I)	Size/Dimensions: 452 mm x 534 mm x 683 mm Features: Automated stitching, scatter and grid automation Tip/tilt function: ± 5° Dual -LED illumination Vision64 analysis software (Annular analysis;

		Optical Analysis; Advanced Image Processing) Maximum scan range: Up to 10 mm Vertical resolution: < 0.01 mm Zoom lenses: 0.55x, 0.75x, 1x, 1.5x, 2x Resolution: 1280 x 960 pixels
	Stereomicroscope (Nikon SMZ18, Fluorescence Microscope)	Size/Dimensions: 337 mm x 300 mm x 492 mm Features: Built in OCC illumination Fibre light source Epi fluorescence attachment Motorised focus unit Parallel optic (zooming type) Magnification range: 3.75 – 270x Zoom ratio: 18:1 Resolution: 1280 x 960 pixels
	Microbiological Incubator (Thermo Scientific, Heratherm TM	Size/Dimensions: 470 mm x 260 mm x 415 mm Features: Control LED display Temperature uniformity (± 1.2 °C) and stability (± 0.2 °C). High temperature accuracy Temperature range: 17°C – 40 °C
	Advanced Protocol Oven (Thermo Scientific, Heratherm TM)	Size/Dimensions: 343 mm x 354 mm x 508 mm Features: Programmable microprocessor control with vacuum fluorescent display. Temperature stability (± 1.8 °C).

		High speed drying and heating Independent data monitoring Function control for rapid heating up Temperature range: up to 330 °C

References

[1] U. S. Eggert, "The why and how of phenotypic small-molecule screens," *Nature chemical biology,* vol. 9, pp. 206-209, 2013.

[2] G. Vecchio, A. Galeone, V. Brunetti, G. Maiorano, L. Rizzello, S. Sabella*, et al.*, "Mutagenic effects of gold nanoparticles induce aberrant phenotypes in Drosophila melanogaster," *Nanomedicine: Nanotechnology, Biology and Medicine,* vol. 8, pp. 1-7, 2012.

[3] D. C. Swinney and J. Anthony, "How were new medicines discovered?," *Nature reviews Drug discovery,* vol. 10, pp. 507-519, 2011.

[4] J. G. Moffat, J. Rudolph, and D. Bailey, "Phenotypic screening in cancer drug discovery—past, present and future," *Nature Reviews Drug Discovery,* vol. 13, pp. 588-602, 2014.

[5] M. Xu, K. Liu, M. Swaroop, F. D. Porter, R. Sidhu, S. Finkes*, et al.*, "δ-Tocopherol reduces lipid accumulation in Niemann-Pick type C1 and Wolman cholesterol storage disorders," *Journal of Biological Chemistry,* vol. 287, pp. 39349-39360, 2012.

[6] K. H. Bleicher, H.-J. Böhm, K. Müller, and A. I. Alanine, "Hit and lead generation: beyond high-throughput screening," *Nature reviews Drug discovery,* vol. 2, pp. 369-378, 2003.

[7] J. Giacomotto and L. Ségalat, "High-throughput screening and small animal models, where are we?," *British journal of pharmacology,* vol. 160, pp. 204-216, 2010.

[8] N. Ranganatha and I. Kuppast, "A review on alternatives to animal testing methods in drug development," *International Journal of Pharmacy and Pharmaceutical Sciences,* vol. 4, pp. 28-32, 2012.

[9] S. B. Hedges, "The origin and evolution of model organisms," *Nature Reviews Genetics,* vol. 3, pp. 838-849, 2002.

[10] A. Repiso, C. Bergantiños, M. Corominas, and F. Serras, "Tissue repair and regeneration in Drosophila imaginal discs," *Development, growth & differentiation,* vol. 53, pp. 177-185, 2011.

[11] J. Bolker, "Model organisms: There's more to life than rats and flies," *Nature,* vol. 491, pp. 31-33, 2012.

[12] T. Burne, E. Scott, B. Van Swinderen, M. Hilliard, J. Reinhard, C. Claudianos*, et al.*, "Big ideas for small brains: what can psychiatry learn from worms, flies, bees and fish?," ed: Nature Publishing Group, 2011.

[13] I. S. Pienaar, J. Götz, and M. B. Feany, "Parkinson's disease: insights from non-traditional model organisms," *Progress in neurobiology,* vol. 92, pp. 558-571, 2010.

[14] A. Chatzigeorgiou, A. Halapas, K. Kalafatakis, and E. Kamper, "The use of animal models in the study of diabetes mellitus," *In Vivo,* vol. 23, pp. 245-258, 2009.

[15] R. T. Peterson, R. Nass, W. A. Boyd, J. H. Freedman, K. Dong, and T. Narahashi, "Use of non-mammalian alternative models for neurotoxicological study," *Neurotoxicology,* vol. 29, pp. 546-555, 2008.

[16] E. A. Jones, "Xenopus: a prince among models for pronephric kidney development," *Journal of the American Society of Nephrology,* vol. 16, pp. 313-321, 2005.

[17] J. B. Karpinka, J. D. Fortriede, K. A. Burns, C. James-Zorn, V. G. Ponferrada, J. Lee*, et al.*, "Xenbase, the Xenopus model organism database; new virtualized system, data types and genomes," *Nucleic acids research,* vol. 43, pp. D756-D763, 2015.

[18] J. Bakkers, "Zebrafish as a model to study cardiac development and human cardiac disease," *Cardiovascular research,* vol. 91, pp. 279-288, 2011.

[19] C. Santoriello and L. I. Zon, "Hooked! Modeling human disease in zebrafish," *The Journal of clinical investigation,* vol. 122, pp. 2337-2343, 2012.

[20] M. Schartl, "Beyond the zebrafish: diverse fish species for modeling human disease," *Disease models & mechanisms,* vol. 7, pp. 181-192, 2014.

[21] B. Müller and U. Grossniklaus, "Model organisms—a historical perspective," *Journal of proteomics,* vol. 73, pp. 2054-2063, 2010.

[22] C. B. Kimmel, W. W. Ballard, S. R. Kimmel, B. Ullmann, and T. F. Schilling, "Stages of embryonic development of the zebrafish," *Developmental dynamics,* vol. 203, pp. 253-310, 1995.

[23] S. Mathavan, S. G. Lee, A. Mak, L. D. Miller, K. R. K. Murthy, K. R. Govindarajan*, et al.*, "Transcriptome analysis of zebrafish embryogenesis using microarrays," *PLoS Genet,* vol. 1, p. e29, 2005.

[24] S. Guo, "Using zebrafish to assess the impact of drugs on neural development and function," *Expert opinion on drug discovery,* vol. 4, pp. 715-726, 2009.

[25] H. Feitsma and E. Cuppen, "Zebrafish as a cancer model," *Molecular Cancer Research,* vol. 6, pp. 685-694, 2008.

[26] N. D. Meeker and N. S. Trede, "Immunology and zebrafish: spawning new models of human disease," *Developmental & Comparative Immunology,* vol. 32, pp. 745-757, 2008.

[27] J. Akagi, K. Khoshmanesh, B. Evans, C. J. Hall, K. E. Crosier, J. M. Cooper*, et al.*, "Miniaturized embryo array for automated trapping, immobilization and microperfusion of zebrafish embryos," *PloS one,* vol. 7, p. e36630, 2012.

[28] Nemtsas et al., "Adult zebrafish heart as a model for human heart? An electrophysiological study," *Journal of molecular and cellular cardiology,* vol. 48, pp. 161-171, 2010.

[29] Duan et al., "Cardiovascular toxicity evaluation of silica nanoparticles in endothelial cells and zebrafish model," *Biomaterials,* vol. 34, pp. 5853-5862, 2013.

[30] P. Goldsmith, "Zebrafish as a pharmacological tool: the how, why and when," *Current opinion in pharmacology,* vol. 4, pp. 504-512, 2004.

[31] S. George, T. Xia, R. Rallo, Y. Zhao, Z. Ji, S. Lin*, et al.*, "Use of a high-throughput screening approach coupled with in vivo zebrafish embryo screening to develop hazard ranking for engineered nanomaterials," *ACS nano,* vol. 5, pp. 1805-1817, 2011.

[32] K. Watanabe, Y. Nishimura, T. Nomoto, N. Umemoto, Z. Zhang, B. Zhang*, et al.*, "In vivo assessment of the permeability of the blood-brain barrier and blood-retinal barrier to fluorescent indoline derivatives in zebrafish," *BMC neuroscience,* vol. 13, p. 101, 2012.

[33] A. J. Hill, H. Teraoka, W. Heideman, and R. E. Peterson, "Zebrafish as a model vertebrate for investigating chemical toxicity," *Toxicological sciences,* vol. 86, pp. 6-19, 2005.

[34] L. Karlsson-Norrgren and P. Runn, "Cadmium dynamics in fish: pulse studies with 109Cd in female zebrafish, Brachydanio rerio," *Journal of fish biology,* vol. 27, pp. 571-581, 1985.

[35] K. P. Chandroo, I. J. Duncan, and R. D. Moccia, "Can fish suffer?: perspectives on sentience, pain, fear and stress," *Applied Animal Behaviour Science,* vol. 86, pp. 225-250, 2004.

[36] T. Braunbeck and E. Lammer, "Fish embryo toxicity assays," *German Federal Environment Agency,* pp. 1-298, 2006.

[37] A. Mohammed, T. Halfhide, and N. Elias-Samlalsingh, "Comparative sensitivity of three life stages of the tropical mysid, Metamysidopsis insularis to six toxicants," *Toxicological and Environ Chemistry,* vol. 91, pp. 1331-1337, 2009.

[38] A. Mohammed, "Why are Early Life Stages of Aquatic Organisms more Sensitive to Toxicants than Adults?," in *New Insights into Toxicity and Drug Testing*, S. Gowder, Ed., ed Rijeka: InTech, 2013, p. Ch. 03.

[39] R. Nagel, "DarT: The embryo test with the Zebrafish Danio rerio--a general model in ecotoxicology and toxicology," *Altex,* vol. 19, pp. 38-48, 2001.

[40] E. Lammer, G. Carr, K. Wendler, J. Rawlings, S. Belanger, and T. Braunbeck, "Is the fish embryo toxicity test (FET) with the zebrafish (Danio rerio) a potential alternative for the fish acute toxicity test?," *Comparative Biochemistry and Physiology Part C: Toxicology & Pharmacology,* vol. 149, pp. 196-209, 2009.

[41] X. Wang, A. L. Robertson, J. Li, R. J. Chai, W. Haishan, P. Sadiku*, et al.*, "Inhibitors of neutrophil recruitment identified using transgenic zebrafish to screen a natural product library," *Disease models & mechanisms,* vol. 7, pp. 163-169, 2014.

[42] A. L. Robertson, G. R. Holmes, A. N. Bojarczuk, J. Burgon, C. A. Loynes, M. Chimen*, et al.*, "A zebrafish compound screen reveals modulation of neutrophil reverse migration as an anti-inflammatory mechanism," *Science translational medicine,* vol. 6, pp. 225ra29-225ra29, 2014.

[43] J. M. Green, J. Metz, O. Lee, M. Trznadel, A. Takesono, A. R. Brown*, et al.*, "High-Content and Semi-Automated Quantification of Responses to Estrogenic Chemicals Using a Novel Translucent Transgenic Zebrafish," *Environmental science & technology,* vol. 50, pp. 6536-6545, 2016.

[44] J. K. Leet, C. D. Lindberg, L. A. Bassett, G. M. Isales, K. L. Yozzo, T. D. Raftery*, et al.*, "High-content screening in zebrafish embryos identifies butafenacil as a potent inducer of anemia," *PloS one,* vol. 9, p. e104190, 2014.

[45] I. Harrold, S. Carbonneau, B. M. Moore, G. Nguyen, N. M. Anderson, A. S. Saini*, et al.*, "Efficient transgenesis mediated by pigmentation rescue in zebrafish," *BioTechniques,* vol. 60, p. 13, 2016.

[46] S. Ali, H. G. Van Mil, and M. K. Richardson, "Large-scale assessment of the zebrafish embryo as a possible predictive model in toxicity testing," *PloS one,* vol. 6, p. e21076, 2011.

[47] N. Bohni, M. L. Cordero-Maldonado, J. Maes, D. Siverio-Mota, L. Marcourt, S. Munck*, et al.*, "Integration of microfractionation, qNMR and zebrafish screening for the in vivo bioassay-guided isolation and quantitative bioactivity analysis of natural products," *PLoS One,* vol. 8, p. e64006, 2013.

[48] L. Sonnack, S. Kampe, E. Muth-Köhne, L. Erdinger, N. Henny, H. Hollert*, et al.*, "Effects of metal exposure on motor neuron development, neuromasts and the escape response of zebrafish embryos," *Neurotoxicology and teratology,* vol. 50, pp. 33-42, 2015.

[49] A. Smith, "Screening for drug discovery: the leading question," *Nature,* vol. 418, pp. 453-459, 2002.

[50] I. W. Selderslaghs, A. R. Van Rompay, W. De Coen, and H. E. Witters, "Development of a screening assay to identify teratogenic and embryotoxic chemicals using the zebrafish embryo," *Reproductive toxicology,* vol. 28, pp. 308-320, 2009.

[51] A. Vogt, A. Cholewinski, X. Shen, S. G. Nelson, J. S. Lazo, M. Tsang*, et al.*, "Automated image-based phenotypic analysis in zebrafish embryos," *Developmental dynamics,* vol. 238, pp. 656-663, 2009.

[52] L. Truong, S. M. Bugel, A. Chlebowski, C. Y. Usenko, M. T. Simonich, S. L. M. Simonich*, et al.*, "Optimizing multi-dimensional high throughput screening using zebrafish," *Reproductive Toxicology,* vol. 65, pp. 139-147, 2016.

[53] L. Truong, S. L. Harper, and R. L. Tanguay, "Evaluation of embryotoxicity using the zebrafish model," *Drug Safety Evaluation: Methods and Protocols,* pp. 271-279, 2011.

[54] R. Pulak, "Techniques for analysis, sorting, and dispensing of C. elegans on the COPAS™ flow-sorting system," in *C. elegans*, ed: Springer, 2006, pp. 275-286.

[55] S. F. Graf, S. Hötzel, U. Liebel, A. Stemmer, and H. F. Knapp, "Image-based fluidic sorting system for automated Zebrafish egg sorting into multiwell plates," *Journal of the Association for Laboratory Automation,* vol. 16, pp. 105-111, 2011.

[56] C. Pardo-Martin, T.-Y. Chang, B. K. Koo, C. L. Gilleland, S. C. Wasserman, and M. F. Yanik, "High-throughput in vivo vertebrate screening," *Nature methods,* vol. 7, pp. 634-636, 2010.

[57] M. F. Yanik, C. B. Rohde, and C. Pardo-Martin, "Technologies for micromanipulating, imaging, and phenotyping small invertebrates and vertebrates," *Annual review of biomedical engineering,* vol. 13, pp. 185-217, 2011.

[58] H. P. Le, "Progress and trends in ink-jet printing technology," *Journal of Imaging Science and Technology,* vol. 42, pp. 49-62, 1998.

[59] E. Bassous, H. Taub, and L. Kuhn, "Ink jet printing nozzle arrays etched in silicon," *Applied Physics Letters,* vol. 31, pp. 135-137, 1977.

[60] S. C. Terry, J. H. Jerman, and J. B. Angell, "A gas chromatographic air analyzer fabricated on a silicon wafer," *IEEE Transactions on Electron Devices,* vol. 26, pp. 1880-1886, 1979.

[61] W. M. Saltzman and W. L. Olbricht, "Building drug delivery into tissue engineering design," *Nature Reviews Drug Discovery,* vol. 1, pp. 177-186, 2002.

[62] C. Kleinstreuer, J. Li, and J. Koo, "Microfluidics of nano-drug delivery," *International Journal of Heat and Mass Transfer,* vol. 51, pp. 5590-5597, 2008.

[63] Q. Xu, M. Hashimoto, T. T. Dang, T. Hoare, D. S. Kohane, G. M. Whitesides*, et al.*, "Preparation of monodisperse biodegradable polymer microparticles using a

microfluidic flow-focusing device for controlled drug delivery," *Small,* vol. 5, pp. 1575-1581, 2009.

[64] A. W. Martinez, S. T. Phillips, and G. M. Whitesides, "Three-dimensional microfluidic devices fabricated in layered paper and tape," *Proceedings of the National Academy of Sciences,* vol. 105, pp. 19606-19611, 2008.

[65] P. Yager, T. Edwards, E. Fu, K. Helton, K. Nelson, M. R. Tam*, et al.*, "Microfluidic diagnostic technologies for global public health," *Nature,* vol. 442, pp. 412-418, 2006.

[66] C. D. Chin, V. Linder, and S. K. Sia, "Commercialization of microfluidic point-of-care diagnostic devices," *Lab on a Chip,* vol. 12, pp. 2118-2134, 2012.

[67] M. A. McClain, C. T. Culbertson, S. C. Jacobson, N. L. Allbritton, C. E. Sims, and J. M. Ramsey, "Microfluidic devices for the high-throughput chemical analysis of cells," *Analytical chemistry,* vol. 75, pp. 5646-5655, 2003.

[68] G. T. Roman, Y. Chen, P. Viberg, A. H. Culbertson, and C. T. Culbertson, "Single-cell manipulation and analysis using microfluidic devices," *Analytical and bioanalytical chemistry,* vol. 387, pp. 9-12, 2007.

[69] A. Nilghaz, D. R. Ballerini, X.-Y. Fang, and W. Shen, "Semiquantitative analysis on microfluidic thread-based analytical devices by ruler," *Sensors and Actuators B: Chemical,* vol. 191, pp. 586-594, 2014.

[70] T. Stieglitz and J.-U. Meyer, "Biomedical microdevices for neural implants," in *BioMEMS*, ed: Springer, 2006, pp. 71-137.

[71] E. Meng and R. Sheybani, "Insight: implantable medical devices," *Lab on a Chip,* vol. 14, pp. 3233-3240, 2014.

[72] J. Fernandes, H. Dinis, L. Gonçalves, and P. Mendes, "Implantable microdevice with integrated wireless power transfer for thermal neuromodulation applications," in *e-Health Networking, Applications and Services (Healthcom), 2016 IEEE 18th International Conference on*, 2016, pp. 1-6.

[73] J. W. Gregory, J. P. Sullivan, G. Raman, and S. Raghu, "Characterization of the microfluidic oscillator," *AIAA journal,* vol. 45, pp. 568-576, 2007.

[74] A. R. Jha, *MEMS and nanotechnology-based sensors and devices for communications, medical and aerospace applications*: CRC Press, 2008.

[75] A. K. Agarwal, L. Dong, D. J. Beebe, and H. Jiang, "Autonomously-triggered microfluidic cooling using thermo-responsive hydrogels," *Lab on a Chip,* vol. 7, pp. 310-315, 2007.

[76] C.-Y. Yin, A. N. Nikoloski, and M. Wang, "Microfluidic solvent extraction of platinum and palladium from a chloride leach solution using Alamine 336," *Minerals Engineering,* vol. 45, pp. 18-21, 2013.

[77] J. P. McMullen and K. F. Jensen, "Integrated microreactors for reaction automation: new approaches to reaction development," *Annual review of analytical chemistry,* vol. 3, pp. 19-42, 2010.

[78] Y. Zhang, C. F. Wang, L. Chen, S. Chen, and A. J. Ryan, "Microfluidic Spinning: Microfluidic-Spinning-Directed Microreactors Toward Generation of Multiple Nanocrystals Loaded Anisotropic Fluorescent Microfibers (Adv. Funct. Mater. 47/2015)," *Advanced Functional Materials,* vol. 25, pp. 7396-7396, 2015.

[79] N.-T. Nguyen, S. Lassemono, and F. A. Chollet, "Optical detection for droplet size control in microfluidic droplet-based analysis systems," *Sensors and actuators B: Chemical,* vol. 117, pp. 431-436, 2006.

[80] B. Kuswandi, J. Huskens, and W. Verboom, "Optical sensing systems for microfluidic devices: a review," *Analytica chimica acta,* vol. 601, pp. 141-155, 2007.

[81] K. Ariga, Y. Yamauchi, Q. Ji, Y. Yonamine, and J. P. Hill, "Research update: Mesoporous sensor nanoarchitectonics," *Apl Materials,* vol. 2, p. 030701, 2014.

[82] D. Janasek, J. Franzke, and A. Manz, "Scaling and the design of miniaturized chemical-analysis systems," *Nature,* vol. 442, pp. 374-380, 2006.

[83] A. Manz, D. J. Harrison, E. M. Verpoorte, J. C. Fettinger, A. Paulus, H. Lüdi*, et al.*, "Planar chips technology for miniaturization and integration of separation techniques into monitoring systems: capillary electrophoresis on a chip," *Journal of Chromatography A,* vol. 593, pp. 253-258, 1992.

[84] N.-T. Nguyen and Z. Wu, "Micromixers—a review," *Journal of micromechanics and microengineering,* vol. 15, p. R1, 2004.

[85] L. Capretto, W. Cheng, M. Hill, and X. Zhang, "Micromixing within microfluidic devices," in *Microfluidics*, ed: Springer, 2011, pp. 27-68.

[86] M. Bäcker, M. Raue, S. Schusser, C. Jeitner, L. Breuer, P. Wagner*, et al.*, "Microfluidic chip with integrated microvalves based on temperature-and pH-responsive hydrogel thin films," *physica status solidi (a),* vol. 209, pp. 839-845, 2012.

[87] T. Kawai, N. Naruishi, H. Nagai, Y. Tanaka, Y. Hagihara, and Y. Yoshida, "Rotatable reagent cartridge for high-performance microvalve system on a centrifugal microfluidic device," *Analytical chemistry,* vol. 85, pp. 6587-6592, 2013.

[88] B. Wu and H.-Q. Gong, "Formation of fully closed microcapsules as microsensors by microfluidic double emulsion," *Microfluidics and nanofluidics,* vol. 14, pp. 637-644, 2013.

[89] I. Gammoudi, V. Raimbault, H. Tarbague, F. Moroté, C. Grauby-Heywang, A. Othmane*, et al.*, "Enhanced bio-inspired microsensor based on microfluidic/bacteria/love wave hybrid structure for continuous control of heavy metals toxicity in liquid medium," *Sensors and Actuators B: Chemical,* vol. 198, pp. 278-284, 2014.

[90] A. TermehYousefi, S. Bagheri, and N. Adib, "Integration of biosensors based on microfluidic: a review," *Sensor Review,* vol. 35, pp. 190-199, 2015.

[91] B.-B. Xu, R. Zhang, X.-Q. Liu, H. Wang, Y.-L. Zhang, H.-B. Jiang*, et al.*, "On-chip fabrication of silver microflower arrays as a catalytic microreactor for allowing in situ SERS monitoring," *Chemical Communications,* vol. 48, pp. 1680-1682, 2012.

[92] L. L. Xu, C. F. Wang, and S. Chen, "Microarrays formed by microfluidic spinning as multidimensional microreactors," *Angewandte Chemie International Edition,* vol. 53, pp. 3988-3992, 2014.

[93] E. Diller, S. Miyashita, and M. Sitti, "Remotely addressable magnetic composite micropumps," *Rsc Advances,* vol. 2, pp. 3850-3856, 2012.

[94] F. Abhari, H. Jaafar, and N. A. M. Yunus, "A comprehensive study of micropumps technologies," *Int. J. Electrochem. Sci,* vol. 7, pp. 9765-9780, 2012.

[95] E.-K. Fleischmann, H.-L. Liang, N. Kapernaum, F. Giesselmann, J. Lagerwall, and R. Zentel, "One-piece micropumps from liquid crystalline core-shell particles," *Nature communications,* vol. 3, p. 1178, 2012.

[96] C. Zhang, D. Xing, and Y. Li, "Micropumps, microvalves, and micromixers within PCR microfluidic chips: advances and trends," *Biotechnology advances,* vol. 25, pp. 483-514, 2007.

[97] J. Teo, P. Di Pietro, F. San Biagio, M. Capozzoli, Y.-M. Deng, I. Barr*, et al.*, "VereFlu™: an integrated multiplex RT-PCR and microarray assay for rapid detection and identification of human influenza A and B viruses using lab-on-chip technology," *Archives of virology,* vol. 156, p. 1371, 2011.

[98] M. Hiraoka, P. Fiorini, J. O'Callaghan, I. Yamashita, C. Van Hoof, and M. O. de Beeck, "Miniature conductive polymer actuators for high pressure generation in lab on chip systems," *Sensors and Actuators A: Physical,* vol. 177, pp. 23-29, 2012.

[99] L. R. Volpatti and A. K. Yetisen, "Commercialization of microfluidic devices," *Trends in biotechnology,* vol. 32, pp. 347-350, 2014.

[100] E. K. Sackmann, A. L. Fulton, and D. J. Beebe, "The present and future role of microfluidics in biomedical research," *Nature,* vol. 507, pp. 181-189, 2014.

[101] D. Mark, S. Haeberle, G. Roth, F. von Stetten, and R. Zengerle, "Microfluidic lab-on-a-chip platforms: requirements, characteristics and applications," *Chemical Society Reviews,* vol. 39, pp. 1153-1182, 2010.

[102] M. J. Madou, *Fundamentals of microfabrication: the science of miniaturization*: CRC press, 2002.

[103] M. W. Kadlec, D. You, J. C. Liao, and P. K. Wong, "A Cell Phone–Based Microphotometric System for Rapid Antimicrobial Susceptibility Testing," *Journal of laboratory automation,* vol. 19, pp. 258-266, 2014.

[104] D. Y. Stevens, C. R. Petri, J. L. Osborn, P. Spicar-Mihalic, K. G. McKenzie, and P. Yager, "Enabling a microfluidic immunoassay for the developing world by integration of on-card dry reagent storage," *Lab on a Chip,* vol. 8, pp. 2038-2045, 2008.

[105] S. Baratchi, K. Khoshmanesh, C. Sacristán, D. Depoil, D. Wlodkowic, P. McIntyre*, et al.*, "Immunology on chip: Promises and opportunities," *Biotechnology advances,* vol. 32, pp. 333-346, 2014.

[106] S. Takayama, E. Ostuni, X. Qian, J. C. McDonald, X. Jiang, P. LeDuc*, et al.*, "Topographical micropatterning of poly (dimethylsiloxane) using laminar flows of liquids in capillaries," *Advanced materials,* vol. 13, pp. 570-574, 2001.

[107] C. W. Shields IV, C. D. Reyes, and G. P. López, "Microfluidic cell sorting: a review of the advances in the separation of cells from debulking to rare cell isolation," *Lab on a Chip,* vol. 15, pp. 1230-1249, 2015.

[108] A. K. White, M. VanInsberghe, I. Petriv, M. Hamidi, D. Sikorski, M. A. Marra*, et al.*, "High-throughput microfluidic single-cell RT-qPCR," *Proceedings of the National Academy of Sciences,* vol. 108, pp. 13999-14004, 2011.

[109] K. Leung, H. Zahn, T. Leaver, K. M. Konwar, N. W. Hanson, A. P. Pagé*, et al.*, "A programmable droplet-based microfluidic device applied to multiparameter analysis of single microbes and microbial communities," *Proceedings of the National Academy of Sciences,* vol. 109, pp. 7665-7670, 2012.

[110] O. J. Miller, A. El Harrak, T. Mangeat, J.-C. Baret, L. Frenz, B. El Debs*, et al.*, "High-resolution dose–response screening using droplet-based microfluidics," *Proceedings of the National Academy of Sciences,* vol. 109, pp. 378-383, 2012.

[111] S. Mondal, E. Hegarty, C. Martin, S. K. Gökçe, N. Ghorashian, and A. Ben-Yakar, "Large-scale microfluidics providing high-resolution and high-throughput screening of Caenorhabditis elegans poly-glutamine aggregation model," *Nature communications,* vol. 7, 2016.

[112] C. M. B. Ho, S. H. Ng, K. H. H. Li, and Y.-J. Yoon, "3D printed microfluidics for biological applications," *Lab on a Chip,* vol. 15, pp. 3627-3637, 2015.

[113] T. A. Duncombe, A. M. Tentori, and A. E. Herr, "Microfluidics: reframing biological enquiry," *Nature Reviews Molecular Cell Biology,* vol. 16, pp. 554-567, 2015.

[114] J. P. Brody, P. Yager, R. E. Goldstein, and R. H. Austin, "Biotechnology at low Reynolds numbers," *Biophysical journal,* vol. 71, pp. 3430-3441, 1996.

[115] E. J. Shaughnessy, I. M. Katz, and J. P. Schaffer, *Introduction to fluid mechanics* vol. 8: Oxford University Press New York, 2005.

[116] A. Groisman and S. R. Quake, "A microfluidic rectifier: anisotropic flow resistance at low Reynolds numbers," *Physical review letters,* vol. 92, p. 094501, 2004.

[117] G. Sun, T. Gao, X. Zhao, and H. Zhang, "Fabrication of micro/nano dual-scale structures by improved deep reactive ion etching," *Journal of Micromechanics and Microengineering,* vol. 20, p. 075028, 2010.

[118] A. Ghobeity, H. J. Crabtree, M. Papini, and J. K. Spelt, "Characterisation and comparison of microfluidic chips formed using abrasive jet micromachining and wet etching," *Journal of Micromechanics and Microengineering,* vol. 22, p. 025014, 2012.

[119] P. Pal and K. Sato, "Fabrication methods based on wet etching process for the realization of silicon MEMS structures with new shapes," *Microsystem technologies,* vol. 16, pp. 1165-1174, 2010.

[120] M. E. Vlachopoulou, G. Kokkoris, C. Cardinaud, E. Gogolides, and A. Tserepi, "Plasma etching of poly (dimethylsiloxane): roughness formation, mechanism, control, and application in the fabrication of microfluidic structures," *Plasma Processes and Polymers,* vol. 10, pp. 29-40, 2013.

[121] M. E. Wilson, N. Kota, Y. Kim, Y. Wang, D. B. Stolz, P. R. LeDuc*, et al.*, "Fabrication of circular microfluidic channels by combining mechanical micromilling and soft lithography," *Lab on a Chip,* vol. 11, pp. 1550-1555, 2011.

[122] D. J. Guckenberger, T. E. de Groot, A. M. Wan, D. J. Beebe, and E. W. Young, "Micromilling: a method for ultra-rapid prototyping of plastic microfluidic devices," *Lab on a Chip,* vol. 15, pp. 2364-2378, 2015.

[123] J. Greener, W. Li, J. Ren, D. Voicu, V. Pakharenko, T. Tang*, et al.*, "Rapid, cost-efficient fabrication of microfluidic reactors in thermoplastic polymers by combining photolithography and hot embossing," *Lab on a Chip,* vol. 10, pp. 522-524, 2010.

[124] R. Osellame, G. Cerullo, and R. Ramponi, *Femtosecond laser micromachining: photonic and microfluidic devices in transparent materials* vol. 123: Springer Science & Business Media, 2012.

[125] K. Sugioka, J. Xu, D. Wu, Y. Hanada, Z. Wang, Y. Cheng*, et al.*, "Femtosecond laser 3D micromachining: a powerful tool for the fabrication of microfluidic, optofluidic, and electrofluidic devices based on glass," *Lab on a Chip,* vol. 14, pp. 3447-3458, 2014.

[126] G. M. Whitesides, "The origins and the future of microfluidics," *Nature,* vol. 442, pp. 368-373, 2006.

[127] L. T.-H. Kao, L. Shankar, T. G. Kang, G. Zhang, G. K. I. Tay, S. R. M. Rafei*, et al.*, "Multiplexed detection and differentiation of the DNA strains for influenza A (H1N1 2009) using a silicon-based microfluidic system," *Biosensors and Bioelectronics,* vol. 26, pp. 2006-2011, 2011.

[128] Z. Wang, W. Wang, W. Wang, L. Xu, G. Chen, and F. Fu, "Separation and determination of β-casomorphins by using glass microfluidic chip electrophoresis together with laser-induced fluorescence detection," *Journal of separation science,* vol. 34, pp. 196-201, 2011.

[129] L. Romoli, G. Tantussi, and G. Dini, "Experimental approach to the laser machining of PMMA substrates for the fabrication of microfluidic devices," *Optics and Lasers in Engineering,* vol. 49, pp. 419-427, 2011.

[130] M. Haiducu, M. Rahbar, I. Foulds, R. Johnstone, D. Sameoto, and M. Parameswaran, "Deep-UV patterning of commercial grade PMMA for low-cost, large-scale microfluidics," *Journal of Micromechanics and Microengineering,* vol. 18, p. 115029, 2008.

[131] S. Prakash and S. Kumar, "Fabrication of microchannels on transparent PMMA using CO2 Laser (10.6 μm) for microfluidic applications: An experimental investigation," *International Journal of Precision Engineering and Manufacturing,* vol. 16, pp. 361-366, 2015.

[132] J. Friend and L. Yeo, "Fabrication of microfluidic devices using polydimethylsiloxane," *Biomicrofluidics,* vol. 4, p. 026502, 2010.

[133] L. K. Fiddes, N. Raz, S. Srigunapalan, E. Tumarkan, C. A. Simmons, A. R. Wheeler*, et al.*, "A circular cross-section PDMS microfluidics system for replication of cardiovascular flow conditions," *Biomaterials,* vol. 31, pp. 3459-3464, 2010.

[134] K. Eyer, K. Root, T. Robinson, and P. S. Dittrich, "A simple low-cost method to enhance luminescence and fluorescence signals in PDMS-based microfluidic devices," *RSC Advances,* vol. 5, pp. 12511-12516, 2015.

[135] X. Zhang, L. Wang, and E. Levänen, "Superhydrophobic surfaces for the reduction of bacterial adhesion," *Rsc Advances,* vol. 3, pp. 12003-12020, 2013.

[136] T.-F. Hong, W.-J. Ju, M.-C. Wu, C.-H. Tai, C.-H. Tsai, and L.-M. Fu, "Rapid prototyping of PMMA microfluidic chips utilizing a CO2 laser," *Microfluidics and nanofluidics,* vol. 9, pp. 1125-1133, 2010.

[137] P. S. Nunes, P. D. Ohlsson, O. Ordeig, and J. P. Kutter, "Cyclic olefin polymers: emerging materials for lab-on-a-chip applications," *Microfluidics and nanofluidics,* vol. 9, pp. 145-161, 2010.

[138] H. Becker and L. E. Locascio, "Polymer microfluidic devices," *Talanta,* vol. 56, pp. 267-287, 2002.

[139] J. C. McDonald and G. M. Whitesides, "Poly (dimethylsiloxane) as a material for fabricating microfluidic devices," *Accounts of chemical research,* vol. 35, pp. 491-499, 2002.

[140] J. Kuncova-Kallio and P. J. Kallio, "PDMS and its suitability for analytical microfluidic devices," in *Engineering in Medicine and Biology Society, 2006. EMBS'06. 28th Annual International Conference of the IEEE*, 2006, pp. 2486-2489.

[141] A. Lamberti, S. Marasso, and M. Cocuzza, "PDMS membranes with tunable gas permeability for microfluidic applications," *Rsc Advances,* vol. 4, pp. 61415-61419, 2014.

[142] D. Qin, Y. Xia, and G. M. Whitesides, "Soft lithography for micro-and nanoscale patterning," *Nature protocols,* vol. 5, pp. 491-502, 2010.

[143] S.-H. Cho, W.-S. Chang, K.-R. Kim, and J. W. Hong, "Femtosecond laser embedded grating micromachining of flexible PDMS plates," *Optics Communications,* vol. 282, pp. 1317-1321, 2009.

[144] W. M. Moreau, *Semiconductor lithography: principles, practices, and materials*: Springer Science & Business Media, 2012.

[145] S. Kumagai, T. Yamamoto, H. Kubo, and M. Sasaki, "Photoresist spray coating for 3D MEMS/NEMS," in *Nanotechnology Materials and Devices Conference (NMDC), 2012 IEEE*, 2012, pp. 124-127.

[146] A. Bonakdar, S. J. Jang, and H. Mohseni, "Novel high-throughput and maskless photolithography to fabricate plasmonic molecules," *Journal of Vacuum Science & Technology B,* vol. 32, p. 020604, 2014.

[147] S. Y. Leigh, A. Tattu, J. S. Mitchell, and E. Entcheva, "M3: Microscope-based maskless micropatterning with dry film photoresist," *Biomedical microdevices,* vol. 13, pp. 375-381, 2011.

[148] Z. Yin, E. Cheng, and H. Zou, "A novel hybrid patterning technique for micro and nanochannel fabrication by integrating hot embossing and inverse UV photolithography," *Lab on a Chip,* vol. 14, pp. 1614-1621, 2014.

[149] Y. Xia and G. M. Whitesides, "Soft lithography," *Annual review of materials science,* vol. 28, pp. 153-184, 1998.

[150] A. Khademhosseini, K. Y. Suh, J. M. Yang, G. Eng, J. Yeh, S. Levenberg, *et al.*, "Layer-by-layer deposition of hyaluronic acid and poly-L-lysine for patterned cell co-cultures," *Biomaterials,* vol. 25, pp. 3583-3592, 2004.

[151] J. R. Anderson, D. T. Chiu, H. Wu, O. Schueller, and G. M. Whitesides, "Fabrication of microfluidic systems in poly (dimethylsiloxane)," *Electrophoresis,* vol. 21, pp. 27-40, 2000.

[152] Y. Zhang, C.-W. Lo, J. A. Taylor, and S. Yang, "Replica molding of high-aspect-ratio polymeric nanopillar arrays with high fidelity," *Langmuir,* vol. 22, pp. 8595-8601, 2006.

[153] D. Sticker, M. Rothbauer, S. Lechner, M.-T. Hehenberger, and P. Ertl, "Multi-layered, membrane-integrated microfluidics based on replica molding of a thiol–ene epoxy thermoset for organ-on-a-chip applications," *Lab on a Chip,* vol. 15, pp. 4542-4554, 2015.

[154] S. Darvishi, T. Cubaud, and J. P. Longtin, "Ultrafast laser machining of tapered microchannels in glass and PDMS," *Optics and Lasers in Engineering,* vol. 50, pp. 210-214, 2012.

[155] R. R. Gattass and E. Mazur, "Femtosecond laser micromachining in transparent materials," *Nature photonics,* vol. 2, pp. 219-225, 2008.

[156] M. Bhuyan, O. Jedrkiewicz, V. Sabonis, M. Mikutis, S. Recchia, A. Aprea*, et al.*, "High-speed laser-assisted cutting of strong transparent materials using picosecond Bessel beams," *Applied Physics A,* vol. 120, pp. 443-446, 2015.

[157] M. Beresna, M. Gecevičius, and P. G. Kazansky, "Ultrafast laser direct writing and nanostructuring in transparent materials," *Advances in Optics and Photonics,* vol. 6, pp. 293-339, 2014.

[158] P. J. Kitson, M. H. Rosnes, V. Sans, V. Dragone, and L. Cronin, "Configurable 3D-Printed millifluidic and microfluidic 'lab on a chip'reactionware devices," *Lab on a Chip,* vol. 12, pp. 3267-3271, 2012.

[159] A. Bertsch, S. Jiguet, P. Bernhard, and P. Renaud, "Microstereolithography: a review," in *MRS Proceedings*, 2002, p. LL1. 1.

[160] C. W. Hull, "Apparatus for production of three-dimensional objects by stereolithography," ed: Google Patents, 1986.

[161] B. C. Gross, J. L. Erkal, S. Y. Lockwood, C. Chen, and D. M. Spence, "Evaluation of 3D printing and its potential impact on biotechnology and the chemical sciences," ed: ACS Publications, 2014.

[162] R. Liska, M. Schuster, R. Inführ, C. Turecek, C. Fritscher, B. Seidl*, et al.*, "Photopolymers for rapid prototyping," *Journal of Coatings Technology and Research,* vol. 4, pp. 505-510, 2007.

[163] M. N. Cooke, J. P. Fisher, D. Dean, C. Rimnac, and A. G. Mikos, "Use of stereolithography to manufacture critical-sized 3D biodegradable scaffolds for bone

ingrowth," *Journal of Biomedical Materials Research Part B: Applied Biomaterials,* vol. 64, pp. 65-69, 2003.

[164] M. Hofmann, "3D printing gets a boost and opportunities with polymer materials," *ACS Macro Letters,* vol. 3, pp. 382-386, 2014.

[165] B. Berman, "3-D printing: The new industrial revolution," *Business horizons,* vol. 55, pp. 155-162, 2012.

[166] F. Zhu, J. Skommer, N. P. Macdonald, T. Friedrich, J. Kaslin, and D. Wlodkowic, "Three-dimensional printed millifluidic devices for zebrafish embryo tests," *Biomicrofluidics,* vol. 9, p. 046502, 2015.

[167] D. Pham and S. S. Dimov, *Rapid manufacturing: the technologies and applications of rapid prototyping and rapid tooling*: Springer Science & Business Media, 2012.

[168] S. Bose, S. Vahabzadeh, and A. Bandyopadhyay, "Bone tissue engineering using 3D printing," *Materials Today,* vol. 16, pp. 496-504, 2013.

[169] P. X. Lan, J. W. Lee, Y.-J. Seol, and D.-W. Cho, "Development of 3D PPF/DEF scaffolds using micro-stereolithography and surface modification," *Journal of Materials Science: Materials in Medicine,* vol. 20, pp. 271-279, 2009.

[170] A. Ronca, L. Ambrosio, and D. Grijpma, "Preparation of designed poly (d, l-lactide)/nanosized hydroxyapatite composite structures by stereolithography," *Acta biomaterialia,* vol. 9, pp. 5989-5996, 2013.

[171] B. C. Gross, J. L. Erkal, S. Y. Lockwood, C. Chen, and D. M. Spence, "Evaluation of 3D printing and its potential impact on biotechnology and the chemical sciences," *Analytical chemistry,* vol. 86, pp. 3240-3253, 2014.

[172] T. Billiet, M. Vandenhaute, J. Schelfhout, S. Van Vlierberghe, and P. Dubruel, "A review of trends and limitations in hydrogel-rapid prototyping for tissue engineering," *Biomaterials,* vol. 33, pp. 6020-6041, 2012.

[173] J. L. Erkal, A. Selimovic, B. C. Gross, S. Y. Lockwood, E. L. Walton, S. McNamara*, et al.*, "3D printed microfluidic devices with integrated versatile and reusable electrodes," *Lab on a Chip,* vol. 14, pp. 2023-2032, 2014.

[174] M. Emons, K. Obata, T. Binhammer, A. Ovsianikov, B. N. Chichkov, and U. Morgner, "Two-photon polymerization technique with sub-50 nm resolution by sub-10 fs laser pulses," *Optical Materials Express,* vol. 2, pp. 942-947, 2012.

[175] R. Anitha, S. Arunachalam, and P. Radhakrishnan, "Critical parameters influencing the quality of prototypes in fused deposition modelling," *Journal of Materials Processing Technology,* vol. 118, pp. 385-388, 2001.

[176] J. W. Stansbury and M. J. Idacavage, "3D printing with polymers: Challenges among expanding options and opportunities," *Dental Materials,* 2015.

[177] J. Meakin, D. Shepherd, and D. Hukins, "Fused deposition models from CT scans," *The British journal of radiology,* 2014.

[178] M. Centola, A. Rainer, C. Spadaccio, S. De Porcellinis, J. Genovese, and M. Trombetta, "Combining electrospinning and fused deposition modeling for the fabrication of a hybrid vascular graft," *Biofabrication,* vol. 2, p. 014102, 2010.

[179] J. Korpela, A. Kokkari, H. Korhonen, M. Malin, T. Närhi, and J. Seppälä, "Biodegradable and bioactive porous scaffold structures prepared using fused deposition modeling," *Journal of Biomedical Materials Research Part B: Applied Biomaterials,* vol. 101, pp. 610-619, 2013.

[180] J. Skowyra, K. Pietrzak, and M. A. Alhnan, "Fabrication of extended-release patient-tailored prednisolone tablets via fused deposition modelling (FDM) 3D printing," *European Journal of Pharmaceutical Sciences,* vol. 68, pp. 11-17, 2015.

[181] F. Ning, W. Cong, J. Qiu, J. Wei, and S. Wang, "Additive manufacturing of carbon fiber reinforced thermoplastic composites using fused deposition modeling," *Composites Part B: Engineering,* vol. 80, pp. 369-378, 2015.

[182] A. K. Sood, R. Ohdar, and S. Mahapatra, "Parametric appraisal of mechanical property of fused deposition modelling processed parts," *Materials & Design,* vol. 31, pp. 287-295, 2010.

[183] CustomPartNet. (2008, 12 November). *Additive fabrication: Ink Jet Printing*. Available: http://www.custompartnet.com/wu/ink-jet-printing

[184] J. Perelaer, B.-J. de Gans, and U. S. Schubert, "Ink-jet printing and microwave sintering of conductive silver tracks," *ADVANCED MATERIALS-DEERFIELD BEACH THEN WEINHEIM-,* vol. 18, p. 2101, 2006.

[185] B. K. Park, D. Kim, S. Jeong, J. Moon, and J. S. Kim, "Direct writing of copper conductive patterns by ink-jet printing," *Thin Solid Films,* vol. 515, pp. 7706-7711, 2007.

[186] P.-E. Delannoy, B. Riou, B. Lestriez, D. Guyomard, T. Brousse, and J. Le Bideau, "Toward fast and cost-effective ink-jet printing of solid electrolyte for lithium microbatteries," *Journal of Power Sources,* vol. 274, pp. 1085-1090, 2015.

[187] N. Caro, E. Medina, M. Díaz-Dosque, L. López, L. Abugoch, and C. Tapia, "Novel active packaging based on films of chitosan and chitosan/quinoa protein printed with chitosan-tripolyphosphate-thymol nanoparticles via thermal ink-jet printing," *Food Hydrocolloids,* vol. 52, pp. 520-532, 2016.

[188] S. L. Sing, Y. Miao, F. E. Wiria, and W. Y. Yeong, "Manufacturability and mechanical testing considerations of metallic scaffolds fabricated using selective laser melting: a review," *Biomedical Science and Engineering,* vol. 1, 2016.

[189] K. Zeng, D. Pal, and B. Stucker, "A review of thermal analysis methods in Laser Sintering and Selective Laser Melting," in *Proceedings of Solid Freeform Fabrication Symposium Austin, TX*, 2012.

[190] E. Olakanmi, R. Cochrane, and K. Dalgarno, "A review on selective laser sintering/melting (SLS/SLM) of aluminium alloy powders: Processing, microstructure, and properties," *Progress in Materials Science,* vol. 74, pp. 401-477, 2015.

[191] I. T. Ozbolat and Y. Yu, "Bioprinting toward organ fabrication: challenges and future trends," *IEEE Transactions on Biomedical Engineering,* vol. 60, pp. 691-699, 2013.

[192] I. T. Ozbolat, H. Chen, and Y. Yu, "Development of 'Multi-arm Bioprinter'for hybrid biofabrication of tissue engineering constructs," *Robotics and Computer-Integrated Manufacturing,* vol. 30, pp. 295-304, 2014.

[193] L. E. Bertassoni, M. Cecconi, V. Manoharan, M. Nikkhah, J. Hjortnaes, A. L. Cristino*, et al.*, "Hydrogel bioprinted microchannel networks for vascularization of tissue engineering constructs," *Lab on a Chip,* vol. 14, pp. 2202-2211, 2014.

[194] K. G. Lee, K. J. Park, S. Seok, S. Shin, J. Y. Park, Y. S. Heo*, et al.*, "3D printed modules for integrated microfluidic devices," *RSC Advances,* vol. 4, pp. 32876-32880, 2014.

[195] O. Paydar, C. Paredes, Y. Hwang, J. Paz, N. Shah, and R. Candler, "Characterization of 3D-printed microfluidic chip interconnects with integrated O-rings," *Sensors and Actuators A: Physical,* vol. 205, pp. 199-203, 2014.

[196] A. K. Au, N. Bhattacharjee, L. F. Horowitz, T. C. Chang, and A. Folch, "3D-printed microfluidic automation," *Lab on a chip,* vol. 15, pp. 1934-1941, 2015.

[197] E. R. Choban, L. J. Markoski, A. Wieckowski, and P. J. Kenis, "Microfluidic fuel cell based on laminar flow," *Journal of Power Sources,* vol. 128, pp. 54-60, 2004.

[198] C.-C. Hong, J.-W. Choi, and C. H. Ahn, "A novel in-plane passive microfluidic mixer with modified Tesla structures," *Lab on a Chip,* vol. 4, pp. 109-113, 2004.

[199] J.-H. Tsai and L. Lin, "Active microfluidic mixer and gas bubble filter driven by thermal bubble micropump," *Sensors and Actuators A: Physical,* vol. 97, pp. 665-671, 2002.

[200] A. Bonyár, H. Sántha, B. Ring, M. Varga, J. G. Kovács, and G. Harsányi, "3D Rapid Prototyping Technology (RPT) as a powerful tool in microfluidic development," *Procedia Engineering,* vol. 5, pp. 291-294, 2010.

[201] C. I. Rogers, K. Qaderi, A. T. Woolley, and G. P. Nordin, "3D printed microfluidic devices with integrated valves," *Biomicrofluidics,* vol. 9, p. 016501, 2015.

[202] H. Gong, A. T. Woolley, and G. P. Nordin, "High density 3D printed microfluidic valves, pumps, and multiplexers," *Lab on a Chip,* vol. 16, pp. 2450-2458, 2016.

[203] S. Takenaga, B. Schneider, E. Erbay, M. Biselli, T. Schnitzler, M. J. Schöning*, et al.*, "Fabrication of biocompatible lab-on-chip devices for biomedical applications by means of a 3D-printing process," *physica status solidi (a),* vol. 212, pp. 1347-1352, 2015.

[204] M. Nakamura, A. Kobayashi, F. Takagi, A. Watanabe, Y. Hiruma, K. Ohuchi*, et al.*, "Biocompatible inkjet printing technique for designed seeding of individual living cells," *Tissue engineering,* vol. 11, pp. 1658-1666, 2005.

[205] L. Krejcova, L. Nejdl, M. A. M. Rodrigo, M. Zurek, M. Matousek, D. Hynek*, et al.*, "3D printed chip for electrochemical detection of influenza virus labeled with CdS quantum dots," *Biosensors and Bioelectronics,* vol. 54, pp. 421-427, 2014.

[206] A. Baraket, N. Zine, M. Lee, J. Bausells, N. Jaffrezic-Renault, F. Bessueille*, et al.*, "Development of a flexible microfluidic system based on a simple and reproducible sealing process between polymers and poly (dimethylsiloxane)," *Microelectronic Engineering,* vol. 111, pp. 332-338, 2013.

[207] X. Lin, S. Wang, X. Yu, Z. Liu, F. Wang, W. T. Li*, et al.*, "High-throughput mapping of brain-wide activity in awake and drug-responsive vertebrates," *Lab on a Chip,* 2015.

[208] M. Heckele and W. Schomburg, "Review on micro molding of thermoplastic polymers," *Journal of Micromechanics and Microengineering,* vol. 14, p. R1, 2003.

[209] J. Faber, P. M. Berto, and M. Quaresma, "Rapid prototyping as a tool for diagnosis and treatment planning for maxillary canine impaction," *American journal of orthodontics and dentofacial orthopedics,* vol. 129, pp. 583-589, 2006.

[210] F. Rengier, A. Mehndiratta, H. von Tengg-Kobligk, C. M. Zechmann, R. Unterhinninghofen, H.-U. Kauczor*, et al.*, "3D printing based on imaging data: review of medical applications," *International journal of computer assisted radiology and surgery,* vol. 5, pp. 335-341, 2010.

[211] N. P. MacDonald, Z. Feng, C. Hall, J. Reboud, K. Crosier, P. Crosier*, et al.*, "Assessment of Biocompatibility of 3D printed Photopolymers using Zebrafish Embryo Toxicity Assays," *Lab on a Chip,* 2015.

[212] A. Bonyár, H. Sántha, M. Varga, B. Ring, A. Vitéz, and G. Harsányi, "Characterization of rapid PDMS casting technique utilizing molding forms fabricated by 3D rapid prototyping technology (RPT)," *International Journal of Material Forming,* vol. 7, pp. 189-196, 2014.

[213] King et al., "Interdroplet bilayer arrays in millifluidic droplet traps from 3D-printed moulds," *Lab on a Chip,* vol. 14, pp. 722-729, 2014.

[214] Y. Hwang, O. H. Paydar, and R. N. Candler, "Pneumatic microfinger with balloon fins for linear motion using 3D printed molds," *Sensors and Actuators A: Physical,* vol. 234, pp. 65-71, 2015.

[215] H. N. Chan, Y. Chen, Y. Shu, Y. Chen, Q. Tian, and H. Wu, "Direct, one-step molding of 3D-printed structures for convenient fabrication of truly 3D PDMS microfluidic chips," *Microfluidics and nanofluidics,* vol. 19, pp. 9-18, 2015.

[216] Y. Hwang, D. Seo, M. Roy, E. Han, R. N. Candler, and S. Seo, "Capillary flow in PDMS cylindrical microfluidic channel using 3-D printed mold," *Journal of Microelectromechanical Systems,* vol. 25, pp. 238-240, 2016.

[217] H. Hwang and H. Lu, "Microfluidic tools for developmental studies of small model organisms–nematodes, fruit flies, and zebrafish," *Biotechnology journal,* vol. 8, pp. 192-205, 2013.

[218] E. Lammer, H. Kamp, V. Hisgen, M. Koch, D. Reinhard, E. Salinas*, et al.*, "Development of a flow-through system for the fish embryo toxicity test (FET) with the zebrafish (Danio rerio)," *Toxicology in vitro,* vol. 23, pp. 1436-1442, 2009.

[219] A. Funfak, A. Brösing, M. Brand, and J. M. Köhler, "Micro fluid segment technique for screening and development studies on Danio rerio embryos," *Lab on a Chip,* vol. 7, pp. 1132-1138, 2007.

[220] Y.-c. Shen, D. Li, A. Al-Shoaibi, T. Bersano-Begey, H. Chen, S. Ali*, et al.*, "A student team in a University of Michigan biomedical engineering design course constructs a microfluidic bioreactor for studies of zebrafish development," *Zebrafish,* vol. 6, pp. 201-213, 2009.

[221] F. Yang, Z. Chen, J. Pan, X. Li, J. Feng, and H. Yang, "An integrated microfluidic array system for evaluating toxicity and teratogenicity of drugs on embryonic zebrafish developmental dynamics," *Biomicrofluidics,* vol. 5, p. 024115, 2011.

[222] D. Choudhury, D. van Noort, C. Iliescu, B. Zheng, K.-L. Poon, S. Korzh*, et al.*, "Fish and Chips: a microfluidic perfusion platform for monitoring zebrafish development," *Lab on a Chip,* vol. 12, pp. 892-900, 2012.

[223] J. Akagi, K. Khoshmanesh, C. J. Hall, K. E. Crosier, P. S. Crosier, J. M. Cooper*, et al.*, "Fish on chips: automated microfluidic living embryo arrays," *Procedia Engineering,* vol. 47, pp. 84-87, 2012.

[224] J. Akagi, K. Khoshmanesh, C. J. Hall, J. M. Cooper, K. E. Crosier, P. S. Crosier*, et al.*, "Fish on chips: Microfluidic living embryo array for accelerated in vivo angiogenesis assays," *Sensors and Actuators B: Chemical,* vol. 189, pp. 11-20, 2013.

[225] C. Zheng, H. Zhou, X. Liu, Y. Pang, B. Zhang, and Y. Huang, "Fish in chips: an automated microfluidic device to study drug dynamics in vivo using zebrafish embryos," *Chemical Communications,* vol. 50, pp. 981-984, 2014.

[226] T. Schwerte and R. Fritsche, "Understanding cardiovascular physiology in zebrafish and Xenopus larvae: the use of microtechniques," *Comparative Biochemistry and Physiology Part A: Molecular & Integrative Physiology,* vol. 135, pp. 131-145, 2003.

[227] P. Jagadeeswaran, R. Paris, and P. Rao, "Laser-induced thrombosis in zebrafish larvae: a novel genetic screening method for thrombosis," *Cardiovascular Disease: Methods and Protocols Volume 2: Molecular Medicine,* pp. 187-195, 2007.

[228] J. Malicki, A. Avanesov, J. Li, S. Yuan, and Z. Sun, "Analysis of cilia structure and function in zebrafish," *Methods Cell Biol,* vol. 101, pp. 39-74, 2011.

[229] T.-Y. Chang, C. Pardo-Martin, A. Allalou, C. Wählby, and M. F. Yanik, "Fully automated cellular-resolution vertebrate screening platform with parallel animal processing," *Lab on a Chip,* vol. 12, pp. 711-716, 2012.

[230] T. Friedrich, F. Zhu, D. Wlodkowic, and J. Kaslin, "A homeostatic, chip-based platform for zebrafish larvae immobilization and long-term imaging," in *SPIE Micro+ Nano Materials, Devices, and Applications*, 2015, pp. 96682Y-96682Y-10.

[231] L. L. Bischel, B. R. Mader, J. M. Green, A. Huttenlocher, and D. J. Beebe, "Zebrafish Entrapment By Restriction Array (ZEBRA) device: a low-cost, agarose-free zebrafish mounting technique for automated imaging," *Lab on a Chip,* vol. 13, pp. 1732-1736, 2013.

[232] J. Akagi, F. Zhu, J. Skommer, C. J. Hall, P. S. Crosier, M. Cialkowski*, et al.*, "Microfluidic device for a rapid immobilization of Zebrafish larvae in environmental scanning electron microscopy," *Cytometry Part A,* vol. 87, pp. 190-194, 2015.

[233] X. Lin, S. Wang, X. Yu, Z. Liu, F. Wang, W. T. Li*, et al.*, "High-throughput mapping of brain-wide activity in awake and drug-responsive vertebrates," *Lab on a Chip,* vol. 15, pp. 680-689, 2015.

[234] S. Hong, P. Lee, S. C. Baraban, and L. P. Lee, "A novel long-term, multi-channel and non-invasive electrophysiology platform for Zebrafish," *Scientific Reports,* vol. 6, 2016.

[235] I. Kevin, K. Wang, Z. Salcic, J. Yeh, J. Akagi, F. Zhu*, et al.*, "Toward embedded laboratory automation for smart lab-on-a-chip embryo arrays," *Biosensors and Bioelectronics,* vol. 48, pp. 188-196, 2013.

[236] J. Akagi, F. Zhu, C. J. Hall, K. E. Crosier, P. S. Crosier, and D. Wlodkowic, "Integrated chip-based physiometer for automated fish embryo toxicity biotests in pharmaceutical screening and ecotoxicology," *Cytometry Part A,* vol. 85, pp. 537-547, 2014.

[237] F. Zhu, J. Akagi, C. J. Hall, K. E. Crosier, P. S. Crosier, P. Delaage*, et al.*, "A high-throughput lab-on-a-chip interface for zebrafish embryo tests in drug discovery and

ecotoxicology," in *SPIE Micro+ Nano Materials, Devices, and Applications*, 2013, pp. 892345-892345-9.

[238] R. Gomez-Sjoberg, A. A. Leyrat, B. T. Houseman, K. Shokat, and S. R. Quake, "Biocompatibility and Reduced Drug Absorption of Sol− Gel-Treated Poly (dimethyl siloxane) for Microfluidic Cell Culture Applications," *Analytical chemistry,* vol. 82, pp. 8954-8960, 2010.

[239] S. Lindström and H. Andersson-Svahn, "Overview of single-cell analyses: microdevices and applications," *Lab on a Chip,* vol. 10, pp. 3363-3372, 2010.

[240] E. M. Wielhouwer, S. Ali, A. Al-Afandi, M. T. Blom, M. B. O. Riekerink, C. Poelma*, et al.*, "Zebrafish embryo development in a microfluidic flow-through system," *Lab on a Chip,* vol. 11, pp. 1815-1824, 2011.

[241] P. M. Valencia, O. C. Farokhzad, R. Karnik, and R. Langer, "Microfluidic technologies for accelerating the clinical translation of nanoparticles," *Nature nanotechnology,* vol. 7, pp. 623-629, 2012.

[242] F. Zhu, A. Wigh, T. Friedrich, A. Devaux, S. Bony, D. Nugegoda*, et al.*, "Automated lab-on-a-chip technology for fish embryo toxicity tests performed under continuous microperfusion (µFET)," *Environmental science & technology,* vol. 49, pp. 14570-14578, 2015.

[243] P. McGrath and C.-Q. Li, "Zebrafish: a predictive model for assessing drug-induced toxicity," *Drug discovery today,* vol. 13, pp. 394-401, 2008.

[244] J. J. Zhu, Y. Q. Xu, J. H. He, H. P. Yu, C. J. Huang, J. M. Gao*, et al.*, "Human cardiotoxic drugs delivered by soaking and microinjection induce cardiovascular toxicity in zebrafish," *Journal of Applied Toxicology,* vol. 34, pp. 139-148, 2014.

[245] W. Heideman, D. S. Antkiewicz, S. A. Carney, and R. E. Peterson, "Zebrafish and cardiac toxicology," *Cardiovascular toxicology,* vol. 5, pp. 203-214, 2005.

[246] N. Rana, M. Moond, A. Marthi, S. Bapatla, T. Sarvepalli, K. Chatti*, et al.*, "Caffeine-induced effects on heart rate in zebrafish embryos and possible mechanisms of action: an effective system for experiments in chemical biology," *Zebrafish,* vol. 7, pp. 69-81, 2010.

[247] D. J. Milan and C. A. MacRae, "Cardiotoxicity studies in zebrafish," *Zebrafish: Methods for Assessing Drug Safety and Toxicity,* pp. 55-63, 2012.

[248] D. R. Brown, L. A. Samsa, L. Qian, and J. Liu, "Advances in the study of heart development and disease using Zebrafish," *Journal of cardiovascular development and disease,* vol. 3, p. 13, 2016.

[249] J. Skommer and D. Wlodkowic, "Successes and future outlook for microfluidics-based cardiovascular drug discovery," *Expert opinion on drug discovery,* vol. 10, pp. 231-244, 2015.

[250] Y. Li, F. Yang, Z. Chen, L. Shi, B. Zhang, J. Pan*, et al.*, "Zebrafish on a chip: a novel platform for real-time monitoring of drug-induced developmental toxicity," *PloS one,* vol. 9, p. e94792, 2014.

[251] J. R. Mathias, M. T. Saxena, and J. S. Mumm, "Advances in zebrafish chemical screening technologies," *Future medicinal chemistry,* vol. 4, pp. 1811-1822, 2012.

[252] S. F. Graf, T. Madigou, R. Li, C. Chesné, A. Stemmer, and H. F. Knapp, "Fully automated microinjection system for Xenopus laevis oocytes with integrated sorting and collection," *Journal of the Association for Laboratory Automation,* vol. 16, pp. 186-196, 2011.

[253] N. P. Macdonald, F. Zhu, C. Hall, J. Reboud, P. Crosier, E. Patton*, et al.*, "Assessment of biocompatibility of 3D printed photopolymers using zebrafish embryo toxicity assays," *Lab on a Chip,* vol. 16, pp. 291-297, 2016.

[254] A. Johnson, E. Carew, and K. Sloman, "The effects of copper on the morphological and functional development of zebrafish embryos," *Aquatic Toxicology,* vol. 84, pp. 431-438, 2007.

[255] O. Bar-Ilan, K. M. Louis, S. P. Yang, J. A. Pedersen, R. J. Hamers, R. E. Peterson*, et al.*, "Titanium dioxide nanoparticles produce phototoxicity in the developing zebrafish," *Nanotoxicology,* vol. 6, pp. 670-679, 2012.

[256] K. Henn and T. Braunbeck, "Dechorionation as a tool to improve the fish embryo toxicity test (FET) with the zebrafish (Danio rerio)," *Comparative Biochemistry and Physiology Part C: Toxicology & Pharmacology,* vol. 153, pp. 91-98, 2011.

[257] OECD, *Test No. 236: Fish Embryo Acute Toxicity (FET) Test*: OECD Publishing.

[258] A. Wigh, S. Bony, A. Devaux, A. Gonzalez-Ospina, and B. Domenjoud, "Proposal for a sublethal toxicity test using zebrafish embryo," *Poster presentation (WE026),* 2015.

[259] G. Eren, O. Aubreton, F. Meriaudeau, L. S. Secades, D. Fofi, A. T. Naskali*, et al.*, "Scanning from heating: 3D shape estimation of transparent objects from local surface heating," *Optics express,* vol. 17, pp. 11457-11468, 2009.

[260] D. T. Frazier and T. Narahashi, "Tricaine (MS-222): effects on ionic conductances of squid axon membranes," *European journal of pharmacology,* vol. 33, pp. 313-317, 1975.

[261] B. S. Muntean, C. M. Horvat, J. H. Behler, W. A. AbouAlaiwi, A. M. Nauli, F. E. Williams*, et al.*, "A comparative study of embedded and anesthetized zebrafish in vivo on myocardiac calcium oscillation and heart muscle contraction," 2010.

[262] A. Kaufmann, M. Mickoleit, M. Weber, and J. Huisken, "Multilayer mounting enables long-term imaging of zebrafish development in a light sheet microscope," *Development,* vol. 139, pp. 3242-3247, 2012.

[263] M. P. Craig, S. D. Gilday, and J. R. Hove, "Dose-dependent effects of chemical immobilization on the heart rate of embryonic zebrafish," *LAB ANIMAL-NEW YORK-,* vol. 35, p. 41, 2006.

[264] O. Renaud, P. Herbomel, and K. Kissa, "Studying cell behavior in whole zebrafish embryos by confocal live imaging: application to hematopoietic stem cells," *Nature protocols,* vol. 6, pp. 1897-1904, 2011.

[265] M. Folkesson, N. Sadowska, S. Vikingsson, M. Karlsson, C.-J. Carlhäll, T. Länne*, et al.*, "Differences in cardiovascular toxicities associated with cigarette smoking and snuff use revealed using novel zebrafish models," *Biology Open,* vol. 5, pp. 970-978, 2016.

[266] B. A. Barton, "Stress in fishes: a diversity of responses with particular reference to changes in circulating corticosteroids," *Integrative and comparative biology,* vol. 42, pp. 517-525, 2002.

[267] A. Zulli, R. M. Smith, P. Kubatka, J. Novak, Y. Uehara, H. Loftus*, et al.*, "Caffeine and cardiovascular diseases: critical review of current research," *European journal of nutrition,* vol. 55, pp. 1331-1343, 2016.

[268] R. E. Wilson, H. S. Kado, R. Samson, and A. B. Miller, "A case of caffeine-induced coronary artery vasospasm of a 17-year-old male," *Cardiovascular toxicology,* vol. 12, pp. 175-179, 2012.

[269] R. S. Rodriguez, R. Haugen, A. Rueber, and C.-c. Huang, "Reversible neuronal and muscular toxicity of caffeine in developing vertebrates," *Comparative Biochemistry and Physiology Part C: Toxicology & Pharmacology,* vol. 163, pp. 47-54, 2014.

[270] A. Massarsky, N. Jayasundara, J. M. Bailey, A. N. Oliveri, E. D. Levin, G. Prasad*, et al.*, "Teratogenic, bioenergetic, and behavioral effects of exposure to total particulate matter on early development of zebrafish (Danio rerio) are not mimicked by nicotine," *Neurotoxicology and teratology,* vol. 51, pp. 77-88, 2015.

[271] E. R. Spindel and C. T. McEvoy, "The role of nicotine in the effects of maternal smoking during pregnancy on lung development and childhood respiratory disease. Implications for dangers of e-cigarettes," *American journal of respiratory and critical care medicine,* vol. 193, pp. 486-494, 2016.

[272] L. D. Ellis, E. C. Soo, J. C. Achenbach, M. G. Morash, and K. H. Soanes, "Use of the zebrafish larvae as a model to study cigarette smoke condensate toxicity," *PloS one,* vol. 9, p. e115305, 2014.

[273] N. J. Palpant, P. Hofsteen, L. Pabon, H. Reinecke, and C. E. Murry, "Cardiac development in zebrafish and human embryonic stem cells is inhibited by exposure to tobacco cigarettes and e-cigarettes," *PloS one,* vol. 10, p. e0126259, 2015.

[274] F. H. Mateus, J. S. Lepera, M. P. Marques, V. B. Boralli, and V. L. Lanchote, "Simultaneous analysis of the enantiomers of verapamil and norverapamil in rat plasma by liquid chromatography-tandem mass spectrometry," *Journal of pharmaceutical and biomedical analysis,* vol. 45, pp. 762-768, 2007.

[275] M. Kaur, K. B. Ita, I. E. Popova, S. J. Parikh, and D. A. Bair, "Microneedle-assisted delivery of verapamil hydrochloride and amlodipine besylate," *European Journal of Pharmaceutics and Biopharmaceutics,* vol. 86, pp. 284-291, 2014.

[276] Y. M. S. Mobarak and M. M. Sharaf, "Lead acetate-induced histopathological changes in the gills and digestive system of silver sailfin molly (Poecilia latipinna)," *International Journal of Zoological Research,* vol. 7, p. 1, 2011.

[277] R. Tendulkar, K. Chaudhari, A. Fernandes, and P. Ratnaparkhi, "AnEvaluation of Lead (Pb) Toxicity in Developing Zebrafish (Daniorerio) Embryos," *International Journal,* vol. 3, pp. 498-504, 2015.

[278] R. L. Donnachie, A. C. Johnson, C. Moeckel, M. G. Pereira, and J. P. Sumpter, "Using risk-ranking of metals to identify which poses the greatest threat to freshwater organisms in the UK," *Environmental Pollution,* vol. 194, pp. 17-23, 2014.